

Managing Florida's Fracture Critical Bridges - Phases I & II



Huy Pham
Jawad Gull, Ph.D.
Alireza Mohammadi
Atorod Azizinamini, Ph.D., P.E.

**Department of Civil and Environmental Engineering
Florida International University
Miami, Florida**

10555 W. Flagler Street, EC 3600
Miami, FL 33174

Sponsored By
Florida Department of Transportation

May 2016

F
I
N
A
L

R
E
P
O
R
T

Disclaimer

The opinions, findings, and conclusions expressed in this publication are those of the authors and not necessarily those of the Florida Department of Transportation.

Metric Conversion Tables

Approximate conversion to SI Units

Symbol	When you know	Multiply by	To find	Symbol
Length				
in	inches	25.4	millimeters	mm
ft	feet	0.305	meters	m
yd	yards	0.914	meters	m
mi	miles	1.61	kilometers	km
Area				
in²	square inches	645.2	square millimeters	mm ²
ft²	square feet	0.093	square meters	m ²
yd²	square yard	0.836	square meters	m ²
ac	acres	0.405	hectares	ha
mi²	square miles	2.59	square kilometers	km ²
Volume				
fl oz	fluid ounces	29.57	milliliters	mL
gal	gallons	3.785	liters	L
ft³	cubic feet	0.028	cubic meters	m ³
yd³	cubic yards	0.765	cubic meters	m ³
Mass				
oz	ounces	28.35	grams	g
lb	pounds	0.454	kilograms	kg
T	short tons (2000 lb)	0.907	megagrams (or "metric ton")	Mg (or "t")
Temperature				
°F	Fahrenheit	5 (F-32)/9 or (F-32)/1.8	Celsius	°C
Illumination				
fc	foot-candles	10.76	lux	lx
fl	foot-Lamberts	3.426	candela/m ²	cd/m ²
Force and Pressure or Stress				
lbf	pound force	4.45	newtons	N
lbf/in²	pound force per square inch	6.89	kilopascals	kPa

Approximate conversion to U.S. Customary Units

Symbol	When you know	Multiply by	To find	Symbol
Length				
mm	millimeters	0.039	inches	in
m	meters	3.28	feet	ft
m	meters	1.09	yards	yd
km	kilometers	0.621	miles	mi
Area				
mm²	square millimeters	0.0016	square inches	in ²
m²	square meters	10.764	square feet	ft ²
m²	square meters	1.195	square yards	yd ²
ha	hectares	2.47	acres	ac
km²	square kilometers	0.386	square miles	mi ²
Volume				
mL	milliliters	0.034	fluid ounces	fl oz
L	liters	0.264	gallons	gal
m³	cubic meters	35.314	cubic feet	ft ³
m³	cubic meters	1.307	cubic yards	yd ³
Mass				
g	grams	0.035	ounces	oz
kg	kilograms	2.202	pounds	lb
Mg (or "t")	megagrams (or "metric ton")	1.103	short tons (2000 lb)	T
Temperature				
°C	Celsius	1.8C+32	Fahrenheit	°F
Illumination				
lx	lux	0.0929	foot-candles	fc
cd/m²	candela/m ²	0.2919	foot-Lamberts	fl
Force and Pressure or Stress				
N	newtons	0.225	pound force	lbf
kPa	kilopascals	0.145	pound force per square inch	lbf/in ²

Technical Report Documentation

1. Report No.	2. Government Accession No.	3. Recipient's Catalog No.	
4. Title and Subtitle Managing Florida's Fracture Critical Bridges - Phases I & II		5. Report Date May 2016	
		6. Performing Organization Code	
7. Author(s) Huy Pham, Jawad Gull, Alireza Mohammadi, Atorod Azizinamini		8. Performing Organization Report No.	
9. Performing Organization Name and Address Florida International University, Miami http://research.fiu.edu/ University Park, Room P.C. 539 Miami, FL 33199-0000 USA		10. Work Unit No. (TRAIS)	
		11. Contract or Grant No. BDV29-977-17	
12. Sponsoring Agency Name and Address Florida Department of Transportation 605 Suwannee Street Tallahassee, FL 32399 USA		13. Type of Report and Period Covered. Final Report May 2011 to May 2016	
		14. Sponsoring Agency Code	
15. Supplementary Notes			
16. Abstract			
<p>Based on the definition given in the <i>AASHTO LRFD Bridge Design Specifications</i>, twin steel box-girder bridges are classified as bridges with fracture critical members (FCMs), in which a failure of a tension member is expected to lead to a collapse of the bridge. However, a number of such bridges with either a partial or full-depth crack in one girder have been reported and are still providing service without collapsing. The main objective of this research project is to understand the behavior of twin steel box-girder bridges and to develop methods for evaluating their redundancy level in the event of the fracture of one tension member.</p> <p>The research project included an experimental investigation on a small-scale steel twin box-girder bridge, field testing of a full-scale twin box-girder, analysis of existing research and design data, and an extensive amount of numerical analyses carried out on calibrated 3-D nonlinear finite element models. The results from this study provide in-depth understanding of twin steel box-girder bridge behavior before and after a fracture in the tension member occurs. In addition to the experimentally verified finite element method, the report also proposes a simplified method for evaluating the performance of twin steel box-girder bridges and provides a list of important factors that could control the reserve capacity of the damaged bridge.</p> <p>A result of this project is the development of a comprehensive roadmap for assessing the redundancy of twin steel box-girder bridges in which the elements of the roadmap are identified, and solutions for several of the steps are provided. The development of solutions for remaining steps of the roadmap is proposed for a future research.</p>			
17. Key Words fracture critical, steel twin box-girder, bridge, redundancy evaluation, finite element analysis		18. Distribution Statement No restrictions.	
19. Security Classif. (of this report) Unclassified	20. Security Classif. (of this page) Unclassified	21. No. of Pages 232	22. Price

Acknowledgements

The authors would like to thank the Florida Department of Transportation (FDOT) and the project manager Richard Kerr.

Executive Summary

Approximately 11% of steel bridges in the United States contain fracture critical members (FCMs), and 386 of them are located in Florida. The majority are twin steel box-girder bridge systems. According to AASHTO *LRFD Bridge Design Specifications* (2010), a failure of a tension member such as bottom flange and web would lead to a collapse of the entire bridge. Since 1988, National Bridge Inspection Standards (NBIS) have required a special hands-on inspection, typically every two years, due to the perceived increased risk of collapse. This requirement imposes an expensive additional cost to the bridge owners and maintenance agencies.

However, a number of such bridges with a partial or full-depth crack in one girder have been reported and are still providing service without collapsing, among them the Lafayette Bridge on US-52 Hwy over the Mississippi River and the Neville Island Bridge in Pittsburgh, PA (Fisher et al., 1977, and Schwendeman and Hedgren, 1978). These examples suggest that the stability of the bridge is not always linked strictly to the performance of FCMs, and a redundant load path might exist even though it is not accredited in the current definition of bridges with FCMs. Therefore, if steel twin box-girder bridge systems can be proved to be redundant and thus eliminated from the fracture critical list, a significant savings in terms of inspection and maintenance costs may be realized.

This research examines the possibility of removing twin steel box-girder bridges from the fracture critical list. The primary objectives are to provide an understanding of the behavior of twin steel box-girder bridges and to develop a tool that can quantify the redundancy level of these bridges in the event that one girder is completely fractured. The outcomes of this research will be used in the future to develop a general comprehensive redundancy assessment procedure for any twin steel box-girder bridge in the next phases of the research.

In order to achieve these objectives, elastic field tests were carried out on an existing twin steel box-girder bridge to comprehend the response of a full-scale bridge under elastic loads. To comprehend the nonlinear behavior of twin steel box-girder bridges, a small-scale test specimen was constructed in the laboratory, and numerous tests were carried out. One of the main objectives of these field and laboratory tests was to develop a test-verified and calibrated 3-D nonlinear finite element model (FEM) that could then be used to carry out parametric studies to better comprehend the behaviors and performance of twin steel box-girder bridges in both elastic and nonlinear ranges.

Field testing of the Ft. Lauderdale Ramp Bridge 860600 was first carried out in May 2012. The structure was a curved steel twin box-girder bridge with three spans and total length of 455 ft. The bridge was tested under a total of eight loading scenarios. The load was applied by running either one truck or two trucks over the bridge at crawling speed and at 30 MPH. The acquired data were

reviewed and analyzed, showing the structure was behaving in a linear elastic manner. The live load impact factor was found to be 1.2.

Laboratory tests of a small-scale steel twin box-girder bridge specimen were carried out from November 2013 to February 2015 in 24 experiments, including 18 elastic static tests, one cyclic test, and five ultimate tests. The specimen was tested under three different damage states, including the undamaged state, the bottom flange fractured state, and the full-web fractured state. In both damage states, the damage or fracture was only simulated in only one girder, the east one. For each damage state, the same six elastic tests were carried out to investigate the effects of railing system, continuity, and loading configurations. Under the bottom flange fractured state, an additional cyclic loading test was performed before tests on the specimen with the full-web fractured damage were carried out. All ultimate load tests were carried out under the full-web fractured damage condition.

For the elastic tests, the specimen was loaded with either 50 kips (1 kip = 1,000 lbf) for unsymmetrical loading case or 100 kips for symmetrical loading case. The load was applied through a 2-in.-thick steel-reinforced elastomeric loading pad over an area of 9 in. x 36 in., covering the entire width of a girder. Depending on the characteristics of each test, the railings, the continuity, or both were installed. Important observations from the 18 elastic tests are summarized as follows:

- The rail and continuity helped to increase the load-carrying capacity of the specimen. As the damage intensity increases, their beneficial effects also increase. For instance, the rail and continuity effects together reduced the displacement of the damaged girder by 14.3%, 17.4%, and 24.8% for the undamaged, bottom flange fractured and full-web fractured damage states, respectively.
- In addition to the deck, cross-frames were found to play an important role in transferring the load from the damaged girder to the intact girder. Similar to the effects of the rail and continuity, the more damage the bridge experienced, the more important the cross-frames were. The estimated contribution of cross-frames was 5%, 5%, and 19% for the undamaged, bottom flange fractured and full-web fractured damage states, respectively. However, it should be mentioned that the relatively large contribution of cross-frames found in these experiments could be related to the scale of the test specimen used.
- In general, the elastic responses of the specimen under the undamaged and bottom flange fractured damage states were comparable. For instance, the maximum displacement of the damaged girder increased by an average of 6.5% when the bottom flange was fractured.
- As a result, the average maximum strain of all six elastic tests, in the intact girder increased 5% when the bottom flange of EG was fractured and 138% when the entire webs of EG

were fractured. This indicates that as the damage takes place, the load resisted by the damaged girder is transferred to the intact girder.

- When the bottom flange and webs were completely fractured, the flexural stiffness of that damaged girder and its contribution to the load-carrying capacity of the specimen were negligible.

During the cyclic test, the initial bottom flange crack penetrated into the web and reached the top flange after about 213,000 loading cycles. Some minor cracks were observed on the deck near the loading area. The collected data showed that the change of responses such as displacement, stiffness, crack base opening, and cross-frame forces was solely dependent on the rate of crack growth.

In ultimate Test A, the load was applied through a 2-in.-thick steel-reinforced elastomeric pad over an area of 9 in. x 36 in., covering the entire width of one girder from the outside facet of the inside top flange to the outside facet of the outside top flange of the fractured girder. The loading pad size in this test was the same as it was in the elastic tests. The bridge specimen obtained its maximum capacity at 156 kips of load at 2.5-in. displacement before crushing of the deck underneath the loading pad was observed. After that damage, the load-carrying capacity of the specimen dropped and fluctuated between 123 kips and 144 kips. The test was halted at 5.5-in. displacement due to a significant decrease in the specimen's load-carrying capacity. During this extended loading period, the cracking and crushing of the concrete deck propagated toward two ends of the specimen, especially along the inside top flange of the damaged girder. Several cross-frame connections failed, and the intact girder was uplifted from the support. No yielding was observed in the intact girder.

In ultimate Test B, which had the same loaded area to Test A but with the loading point moved over the intact girder, the specimen was loaded up to 270 kips until the loading plateau was observed. No major damage occurred, except for minor cracking on the top surface of the deck. The intact girder yielded significantly. Similar displacements along the length in both girders and data in transverse and longitudinal reinforcement bars showed that most of the applied load was mainly resisted by the intact girder. The plastic capacity of the composite section of only one girder (or the plastic capacity of one half of the bridge) was estimated at approximately 248 kips by hand calculation. Since the plastic capacity of the composite section of one girder is close to the capacity obtained in this test, this suggests that the contribution of the damaged girder to the load-carrying capacity of the specimen in Test B was not significant.

In ultimate Test C, the loading area was reduced by using a 10-in.-square steel-reinforced elastomeric pad placed over the center of the intact girder. The specimen carried up to 180 kips before the loading pad suddenly punched through the deck. In general, the specimen showed similar behaviors to those observed in ultimate Test B. The fact that both of the girders didn't yield and the participation of the damaged girder in resisting the applied load was small indicated that

the capacity of the specimen under this loading scenario was strongly dependent on the capacity of the deck and its support conditions provided by the intact girder.

In ultimate Test D, the load was applied through a 10-in.-square steel-reinforced elastomeric pad placed over the center of the damaged girder at the damaged location. The specimen carried up to 83 kips of load before the loading pad punched completely through the deck. The obtained data indicated that the applied load was transferred to the intact girder through both the external cross-frames and the deck, but mainly through the deck. Although the specimen had the same failure mode in both Test C and Test D, the deck was punched through more quickly in Test C than it was in Test D. This suggested that changing the supporting conditions from an undamaged state to a full-web fracture damage state significantly reduced the punching shear capacity of deck at the damage location.

In ultimate Test E, the load was spread through four points, representing four wheels of a truck. The contact area for each loading point was 10 in. x 10 in. The distance between north wheels and south wheels was 72 in. while the distance between west wheels and east wheels was 27 in. from center to center (north-south direction represents the longitudinal direction of the specimen). The west wheels were placed at the center of cross-section while the east wheels were at the center of damaged girder. The specimen carried up to 230 kips. The specimen was strongly damaged along the centerline of the bridge, especially underneath the west wheels. The intact girder slightly yielded. Data in the girders and cross-frames indicated that the load was transferred to the intact girder mainly through the deck.

Overall, the concrete deck was found to fail dominantly in shear in all the tests except ultimate Test B, in which the specimen was loaded only to its loading plateau. Under the 10 in. x10 in. concentrated loading scenario, two-way shear failure modes, commonly referred to as punching shear, prevailed. When the specimen was loaded over the entire width of the girder or over more than one loading point, the bridge deck failed predominantly in a one-way shear failure mode. The obtained capacities were found to be much higher than the empirical punching shear capacity of slab computed by ACI-318 building code design provisions for either one-way or two-way shear failure modes.

In addition to their value for general experimental investigation purposes, the experimental results were primarily used to verify and calibrate nonlinear finite element models. Moreover, nonlinear material properties of concrete, such as cracking and crushing characteristics, were also incorporated in these finite element models. In general, the finite element analysis (FEA) results and test data showed good agreement in both elastic and inelastic ranges. These experimentally verified finite element models serve as one of the main tools in evaluating the redundancy of damaged two steel box-girder bridges.

A parametric study was also carried out by means of finite element analysis to generate a list of factors that significantly affect the redundancy of twin steel box-girder bridge. Overall, the

presence of cross-frames, railings, and continuity was found to increase the stiffness and reduce the overall displacement of the bridge. The railing system and the continuity were found to improve the capacity of the damaged bridge.

This project has also resulted in development of an overall roadmap for assessing the redundancy of the damaged twin steel box-girder bridges. Solutions for some of the steps are provided within this report, and remaining portions are left for suggested pooled fund projects.

Table of Contents

Disclaimer	ii
Metric Conversion Tables	iii
Technical Report Documentation	v
Acknowledgements	vi
Executive Summary	vii
List of Figures	xvi
List of Tables	xxvii
Chapter 1 Introduction	1
1.1 Problem Statement	1
1.2 Background	2
1.3 Current Approaches	7
1.3.1 Direct Analysis Approach with Redundancy Criteria - NCHRP Report 406	7
1.3.2 Simplified Analytical Modeling Methods for Redundancy Assessment of Twin Box-Girder Bridges	9
1.3.3 Limitations and Shortcomings	10
1.4 Research Objectives	11
1.5 Report Organization	12
Chapter 2 Research Methodology	13
2.1 Main Characteristics of Comprehensive Methodology for Assessment	14
2.2 Proposed Pooled Fund Project	17
Chapter 3 Laboratory Testing on Small-Scale Specimen	18
3.1 Specimen Design	18
3.1.1 Analysis of Composite Section	21
3.2 Specimen Construction	23
3.3 Instrumentation Plan	25
3.4 Test Setup	30
3.5 Testing Plan	32
3.5.1 Elastic Tests	33

3.5.2	Cyclic Test	34
3.5.3	Ultimate Load Tests	35
Chapter 4	Laboratory Testing Results	37
4.1	Elastic Tests.....	37
4.1.1	On Undamaged Specimen.....	37
4.1.2	On Damaged Specimen with Bottom Flange Fractured in One Girder	38
4.1.3	On Damaged Specimen with Bottom Flange and Webs Fractured in One Girder .	40
4.1.4	Summary of Elastic Tests	42
4.2	Cyclic Test.....	45
4.3	Ultimate Test A	54
4.3.1	Global Behavior	54
4.3.2	Local Behavior.....	59
4.3.3	Load-Transferring Mechanism	65
4.4	Reconstruction of Bridge Specimen.....	66
4.5	Ultimate Test B	69
4.5.1	Global Behavior	69
4.5.2	Local Behavior.....	71
4.6	Ultimate Test C	76
4.6.1	Global Behavior	77
4.6.2	Local Behavior.....	80
4.7	Ultimate Test D	84
4.7.1	Global Behavior	85
4.7.2	Local Behavior.....	88
4.8	Damage Repair	92
4.9	Ultimate Test E.....	93
4.9.1	Global Behavior	94
4.9.2	Local Behavior.....	98
Chapter 5	Finite Element Modeling — Procedures and Verification	102
5.1	FEM of Bridge Specimen.....	102
5.2	Fracture Damage and Connection Modeling	103
5.3	Steel Behavior Modeling.....	104

5.4	Concrete Material Properties.....	105
5.5	Concrete and Reinforcement Behavior Modeling.....	108
5.6	Bearing Pads Modeling	111
Chapter 6	Validating FE Models with Experimental Data.....	115
6.1	Undamaged Bridge Specimen	115
6.1.1	Test 1 - No Rail, No Continuity, Symmetric Loading (NNS)	115
6.1.2	Test 2 - No Rail, No Continuity, Unsymmetrical Loading (NNU)	117
6.1.3	Test 3 - No Rail, with Continuity, Unsymmetrical Loading (NYU)	120
6.2	Bridge Specimen with Bottom Flange Fractured in One Girder.....	122
6.2.1	Test 9 - with Rail, No Continuity, Unsymmetrical Loading (YNU)	122
6.2.2	Test 10 - No Rail, No Continuity, Symmetric Loading (NNS)	124
6.3	Bridge Specimen with Full-Web Fractured in One Girder	126
6.3.1	Test 16 - with Rail, No Continuity, Unsymmetrical Loading (YNU)	126
6.3.2	Test 17 - No Rail, No Continuity, Symmetric Loading (NNS)	128
6.4	Verification of FEMs with Ultimate Test A.....	130
6.5	Verification of FEMs with Ultimate Test B.....	137
6.6	Summary	140
Chapter 7	Field Testing of Ft. Lauderdale Twin Box-Girder Bridge 860600.....	142
7.1	Objective	144
7.2	Bridge Configuration.....	144
7.3	Instrumentation.....	147
7.3.1	Potentiometers (Displacement Sensors)	148
7.3.2	Strain Gauges	152
7.4	Loading.....	154
7.5	Finite Element Modeling.....	159
7.6	Qualitative Review of Test Data	160
7.7	Comparison of Field Test Data and FEA Results	164
Chapter 8	Redundancy Analysis of Ft. Lauderdale Twin Box-Girder Bridge 860600	178
8.1	Bridge Girder Flexural Capacity	178
8.1.1	Effective Width of Concrete Deck.....	179
8.1.2	Section Compactness	180

8.1.3	Nominal Moment Capacity.....	180
8.2	Linear Elastic Analysis of the Bridge	183
8.3	Nonlinear Finite Element Analysis	186
8.4	Redundancy Analysis.....	189
8.4.1	Member Failure (LF_1).....	189
8.4.2	Ultimate Limit State (LF_u).....	189
8.4.3	Damage Condition Limit State (LF_d).....	190
8.4.4	Functionality Limit State (LF_f).....	191
8.5	Summary	192
Chapter 9	Parameters Affecting Load-Carrying Capacity of Bridge	193
9.1	Cross-frames.....	193
9.2	Railing	194
9.3	Structural Indeterminacy and Cantilever End	195
9.4	Bridge Span Length.....	196
9.5	Summary	197
Chapter 10	Summary and Future Considerations.....	198
10.1	Research Summary	198
10.2	Field Tests of In-Service Bridge.....	199
10.3	Laboratory Tests on Small-Scale Specimen.....	200
10.3.1	Conclusions from Elastic Tests Conducted on Laboratory Test Specimen	201
10.3.2	Conclusions from Cyclic Tests Conducted on Laboratory Test Specimen	201
10.3.3	Conclusions from Ultimate Load Tests Conducted on Laboratory Test Specimen.....	202
10.4	Suggestions for Future Study	204
References	205

List of Figures

Figure 1-1 FSEL twin box-girder bridge (Source: FHWA Report No FHWA/TX-10/9-5498-1).	4
Figure 1-2 FSEL first bridge fracture test (Source: FHWA Report No FHWA/TX-10/9-5498-1).	5
Figure 1-3 Bottom flange cut after the explosion (Source: FHWA Report No FHWA/TX-10/9-5498-1).	5
Figure 1-4 FSEL second bridge fracture test (Source: FHWA Report No FHWA/TX-10/9-5498-1).	6
Figure 1-5 FSEL third bridge fracture test (Source: FHWA Report No FHWA/TX-10/9-5498-1).	6
Figure 1-6 Yield line model proposed by Barnard et al. (2010).	10
Figure 2-1 Probability density functions of load and resistance of damaged and undamaged bridges.	17
Figure 3-1 Dimension of one steel box girder.	19
Figure 3-2 Center-to-center flange distance (Adopted from AASHTO <i>LRFD Bridge Design Specifications</i>).	20
Figure 3-3 Cross-section of the testing specimen.	20
Figure 3-4 Internal bracing locations in each box girder.	21
Figure 3-5 The top plan view of the testing specimen.	21
Figure 3-6 Location of plastic neutral axis.	23
Figure 3-7 Welding details.	24
Figure 3-8 Complete specimen ready for casting.	24
Figure 3-9 Casting the concrete deck.	25
Figure 3-10 Locations of strain gauges and potentiometers along the length of the specimen.	26
Figure 3-11 Strain gauges in the Section 2.	26
Figure 3-12 Strain gauges in the Section 3.	27
Figure 3-13 Strain gauges in the Section 4.	27

Figure 3-14 Strain gauges in the Section 5.	28
Figure 3-15 Strain gauges in the Section 6.	28
Figure 3-16 Strain gauges in the Section 8.	29
Figure 3-17 Potentiometers in Section 5.	29
Figure 3-18 Potentiometers in Section 2.	30
Figure 3-19 Longitudinal view of test specimen.	30
Figure 3-20 Setup for continuity effect.	31
Figure 3-21 Schematic drawing of loading system.	32
Figure 3-22 Specimen with complete loading setup.	32
Figure 3-23 Typical three-ramp loading history for the elastic tests.	33
Figure 4-1 Saw cutting of bottom flange in east girder.	38
Figure 4-2 East girder with bottom flange and web fractured in one girder.	40
Figure 4-3 Results of elastic tests on undamaged specimen.	43
Figure 4-4 Results of elastic tests on specimen with bottom flange fractured in east girder.	43
Figure 4-5 Results of elastic tests on specimen with full-depth fracture in east girder.	44
Figure 4-6 Schematic description of the cyclic loading test.	46
Figure 4-7 Cracks on the deck surface during cyclic test.	46
Figure 4-8 Crack in the damaged girder: (a) before and (b) after the cyclic test.	47
Figure 4-9 Crack growth in the damaged girder.	48
Figure 4-10 Crack opening measuring gauge on the exterior face.	49
Figure 4-11 Crack base opening vs. number of loading cycles.	49
Figure 4-12 Mid-span displacement vs. number of loading cycles in the fractured girder.	50
Figure 4-13 Displacement range (max – min) vs. number of loading cycles.	51
Figure 4-14 Stiffness of each girder during the cyclic test.	52
Figure 4-15 (a) Strain locations and (b) Strain profile in each cross-frame brace.	53

Figure 4-16 Maximum shear transfer in one cross-frame.....	53
Figure 4-17 Schematic description of Test A.	54
Figure 4-18 Load vs. deflection curve of the specimen during ultimate load test A.....	55
Figure 4-19 Punching in the top of the concrete surface looking to South.....	56
Figure 4-20 Punching in the bottom of the deck.....	56
Figure 4-21 Damage at North end (left) and South end (right).	57
Figure 4-22 Location of potentiometers at supports.	58
Figure 4-23 Displacement of the both girders near the south support.....	58
Figure 4-24 Displacement of the both girders near the north support.	58
Figure 4-25 Uplift at (a) north support and (b) south support.	59
Figure 4-26 Strain gauges at the mid-span section.	61
Figure 4-27 Longitudinal strain in the top and bottom flanges of west girder at mid-span.	62
Figure 4-28 Longitudinal strain at the top flanges of east girder at mid-span.....	62
Figure 4-29 Strains of the transverse rebar at mid-span.	63
Figure 4-30 Longitudinal strain of rebars in longitudinal direction at mid-span.....	64
Figure 4-31 Transverse strain at the top and bottom of deck at mid-span.....	64
Figure 4-32 Shear transferred through one cross-frame in Test A.	66
Figure 4-33 Damage in (a) the inner top flange, (b) the outer top flange of the damaged girder. 67	
Figure 4-34 Alignment of two fractured segments.	68
Figure 4-35 The reconstructed specimen before (left) and after casting (right).	68
Figure 4-36 Schematic description of Test B.	69
Figure 4-37 Test B: Load vs. displacement curves at (a) mid-span, (b) Section 5 and (c) cantilever end.	70
Figure 4-38 Displacement near supports.	71
Figure 4-39 Shear transferred through a cross-frame in Test B.....	71

Figure 4-40 Average longitudinal strains at top flanges of the intact girder.	73
Figure 4-41 Longitudinal strains at the bottom flange of the intact girder.	73
Figure 4-42 Comparison of longitudinal strains in the intact and damaged girders at Section 5.	74
Figure 4-43 Longitudinal strain in rebars at mid-span.	74
Figure 4-44 Transverse strain in rebars at mid-span.	75
Figure 4-45 Schematic deflection shape of the deck.	75
Figure 4-46 Transverse strain of the deck near mid-span.	76
Figure 4-47 Schematic description of Test C.	76
Figure 4-48 Test C: Load vs. displacement curves at (a) mid-span, (b) Section 5 and (c) cantilever end.	78
Figure 4-49 Punching damage in test C.	79
Figure 4-50 Near-support displacement.	79
Figure 4-51 Shear transferred through a cross-frame in test C.	80
Figure 4-52 Average longitudinal strains at top flanges of the intact girder.	82
Figure 4-53 Longitudinal strains at the bottom flange of the intact girder.	82
Figure 4-54 Comparison of longitudinal strains in the intact and damaged girders at Section 5.	83
Figure 4-55 Longitudinal strain in rebars at mid-span.	83
Figure 4-56 Transverse strain in rebars at mid-span.	84
Figure 4-57 Transverse strain on the deck near mid-span.	84
Figure 4-58 Schematic description of Test D.	85
Figure 4-59 Test D: Load vs. displacement curves at (a) mid-span, (b) Section 5 and (c) cantilever end.	86
Figure 4-60 Punching damage in Test C.	87
Figure 4-61 Near-support displacements.	87
Figure 4-62 Shear transferred through a cross-frame in Test C.	88
Figure 4-63 Average longitudinal strains at top flanges of the intact girder.	89

Figure 4-64 Longitudinal strains in bottom flange of the intact girder at Sections 2, 3, 4, and 5.	90
Figure 4-65 Comparison of longitudinal strains in the intact and damaged girders at Section 5.	90
Figure 4-66 Longitudinal strain in rebars at mid-span.....	91
Figure 4-67 Transverse strain in rebars at mid-span.....	91
Figure 4-68 Transverse strain on the deck near mid-span.	92
Figure 4-69 Repair of punching shear damage from Tests C and D.	93
Figure 4-70 (a) Test setup for Test E and (b) schematic locations of loading foot prints.	94
Figure 4-71 Test E: Load vs displacement curves at (a) mid-span, (b) Section 5 and (c) cantilever end.....	96
Figure 4-72 Damage in Test E.....	97
Figure 4-73 Shear damage at ends in Test E.....	97
Figure 4-74 Near-support displacement.....	98
Figure 4-75 Shear transferred through a cross-frame in Test E.....	98
Figure 4-76 Average longitudinal strains at top flanges of the intact girder.	99
Figure 4-77 Longitudinal strains at the bottom flange of the intact girder.....	100
Figure 4-78 Comparison of longitudinal strains in the intact and damaged girders at Section 5.	100
Figure 4-79 Longitudinal strain of rebars at mid-span.	101
Figure 4-80 Transverse strain on the deck near mid-span.	101
Figure 5-1 Finite element bridge model.....	103
Figure 5-2 Process to simulate a fracture condition.....	104
Figure 5-3 Finite element model with full-web fracture condition.....	104
Figure 5-4 Stress-strain behavior of steel girder and rebars.	105
Figure 5-5 Stress-strain curve of concrete in compression.....	108
Figure 5-6 Solid65 concrete element in ANSYS.....	109
Figure 5-7 Smearred reinforcement bars.....	109

Figure 5-8 Failure surfaces of concrete under (a) biaxial and (b) triaxial loading states (Willam and Warnke, 1975).....	111
Figure 5-9 Typical stress-strain curve for steel-reinforced bearings (AASHTO-C14.7.6.3.3-1).	112
Figure 5-10 Mid-span displacement before and after modeling the bearing pads.....	113
Figure 5-11 Contact surface between the bearing pad and bottom flange of girder.....	114
Figure 6-1 Schematic description of Test 1.	115
Figure 6-2 Comparison of vertical displacement at the bottom flange of each girder in Test 1.	116
Figure 6-3 Comparison of longitudinal strain at the bottom flange of each girder in Test 1.	116
Figure 6-4 Comparison of longitudinal strain at the top flange of each girder in Test 1.....	117
Figure 6-5 Schematic description of Test 2.	117
Figure 6-6 Comparison of vertical displacement at the bottom flange of each girder in Test 2.	118
Figure 6-7 Comparison of longitudinal strain at the bottom flange of each girder in Test 2.	119
Figure 6-8 Comparison of longitudinal strain at the top flange of each girder in Test 2.....	119
Figure 6-9 Schematic description of Test 3.	120
Figure 6-10 Comparison of vertical displacement at the bottom flange of each girder in Test 3.	120
Figure 6-11 Comparison of longitudinal strain at the bottom flange of each girder in Test 3. ..	121
Figure 6-12 Comparison of longitudinal strain at the top flange of each girder in Test 3.....	121
Figure 6-13 Schematic description of Test 9.	122
Figure 6-14 Comparison of vertical displacement at the bottom flange of each girder in Test 9.	123
Figure 6-15 Comparison of longitudinal strain at the bottom flange of each girder in Test 9. ..	123
Figure 6-16 Comparison of longitudinal strain at the top flange of each girder in Test 9.....	124
Figure 6-17 Schematic description of Test 10.	124
Figure 6-18 Comparison of vertical displacement at the bottom flange of each girder in Test 10.	125

Figure 6-19 Comparison of longitudinal strain at the bottom flange of each girder in Test 10.	125
Figure 6-20 Comparison of longitudinal strain at the top flange of each girder in Test 10.....	126
Figure 6-21 Schematic description of Test 16.	127
Figure 6-22 Comparison of vertical displacement at the bottom flange of each girder in Test 16.	127
Figure 6-23 Comparison of longitudinal strain at the bottom flange of undamaged Girder in Test 16.....	128
Figure 6-24 Schematic description of Test 17.	128
Figure 6-25 Comparison of vertical displacement at the bottom flange of each girder in Test 17.	129
Figure 6-26 Comparison of longitudinal strain at the bottom flange of undamaged girder in Test 17.....	129
Figure 6-27 Comparison of load vs. vertical deflection curves using displacement-control analysis.....	130
Figure 6-28 Comparison of load vs. vertical deflection curve using load-control analysis.	131
Figure 6-29 Vertical displacements at the bottom flange of each girder and at center of the deck at mid-span.....	132
Figure 6-30 Reactions vs. EG vertical displacement.	133
Figure 6-31 Prediction of uplift in finite element analysis.	133
Figure 6-32 Comparison of longitudinal strains at the top flange of WG at mid-span.	134
Figure 6-33 Comparison of longitudinal strain at bottom flange at mid-span.....	134
Figure 6-34 Comparison of transverse strain on the top of deck.....	135
Figure 6-35 Location of concrete crushing in FEA and in experiment.	135
Figure 6-36 Shear cracking in south (left) and north (right) supports.	136
Figure 6-37 Stress contour at mid-span in the steel girders.....	137
Figure 6-38 Load vs average vertical displacements at (a) mid-span, (b) Section 5, and (c) cantilever end.....	138

Figure 6-39 Comparison of longitudinal strains at the bottom flange of the intact girder at (a) mid-span, (b) Section 3, and (c) Section 5.....	139
Figure 6-40 Transverse strain on the deck at mid-span.	140
Figure 7-1 First two spans of the ramp bridge - underneath view.	143
Figure 7-2 First span of the ramp bridge 860600 - elevation view from west.....	144
Figure 7-3 Elevation view of the bridge.	145
Figure 7-4 Cross-section of the Ft. Lauderdale bridge 860600.	145
Figure 7-5 Internal bracing of superstructure girders.	146
Figure 7-6 Locations of potentiometers in the first two spans.....	148
Figure 7-7 Arrangement of potentiometers at Location 1 in the first span.....	149
Figure 7-8 Gauge and channel ID of first span displacement sensors.	149
Figure 7-9 Displacement sensor beneath bottom flange of box-girder (typical).	150
Figure 7-10 Displacement sensor on SIP form below concrete deck.	150
Figure 7-11 Arrangement of the potentiometers at Location 2 in the second span.	151
Figure 7-12 Gauge and channel ID of displacement sensors at Location 2.....	151
Figure 7-13 Locations of strain gauges in the first span.	152
Figure 7-14 Strain transducers on box-girders (typical).	152
Figure 7-15 Gauge and channel ID's of strain gauges at Section 1.....	153
Figure 7-16 Gauge and channel ID's of strain gauges at Section 2.....	153
Figure 7-17 Gauge and channel ID's of strain gauges at Section 3.....	154
Figure 7-18 Test Truck-1 axle spacing.	156
Figure 7-19 Test Truck-2 axle spacing.	157
Figure 7-20 Test truck path locations.	157
Figure 7-21 Finite element model of the first span of Ft. Lauderdale bridge 860600.....	160
Figure 7-22 Reproducibility of strain response histories (typical).	161

Figure 7-23 Reproducibility of displacement response histories (typical).	162
Figure 7-24 Example of variable thermal drift observed during testing.....	163
Figure 7-25 Comparison of raw and thermally corrected strain data.	163
Figure 7-26 Strain history comparison – crawl speed vs. roadway speed at Section 2.	164
Figure 7-27 Vertical deflection of west edge of WG: 59 ft from north abutment, Truck-1 on path-3.....	165
Figure 7-28 Vertical deflection of west edge of WG: 225.5 ft from north abutment, Truck-1 on path-3.	165
Figure 7-29 Vertical deflection of west edge of EG: 59 ft from north abutment, Truck-1 on path-3 and Truck-2 on path-1.....	166
Figure 7-30 Vertical deflection of west edge of WG: 225.5 ft from north abutment, Truck-1 on path-3 and Truck-2 on path-1.	166
Figure 7-31 Vertical deflection of west edge of EG: 59 ft from north abutment, Truck-1 followed by Truck-2 on path-1.	167
Figure 7-32 Vertical deflection of east edge of EG: 225.5 ft from north abutment, Truck-1 followed by Truck-2 on path-1.	167
Figure 7-33 Longitudinal stress at 6 ft from north abutment in the west edge of bottom flange of WG: Truck-1 on Path-3.	168
Figure 7-34 Longitudinal stress at 6 ft from North Abutment in the west edge of bottom flange of EG: Truck-1 on path-3.....	168
Figure 7-35 Longitudinal stress at 58 ft from north abutment in the west edge of bottom flange of WG: Truck-1 on path-3.....	169
Figure 7-36 Longitudinal stress at 58 ft from north abutment in the east edge of bottom flange of WG: Truck-1 on path-3.....	169
Figure 7-37 Longitudinal stress at 138 ft from north abutment in the west edge of bottom flange of WG: Truck-1 on path-3.	170
Figure 7-38 Longitudinal stress at 138 ft from north abutment in the east edge of bottom flange of WG: Truck-1 on path-3.	170
Figure 7-39 Longitudinal stress at 6 ft from north abutment in the west edge of bottom flange of WG: loading scenario-5.	171

Figure 7-40 Longitudinal stress at 6 ft from north abutment in the west edge of bottom flange of EG: loading scenario-5.	171
Figure 7-41 Longitudinal stress at 58 ft from north abutment in the west edge of bottom flange of WG: loading scenario-5.	172
Figure 7-42 Longitudinal stress at 58 ft from north abutment in the east edge of bottom flange of WG: loading scenario-5.	172
Figure 7-43 Longitudinal stress at 138 ft from north abutment in the west edge of bottom flange of WG: loading scenario-5.	173
Figure 7-44 Longitudinal stress at 138 ft from north abutment in the east edge of bottom flange of WG: loading scenario-5.	173
Figure 7-45 Longitudinal stress at 6 ft from north abutment in the west edge of bottom flange of EG - Truck-1 followed by Truck-2 on path-1.	174
Figure 7-46 Longitudinal stress at 6 ft from north abutment in the east edge of bottom flange of EG: Truck-1 followed by Truck-2 on path-1.	174
Figure 7-47 Longitudinal stress at 58 ft from north abutment in the west edge of bottom flange of EG: Truck-1 followed by Truck-2 on path-1.	175
Figure 7-48 Longitudinal stress at 58 ft from north abutment in the east edge of bottom flange of EG: Truck-1 followed by Truck-2 on path-1.	175
Figure 7-49 Longitudinal stress at 138 ft from north abutment in the west edge of bottom flange of WG: Truck-1 followed by Truck-2 on path-1.	176
Figure 7-50 Longitudinal stress at 138 ft from north abutment in the east edge of bottom flange of EG: Truck-1 followed by Truck-2 on path-1.	176
Figure 8-1 Box-girder composite section, Ft Lauderdale bridge.	178
Figure 8-2 Rebar layout in concrete slab.	181
Figure 8-3 Worst case scenario for HS-20 loading of the bridge.	184
Figure 8-4 Worst case scenario of loading for two trucks with unit weight.	184
Figure 8-5 Web reactions due to application of two trucks with unit weight.	185
Figure 8-6 Position of the HS-20 truck for maximum moment in girders.	186
Figure 8-7 Von Mises stresses in single-span bridge under maximum moment, undamaged condition.	187

Figure 8-8 Von Mises stresses in single-span bridge under maximum moment, full-web cracked condition. 187

Figure 8-9 Load vs. vertical deflection of single- and three-span bridges with different conditions. 188

Figure 9-1 Effects of cross-frames. 194

Figure 9-2 Effects of railing system. 195

Figure 9-3 Effects of continuity. 196

List of Tables

Table 3-1 Plan for Elastic and Cyclic Tests.....	34
Table 3-2 Plan for Ultimate Load Tests.....	36
Table 4-1 Summary of Elastic Tests on Undamaged Specimen.....	37
Table 4-2 Summary of Elastic Tests on Bottom Flange Fractured Specimen.....	39
Table 4-3 Summary of Elastic Tests on Full-Web Fractured Specimen	40
Table 4-4 Summary of all Elastic Tests.....	45
Table 5-1 Concrete Cylinder Strengths for First Specimen.....	106
Table 5-2 Concrete Cylinder Strengths for Reconstructed Specimen	107
Table 5-3 Concrete Tensile Strengths for Reconstructed Specimen	107
Table 5-4 Input Parameters for Properties of Concrete Materials	110
Table 6-1 Comparison of Displacement between FEA Results and all Elastic Tests.	141
Table 7-1 Thickness of Top and Bottom Flanges of the Bridge Girders.....	146
Table 7-2 General Structure and Testing Specifications	147
Table 7-3 Test Truck-1 Specifications.....	155
Table 7-4 Test Truck-2 Specifications.....	156
Table 7-5 Loading Path Definitions.....	158
Table 7-6 Loading Scenario Definitions.....	159
Table 8-1 Live Load Capacity of the Bridge as a Multiplier of HS-20 Trucks.....	188
Table 8-2 Summary of Redundancy Analysis Results on the Ft. Lauderdale Bridge	192
Table 9-1 Effects of Span Length on the Bridge Performance.....	196

Chapter 1 Introduction

1.1 Problem Statement

Sudden collapse of bridges such as the Silver Bridge (West Virginia DOT, 2016) and the I-35W Mississippi River Bridge (National Transportation Safety Board, 2008) show that fracture of a single member can cause the collapse of an entire bridge. In bridge engineering parlance, these members are known as fracture critical members (FCMs), although the precise definition may vary. In 2010 the American Association of State Highways and Transportation Officials (AASHTO) defined an FCM as a “component in tension whose failure is expected to result in the collapse of the bridge or the inability of the bridge to perform its function.” Although design and construction of bridges with FCMs is not currently prohibited, these bridges must be designed and fabricated to special requirements, and since 1988 the National Bridge Inspection Standards have required a hands-on, full inspection, typically every two years. These requirements burden bridge owners and transportation agencies with huge initial and annual expenses.

Currently, all two-girder bridges, regardless of their configurations, are classified as bridges with fracture critical elements. However, a number of two-girder bridges with cracks in one girder, even full-depth, have been reported and were still in service without collapse. One example is the Lafayette Bridge, part of US-52 Hwy over the Mississippi River near Savanna, IL. The Lafayette Bridge is composed of two side-by-side units, each containing two plate girders. Cross-frames exist between the girders within each unit; however, the units themselves are unconnected. In 1975, after eight years of service, the Lafayette Bridge experienced a full-depth fracture of one of the main girders, and the bridge deck sagged 7 in., but the structure did not collapse (Fisher et al., 1977). In 1977, the I-79 Neville Island Bridge in Pittsburgh, PA, was found to have a full-depth fracture of one of its two girders and remained in service and displayed only a slight deflection, until a boater noticed the fracture (Schwendeman and Hedgren, 1978). These examples suggest that the stability of the bridge is not always linked strictly to the performance of fracture critical members, and a redundancy load path might exist in bridges with FCMs even though it is not acknowledged based on the current definition of fracture critical structures.

There has been increased interest in the fracture critical classification of twin box-girder bridges due to several recent cases of bridges with FCMs performing well and supporting highway live loads after a fracture of one of the main-supporting girders. One of the first research studies on the redundancy evaluation of twin steel box-girder bridges was performed by HNTB Corporation and Milwaukee Transportation Partners (2005). In addition, full-scale testing of a simple span twin box-girder superstructure at the University of Texas, Austin, has shown that under uniform loading, twin box-girder superstructures have significant levels of redundancy and can remain stable after a complete fracture of the bottom flange and webs of one of the girders (Barnard et al.,

2010). If twin steel box-girder bridges are proved to be redundant structures, the requirements of hands-on inspection every two years might not be necessary and significant savings will be realized.

1.2 Background

National Cooperative Highway Research Program (NCHRP) Report 406 (Ghosn and Moses, 1998) is one of the first of several research projects on fracture critical bridges that have been conducted by bridge researchers for different sponsoring agencies in recent years. In that report, an attempt was made to quantify the redundancy of different bridge structures. To that end, four load factors and three reserve ratios based on the load factors are defined. Limiting values for each reserve ratio are intended to ensure redundancy. The results of other studies are also available for researchers in this field, among them Ghosn et al. (2010), Connor et al. (2005), Frangopol et al. (1991 and 2007).

In June 2012, the Federal Highway Administration (FHWA) issued a memo intended to clarify the agency's policy regarding the design, fabrication, and inspection of fracture critical bridges. In addition, two major research projects on redundancy of twin box-girder bridges were conducted by HNTB/MTP for the Wisconsin Department of Transportation (DOT) and by the University of Texas-Austin for the Texas DOT. Additional information on these three resources is provided below.

FHWA Memo

In June 2012, FHWA issued a memorandum on clarification of requirements for fracture critical members. The memo stated:

“The purpose of this memo is to provide clarification of the FHWA policy for the classification of Fracture Critical Members. For design and fabrication, only Load Path Redundancy may be considered. For in-service inspection protocol, Structural Redundancy demonstrated by refined analysis is now formally recognized and may also be considered. Internal member redundancy is currently not recognized in the classification of Fracture Critical Members for either design and fabrication or in-service inspection. Finally, this memo introduces a new member classification, a System Redundant Member (SRM), which is a non-load-path-redundant member that gains its redundancy by system behavior.”

The memo clarifies the FHWA policy on specification of proper material and testing for design and fabrication and also proper in-service inspection protocol. It also mentions that the analysis requirements of AASHTO LRFD section 6.6.2 is supported, which requires bridge owner and bridge engineer agreement on the level of complexity of the bridge analysis.

HNTB/MTP Research Project (2005)

In 2005, Milwaukee Transportation Partners (MTP), in collaboration with HNTB Corp., published a report on “Redundancy of Box Girder Steel Bridges” based on a study on the Marquette Interchange HPS twin box-girder bridges. The intent of that project was to either demonstrate that the selected twin box-girder bridges are redundant in their as-designed condition or to make recommendations to render them redundant.

Marquette Interchange includes eight directional ramps to be constructed using a twin box-girder system. It was decided that these bridges be designed and fabricated in accordance to fracture critical requirements and the major target was to eliminate the two-year inspection requirement. Therefore, two of the ramp bridges were modeled using elaborate nonlinear finite element models, while the other six bridges of the interchange were modeled using simplified grillage models. In these grillage models, all main girders, slab strips, and diaphragms were modeled using beam elements in a 2-D planar grid. The 2-D models were calibrated against the results of the two 3-D models to make them more reliable. The considered damage for each bridge was a total steel section fracture of one of the two box girders at 0.4 times of the end span. A stepwise pushover analysis was used to monitor the responses of all of the bridge elements through the incremental loading process.

The results of both 2-D and 3-D analyses show that these bridges were able to carry the live loads greater than the minimum required loads. In addition, the dynamic effects due to sudden failure of one of the box girders on global stability of the bridge were evaluated, which was beyond the requirements of NCHRP Report 406. A simplified approach was selected to attack this problem. Although, the analyses showed that this dynamic effect controls the failure, the two girder bridges proved to have enough capacity to accommodate such sudden failures.

This project demonstrated that twin box-girder bridges in their as-designed condition have sufficient reserved capacity to be classified as non-fracture critical and no additional requirement should be added to the current design methods. The redundancy of this type of bridge comes from the alternate load path embedded in these structures, such as continuity of girders, concrete deck 3-D action, and participation of cross-frames and diaphragms to carry the loads of damaged girder.

Texas DOT Research Project 9-5498 (2006-2010)

Texas DOT and Federal Highway Administration (FHWA) co-sponsored a full-scale experimental study at the Ferguson Structural Engineering Laboratory (FSEL) in the University of Texas-Austin. In this research project, Karl Frank et al. conducted a valuable full-scale experiment and presented analytical and finite element solutions to evaluate the load carrying capacity of a composite twin steel box-girder bridge. The outcome of the research was analytical and numerical solutions to find the “redundant capacity” of twin box-girder bridges. Major experimental and computational resources for this FSEL project were continued for four years (2006-2010). Different aspects of this project included analytical structural analysis presented through hand

calculations, numerical structural analyses conducted through finite element modeling, laboratory experiments to evaluate the capacity of specific bridge elements, and a full-scale test on a reconstructed twin box-girder bridge.

In the analytical part of this study, the capacity of the bridge was estimated using the yield line method. In this method, a failure pattern (Yield Line) is assumed for the bridge and then by equating the internal work done by the internal forces and the external work done by the external forces, the maximum capacity of the structure is found. This method was successfully applied to the tested bridge and a lower bound solution was resulted for the load capacity of the bridge.

The laboratory tests focused on the pullout capacity of the shear connectors of the bridge girders, which connect the girders to the concrete deck. One of the conclusions of the Texas research is that the shear connectors play a key role in the redundancy of damaged two steel box-girder bridges. As a result, tests were conducted to comprehend the behavior of shear studs in static and dynamic states.

The full-scale bridge test of this research project revealed the intrinsic redundant behavior of twin box-girder bridges, despite the fact that the test was conducted in the worst-case scenario from the point of view of redundancy. The tested bridge was a simple-span bridge and therefore it had no redundancy due to continuity of its superstructure. All external diaphragms of this bridge were removed. The railings of the bridge were constructed with expansion joints that limit the contribution of the railing to the load-carrying capacity of the bridge. The bridge had a horizontal curvature and the fractured girder was the outside girder that has the maximum internal forces. Therefore, it is observed that the situation of a real-life bridge cannot be worse than this bridge from redundancy standpoint. Figure 1-1 shows a picture of this test bridge before conducting the tests.



Figure 1-1 FSEL twin box-girder bridge (Source: FHWA Report No FHWA/TX-10/9-5498-1).

Three different tests were conducted on this bridge. In the first test, the bottom flange of the exterior girder was suddenly failed using an explosive to simulate a sudden fracture while an equivalent HS-20 load was positioned above the fractured girder and in the worst possible location. Figure 1-2 illustrates the bridge during the explosion and Figure 1-3 shows the bottom flange cut after the explosion. The response of the bridge during and after this test was satisfactory and its maximum deflection was less than 1 in.



Figure 1-2 FSEL first bridge fracture test (Source: FHWA Report No FHWA/TX-10/9-5498-1).



Figure 1-3 Bottom flange cut after the explosion (Source: FHWA Report No FHWA/TX-10/9-5498-1).

In the second test, the bridge and equivalent HS-20 truck loading were supported by means of a scissor jack while about 83% of the webs of the cracked girder were manually cut. The scissor jack was then removed suddenly using an explosive charge attached on the jack. This simulated the sudden nature of the crack. Figure 1-4 shows the supporting scissor jack before, during, and after the explosion. Again, the bridge safely sustained the load with a maximum deflection of 7 in.



Figure 1-4 FSEL second bridge fracture test (Source: FHWA Report No FHWA/TX-10/9-5498-1).

The third test was a static test to measure the load capacity of the damaged bridge. In this test, the load on the bridge was increased incrementally until the bridge was not able to carry more loads. In this test, the bridge carried 363 kips of load which, considering the extent of the damage, was a remarkable capacity. Figure 1-5 shows the incremental loading of the bridge and also the bridge in its collapsed mode.



Figure 1-5 FSEL third bridge fracture test (Source: FHWA Report No FHWA/TX-10/9-5498-1).

The capacity of the tested bridge is also evaluated by means of a numerical simulation. In this approach, a sophisticated finite element model of the bridge is developed using Abaqus/Standard finite element program. In the simulation, the nonlinear material properties of steel and concrete, contact properties of railing joint, and the stud connection failure were taken into account. The results of the numerical simulation showed a good agreement with the collected data. In addition, the finite element models were able to capture the observed failures during the second and third tests.

Based on the performed experiment and computer simulations, major failures in this type of bridges include:

- Pull-out failure of shear studs (which is tension failure of the concrete surrounding the studs) resulting in haunch separation, and

- Crushing of railing concrete in compression.

A number of theses and reports were published by Barnard (2006), Hovell (2007), Neuman (2009), and others based on the results of this experimental work, each of them investigating different aspects of the tested bridge's behavior.

These studies provide valuable information about the redundancy of twin box-girder bridges; however, they do not completely explain the behavior and failure modes of these bridges under different loading conditions.

1.3 Current Approaches

Following are brief description of two available methods for assessing the redundancy of two steel box-girder bridges, together with their limitations.

1.3.1 Direct Analysis Approach with Redundancy Criteria - NCHRP Report 406

NCHRP Report 406 was one of the first studies undertaken to study the redundancy of bridges at system level and develop a step-by-step-procedure, called direct analysis approach, to evaluate the redundancy of highway bridges (Ghosn and Moses, 1998). This procedure introduces four critical limit states that need to be checked and the minimum load levels (or load factors) that bridges can carry before these limit states are reached. These limit states and their corresponding load factors are described as follows:

- **Member failure limit state** is a check of individual member safety using elastic analysis or the capacity of the structure to resist its first member failure.

$$LF_1 = \frac{R - D}{L} \leftarrow \text{Linear Elastic Analysis} \quad \text{EQ 1.1}$$

Where:

- R = Resistance
- D = Dead load effects
- L = Live load effects

- **Ultimate limit state** is defined as the ultimate capacity of the undamaged bridge system or the load required for the formation of a collapse mechanism in the bridge system divided by the weight of two HS-20 trucks. In mathematical format, this definition yields in:

$$LF_u = \frac{\text{Ultimate Load Capacity of Undamaged Bridge from Nonlinear FEA}}{2 \times 72 \text{ kips}} \quad \text{EQ 1.2}$$

Where:

$$72 \text{ kips} = \text{Weight of one HS-20 Trucks}$$

- **Damaged condition limit state** is defined as the ultimate capacity of the bridge system after removal or cracking of one load-carrying component from the structure model.

$$LF_d = \frac{\text{Ultimate Load Capacity of Damaged Bridge}}{2 \times 72 \text{ kips}} \quad \text{EQ 1.3}$$

- **Functionality limit state** is defined as the capacity of the structure to resist a live load displacement in a main longitudinal member equal to the span length/100. The functionality limit state load factor is obtained from dividing this capacity by the weight of two HS-20 trucks.

$$LF_f = \frac{\text{Load Capacity corresponding to } \frac{L}{100} \text{ deflection}}{2 \times 72 \text{ kips}} \quad \text{EQ 1.4}$$

In this study, redundancy of a bridge is defined as the capability of the bridge structure to continue to carry loads after the failure of one main member, hereby ratios of LF_u , LF_f , LF_d to LF_1 are measures of the redundancy level of bridges in the ultimate, functional and damaged limit states, respectively. These ratios are also called as system reserve factors. A bridge will be considered as redundant if all system reserve factors satisfy the following criteria:

$$\text{For ultimate limit state: } R_u = \frac{LF_u}{LF_1} \geq 1.30$$

$$\text{For damaged conditioned limit state: } R_d = \frac{LF_d}{LF_1} \geq 0.5$$

$$\text{For functional limit state: } R_f = \frac{LF_f}{LF_1} \geq 1.10$$

These three minimum redundancy criteria, 1.30, 0.5, and 1.10, came from target reliability indices, which were collected from reliability analysis of a large number of common-type four-girder bridges. It was assumed that four-girder bridges are always redundant while two-girder bridges are non-redundant. The target reliability indices for ultimate limit state, functional limit state and damaged limit states were found to be 4.35, 3.75 and 0.8 respectively.

In addition to the direct analysis procedures as described above, the research also developed tables of system reserve factors for typical bridge configurations so that practice bridge engineers and owners can use without performing any nonlinear finite element analysis (FEA).

In order to evaluate the redundancy of a bridge using this approach, it is necessary to carry out nonlinear finite element analysis of the bridge systems.

1.3.2 Simplified Analytical Modeling Methods for Redundancy Assessment of Twin Box-Girder Bridges

The simplified analytical methods are developed to evaluate the redundancy of twin steel box-girder bridges (Barnard et al. 2010). These simplified methods were developed based on the results of experimental tests on full-scale twin steel box-girder bridge carried out in Texas DOT Research Project 9-5498 which was summarized previously.

First, Barnard et al. (2010) proposed initial strength checks such that if the bridge under investigation satisfied these checks, it could be considered a redundant structure. The main philosophy of these checks was to ensure that 1) the intact girder can support the weight of the bridge and of a HS-20 truck, 2) the deck has sufficient strength to transmit the load carried by the fractured girder to the intact girder, and 3) the shear studs have sufficient tension capacity. These initial checks were considered as a first-level screening. Barnard et al. also demonstrated that if the first two conditions were satisfied, the twin steel box-girder bridge can still sustain the load without collapsing. Under this scenario, a yield line analysis can be employed to evaluate “the ability of the deck to transmit load to the intact girder without the shear studs connecting the deck to the fractured girder.” The simplified procedure, developed by Barnard et al. (2010), requires carrying out a refined analysis (nonlinear finite element analysis), if the capacity predicted from the yield line analysis proves to be inadequate. In all the redundancy assessment approaches suggested by the Texas investigation, an arbitrary load equal to two times the weight of an HS-20 truck is utilized.

In the yield line analysis approach, once the yield line pattern is chosen, the analysis is performed using a virtual work principle. The principle of virtual work requires that the external virtual work done by the external forces be equal to the internal virtual work done by the internal forces of each element. The yield line pattern, chosen for the bridge tested in Texas, is illustrated in Figure 1-6. In this yield line analysis approach, three parameters are required to define the yield line pattern. These parameters are angle ϕ , length a , and angle θ . The angle θ can be calculated based on the curvature of the bridge and it is zero for a straight bridge. The angle ϕ , is suggested to be constant at 55 degrees according to the results of a parametric study. The length a , is determined by finding the value that produces minimum truck load. It is important to note that length a , and magnitude of truck load are mutually dependent; therefore, one needs to be fixed to find the other. The minimum truck load is the last one that gave a physically admissible solution for the length a .

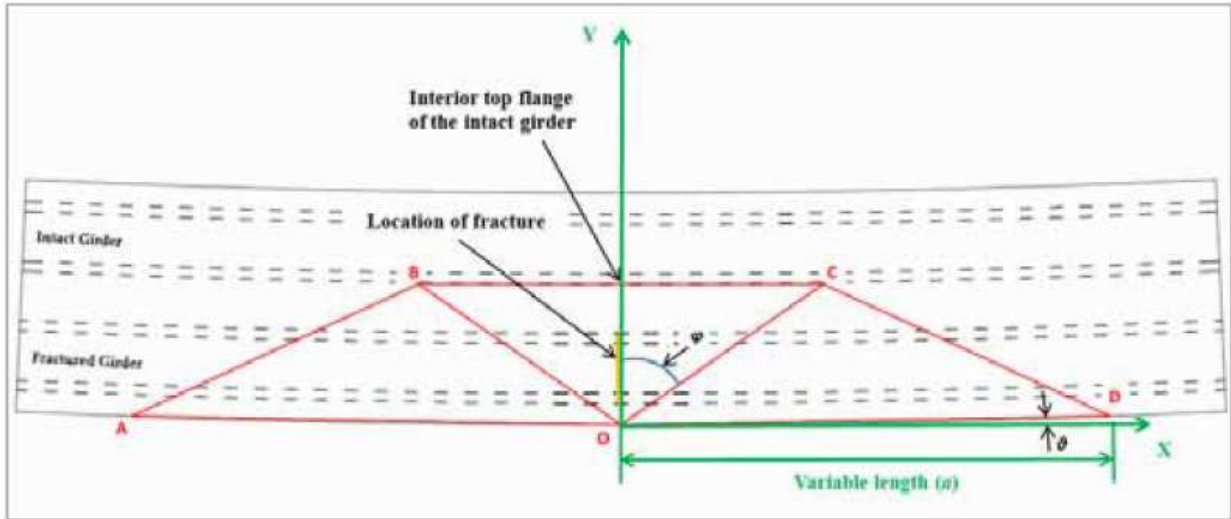


Figure 1-6 Yield line model proposed by Barnard et al. (2010).

The internal work of each line with length l can be calculated as:

$$dIW = m_b * l * \theta_{rotation}$$

where m_b is bending moment of each deck strip along each yield line and $\theta_{rotation}$ is angle of rotation of each plate. Then the external work is calculated by summing each point load multiplied by the virtual deflection of each location. Finally, by setting internal work equal to external work and solving the equation, either length a , or the magnitude of truck load will be determined depending upon which variable is fixed at the beginning. If the magnitude of truck load is fixed, then both the internal work and external work can be expressed as a function of length a , and vice versa.

The detailed information on how to calculate m_b , l , $\theta_{rotation}$ and external work can be found in the report “Modeling the Response of Fracture Critical Steel Box-Girder Bridges” (Barnard et al., 2010).

1.3.3 Limitations and Shortcomings

Direct Analysis Approach (NCHRP Report 406)

Although the framework developed in NCHRP Report 406 is comprehensive and has been used in several research projects such as HNTB/MTP project on Marquette Interchange HPS twin box-girder bridges, it contains limitations and drawbacks that need to improve as following:

1. Although this study provides a tabulated system of factors for several common types of bridge configurations, it doesn't include any steel box-girder bridges. It means nonlinear finite element analysis for every single steel box-girder bridge is required for each redundancy assessment. Performing nonlinear FEAs and repeating the procedure for all steel box-girder bridges in the fracture critical list can be very costly and time-consuming.

2. The redundancy criteria proposed in this research were determined based on calibration of reliability indices of a large number of multi-girder common-type bridges. This might be not fully applicable to bridges with fracture critical members, particularly twin steel box-girder bridges that are investigated in this research.
3. Since the deck was modeled as several parallel beams, it might not capture well the true nonlinear behavior of concrete. In addition, the failure of slab due to crushing of the concrete under transverse bending or shear failure was not considered during the finite element analysis.
4. Private discussion with the principal investigator of NCHRP 406 indicates that assessing the redundancy of two steel box-girder bridges after damage was not the objective of this particular investigation. Therefore, the application of recommendations made by NCHRP 406 to assess the redundancy of damaged two steel box-girder bridges is questionable.

Simplified Methods Proposed by Barnard et al. (Texas DOT Research Project 9-5498)

It is important to note that the methods of predicting the capacity of twin steel box-girder bridges, proposed in Texas DOT Research Project 9-5498, focused on a single loading condition of a fully distributed load. The loading configurations used in the research could have created different responses than what could happen in a more realistic loading state. Furthermore, the yield line analysis that was proposed in case the shear studs didn't have sufficient strength included several limitations, including:

1. The failure mode observed in the test was based on uniform loading. Therefore, the statement that the same failure mode would be obtained under an HS-20 truck load is questionable and needs justification and verification.
2. This method requires an assumed failure mode/pattern; however, under different loading circumstances, a different failure mode/pattern can be obtained. This would imply that the suggested method can't be generalized.
3. This analysis might not be applicable to abrupt failure modes like shear and punching shear of the deck.
4. As an upper bound method, this yield line analysis will predict a collapse load that may be greater than the true collapse load.
5. Arbitrary use of load factor of 2 against HS-20 trucks needs justification.

1.4 Research Objectives

The main objective of this research is to assess the redundancy of two steel box-girder bridges and ultimately lead to the development of practical tools to assess their redundancy and remove them from fracture critical list, where feasible.

1.5 Report Organization

The research project involved conducting a significant amount of analytical, numerical and experimental work. The entire effort is summarized in this final report.

Chapter 1 presents the introduction and an overview of available information.

Chapter 2 provides an overall philosophy for assessing the redundancy of two steel box-girder bridges. This chapter provides the roadmap that ultimately could lead to development of tools that will assist departments of transportation and bridge owners assessing the redundancy of the two steel box-girder bridges and removing them from the fracture critical list, where feasible. The development of complete tools needed is beyond the scope of this project. Therefore, this chapter provides a list of technical challenges that were addressed within this project together with a list of remaining technical questions that will be the subject of a proposed pooled fund project under development. This chapter also provides justification for different activities undertaken within this project.

Chapter 3 provides design, details and instrumentation plans for the small-scale laboratory test specimen constructed and tested in the FDOT structural laboratory.

Chapter 4 presents the results obtained from the testing of small-scale test specimen.

Chapter 5 presents the finite element modeling techniques used for development of nonlinear model.

Chapter 6 presents the calibration process for nonlinear finite element model utilizing results of small-scale test specimen tested in the structural laboratory.

Chapter 7 presents the results of field tests conducted on a multi-span two steel box-girder bridge in service.

Chapter 8 provides application of recommended procedures by NCHRP 406 to assess redundancy of two steel box-girder bridges after damage.

Chapter 9 provides summary of parametric studies conducted using calibrated nonlinear finite element model developed and described in Chapter 6.

Chapter 10 provides a summary and conclusions.

Chapter 2 Research Methodology

There is ample evidence indicating that two steel box-girder bridges are redundant, even if tension flanges of one steel box-girder are completely fractured, including the behavior of bridges that have continued to carry traffic load after damage and with little noticeable change to their global behavior, as well as the full-scale tests on test specimens loaded to failure. However, as is the case with any engineering process, it is still necessary to develop a sound and scientific approach to prove that two steel box-girder bridges are redundant and safe after damage. The need for the development of this comprehensive assessment procedure is grounded in the creation of the fracture critical concept within the bridge community in the United States. It is interesting to note that the need to prove that two steel box-girder bridges are redundant after damage, is not as a result of collapse of these bridge types after damage.

The guidelines provided by AASHTO *LRFD Bridge Design Specifications* and FHWA and summarized in Chapter 1, allow the assessment of the safety and redundancy of two steel box-girder bridges using detailed numerical work.

Commentary section 6.6.2 of the AASHTO *LRFD Bridge Design Specifications* provides general guidelines that can be used to evaluate the performance of bridges with fracture critical members and states: "... The criteria for a refined analysis used to demonstrate that part of a structure is not fracture-critical have not yet been codified. Therefore, the loading cases to be studied, location of potential cracks, degree to which the dynamic effects associated with a fracture are in the analysis, and fineness of the models and choice of element type should all be agreed upon by the owner and the engineer. The ability of a particular software product to adequately capture the complexity of the problem should also be considered and the choice of software should be mutually agreed upon by the owner and the engineer. Relief from the full factored loads associated with the strength I load combination of Table 3.4.1-1 should be considered, as should the number of loaded design lanes versus the number of striped traffic lanes".

AASHTO *LRFD Bridge Design Specifications* and FHWA requirements for assessing the redundancy of damaged two steel box-girder bridges are feasible through detailed nonlinear three dimensional finite element analyses, using calibrated model. However, even with such an approach there is still one important missing piece of information to complete the process: the load level that the damaged bridge must sustain with respect to strength and deflection and other applicable serviceability criteria. The research study conducted in Texas arbitrarily uses two times HS-20 truck load and doesn't address the loading combination that must be used during analysis.

It is also important to note that the work sponsored by the National Steel Bridge Alliance and carried out at Purdue University is limited to the development of the nonlinear finite element model of damaged bridges, which has been accomplished in a number of studies and does not address any other technical issues involved. The main advantage of the Purdue work is the development

of the mesh generation procedure for specific software. The proposed pooled fund project will take advantage of this valuable addition to the body of knowledge, as described later in this chapter.

2.1 Main Characteristics of Comprehensive Methodology for Assessment

The requirements stated above necessitate that the methodology to assess the redundancy of two steel box-girder bridges after damage should have the following characteristics:

1. Methodology must develop the load level that the damaged bridge must resist using a rational process.
2. The suggested approach for assessment of redundancy of the damaged bridge is in the form of conducting detailed nonlinear finite element analyses.

Based on the results of this current research study, discussions with various sectors of the steel bridge industry, and practical considerations, the following paths are suggested to assess the redundancy of two steel box-girder bridges.

Modified Simple Texas Approach

The first step in the suggested methodology is the use of simple hand calculation in the form of a modified simple approach suggested by Texas DOT Research Project 9-5498. Additional work needs to be carried out to further develop the suggested simple evaluation approach by Texas DOT, and this could be achieved by reducing the level of conservatism inherent in the Texas suggested approach, using the results of this research project. In its present form the results from the Texas simplified approach are highly conservative as compared to the test results. For instance, the full-scale bridge tested in Texas demonstrated 363 kips of load capacity, while the current version of simplified Texas method prediction is 107 kips.

Once developed, the modified Texas simple approach could be used as the first step in the process of evaluating the redundancy of damaged two steel box-girder bridges without any need for conducting detailed finite element analysis. The entire process could be carried out using hand calculations and will involve considering each bridge, one at a time. Still-missing information in this process are the strength criteria such as the minimum load level that the damaged bridge should resist and other applicable serviceability criteria, such as deflection of the bridge after damage and before retrofitting the bridge. The suggested approach to develop such criteria is explained in the next section in the proposed notional approach.

In the event that a modified Texas simple approach does not result in removing the two steel box-girder bridges from the fracture critical list, the notional approach, which is described in the next section, could then be used.

Proposed Notional Approach to Assess the Redundancy of Damaged Two Steel Box-Girder Bridges

Conducting detailed nonlinear finite element analysis remains the only viable approach for assessing the redundancy of damaged two steel box-girder bridges. However, as mentioned previously, the level of effort involved in addressing the redundancy of all two steel box-girder bridges within inventory of a given state requires significant amounts of financial, labor and computer resources. The notional approach to reduce the level of effort involved, consists of grouping the two steel box-girder bridges within a state inventory into several groups and developing a notional simple-span two steel box-girder bridge that would represent each group and carries out the detailed nonlinear finite element analysis on the notional bridge. This approach reduces the level of efforts involved at two different levels. First, conducting a detailed nonlinear analysis on a simple-span bridge is much easier than conducting similar analysis on a multi-span bridge. Second, only one analysis will need to be carried out for each group. In this approach, proving the redundancy of a notional bridge will be equivalent to proving that all bridges within the group of simple- and multi-span two steel box-girder bridges in the group, under consideration, are redundant.

The notional approach demands comprehension of the following issues:

1. Development of a calibrated nonlinear finite element model that accurately depicts the modes of failure under types of loading specified by *AASHTO LRFD Bridge Design Specifications*. It should be noted that this current research project demonstrates that punching shear is a possible failure mode in damaged two steel box-girder bridges, and that the capacity of the damaged bridge is influenced by presence of damage in fractured girder. The Texas research study was not able to identify this mode of failure because of the type of loading used in their research.
2. Development of criteria to group two steel box-girder bridges within the inventory of a given state DOT and developing notional simple-span two steel box-girder bridge representing the group.
3. Establishment of the load level that damaged two steel box-girder bridges must resist as, well as establishment of other serviceability limit states that must be checked to ensure public safety.
4. Development of a Guide for application of the notional approach for assessing redundancy of damaged two steel box-girder bridges with examples and other documentations, such as video tapes that would assist state DOTs.

Following is a brief discussion of information that has been developed as a result of this current study. Chapters 3 through 7 of this report provide documentation of efforts that were undertaken to develop a test-verified calibrated three dimensional finite element model that could be used to assess the redundancy of the damaged two steel box-girder bridges. Chapter 8 provides a summary of assessment of the redundancy of a full-scale bridge using the direct analysis approach, proposed in NCHRP Report 406. Chapter 9 provides a summary of the efforts and start of the process for establishing the notional simple-span two steel box-girder bridges and grouping criteria.

Following is brief discussion of procedures that could be used to develop the load level that damaged two steel box-girder bridges must sustain before retrofit or complete replacement. The development of load level that two damaged two steel box-girder bridges must resist will demand carrying out reliability-based analysis with a safety level agreed upon by bridge owners. This effort could consist of the following steps.

1. Establish a probability density function (PDF) for load-carrying capacity of the damaged bridges, considering realistic modes of failure. This step will demand a large number of simulations. For the purpose of research, there will be a need to develop an approximate method for estimating the remaining capacity of damaged bridges. This current research study demonstrates that punching shear is most likely mode of failure, which in turn could significantly simplify the efforts involved in this step.
2. Establish the required load level. As damage to a bridge increases, the PDF for resistance, as shown in Figure 2-1, shifts to the left and the overlapping area between PDFs of load and resistance increases. The increase in overlapping area increases the probability of failure and lowers the safety level. This is true if PDF of load remains unchanged.

The determination of the load level that damaged two steel box-girder bridges must resist could be established by first establishing the level of safety (beta index) for damaged bridges that is agreeable by owners. This safety level could be established by consensus or through analysis of bridges that are agreed to be redundant (Ghosn and Moses, 1998). Once the safety level is established, the PDF of load could be shifted to the left or right until the overlapping area under the two PDFs results in a desired safety level. This process will establish the position of PDF for load, which in turn will establish the load level that damaged two steel box-girder bridges must resist.

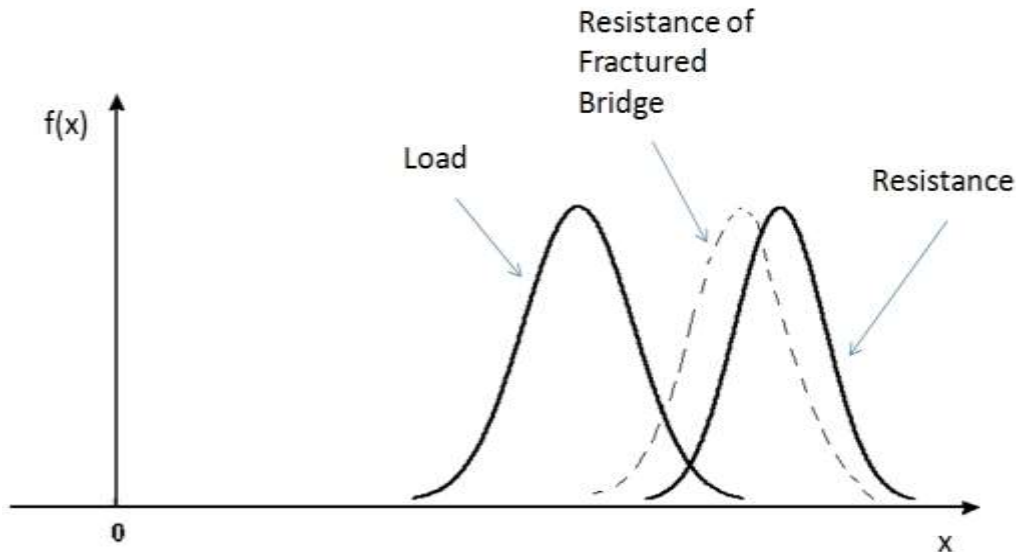


Figure 2-1 Probability density functions of load and resistance of damaged and undamaged bridges.

Another important practical consideration is the ability of a damaged bridge to carry the traffic until the damage is detected and repaired without jeopardizing public safety. This consideration could demand checking the deflection of the damaged bridge and ensuring the serviceability of the bridge during the time period that damage will go on without detection. This aspect of the problem could be checked approximately while conducting analysis on the notional bridge.

2.2 Proposed Pooled Fund Project

Results of efforts carried out under this current FDOT-sponsored research study are summarized within this report. This chapter provides the overall approach that could ultimately lead to development of step-by-step procedures allowing state DOTs to assess the redundancy of damaged two steel box-girder bridges and eliminate them from the fracture critical list, where possible. As mentioned previously, the level of efforts needed to address the problem completely is beyond the scope of this project. Therefore, a scope of work for a future research project is envisioned to be submitted to the FDOT.

Chapter 3 Laboratory Testing on Small-Scale Specimen

In order to investigate the behavior of twin steel box-girder bridges in nonlinear range and modes of failure, and to calibrate nonlinear 3-D finite element model, laboratory testing of a small-scale twin steel box-girder bridge specimen was incorporated into this project. Detailed information on design and construction of the small-scale specimen, the instrumentation and testing plan is discussed in the following sections.

3.1 Specimen Design

This small-scale bridge was designed based on AASHTO *LRFD Bridge Design Specifications* (2010). Even though the specimen was a small-scale version, it was designed to replicate the proportions of a typical cross-section of a twin steel box-girder bridge. The span to depth ratio of the specimen is proportioned to satisfy the traditional deflection criteria of the AASHTO *LRFD Bridge Design Specifications*. The test specimen was proportioned to flange and web slenderness ratios based on AASHTO criteria. The slenderness of the webs and bottom flange was limited so that longitudinal stiffeners were required only at the bottom flange near the interior support. The final cross-section details of the box-girder were designed as follows and are also illustrated in Figure 3-1.

$$D = 20.6875 \text{ in. (depth of web)}$$

$$t_w = \frac{3}{8} \text{ in. (thickness of web)}$$

$$b_{tf} = 6 \text{ in. (width of top flange)}$$

$$t_{tf} = \frac{1}{2} \text{ in. (thickness of top flange)}$$

$$b_{bf} = 18 \text{ in. (width of bottom flange)}$$

$$t_{bf} = \frac{1}{2} \text{ in. (thickness of bottom flange)}$$

$$d = D + t_{bf} + t_{tf} = 21.6875 \text{ in. (depth of girder)}$$

$$D_t = d + \text{slab thickness} = 21.6875 + 5 = 26.6875 \text{ in. (total depth of the cross section)}$$

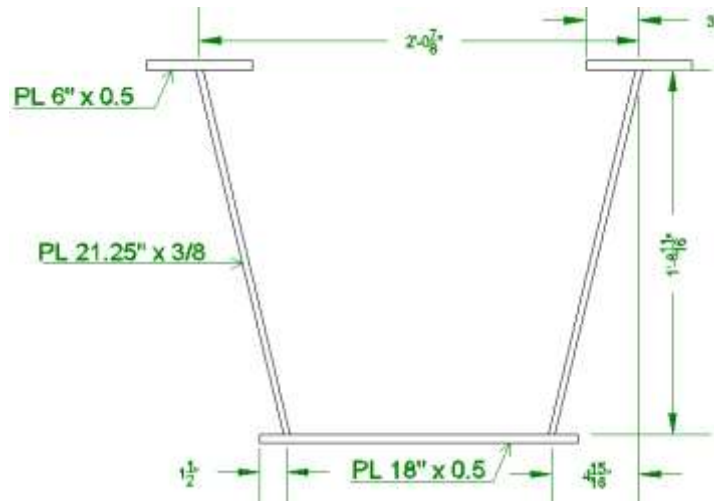


Figure 3-1 Dimension of one steel box girder.

Although AASHTO 6.11.6.2.2 requires all curved steel box girders to be designed as non-compact sections, straight steel box girders can be designed as compact sections. The depth to thickness ratio of the web was designed to be 56 and less than the limit of 150 for webs without longitudinal stiffeners. The width of bottom flange was 18 in., which is less maximum of one fifth of the span length. The web was designed to be entirely in tension, meaning $D_{cp} = 0$ (see plastic moment calculation for verification). All of the compactness checks below verify that the section is compact.

Cross-section proportion limit checks:

$$\frac{D}{t_w} = 56 < 150 \text{ (OK)}$$

$$\frac{b_{tf}}{2 * t_{tf}} = 6 < 12 \text{ (OK)}$$

$$b_{tf} = 6 \geq \frac{D}{6} \text{ (OK)}$$

$$a = 29.688 \text{ in.}, \quad w = 24.875 \text{ in.}, \quad 0.8 * w \leq a \leq 1.2 * w \text{ (OK) see Figure 3-2.}$$

$$\text{Slope of web} = \frac{1}{4.2} \leq \frac{1}{4} \text{ (OK)}$$

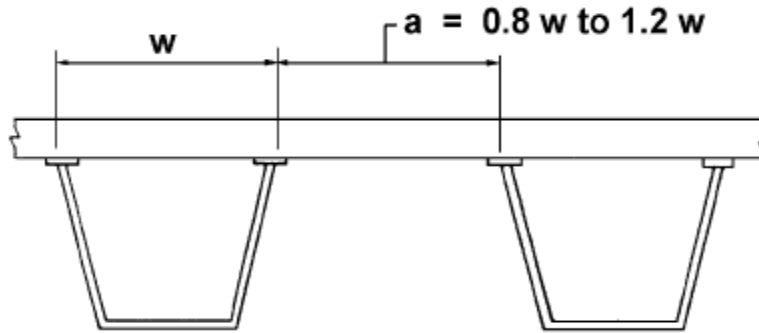


Figure 3-2 Center-to-center flange distance (Adopted from AASHTO LRFD Bridge Design Specifications).

The width of the specimen was 109 in. and the distance between two box-girders, from center to center, was 54.5 in. Since the deck thickness couldn't be scaled directly as the box-girder, the deck thickness was chosen to allow enough space for four mats of conventional reinforcement bars. For these reasons, the specimen deck was set at 5-in. depth. The deck was reinforced by #4 bars at every 6 in. in longitudinal direction for both top and bottom reinforcement mat. The transverse bars were also #4 and installed every 6 in. as well. The railing system was a removable system including several railing segments, and each segment has a dimension of 5 in. x 8 in. x 10 ft. The rail was sized to increase elastic stiffness of the entire structure by 10%, which is comparable to the rail contribution for a full size structure. Each rail segment was reinforced by four longitudinal bars with stir-ups spaced at every 10 in. The rail was connected to the deck by bolt connections (1.5" diameter B7 rods) at the ends of each railing segment. The final detail of the specimen cross-section is illustrated in Figure 3-3.

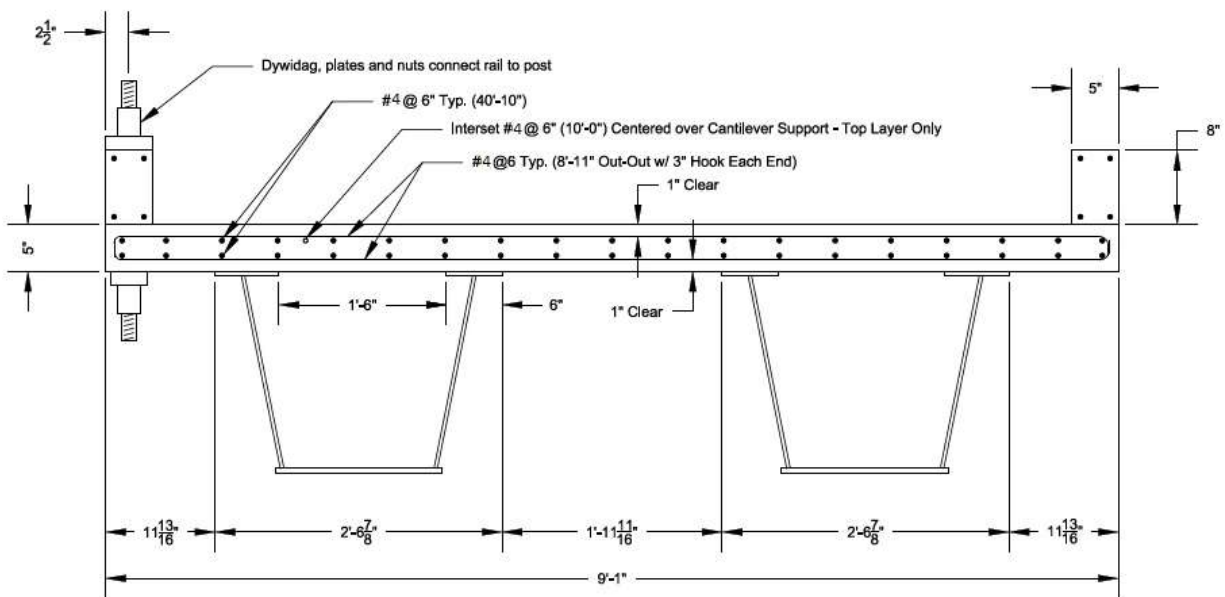


Figure 3-3 Cross-section of the testing specimen.

Each box-girder was designed to have two internal diaphragms at the supports and two internal cross-frames at the quarter lengths of the main span and one internal cross-frame 2 ft away from the cantilever end. The internal cross-frames are denoted as X-bracing in Figure 3-4.

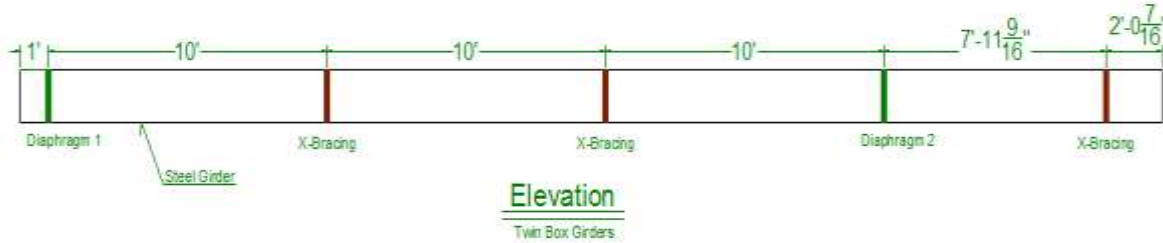


Figure 3-4 Internal bracing locations in each box girder.

At every location where the internal diaphragms and internal cross-frames are present, one external cross-frame was installed connecting two box-girders. Five sets of top lateral bracings were constructed and welded to the top flanges in each box-girder. All locations of cross-frame, diaphragm and top lateral bracing are plotted schematically in Figure 3-5. All the internal and external cross-frames are connected to the box girders by bolt connections through stiffener plates.

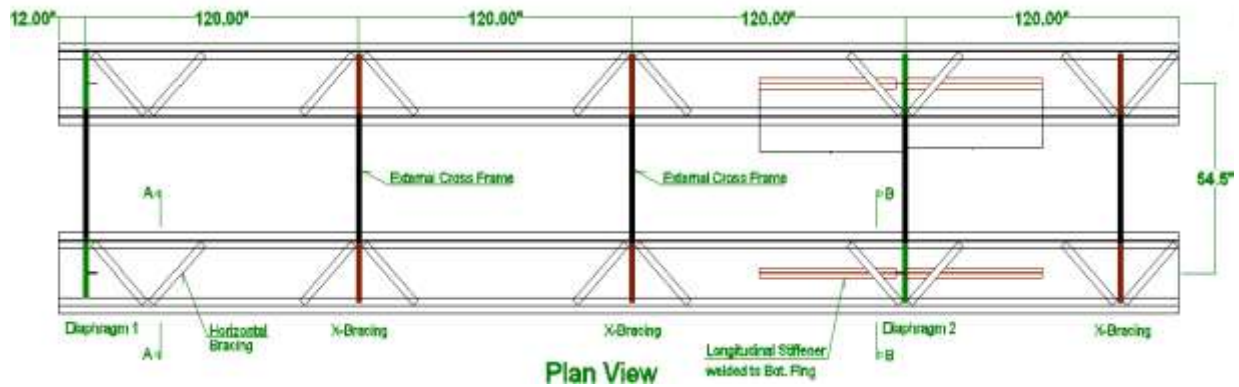


Figure 3-5 The top plan view of the testing specimen.

3.1.1 Analysis of Composite Section

For material properties, all steel plates are grade 50 steel and were assumed to have yield strength of 50 ksi (1 ksi = 1,000 lbf per square inch), and compressive strength of concrete was assumed to be 4.5 ksi for design purposes. The reinforcements are grade 60 steel and were assumed to have yield strength of 60 ksi. (The actual concrete properties that were determined at the time the deck was poured and when tests were performed are reported in Chapter 5.) The effective width of the concrete deck for the composite section of each girder was found to be 54.5 in., which is one-half of the width of the entire deck. Assuming the concrete deck and rebar to be in compression and steel girder in tension, the force in each element is calculated as follows:

$$C_c = 0.85 \times f_c' \times b_{eff} \times t_s = 0.85 \times 4.5 \text{ ksi} \times 54.5 \text{ in} \times 5 \text{ in} = 1,042 \text{ kips}$$

$$C_{rebar_top} = A_{rebar_top} \times F_{y_{rebar}} = 1.78 \text{ in}^2 \times 60 \text{ ksi} = 107 \text{ kips}$$

$$C_{rebar_bot} = A_{rebar_bot} \times F_{y_{rebar}} = 1.78 \text{ in}^2 \times 60 \text{ ksi} = 107 \text{ kips}$$

$$T_{girder} = A_{girder} \times F_y = 30.937 \text{ in}^2 \times 50 \text{ ksi} = 1,547 \text{ kips}$$

Since $T_{girder} > C_c + C_{rebar_top} + C_{rebar_bot}$, the plastic neutral axis (PNA) is in the steel girder. Now, assuming the PNA is in the top flanges, the location of PNA measured from the top fiber of the top flanges can be determined as following:

$$PNA = \frac{1}{2} \times \left(\frac{T_{girder} - C_c - C_{rebar_top} - C_{rebar_bot}}{2 \times F_y \times b_{tf} \times t_{tf}} \right) = 0.243 \text{ in.}$$

The nominal plastic moment capacity can be calculated by taking moments of the forces from the steel girder, rebar and deck about PNA. Since PNA is in the top flanges, this suggests that a portion of top flange above the PNA is in compression and the portion below the PNA is in tension. Location of neutral axis of bottom flange, webs and top flanges, reinforcements, and deck measured from the location of PNA are as follows:

$$y_c = PNA + \frac{t_s}{2} = 2.743 \text{ in.}$$

$$y_{rebar_top} = 4.0 \text{ in.}$$

$$y_{rebar_bot} = 1.5 \text{ in.}$$

$$y_{tf_c} = 0.122 \text{ in.}$$

$$y_{tf_t} = 0.129 \text{ in.}$$

$$y_w = 10.6 \text{ in.}$$

$$y_{bf} = 21.2 \text{ in.}$$

$$M_c = C_c \times y_c = 2858 \text{ kips} - \text{in}$$

$$M_{rebar_top} = C_{rebar_top} \times y_{rebar_top} = 428 \text{ kips} - \text{in}$$

$$M_{rebar_bot} = C_{rebar_bot} \times y_{rebar_bot} = 160 \text{ kips} - \text{in}$$

$$M_{tf_c} = C_{tf_c} \times y_{tf_c} = PNA \times b_{tf} \times 2 \times F_y \times y_{tf_c} = 18 \text{ kips} - \text{in}$$

$$M_{tf_t} = C_{tf_t} \times y_{tf_t} = (t_{tf} - PNA) \times b_{tf} \times 2 \times F_y \times y_{tf_t} = 20 \text{ kips} - \text{in}$$

$$M_w = C_w * \times = A_w \times F_y \times y_w = 2 \times 7.97 \text{ in}^2 \times 50 \text{ ksi} \times 10.6 \text{ in} = 8,448 \text{ kips} - \text{in}$$

$$M_{bf} = C_{bf} \times y_{bf} = A_{bf} \times F_y \times y_{bf} = 9 \text{ in}^2 \times 50 \text{ ksi} \times 21.2 \text{ in} = 9,540 \text{ kips} - \text{in}$$

$$M_p = M_c + M_{rebar_{top}} + M_{rebar_{top}} + M_{t_{fc}} + M_{t_{ft}} + M_w + M_{bf} = 21,472 \text{ kips} - \text{in} = 1,789 \text{ kips} - \text{ft}$$

In addition, the yielding moment calculation yields M_y equal 1364 kips-ft. The nominal capacity of the section is calculated as following:

$$M_n = M_p \times \left(1.07 - 0.7 \times \frac{D_p}{D_t}\right) = 1789 \times \left(1.07 - 0.7 \times \frac{t_s + PNA}{26.6875}\right) = 1,668 \text{ kips} - \text{ft}$$

$$M_n \leq 1.3 * M_y = 1,773 \text{ kips} - \text{ft} \text{ (OK)}$$

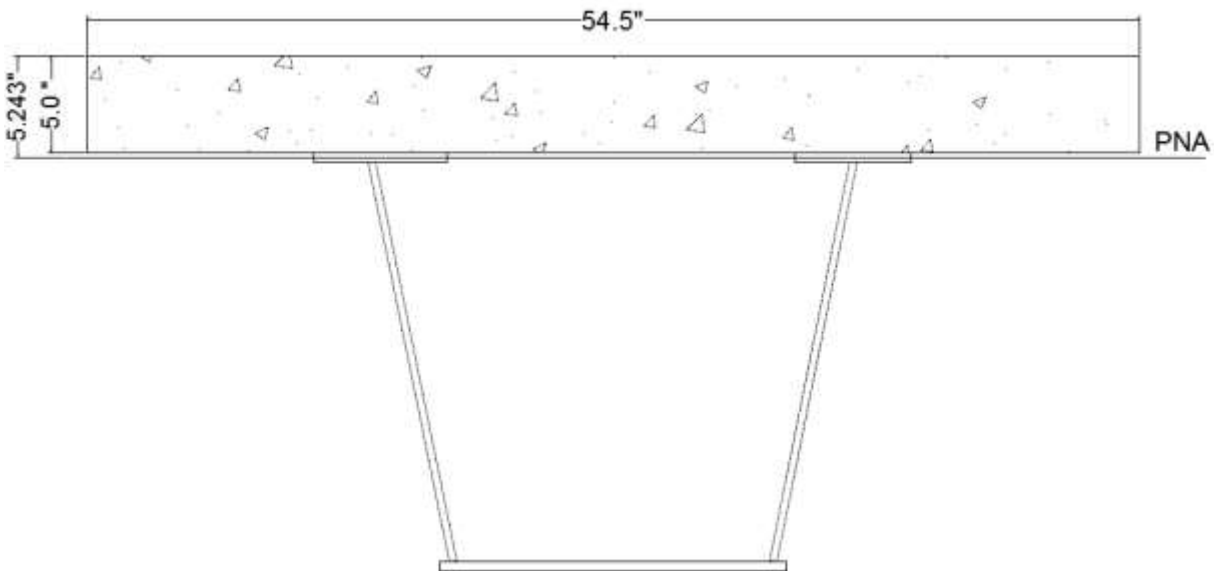


Figure 3-6 Location of plastic neutral axis.

3.2 Specimen Construction

After completing the design phase, the shop drawings for steel girders, stiffeners, diaphragms and cross-frames were prepared. All steel components were fabricated at Tampa Steel Erecting Company. The steel material used for fabrication is ASTM A709 Grade 50. Bolts are A325 Type 1 material with 0.625 in. in diameter. The diameter for holes is slightly larger than that of the bolts with 0.6875-in. diameter. All steel was blast-cleaned to near-white condition and the steel surfaces were coated with self-curing inorganic zinc primer. The welding was performed in accordance with the bridge welding code D1.5 Specifications. All of the fillet welds were terminated within

either 0.5 ± 0.25 in. or 0.25 ± 0.125 in. from the edge of a plate, depending on the length of welded leg, as illustrated in Figure 3-7.

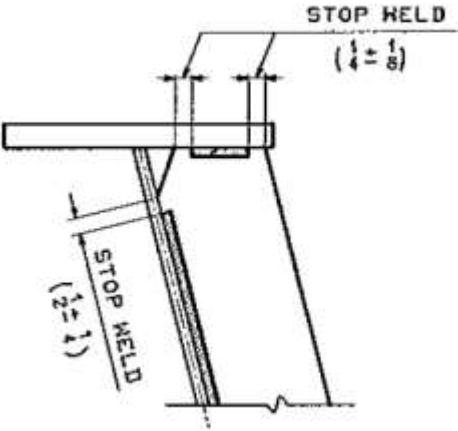


Figure 3-7 Welding details.

After the fabrication was completed, two steel girders and five external cross-frames were assembled at the shop to check for any fit-up issue. Then, they were disassembled and shipped to FDOT Structures Laboratory to complete the remaining construction works. At FDOT Structures Laboratory, the girder and cross-frames were reassembled and then the formworks and the reinforcements were installed as shown in Figure 3-8. The instrumentations were also installed. Details on the instrumentation plan are discussed in the next section.



Figure 3-8 Complete specimen ready for casting.

The bridge deck was casted using class II concrete mix with 28-day strength of 4,500 psi, 3 in. slump and 0.75 in. maximum aggregate size. This is also the type of concrete that is used by FDOT in other construction projects. The casting process is shown in Figure 3-9. After the concrete got hardened, the entire specimen was relocated to a final position and ready for testing as illustrated in Figure 3-22.



Figure 3-9 Casting the concrete deck.

3.3 Instrumentation Plan

In order to obtain useful data with the most economical setup, the strain gauges and potentiometers were installed differently for each section. Strains were monitored in the steel girders, the cross-frames, and the deck in order to capture responses of each component as well as load-transferring mechanisms.

Sections where potentiometers and strain gauges were installed are illustrated in Figure 3-10. In the original plan, strains were monitored at eight sections, labeled by Section 1 to 8 in green. However, a decision was made to remove gauges at Sections 1 and 7 due to the limitation of the channels in the data acquisition system and the sections were not renumbered. The details of instrumentation for each section are illustrated schematically from Figure 3-11 to Figure 3-18. Section 2, located at mid-span of the main span is the most critical section and was therefore treated very carefully. In Section 5, strains in cross-frames were also monitored. This setting of strain gauges allows the data to be collected in almost all of the important sections.

The deflections were monitored at five locations, labeled in red as “North,” “Location 2,” “Location 5,” “South,” and “End.” At each of these sections, there were four potentiometers attached to the top flanges of both box-girders. The typical potentiometer locations are shown in Figure 3-17. However, in Section 2 at mid-span, an additional potentiometer was installed to measure the deflection at the center of the deck as illustrated in Figure 3-18.

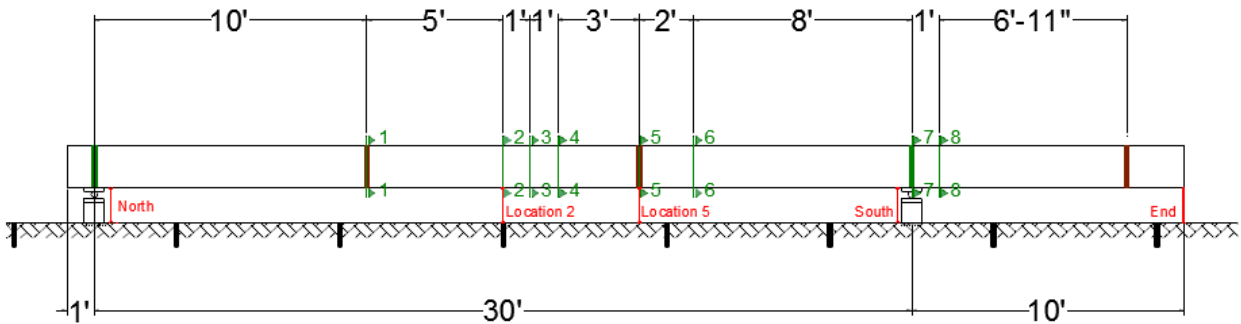


Figure 3-10 Locations of strain gauges and potentiometers along the length of the specimen.

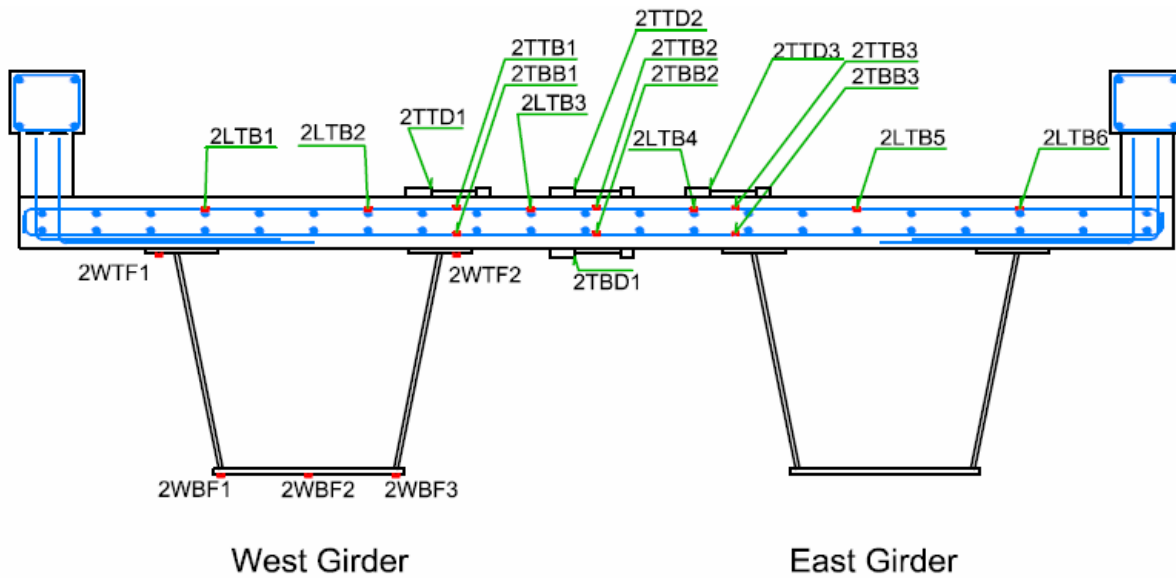


Figure 3-11 Strain gauges in the Section 2.

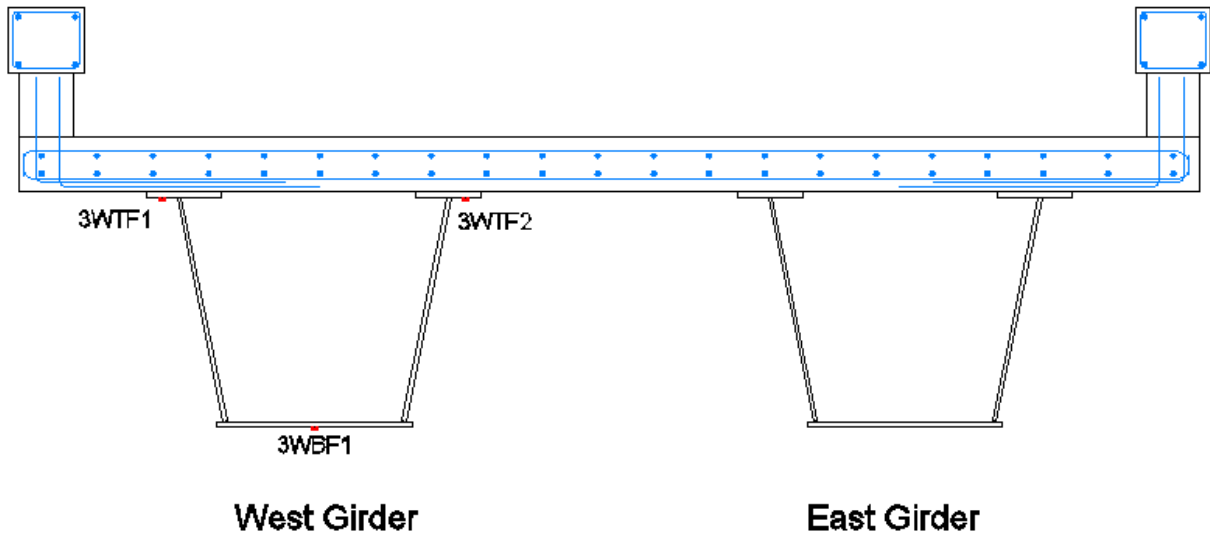


Figure 3-12 Strain gauges in the Section 3.

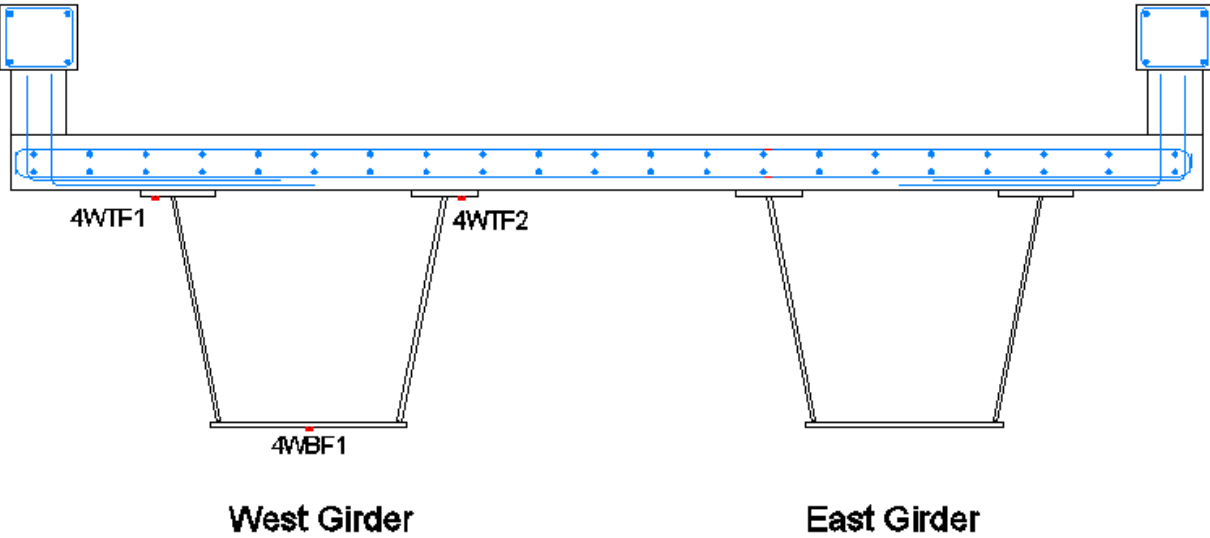


Figure 3-13 Strain gauges in the Section 4.

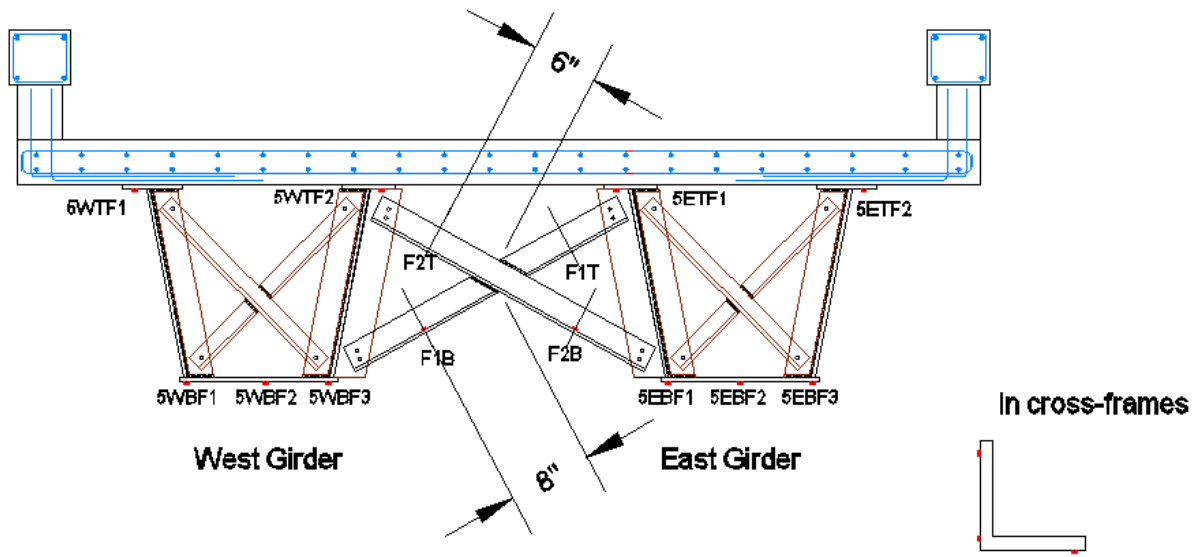


Figure 3-14 Strain gauges in the Section 5.

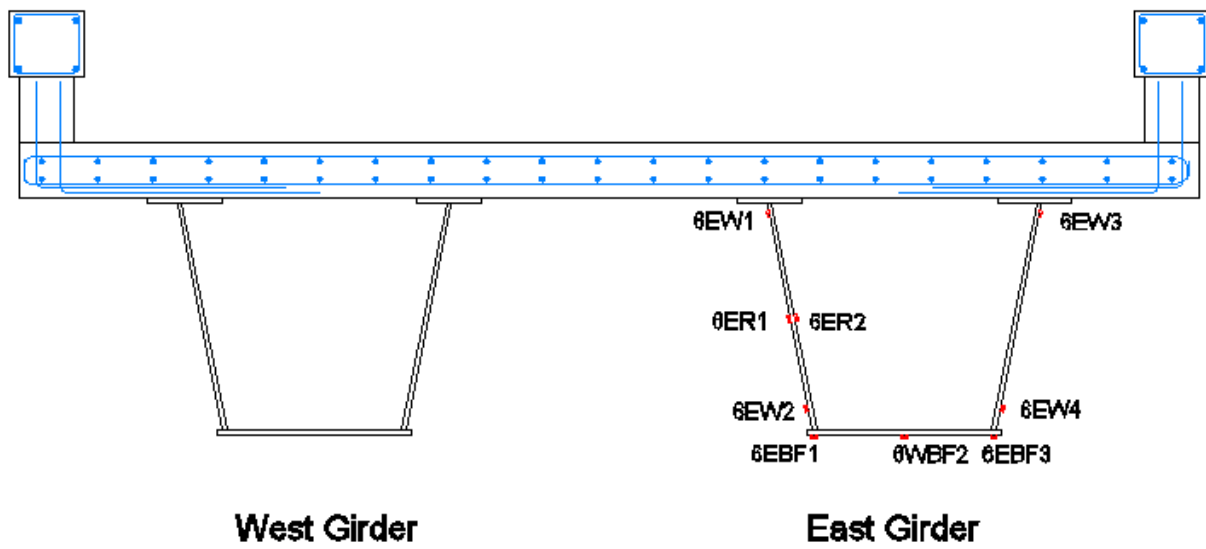


Figure 3-15 Strain gauges in the Section 6.

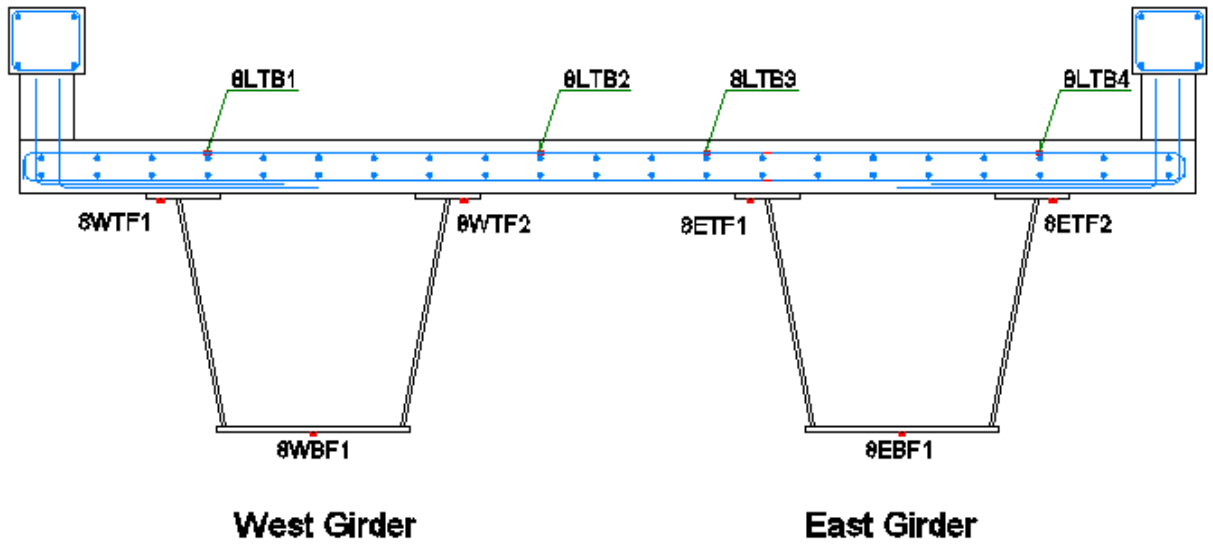


Figure 3-16 Strain gauges in the Section 8.

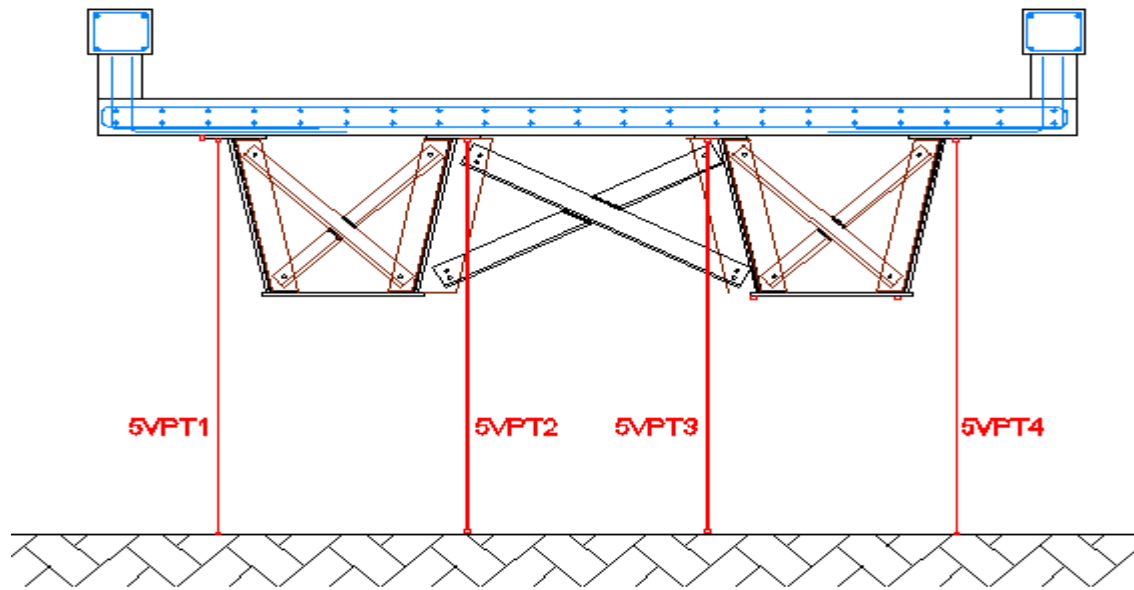


Figure 3-17 Potentiometers in Section 5.

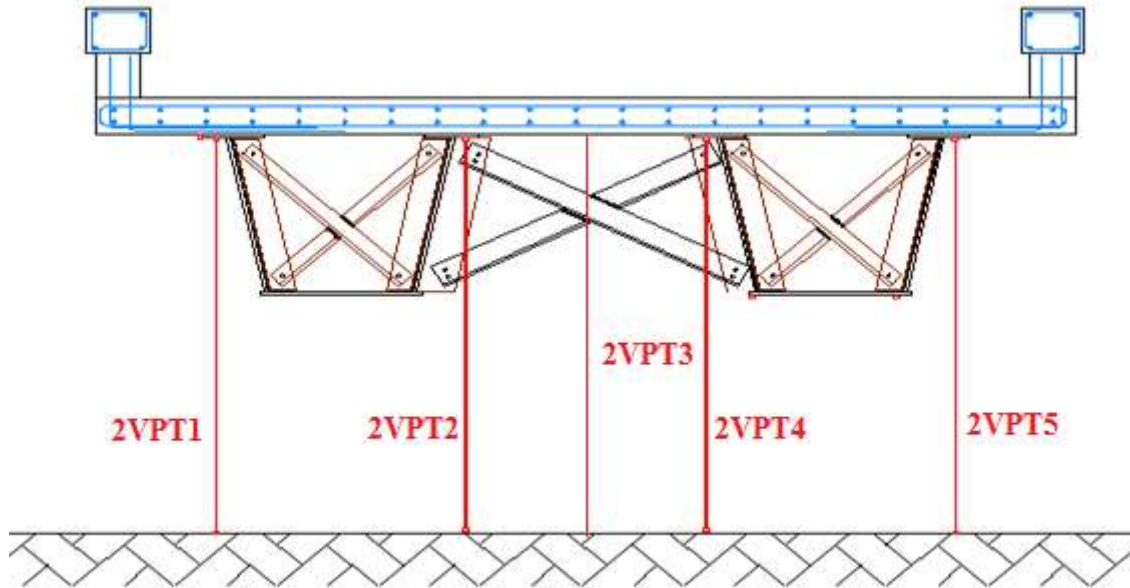


Figure 3-18 Potentiometers in Section 2.

3.4 Test Setup

Since this research was intended to investigate and gather information on the behavior of the twin steel box-girder bridges under both simple span and continuous span conditions, a unique specimen configuration was devised so that both cases can be studied. The total length of the specimen is 41 ft comprising a 31-ft main span and a 10-ft second span as shown in Figure 3-19. The support, which is closer to the second span, is labeled as the south support. The one further away from the second span is labeled as the north support. The second span was configured so that it may act as a free cantilever in the non-loaded or non-anchored state. But when it is restrained to move vertically at its free end, the bridge will become a continuous structure with two spans. The restraining system at the cantilever end is composed of a transverse stiff I-beam anchored to the strong floor through two steel rods as shown in Figure 3-20. Two load cells were placed between the deck and the I-beam. As the load cells are in contact with the I-beam, the anchoring forces that will prevent the cantilever end from moving upwards are recorded. The I-beam can be raised out of the way to remove the restraint.

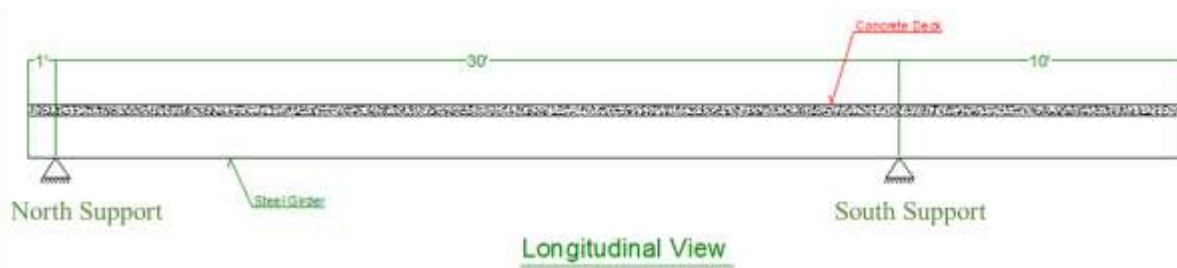


Figure 3-19 Longitudinal view of test specimen.



Figure 3-20 Setup for continuity effect.

Loading system used for this experiment included a FDOT loading frame of 130-in. width, two actuators, a loading beam (stiff I-beam) and steel reinforced elastomeric bearing pads as shown in Figure 3-21. One actuator has an 800-kip capacity and the other one has a 450-kip capacity. With this loading setup either one-point loading or two-point loading scenarios can be carried out. Figure 3-22 shows the complete specimen that was ready to be tested.

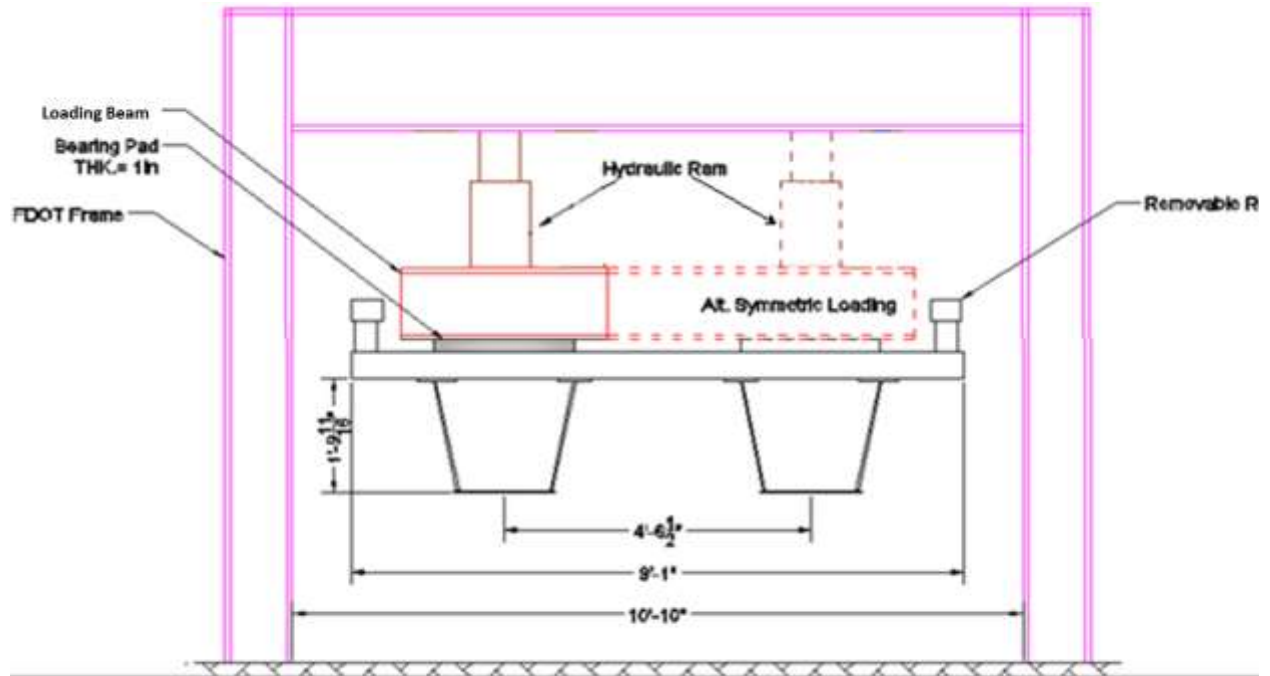


Figure 3-21 Schematic drawing of loading system.



Figure 3-22 Specimen with complete loading setup.

3.5 Testing Plan

In order to comprehend the behavior of two steel box-girder bridges in both linear and nonlinear range and to examine the modes of failures, a number of tests including elastic tests, cyclic fatigue test, and ultimate load tests were carried out on the laboratory small-scale specimens. The testing plan for each test is discussed in the following sections.

3.5.1 Elastic Tests

The goals of the elastic tests were to investigate the effects of rail, continuity, and loading configuration on elastic behaviors of laboratory specimen before and after damage was simulated in one girder, and to establish a baseline for the finite element model calibration.

The specimen was tested in a total of 18 elastic tests, under three different damage conditions. The first set of tests was carried out on the undamaged specimen. The second set of tests was carried out after the bottom flange in one of the girders was fractured. The last set of tests was carried out with bottom flange and webs completely fractured in one of the girders. Each set consisted of six tests with different combinations of rail, continuity, and loading configuration. The testing plan for all elastic tests is summarized in Table 3-1. In this table, the letter “Y” stands for “Yes” and the letter “N” stands for “No”. The letter “S” stands for symmetrical loading configuration indicating the loads are applied to both girders, while the letter “U” stands for unsymmetrical loading configuration. It should be noted that throughout the elastic tests, the west girder (WG) remained intact. The east girder (EG) was the only girder that was cut to simulate fracture and also the one to which the load was applied in unsymmetrical loading scenarios.

In all of the elastic tests, the load was applied to the specimen through 2”x9”x36” loading pad(s), with three slow dynamic loading ramps. Figure 3-23 shows one example of one loading history of one elastic test. Based on the finite element analysis and hand calculation results, the applied loads were selected to be 50 kips for unsymmetrical loading or 100 kips for symmetrical loading with 50 kips over each girder, in order to ensure the responses of the specimen to be in a linear range under both undamaged and damaged conditions.

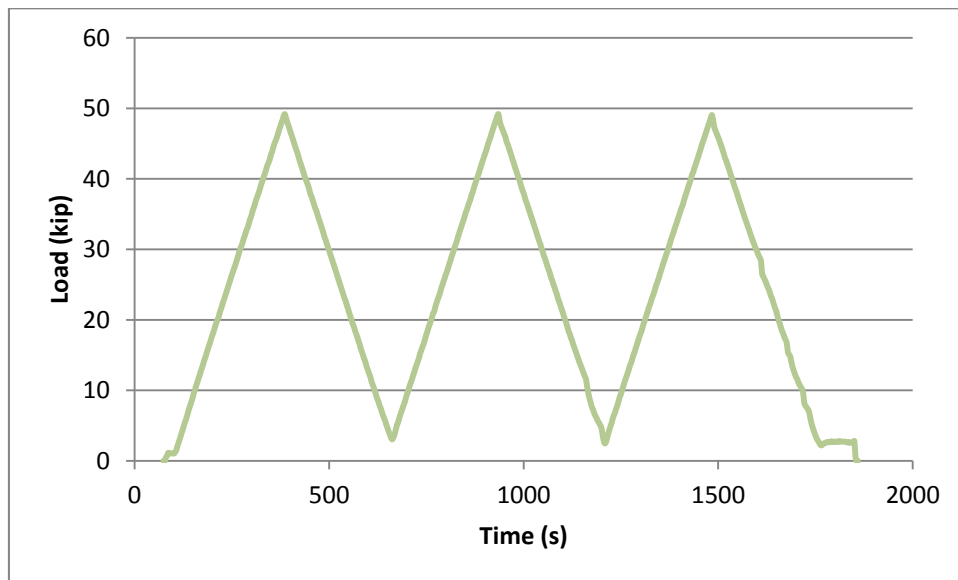


Figure 3-23 Typical three-ramp loading history for the elastic tests.

Table 3-1 Plan for Elastic and Cyclic Tests

Test	Name	Number of Loaded Girder	Rail	Continuity	Loading Type	Max Load (kips)
Undamaged Condition						
1	Static	2	N	N	S	50 each
2		1	N	N	U	50
3		1	N	Y	U	50
4		2	Y	N	S	50 each
5		1	Y	Y	U	50
6		1	Y	N	U	50
Bottom Flange Fractured Condition						
7	Static	2	Y	N	S	50 each
8		1	Y	Y	U	50
9		1	Y	N	U	50
10		2	N	N	S	50 each
11		1	N	N	U	50
12		1	N	Y	U	50
13	Cyclic	1	Y	N	U	60 kips and almost million cycles
Webs and Bottom Flange Fractured Condition						
14	Static	2	Y	N	S	50 each
15		1	Y	Y	U	50
16		1	Y	N	U	50
17		2	N	N	S	50 each
18		1	N	N	U	50
19		1	N	Y	U	50

Notation: Y is Yes; N is No; S is Symmetric; U is unsymmetrical.

3.5.2 Cyclic Test

As indicated in Table 3-1, the cyclic test was carried out under the damage condition in which EG had its entire bottom flange fractured. The purpose of this cyclic test was to see what would happen to the bridge under the traffic load assuming a fracture/damage occurred in the bottom flange without being noticed. The cyclic load magnitude was determined based on the AASHTO *LRFD Bridge Design Specifications* (2010). First, the fatigue category for the bridge specimen was selected based on its structural characteristics such as cross-frame and stiffener design details. The cyclic load is then defined as the load required such that the maximum stress produced on the specimen would be equal to the threshold stress of the selected fatigue category according to the AASHTO *LRFD Bridge Design Specifications*. The determination of the cyclic load required several iterative finite element analyses of the bridge.

It should be noted that this procedure assumes the structure is designed for infinite life and is most efficient when it just meets this requirement (threshold stress). Therefore, if a fracture would occur without being noticed, the same (design) load causing the threshold stress would continue to be applied. This same load was then applied to the damaged bridge at the traffic rate equivalent to infinite life for a period of two years.

This laboratory specimen satisfies the requirements for type C fatigue category. The threshold stress for type C category is 10 ksi. The load on the undamaged structure required to cause a maximum stress of 10 ksi is 60 kips, which was determined from finite element analysis. The average daily traffic truck passing the bridge equivalent to infinite life is 1286 trucks per day (AASHTO, 2010). For every two years, the total trucks that would pass the bridge will be 938667 trucks or cycles. The truck load is applied to the specimen at a rate of 1 Hz, so the total estimated time to perform the cyclic test was 10.9 days.

3.5.3 Ultimate Load Tests

A total of five ultimate load tests were carried out. In these ultimate load tests, the laboratory specimens were loaded to failure with one girder completely fractured at mid-span. The purposes of the ultimate load tests were to investigate the inelastic behavior, maximum load-carrying capacities and modes of failure of a twin steel box-girder bridge when the bottom flange and the webs are completely fractured in one girder. All of the ultimate load tests are summarized in Table 3-2.

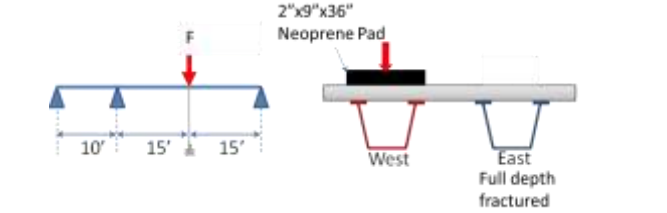
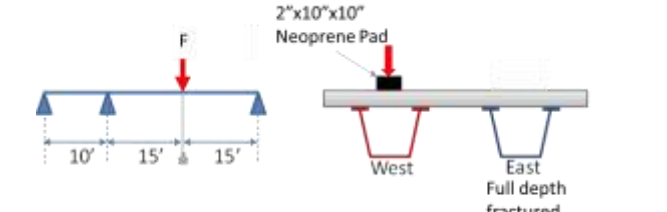
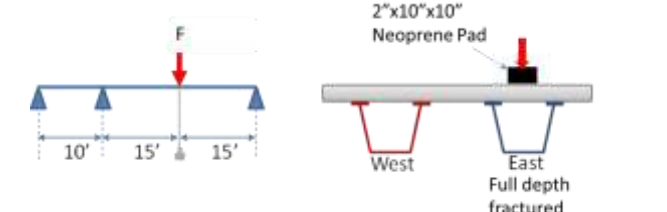
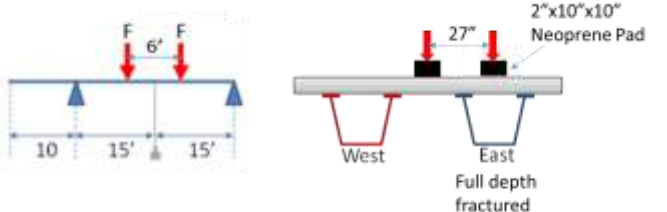
In Tests A and D, the specimen was loaded incrementally to failure over the fracture location at mid-span. These test setups were to generate the worst-case loading scenarios. The results from these tests will provide the remaining capacities of the system and explain how the bridge system remains stable after a full-depth fracture of one of the girders. In test A, the load was applied through a 9 in. x 36 in. elastomeric pad covering the entire width of the damaged girder, while in Test D, the load was applied through a 10 in. square elastomeric pad placed at the center of the damaged girder. The difference, between Test A and D, will explain how much the capacity of the damaged structure will be affected by the distance between the loading point and top flanges.

In Test B and C, the specimen was loaded incrementally at mid-span over the intact girder. Similar to Test A, the load was applied through 9 in. x 36 in. elastomeric pad covering the entire width of the intact girder in Test B. In Test C, the specimen was loaded through 10 in. x 10 in. loading pad placed at the center of the intact girder. The results from Test B and C, in combination with the results of Test A and D, can be used to evaluate how much the intact girder and damaged girder, as components, contribute to the total load-carrying capacity of the whole system.

Test E was set up with four-point loading to simulate truck footprints. Each truck footprint was simulated by a 10-in. square elastomeric pad. The main purpose of this test was to see how much load the damaged bridge system can carry and, more importantly, to investigate how the specimen

will fail ultimately and to investigate how the failure modes vary as it changes from a single point load to a truck configuration.

Table 3-2 Plan for Ultimate Load Tests

Test #	Loading Configuration	Type of Load
A		Load was applied incrementally until failure occurred.
B		Load was applied until the plateau in load-deflection curve was observed. Test was discontinued before the failure.
C		Load was applied until the failure occurred by punching through the slab
D		Load was applied until the failure occurred by punching through the slab
E		Load was applied until failure occurred.

Chapter 4 Laboratory Testing Results

4.1 Elastic Tests

Results of 18 elastic tests are split into three sections corresponding to the three damage levels of the specimen. Experimental results for the undamaged specimen, and the damaged specimen with bottom flange fractured and full-web fractured in one girder are presented respectively in Section 4.1.1, Section 4.1.2 and Section 4.1.3. The results provided in this section will focus on only the steel box-girder responses. It is important to note that the maximum displacements, reported here, are the average of top flange vertical displacements of each girder at mid-span while the maximum strains are the average of longitudinal strains measured in the bottom flange of each girder at mid-span. The shear forces in the cross-frame reported in the following sections are measured at the cross-frame, located at Section 5, 5 ft away from the mid-span. Again, note that WG was the intact girder and EG was the only girder to be damaged.

4.1.1 On Undamaged Specimen

Six tests were carried out to examine linear elastic responses of the undamaged bridge specimen with different combinations of rail, continuity and loading configuration. Results for each elastic test are summarized in Table 4-1.

Table 4-1 Summary of Elastic Tests on Undamaged Specimen

	Test	Characteristics (Rail/Continuity/Load)	Max Displacement in WG (in)	Max Displacement in EG (in)	Max Strain in WG (in/in*10 ⁶)	Max Strain in EG (in/in*10 ⁶)	Shear Force in Cross-Frame (kip)
Undamaged	1	NNS	0.317	0.324	460	464	0.5
	2	NNU	0.110	0.203	168	286	1.6
	3	NYU	0.091	0.179	140	257	1.6
	4	YNS	0.285	0.303	418	410	0.3
	5	YYU	0.109	0.174	137	238	1.6
	6	YNU	0.124	0.194	162	263	1.5

As expected, for symmetrical loading scenarios as in Tests 1 and 4, both girders experienced almost identical behaviors as indicated by the maximum displacement and strain in two girders. These symmetrical loading tests can be treated as tests of only one half of specimen. The results from Test 1 indicated that 50 kips of load would produce approximately 460 $\mu\epsilon$ ($1 \mu\epsilon = \text{in/in} \cdot 10^6$) longitudinal strain in the bottom flange of one girder. The maximum longitudinal strain in WG in Test 2 was 168 $\mu\epsilon$ and this suggests that the WG resisted 36.5% of the total applied load. For

unsymmetrical loading tests, the maximum displacement of EG was 72.8% higher than that of WG, on average.

Between Tests 2 and 3, the presence of continuity decreased the maximum displacement and strain in EG approximately by 11.8% and 10.1%, respectively. The railing system decreased the maximum displacement by 4.4% and the maximum strain by 8.0% for EG as shown in Tests 2 and 6.

Altogether, the effects of railing systems and continuity reduced the maximum displacement and strain in EG by 14.3% and 16.8%, respectively as illustrated in Tests 2 and 5. These numbers were 1% and 18.5% for WG.

Under symmetrical loading configuration, the role of cross-frames was insignificant. However, under unsymmetrical loading configuration, the effect of cross-frames became clearer as the forces in the cross-frame increased triple from 0.4 kips to 1.6 kips, on average. The total shear forces transferred through two cross-frames were approximately 3.2 kips which was equivalent to 6% of the applied load (assuming two cross-frames at Sections 1 and 5 transferred the same amount of forces).

4.1.2 On Damaged Specimen with Bottom Flange Fractured in One Girder

In this series of tests, the bottom flange in the EG was fractured at mid-span as illustrated in Figure 4-1. Due to that fracture in bottom flange, the maximum longitudinal strain in EG was now measured from its webs, while maximum longitudinal strain in WG was still measured from its bottom flange. The same six tests that had been carried out for the undamaged bridge were repeated. Again, the effects of each parameter, including rail, continuity, and loading configuration, were investigated based on the responses of the steel box-girders.

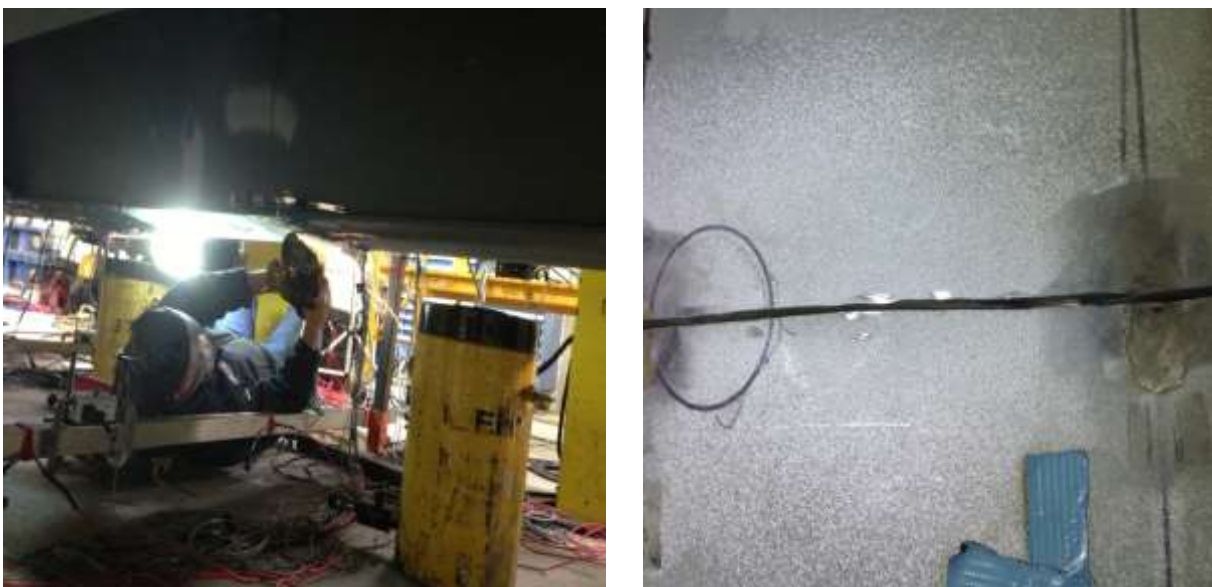


Figure 4-1 Saw cutting of bottom flange in east girder.

The overall maximum responses in the steel box-girders are summarized in Table 4-2.

Table 4-2 Summary of Elastic Tests on Bottom Flange Fractured Specimen

	Test	Characteristics (Rail/Continuity /Load)	Max Displacement in WG (in)	Max Displacement in EG (in)	Max Strain in WG (in/in*10 ⁶)	Max Strain in EG (in/in*10 ⁶)	Shear Force in Cross-Frames (kip)
Bottom Flange Fracture	7	YNS	0.293	0.337	459	851	0.3
	8	YYU	0.089	0.180	146	506	1.7
	9	YNU	0.107	0.206	176	578	1.7
	10	NNS	0.308	0.337	449	1260	0.2
	11	NNU	0.114	0.218	180	610	1.7
	12	NYU	0.094	0.188	148	539	1.7

As illustrated in Test 7 and Test 10 with symmetrical loading, EG experienced clearly higher displacements than WG. For instance, for the test NNS, the difference in the displacement between WG and EG increased from 2.2% for the undamaged specimen to 9.4% for this bottom flange fractured damage condition. It was because stiffness of EG decreased after its bottom flange was fractured.

Between Tests 11 and 12, the presence of continuity decreased the maximum displacement and strain in EG by approximately 13.8% and 11.6%, respectively. Tests 9 and 11 indicated that the railing system decreased the displacement by 5.5% and strain by 5.2% in EG. Comparing the results from Tests 8 and 11, the effects of railing systems and continuity together reduced the displacement and strain in EG by 17.4% and 17%, respectively. Compared with the undamaged specimen, the effects of railing system and continuity were comparable with respect to reduction in the maximum displacement and strain in EG (17.4% and 17% for the bottom flange fractured specimen vs 14.3% and 16.8% for the undamaged specimen).

Similarly, the data in the WG and cross-frames were found comparable to those before the bottom flange fracture occurred. The maximum displacement in EG increased 6.5% on average as the bottom flange was fractured. Only strains in EG increased significantly. It was because of high local stress intensity at the junction of the web and bottom flange that was produced when bottom flange fractured. Considering the worst-loading scenario which is NNU, the effect of fracture of bottom flange in EG increased the maximum strain in WG by 7%. This suggested the load transferred to WG now increased from 36.5% to 39.1%.

Overall, the elastic responses of bottom flange fractured and undamaged specimen were comparable.

4.1.3 On Damaged Specimen with Bottom Flange and Webs Fractured in One Girder

In this testing series, the damage intensity was extended by fracturing the entire webs of EG in addition to the existing fracture in the bottom flange as illustrated in Figure 4-2. It is also important to note that since the web was now fully fractured, the longitudinal strain data in EG at mid-span were lost and not reported here.



Figure 4-2 East girder with bottom flange and web fractured in one girder.

The maximum responses in the steel box-girders under the full-web fracture condition are presented in Table 4-3.

Table 4-3 Summary of Elastic Tests on Full-Web Fractured Specimen

	Test	Characteristics (Rail/Continuity/Load)	Max Displacement in WG (in)	Max Displacement in EG (in)	Max Strain in WG (in/in*10 ⁶)	Max Strain in EG (in/in*10 ⁶)	Force in Cross-Frames (kip)
Web Fracture	14	YNS	0.449	0.675	867	N/A	3.6
	15	YYU	0.197	0.446	390	N/A	5.3
	16	YNU	0.268	0.542	479	N/A	5.1
	17	NNS	0.511	0.757	891	N/A	4.0
	18	NNU	0.297	0.593	503	N/A	4.8
	19	NYU	0.212	0.472	398	N/A	5.5

The results from tests with symmetrical loading indicated that the maximum displacements in EG were now significantly higher than that of WG. For instance, in Test 17 (NNS), EG experienced 48.1% higher displacement than WG did while it was only 2.2% and 9.4% for the undamaged state and the bottom flange fractured damage state, respectively. Also, the displacements in both girders increased dramatically compared to previous damage states. The maximum displacement in WG, averaged from six elastic tests, increased 88% and 91% for the undamaged state and bottom flange fractured damage state, respectively. For EG, these numbers were 152% and 140%.

Between Tests 18 and 19, the presence of continuity decreased the maximum displacement by 20.4% for EG and 28.6% for WG. Tests 18 and 16 indicated that presence of the railing system reduced the maximum displacement by 8.6% for EG and 9.7% for WG. The effects of continuity and rail together reduced the maximum displacement by 24.8% for EG and 33.7% for WG. The effects of continuity and rail increased more significantly than that of two previous damage states. This suggests that as the damage intensity increases, the continuity and rail effects will increase.

The maximum longitudinal strain in WG increased significantly, compared to two previous cases. The maximum longitudinal strain in WG was 891 $\mu\epsilon$ for Test 17 (NNS) and 503 $\mu\epsilon$ for Test 18 (NNU). For the undamaged specimen, these numbers were 460 $\mu\epsilon$ and 168 $\mu\epsilon$ for Test 1 (NNS) and Test 2 (NNU), respectively. This comparison suggested that the majority of the applied load was transferred to the intact girder by assuming the 50 kips of load would produce an amount of 460 $\mu\epsilon$ in the bottom flange of one girder. In other words, the contribution of the damaged girder, after its entire webs and flange were fractured, was negligible. This conclusion was later verified by means of finite element analysis in which the stress in the damaged girder was found to be negligible.

The forces in cross-frames also increased as compared to previous damage cases. The cross-frame forces increased from 1.21 kips on average on bottom flange fractured tests to 4.72 kips on average when the whole web and bottom flange were fractured. Assuming two cross-frames in the main span carried the same amount of forces, the total load carried by the cross-frames would be 9.44 kips (4.72 kips x 2). It was equivalent to 19% of the applied load.

Overall, the specimen with complete fracture in the bottom flange and webs in EG, had its stiffness reduced significantly as the EG almost lost all of its flexural stiffness. As a result, the maximum displacement and strain increased significantly in the intact girder, WG. However, the beneficial effects of both continuity and rail system and cross-frames increased clearly.

4.1.4 Summary of Elastic Tests

Overall, all elastic tests were performed successfully. The test data showed that the bridge had completely linear-elastic responses in all three damage conditions as shown from Figure 4-3 to Figure 4-5. Several important observations for all elastic tests are summarized as follows:

- The rail and continuity helped to increase the load-carrying capacity of the specimen. As the damage intensity increases, their beneficial effects also increase. For instance, the rail and continuity effects together reduced the displacement of the damaged girder by 14.3%, 17.4% and 24.8%, for the undamaged, bottom flange fractured and full-web fractured damage states, respectively.
- In addition to the deck, cross-frames were found to play an important role in transferring the load from the damaged girder to intact girder. Similar to the effects of the rail and continuity, the more damage the bridge experienced, the more important the cross-frames were. The estimated contribution of cross-frames were 5%, 5% and 19% for the undamaged, bottom flange fractured and full-web-fractured damage states, respectively. However, it should be mentioned that the relatively large contribution of cross-frames found in these experiments could be related to the scale of the test specimen used.
- In general, the elastic responses of the specimen, under the undamaged and bottom flange fractured damage states, were comparable. For instance, the maximum displacement of EG increased by an average of 6.5% when the bottom flange was fractured.
- With the bottom flange and webs completely fractured, the flexural stiffness of the damaged girder was negligible. Under the same loading configuration, more load was transferred to the intact girder, or the strain in the intact girder increased as the damage intensity increases. For instance, the average maximum strain in all six elastic tests in the intact girder increased 5% when the bottom flange of EG was fractured and 138% when the entire webs of EG were fractured. This indicates that as the damage takes place, the load resisted by the damaged girder is transferred to the intact girder.

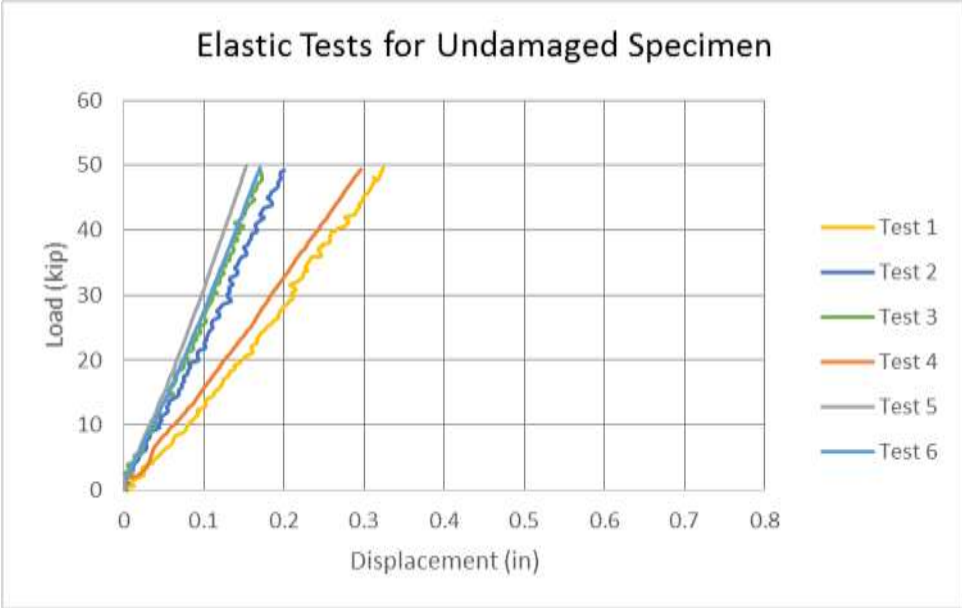


Figure 4-3 Results of elastic tests on undamaged specimen.

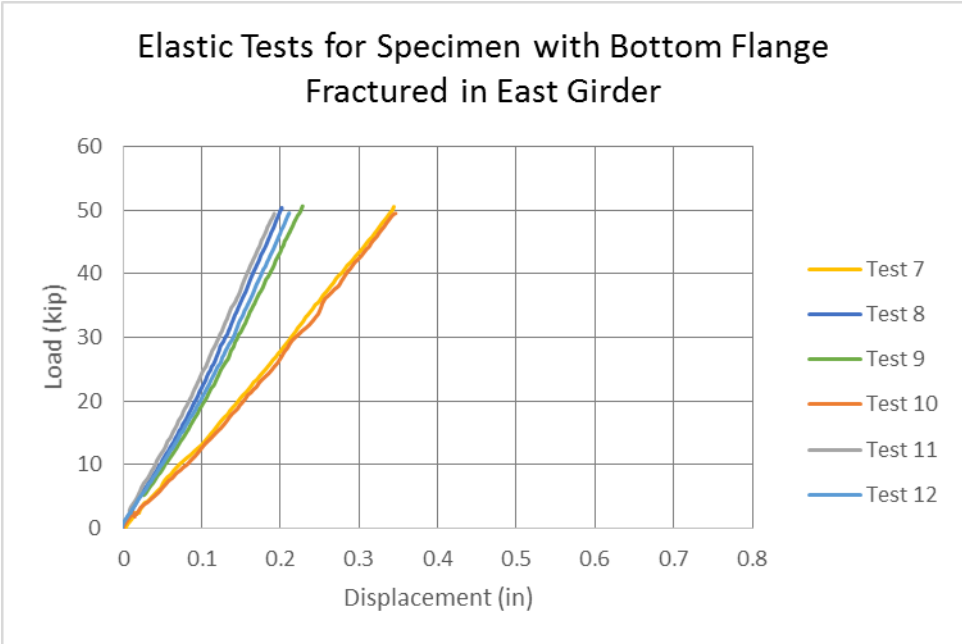


Figure 4-4 Results of elastic tests on specimen with bottom flange fractured in east girder.

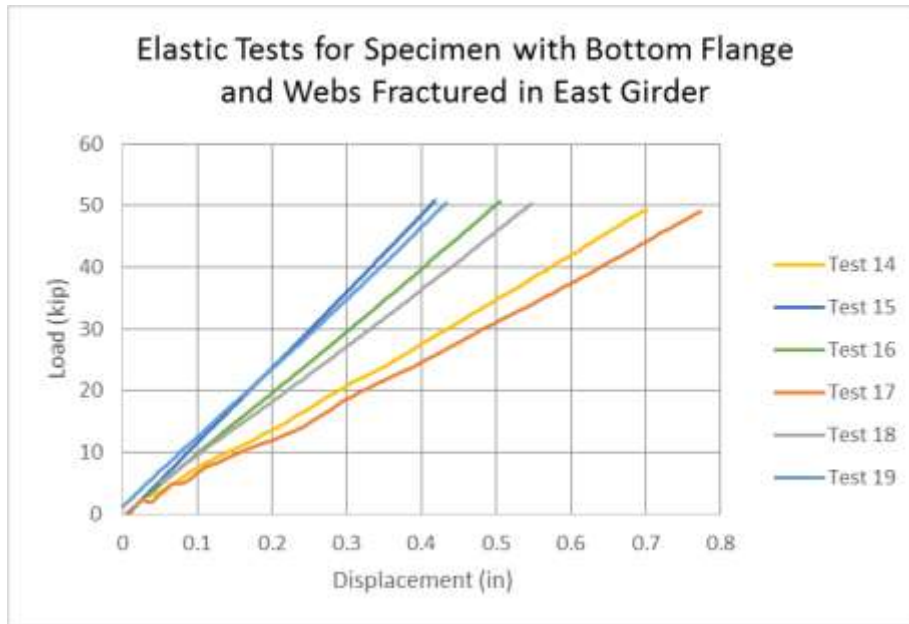


Figure 4-5 Results of elastic tests on specimen with full-depth fracture in east girder.

Results of all elastic tests are summarized in Table 4-4.

Table 4-4 Summary of all Elastic Tests

Test	Characteristics (Rail/Continuity /Load)	Max Displacement in WG (in)	Max Displacement in EG (in)	Max Strain in WG (in/in*10 ⁶)	Max Strain in EG (in/in*10 ⁶)	Force in Cross-Frame (kip)
Undamaged						
1	NNS	0.317	0.324	460	464	0.5
2	NNU	0.110	0.203	168	286	1.6
3	NYU	0.091	0.179	140	257	1.6
4	YNS	0.285	0.303	418	410	0.3
5	YYU	0.109	0.174	137	238	1.6
6	YNU	0.124	0.194	162	263	1.5
Fractured bottom flange (from Test 7 to Test 13)						
7	YNS	0.293	0.337	459	851	0.3
8	YYU	0.089	0.180	146	506	1.7
9	YNU	0.107	0.206	176	578	1.7
10	NNS	0.308	0.337	449	1260	0.2
11	NNU	0.114	0.218	180	610	1.7
12	NYU	0.094	0.188	148	539	1.7
13	Cyclic Loading (YNU)	---- ¹	---- ¹	---- ¹	---- ¹	---- ¹
Fractured web in addition to the bottom flange (from Test 14 to Test 19)						
14	YNS	0.449	0.675	867	N/A	3.6
15	YYU	0.197	0.446	390	N/A	5.3
16	YNU	0.268	0.542	479	N/A	5.1
17	NNS	0.511	0.757	891	N/A	4.0
18	NNU	0.297	0.593	503	N/A	4.8
19	NYU	0.212	0.472	398	N/A	5.5

¹ See Section 4.2

4.2 Cyclic Test

It is important to note that the bridge specimen was tested under cyclic load when the bottom flange in the east girder was fractured. The specimen was tested with rail, no continuity and under unsymmetrical loading, as illustrated in Figure 4-6. The magnitude of cyclic load was 60 kips as explained in Section 2.4.1. The loading rate was 1 Hz. (one second for each loading cycle) and the estimated number of loading cycle was 938,667. However, after 213,101 cycles, the test was stopped. It was because the initial bottom flange fracture started propagating through the entire webs and reached top flanges as shown in Figure 4-8. Some minor cracks were observed on the deck surface at the center of the bridge as illustrated in Figure 4-7. One reason for stopping the test was to prevent the crack from growing and damaging the deck, which then might collapse the bridge, while the ultimate goal of this project was to determine the maximum load-carrying capacity of the bridge under static loading. The results from the ultimate load test were necessary

to calibrate the nonlinear finite element model. The duration of this cyclic test at the time of stop was equivalent to 5.5 months of daily traffic. This suggests a complete cyclic loading test might be needed in the future research to determine if the bridge will collapse under the fatigue test.

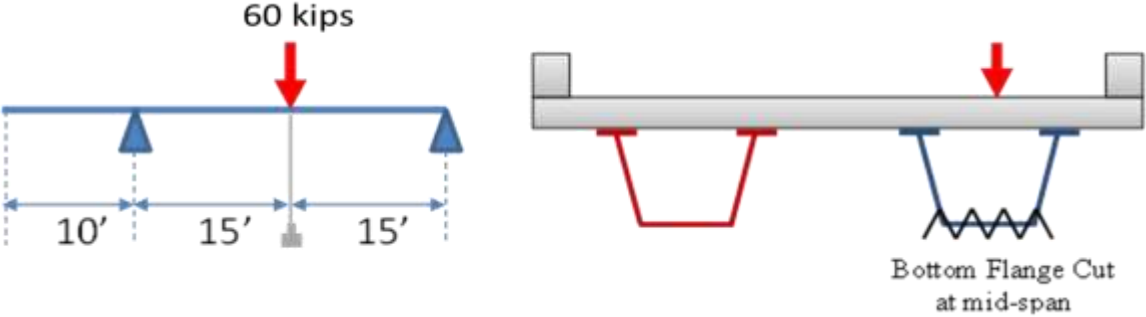


Figure 4-6 Schematic description of the cyclic loading test.



Figure 4-7 Cracks on the deck surface during cyclic test.

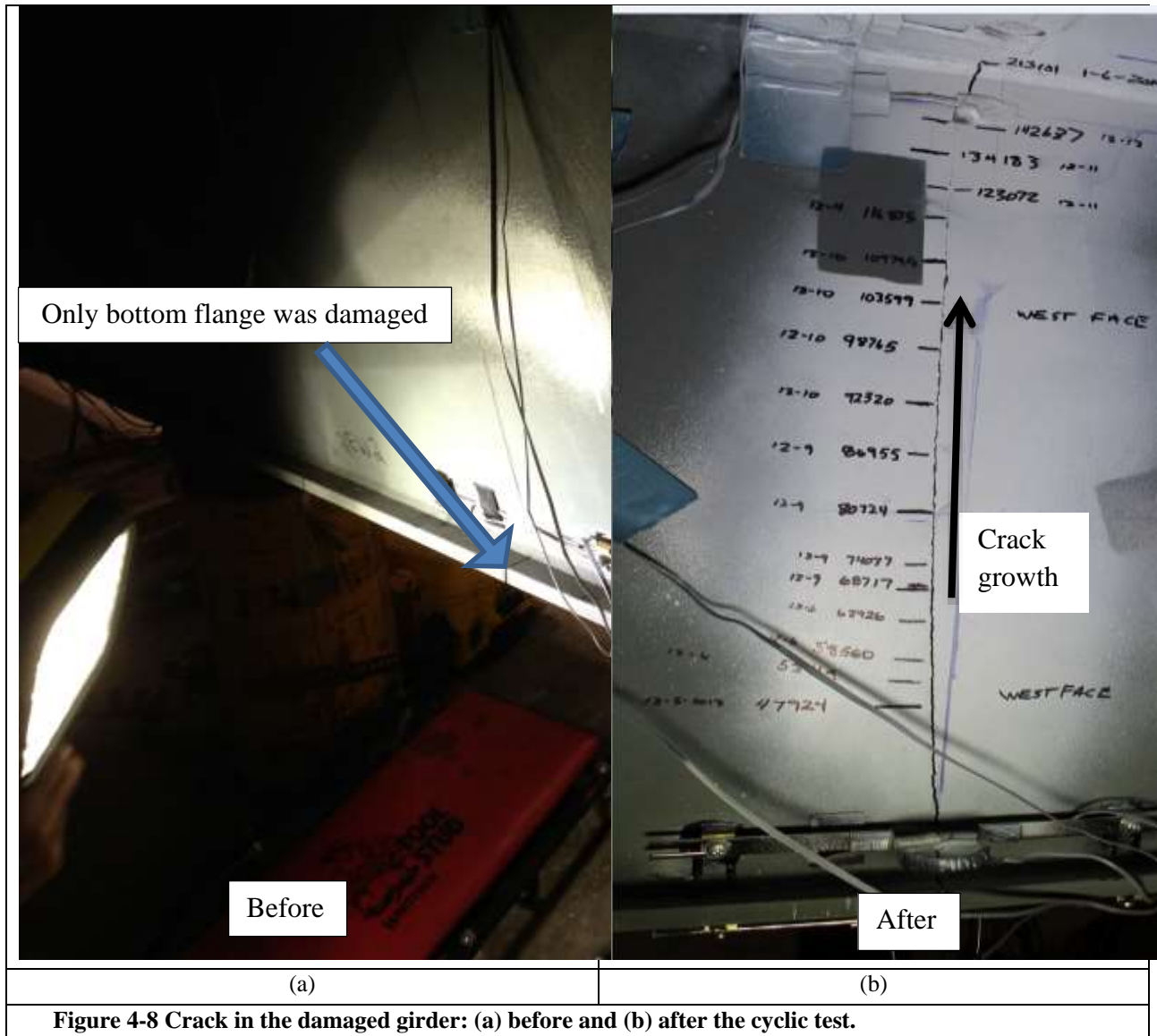


Figure 4-8 Crack in the damaged girder: (a) before and (b) after the cyclic test.

One of the responses observed visibly was the crack propagation from the bottom flange to the web of the damaged girder. Figure 4-9 shows growth of the crack length in the damaged girder during the cyclic test. The crack length data between the 1st and 50,000th cycle was missing because the crack propagation began overnight and was not observed until the next morning. The crack length was linearly proportional to the number of cycles until around the 160,000 cycles when the crack began to reach the webs, at which point the rate of growth slowed. The crack grew nearly evenly in both sides of the web of east girder until loading cycles of 80,000th. After that, the crack grew with a slower rate in the inside web than the outside web due to contributions of the cross-frames and the intact girder to the inside web of the damaged girder. This was consistent with experimental data from elastic tests and FEA results, which showed the outside face of the damaged girder always had higher displacement and stress than the inside face.

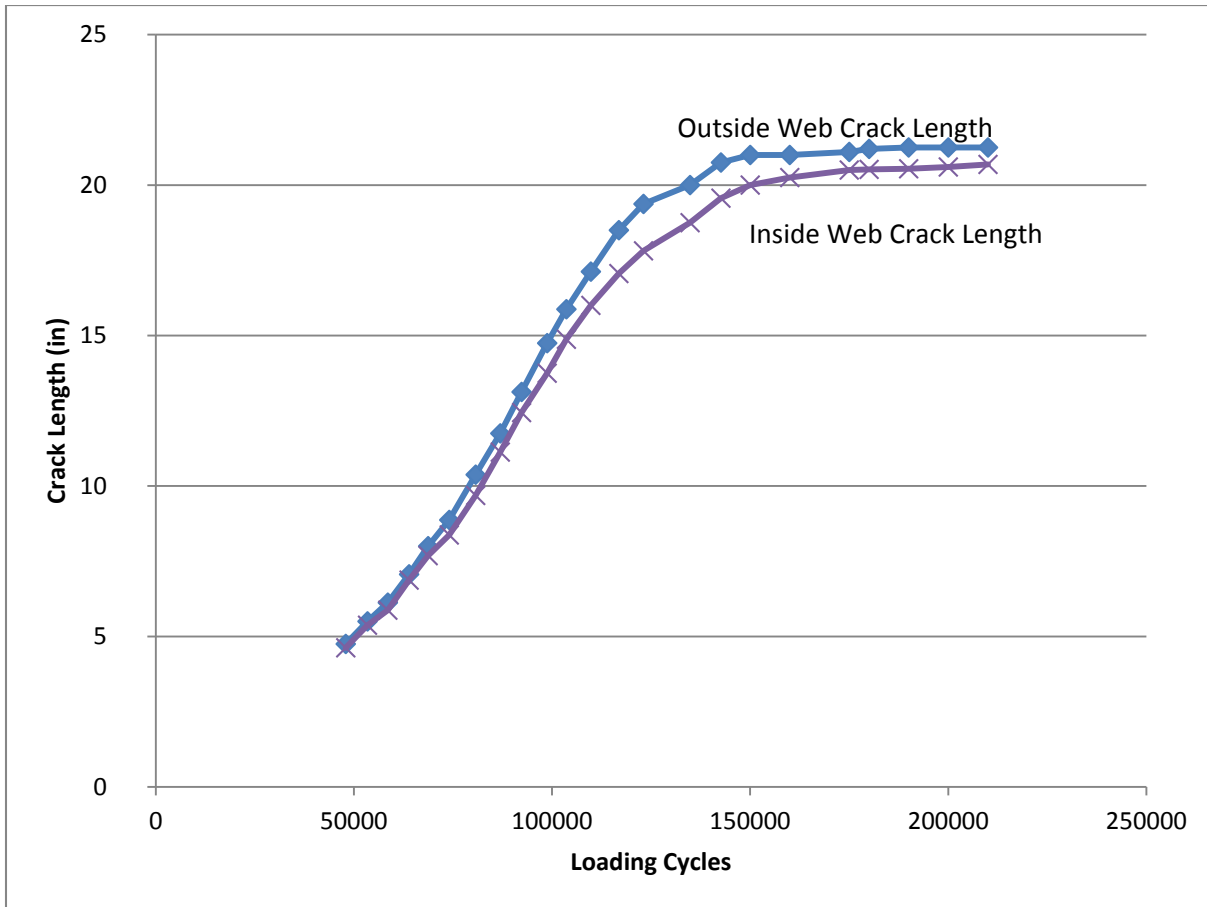


Figure 4-9 Crack growth in the damaged girder.

As the cracks grew into the webs, the stiffness of the specimen changed. For this reason, all of the monitored data including the crack opening at the base, displacement, displacement range, and shear force show similar patterns to that of the growth of crack length when they are plotted versus the number of cycles.

The setup to measure the crack base opening, or the separation between two halves of the fractured girder in longitudinal direction, is illustrated in Figure 4-10. The crack base opening was measured at both the inside and outside faces of the bottom flange of the fractured girder and is illustrated in Figure 4-11. During the first 25,000 cycles, the difference between maximum and minimum crack opening was nearly constant and suggests the bottom flange fracture had not yet begun to propagate into web. Between 50,000 and 10,000 cycles, the crack opening increased rapidly. At the last cycle, the maximum crack opening was around 0.19 in. for the outside web and 0.175 in. for the inside one.

At the same time, the stiffness of the bridge measured at the fractured location was found to have decreased approximately 54% from 260 kips/in to 120 kips/in.



Figure 4-10 Crack opening measuring gauge on the exterior face.

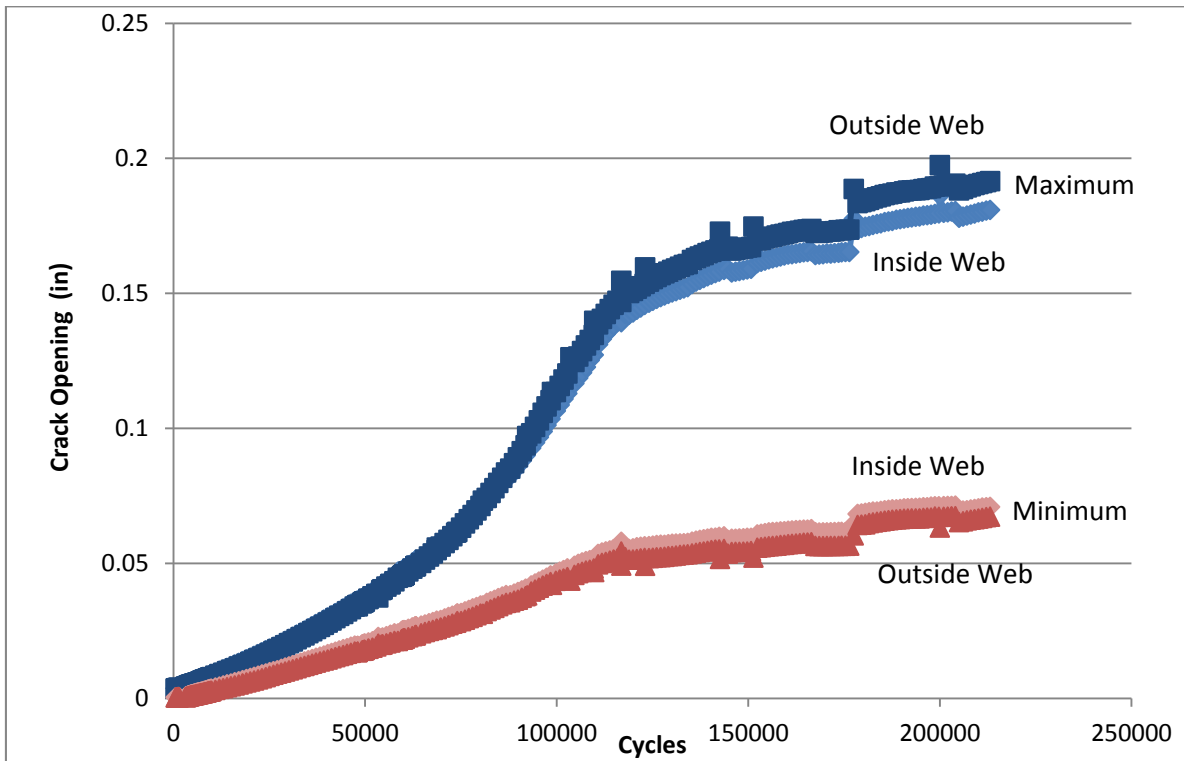


Figure 4-11 Crack base opening vs. number of loading cycles.

The maximum displacement and minimum displacement of the girders were collected for each loading cycle. Figure 4-12 shows how the maximum and minimum displacement of the fractured girder changed over time. Figure 4-13 plots the displacement range for both girders (which is equal to maximum displacement minus minimum displacement in each girder) that shows the vertical deflection of each girder in a cycle. Both plots show similar behavior and trends to that of the crack length growth plot. The maximum displacement increased from 0.25 in. to 0.7 in. while the minimum displacement also increased from 0.03 in. to 0.24 in. during the test.

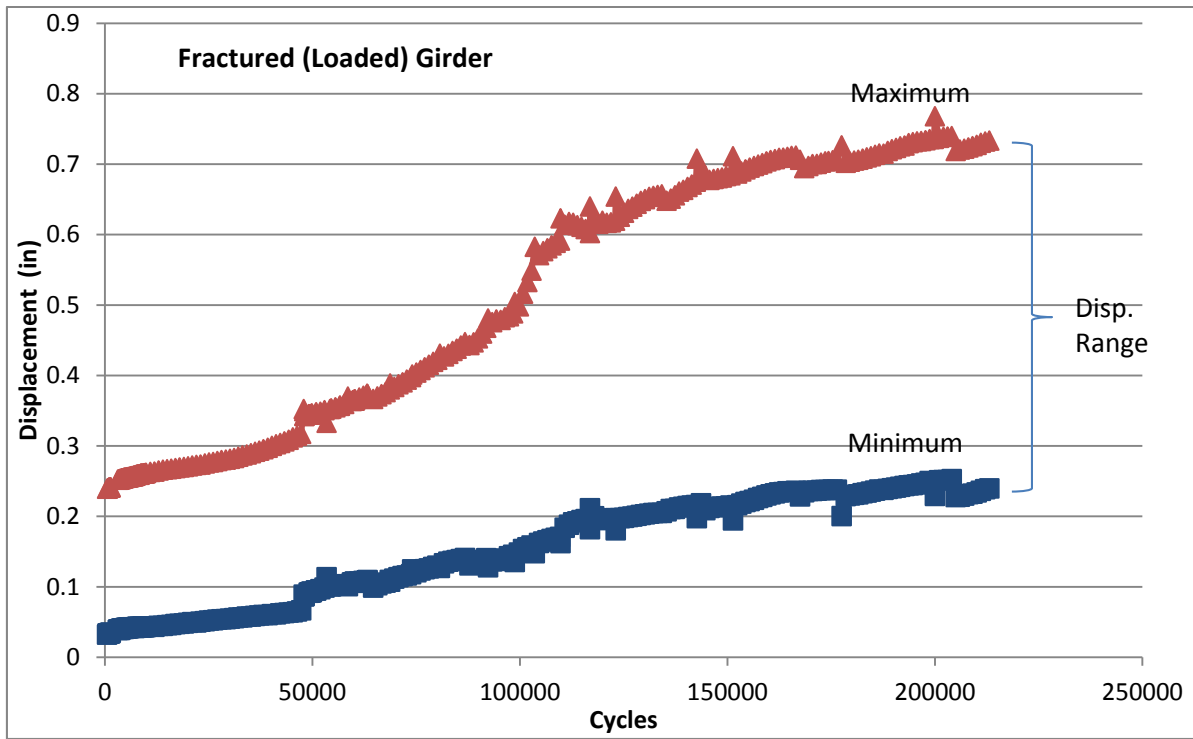


Figure 4-12 Mid-span displacement vs. number of loading cycles in the fractured girder.

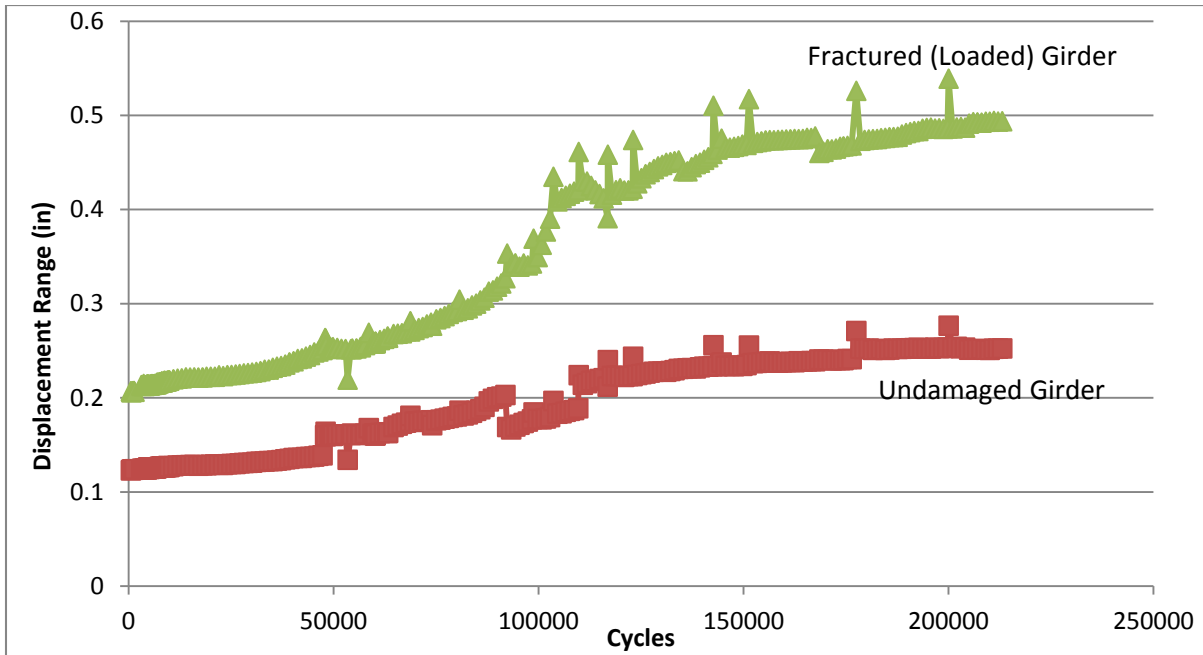


Figure 4-13 Displacement range (max – min) vs. number of loading cycles.

The stiffness of each girder over time is plotted in Figure 4-14. The stiffness of each girder is calculated by dividing the applied load by the displacement range in each cycle. Since the applied load for each cycle was constant at 60 kips, the stiffness curve was shown inversely proportional to displacement range curve. The damaged girder had a stiffness of 260 kips/in at the beginning of the cyclic test when bottom flange fractured. The stiffness reduced 60%, to 105 kips/in, at the end of the test when the web was completely fractured. Similarly, the stiffness reduction, for the undamaged girder, was around 235 kips/in, which was equivalent to 52% of its initial stiffness.

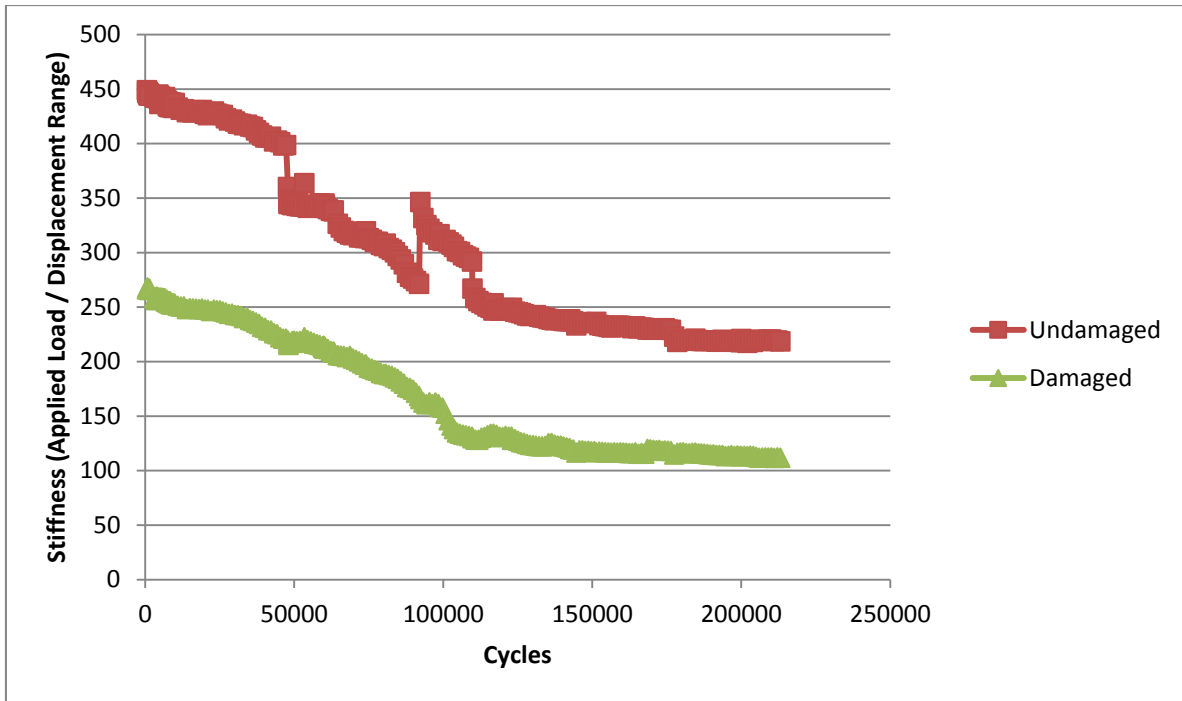


Figure 4-14 Stiffness of each girder during the cyclic test.

The locations of strain gauges in each cross-frame brace are denoted as e_1 , e_2 , and e_3 as shown in Figure 4-15a. The strain profile was assumed linear in each brace leg as illustrated in Figure 4-15b. The average axial strain in the angle cross-section can be calculated using the following equation:

$$e_{avg} = \frac{e_1}{4} + \frac{e_2}{2} + \frac{e_3}{4}$$

With that average axial strain, the axial force in a cross-frame brace can be calculated by multiplying the average axial strain by the cross-section area of the brace and steel Young's modulus. Then, the shear transfer force, or the vertical component of the axial force, can be calculated based on the cross-frame geometry.

Figure 4-16 shows the maximum shear transfer in one cross-frame with respect to the number of loading cycles. The maximum shear transfer in the cross-frame was found to have increased from 2.5 kips at the beginning to almost 6.5 kips when the web was completely fractured.

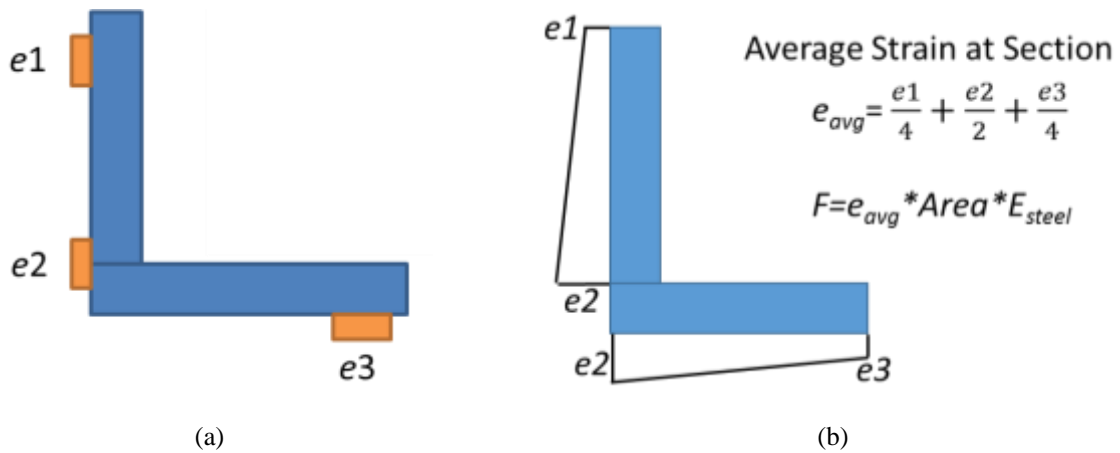


Figure 4-15 (a) Strain locations and (b) Strain profile in each cross-frame brace.

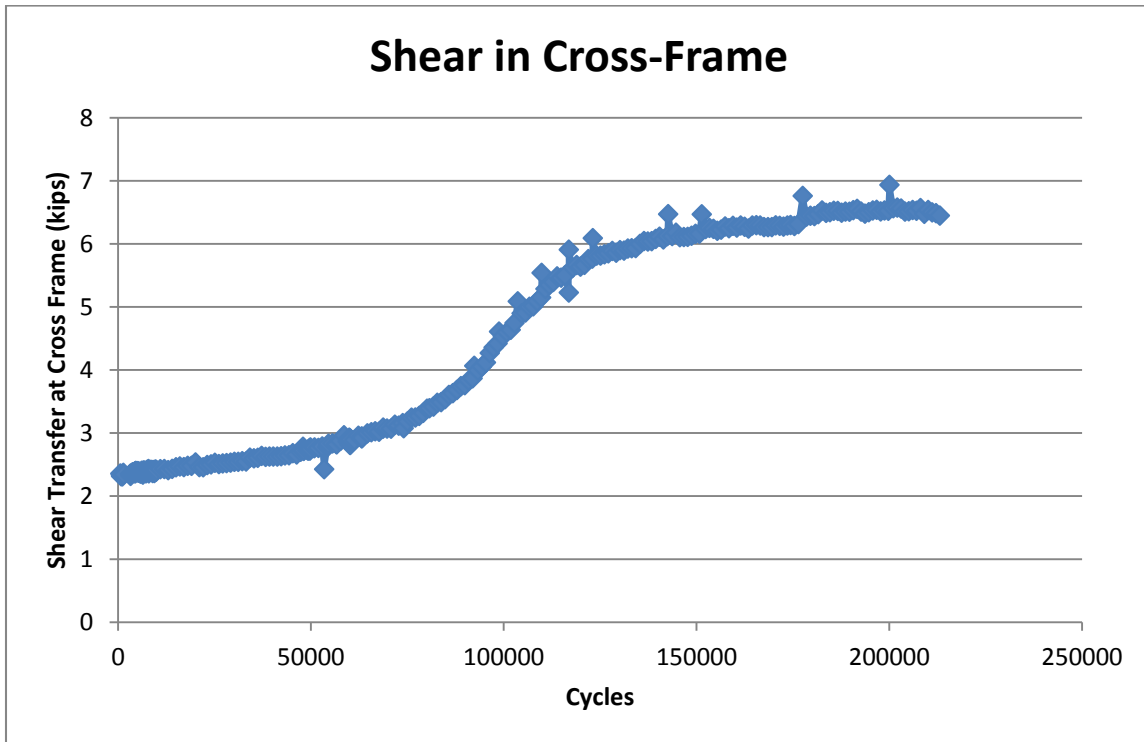


Figure 4-16 Maximum shear transfer in one cross-frame.

In general, as the crack length grew into the webs, the stiffness of the specimen decreased. It led to an increase in the crack opening at the base, the girder displacements, the displacement range as well as the cross-frame transfer force. It is important to note that all of these behaviors, when plotted versus the number of loading cycles, showed a similar pattern to that of the growth of crack length.

4.3 Ultimate Test A

In the ultimate load test A, the bridge specimen was tested under a full-web fracture damage condition, without rail system and continuity. The load was applied through a displacement-controlled hydraulic ram, over the damaged girder through a 2 in. x 9 in. x 36 in. loading pad placed at the mid-span location as illustrated in Figure 4-17.

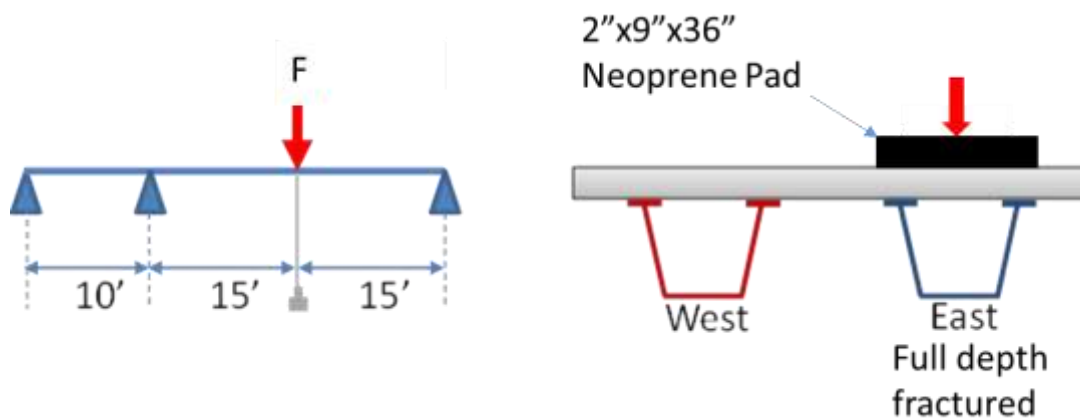


Figure 4-17 Schematic description of Test A.

4.3.1 Global Behavior

The overall responses during Test A are illustrated in Figure 4-18. Up to 60 kips of loading the bridge specimen showed a linearly elastic response with an initial stiffness of approximately 90 kips/in. As the load increased from 80 kips to 140 kips, some cracks in the deck were noticed and at the same time, the stiffness of the specimen was decreasing visibly. Twisting of the girders was observed as well. At the load of 140 kips, the capacity of the bridge slightly decreased by 1 kip because one bolt in the bottom connection of the cross-frame near mid-span was sheared. The intact girder started showing uplift at the cantilever support. The specimen reached its maximum capacity at 156 kips with 2.5 in. of displacement.

After reaching the maximum capacity of 156 kips, the concrete deck was crushed by the loading pad and the load dropped to 133 kips. The test continued and the specimen was still able to sustain some additional load with many ups and downs until it failed at 5.5 in. of displacement. These ups and downs in this loading period corresponded to several damages observed, including: 1) the visible cracking and crushing in concrete propagating toward the ends of specimen, 2) the bottom of the concrete deck between the two girders near mid-span spalling off, 3) the uplifting at the support and 4) the tear up of the deck at both ends of intact girder. As seen in Figure 4-18, during this loading period, the load fluctuated and reached a local maximum load of 144 kips at 4-in. displacement. It, then, slowly dropped down to 123 kips at 5.5-in. displacement before the test was halted. This sequence of failure suggests that the bridge was trying to transfer the load to the intact

girder through an alternative load path after the primary load path had failed. This load-transfer mechanism is discussed further in the following section.

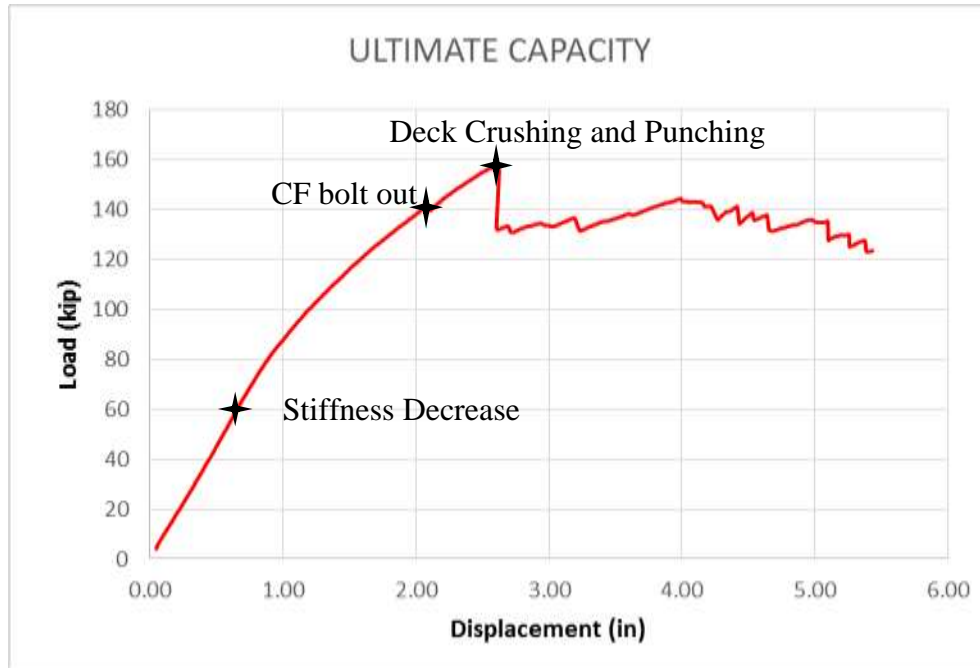


Figure 4-18 Load vs. deflection curve of the specimen during ultimate load test A.

A 1 ft by 1 ft grid was marked on the concrete surface to map the damage area more accurately as illustrated in Figure 4-19. In general, the major damage was observed in the deck over an area of 5 ft long by 3 ft wide at where the load was applied. Cracking started along the inside top flange of the damaged girder, then it propagated toward the intact girder. The cracking pattern was approximated by the black lines in Figure 4-19. This cracking pattern indicates that the deck failed predominantly in one-way shear failure mode. The deck damage showed that the damage propagated toward the north support more than the south support. It could be due to the presence of the cantilever portion in the south end. This cantilever made the south portion of the specimen measured from the loading point was stiffer than the north portion of the specimen. Eventually, the deck was punched by the loading pad along the inside top flange of the damaged girder when the specimen reached its maximum capacity. The spalling of concrete in the bottom of the deck is illustrated in Figure 4-20.



Figure 4-19 Punching in the top of the concrete surface looking to South.



Figure 4-20 Punching in the bottom of the deck.

The concrete deck was also damaged at both ends of the specimen. The mechanism for the observed failure can be explained by considering the hypothetical situation in which the deck is cut longitudinally between the girders leaving two separate and independent structures. The east structure is then damaged and the load point is displaced downward the same magnitude as produced in the actual test. Obviously, the magnitude of load causing this displacement will be much less than what observed in test. Due to the low flexural capacity at the damage location, the

displaced shape will essentially be a mechanism with hinge rotation about the load point and linear segments to the supports. It is important to note how the ends of the girder will now project above the supports and that the undamaged girder has no load applied and is therefore straight and level. Finally, keeping the load point of the damaged girder at the fixed level of displacement, consider the forces required to re-join the two separate structures and fuse the deck back together. At the ends of the girder, the (hypothetical) damaged girder will be above the undamaged one and need to be pulled downward, which then imparts an equal and opposite upward force on the undamaged girder. The effects of this transverse shear can be clearly seen in Figure 4-21 where the deck above the undamaged girder appears to have been pulled upwards and seemingly ripped off at the ends.

This same hypothetical situation can be used to examine the failure mechanism near the load point. In this region, the (hypothetical) damaged girder will be below the undamaged. Since the displacement level is being held by the loading beam, the undamaged girder will be pulled downward when the two separate structures are hypothetically re-joined. The effect of the resulting shear force can be seen in Figure 4-20.

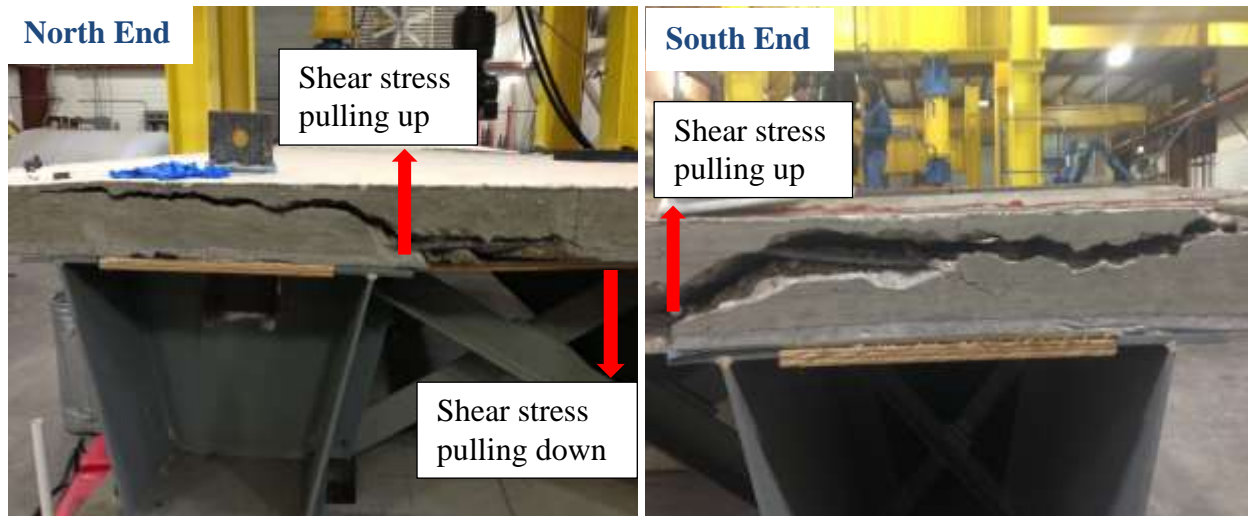


Figure 4-21 Damage at North end (left) and South end (right).

Another important behavior observed was the uplift at supports of the intact girder. Displacements near the supports were monitored at location 1 (14 in. from the bearing line of the South support) and location 2 (17 in. from the north end of steel box girders) as depicted in Figure 4-22. Figure 4-23 and Figure 4-24 plot the vertical displacements at these two locations. These plots show that the intact girder (or the West Girder) began to uplift at the south support shortly at 100 kips before the specimen reached its maximum capacity of 156 kips while the north support was uplifted just right after the maximum capacity was reached. The final uplifts were measured as 0.48 in. near the south support and 0.11 in. near the north support.



Figure 4-22 Location of potentiometers at supports.

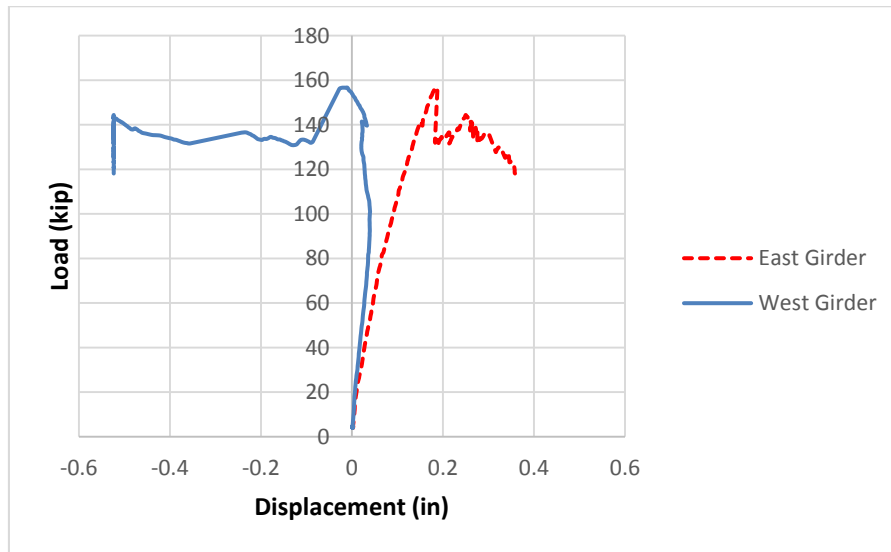


Figure 4-23 Displacement of the both girders near the south support.

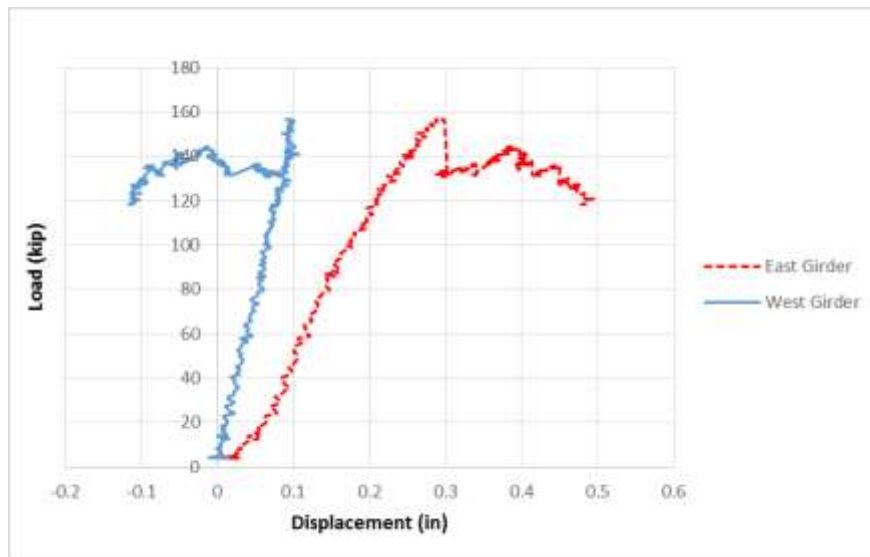
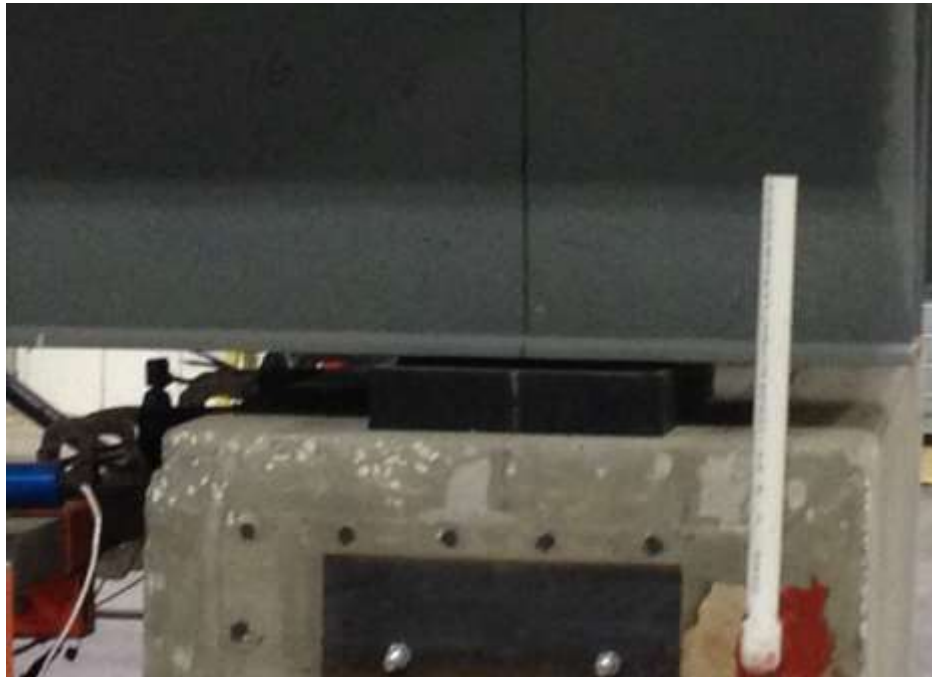


Figure 4-24 Displacement of the both girders near the north support.



(a) North support



(b) South support

Figure 4-25 Uplift at (a) north support and (b) south support.

4.3.2 Local Behavior

It is important to note that responses of the reinforcements and the deck were only monitored at the mid-span section. All of the strain gauges at the mid-span section are provided again in

Figure 4-26. Some of these strain gauges were damaged after the maximum load capacity was reached; therefore, their data will be omitted. Following are assumptions regarding the direction of the strain gauges and material properties of steel plates.

- Sign Convention:

Positive longitudinal strain: the member is in tension.

Negative longitudinal strain: the member is in compression.

Positive transverse strain: the member is in tension.

Negative transverse strain: the member is in compression.

* Note that the directions of measured strains that are mentioned in this report are with respect to the global coordinate system.

- Material Properties:

Yield stress for the reinforcement bars: 60 ksi.

Yield strain for the reinforcement bars: $60 \text{ ksi} / 29,000 \text{ ksi} * 10^6 = 2,070 \text{ } \mu\epsilon$.

Yield stress for the steel: 50 ksi.

Yield strain for the steel: $50 \text{ ksi} / 29,000 \text{ ksi} * 10^6 = 172 \text{ } \mu\epsilon$.

It is noted that gauges 2TTD1, 2TTD2 and 2TTD3 were shifted away from the mid-span by 1 ft toward the south support to avoid contact with loading pads.

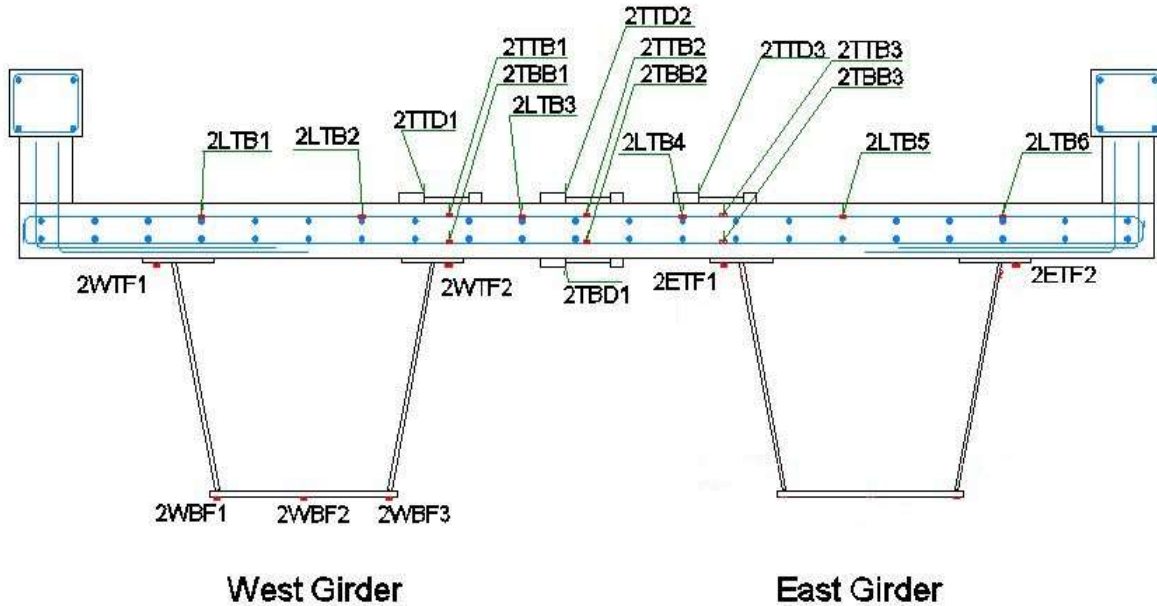


Figure 4-26 Strain gauges at the mid-span section.

Figure 4-27 and Figure 4-28 show longitudinal strains in both girders at the mid-span section. On the intact girder (WG), the top flanges were in compression and the bottom flange was in tension. On the damaged girder (EG), the top flanges were in tension, as expected, to balance the compressive force in the concrete deck since the fractured bottom flange and web at this location was expected to carry zero force. The linearity of the resulting curve that plots longitudinal strain in the intact girder is illustrated in Figure 4-27. The maximum strain, in the intact girder, was less than $1300 \mu\epsilon$ suggesting that the intact girder was still in the elastic range. The damaged girder experienced significant yielding at the outside top flange at approximately 80 kips.

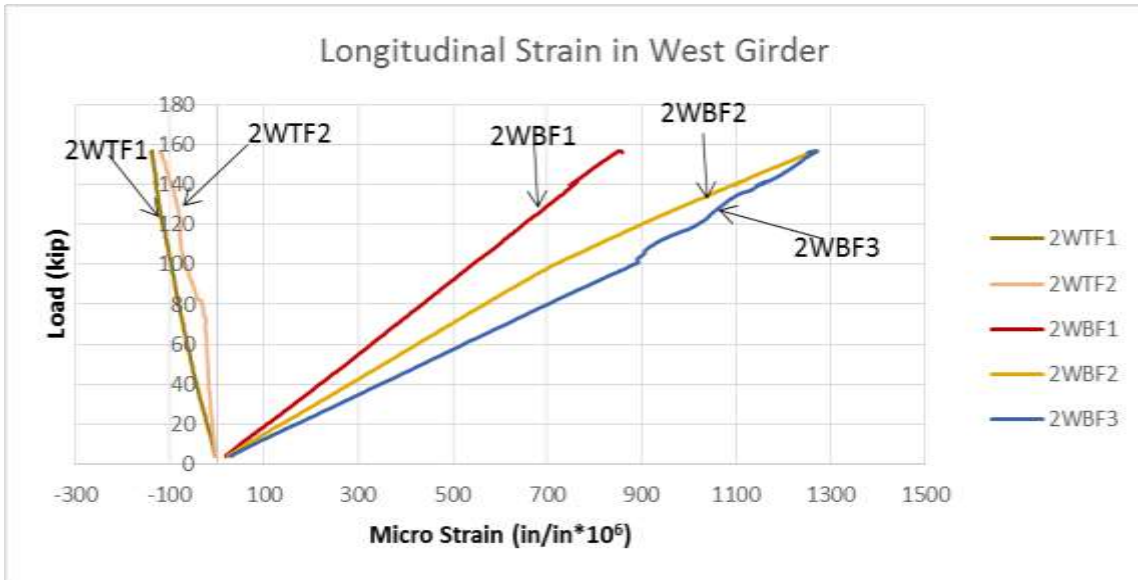


Figure 4-27 Longitudinal strain in the top and bottom flanges of west girder at mid-span.



Figure 4-28 Longitudinal strain at the top flanges of east girder at mid-span.

Responses in transverse rebars at mid-span were measured from six strain gauges 2TTB1, 2TBB1, 2TTB2, 2TBB2, 2TTB3 and 2TBB3 (see Figure 4-26 for their locations.) All of the strains in the transverse rebars were positive or in tension except at gauge 2TBB3, located near the damaged girder as illustrated in Figure 4-29. However, gauge 2TTB2, which was located at the center of the cross-section, had its strain fluctuating around zero. This suggests that the gauge 2TTB2 was an inflection point in the deflected shape of the cross-section. The plot also suggests that the strains at gauges 2TTB1 and 2TTB3 were much higher than that of other gauges. Gauge

2TTB1 had a strain of 2600 $\mu\epsilon$ suggesting the transverse re-bar yielded at this location, which is the inside top flange of the intact girder.

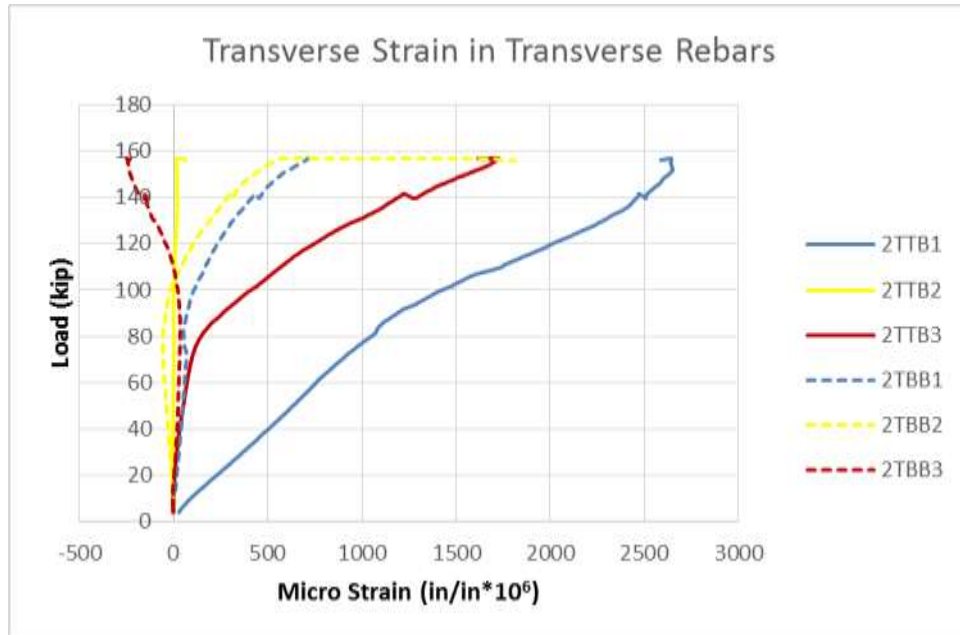


Figure 4-29 Strains of the transverse rebar at mid-span.

Responses in longitudinal top rebars from six strain gauges 2LTB1, 2LTB2, 2LTB3, 2LTB4, 2LTB5, 2LTB6 (see Figure 4-26 for their locations) are plotted in Figure 4-30. The strain gauge 2LTB3 data was exactly zero throughout the test suggesting this gauge was either broken or lost its connection. Two gauges, 2LTB1 and 2LTB2, located over the top of the intact girder, and gauge 2LTB4, located between two girders, had negative transverse strain while the other two 2LTB5 and 2LTB6 located over the top of the damaged girder had positive strains. This suggests the deck changed its deflected shape from concave up to concave down at a location somewhere between gauges 2LTB4 and 2LTB5.

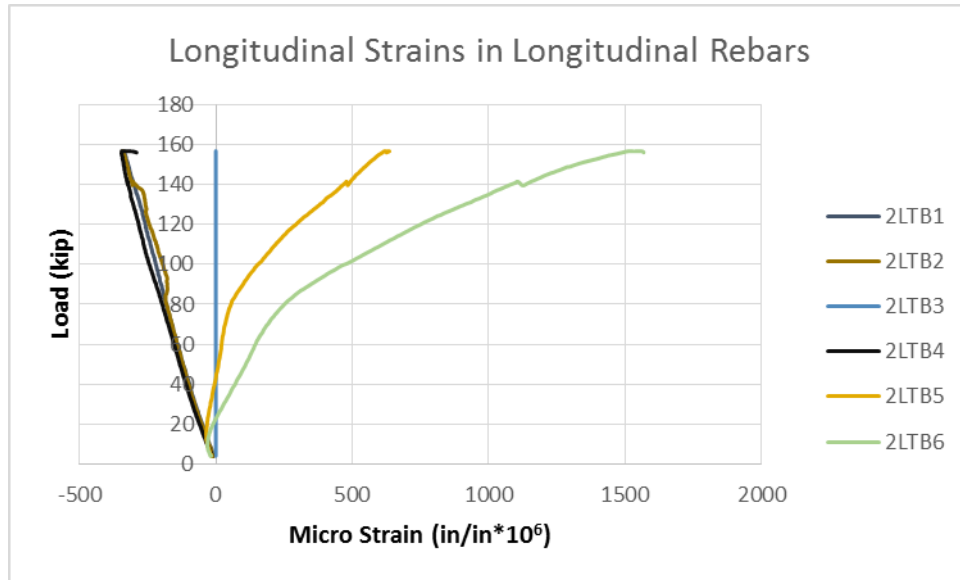


Figure 4-30 Longitudinal strain of rebars in longitudinal direction at mid-span.

Figure 4-31 showed the deck experienced positive transverse strains at location of 2TTD1, 2TTD2, and 2TBD1; and negative strain at location 2TTD3. This suggests that the top of deck was in compression at location 2TTD3, right on the top of the inside top flange of the damaged girder, while the other gauges showed the deck was in tension, which further suggests the inflection point of the deflected curve of the deck cross-section was somewhere close to the top flange of the damaged girder. This observation was consistent with data obtained from transverse and longitudinal reinforcement bars.

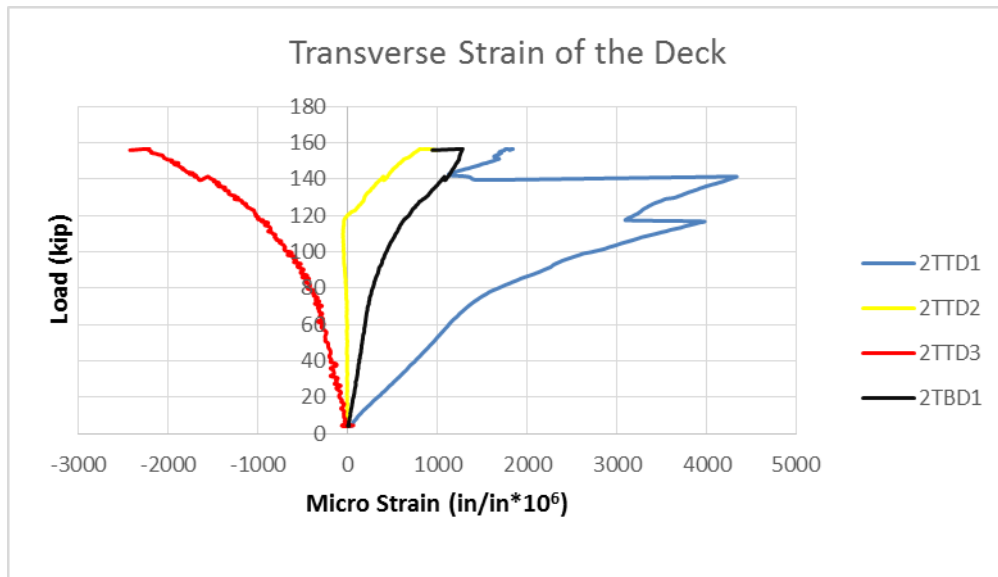


Figure 4-31 Transverse strain at the top and bottom of deck at mid-span.

4.3.3 Load-Transferring Mechanism

Based on the collected data, a major portion of the applied load was transferred directly, in transverse direction, to the intact girder mainly through the deck before the maximum capacity of the specimen was reached. After that, the concrete deck was punched by the loading pad, and the applied load was redistributed through a secondary load path. In this second load path, the cross-frames were found to be involved more actively than they had before. As illustrated in Figure 4-32b, the shear transfer capacity of one cross-frame increased and also at a faster rate. This explains why most cross-frame connections failed during this loading period, after the deck was punched by the loading pad. At the end of the test, every single external cross-frame was found to have at least one bolt connection broken. The locations of all broken cross-frame connections are illustrated in Figure 4-32a.

Since the deck and external cross-frames were found to be two major components that transferred the load from damaged girder to undamaged girder, it is interesting to quantify how much load was transferred through these components. It is important to note that there were only two external cross-frames in the main span of the specimen. Each of them is located 5 ft away from the mid-span. Figure 4-32b shows the amount of shear force transferred (vertical direction) in one external cross-frame. This figure shows that two significant drops occurred, which corresponded to the failures of two connections at the bottom of this cross-frame. The first shear drop was 7 kips at 2.1-in. displacement and it was due to the failure of bottom connection of the brace in tension. It should be noted that even though the capacity of the cross-frame dropped 7 kips, the capacity of the specimen decreased only 1 kip as seen in Figure 4-18. It could be because some of the load lost in the cross-frame was immediately re-taken up by other components such as the deck and girders.

After one connection failed, this cross-frame should have lost its load-resisting capability completely. However, the welded connection between two L-angle braces as shown by the red dot in Figure 4-32b enabled this tension brace to still carry forces, and this cross-frame continued to carry up to 21 kips. Then, the second failure of the bottom connection of the compression brace caused another drop of approximately 11 kips at 4.4-in. displacement. After that, the cross-frame was shown continuing to carry the load up to 23 kips until the end of the test. The reason that this cross-frame was still able to continue carrying the load after the second connection failure could be because the bottom end of the compression brace was still locked between the bottom flange and the web of the intact girder due to the way the bridge twisted and displaced. Assuming the other cross-frame carried a similar load, the total load that was transferred to the intact girder through cross-frames was approximately 46 kips, which was 29% of the applied load.

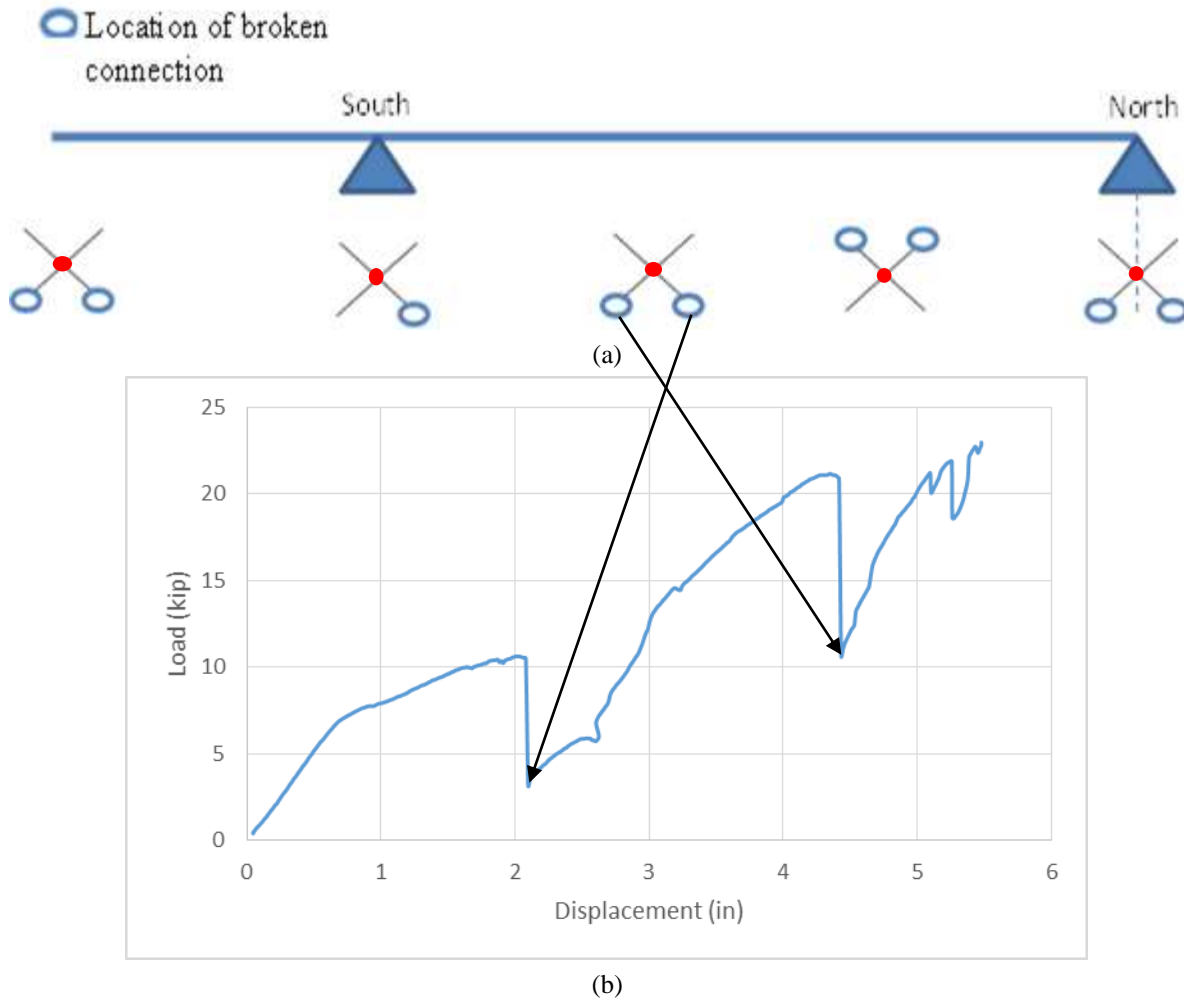


Figure 4-32 Shear transferred through one cross-frame in Test A.

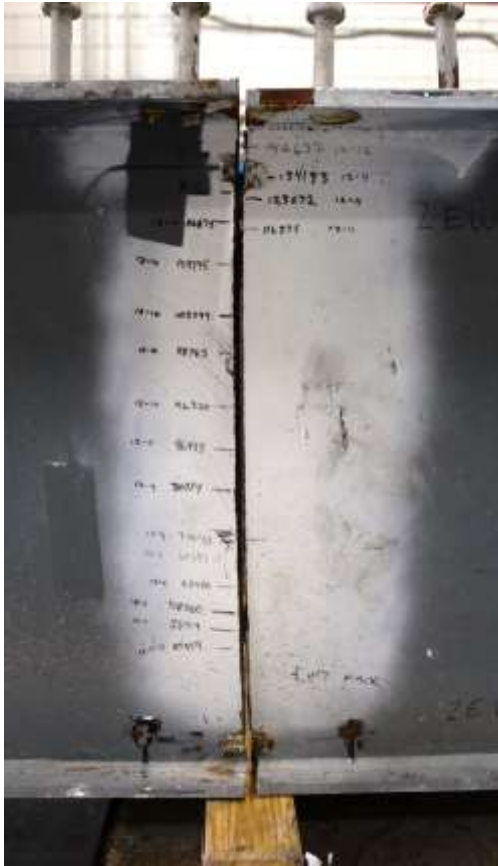
4.4 Reconstruction of Bridge Specimen

As illustrated in Test A, recorded strains in the steel box girders indicated that these girders were still in a good condition. Therefore, these girders were retained so that a new specimen can be reconstructed by casting a new deck for additional ultimate load tests. For that reason, only the deck was demolished and reinforcements were removed. After detaching the steel box girders from the deck, a thorough inspection showed only the top flanges of fractured girder at fracture location experienced severe damage which had been already expected, and this damage almost cut the damaged girder into halves as illustrated in Figure 4-33.



Figure 4-33 Damage in (a) the inner top flange, (b) the outer top flange of the damaged girder.

Eventually, it was decided that this damaged girder should be cut into two halves to make the reconstruction of the specimen easier. The results of FEAs showed that the effect of having the damaged girder cut completely into two separate pieces is negligible. However, misalignment of two fractured segments, as shown in Figure 4-34a, brought up some difficulties during the reconstruction process. In order to fix it, the bolts connecting the external cross-frames were loosened, and then the slop in the bolt holes were used to shift the girder segments into better alignment. Then the cross-frame bolts were tightened up again. Finally, scab plates were used to bring these two segments closer as much as possible. Figure 4-34b illustrates the damaged girder with the welded scab plates. Please note that once the deck was cast, these scab plates were removed.



(a) Before aligned



(b) After aligned

Figure 4-34 Alignment of two fractured segments.

After aligning the fractured segments, the new specimen was reconstructed as it had been previously. Figure 4-35 shows the complete specimen after the reconstruction.



Figure 4-35 The reconstructed specimen before (left) and after casting (right).

4.5 Ultimate Test B

In this test, the specimen was tested with the same loaded area as it was in Test A, except the loading was now moved over the intact girder as illustrated in Figure 4-36. In this test, the specimen was loaded until the plateau in load-deflection curve was observed without any failure. The purpose of this test to examine the behavior and verify the capacity and behavior of the intact girder.

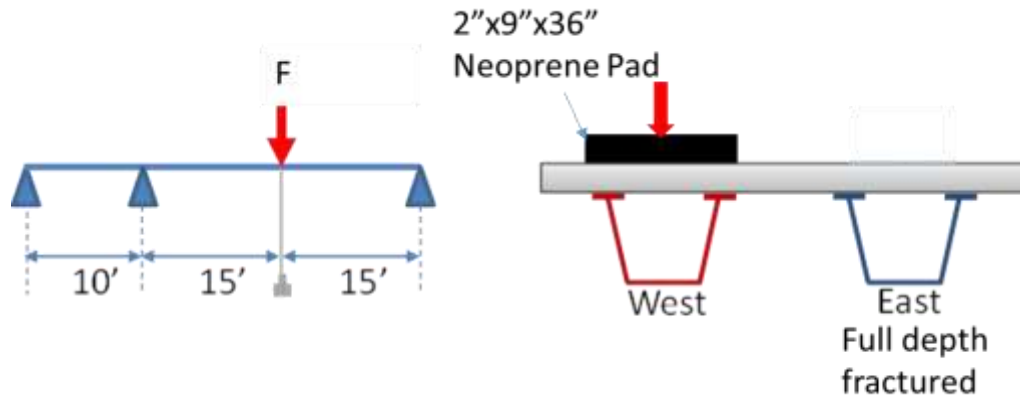


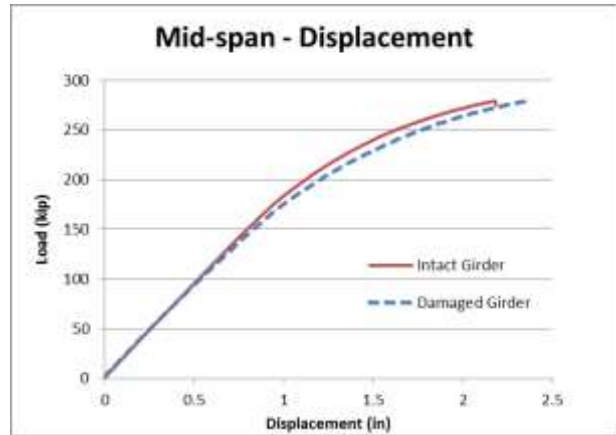
Figure 4-36 Schematic description of Test B.

4.5.1 Global Behavior

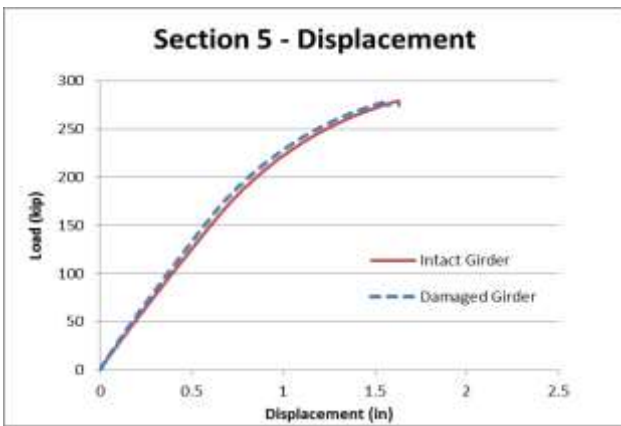
The specimen was loaded up to approximately 270 kips in which the nonlinear plateau of load-deflection curve was observed. This load-deflection curve, which is illustrated in Figure 4-37a, shows the specimen responded linearly up to 150 kips of load with 0.82 in. of displacement before the system stiffness started decreasing. The initial stiffness of the specimen was approximately 200 kips/in. There was no significantly visible damage observed during this test. However, the deck showed some minor cracks around loading pads. The longitudinal strains measured at mid-span indicated that the intact girder has yielded and permanent deformation was observed after unloading.

Figure 4-37 shows that the specimen displaced uniformly across its cross-section as well as along the length of the specimen. The average displacements were 2.25 in. at mid-span, 1.63 in. at Section 5, and 1.71 in. at cantilever end. Unlike Test A, this test didn't show any up-lift of the support and the displacements monitored near the supports are shown in Figure 4-38. Shear force in one cross-frame is plotted in Figure 4-39. This indicates the shear transferred from the undamaged girder to the damaged girder was less than 1 kip. That negligible shear force in cross-frame, plus the nearly identical displacement across the cross-section indicates that the contribution of damaged girder the load-resisting capacity of the specimen under this loading configuration wasn't significant. This suggests that the capacity, obtained in this test, should be

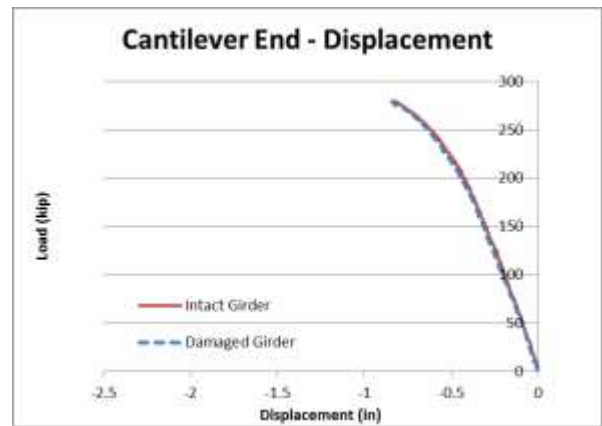
similar to the plastic capacity of the composite section of the undamaged bridge. As shown in Section 3.2, the plastic moment capacity of cross-section is found to be 1789 kips-ft. This indicates the maximum capacity of the section under a concentrated load at mid-span is 239 kips using the formula, $P=M_n \times 4/L$. A similar prediction was achieved by FEA of single undamaged girder bridge with 245 kips of load. This hand calculation and finite element predictions were in good agreement with the capacity of the specimen obtained from this test which was 270 kips. This small difference could be attributed to the contribution of the damaged girder.



(a)



(b)



(c)

Figure 4-37 Test B: Load vs. displacement curves at (a) mid-span, (b) Section 5 and (c) cantilever end.

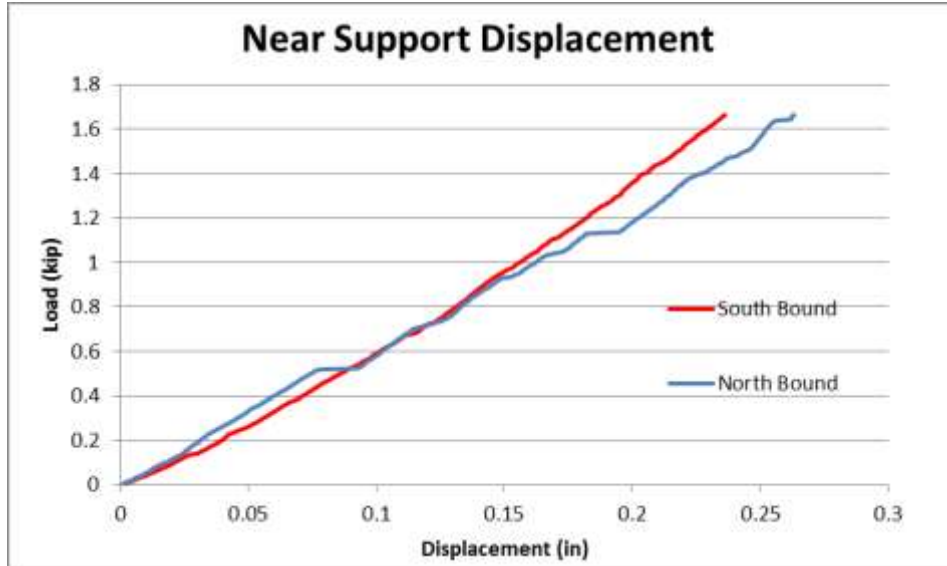


Figure 4-38 Displacement near supports.

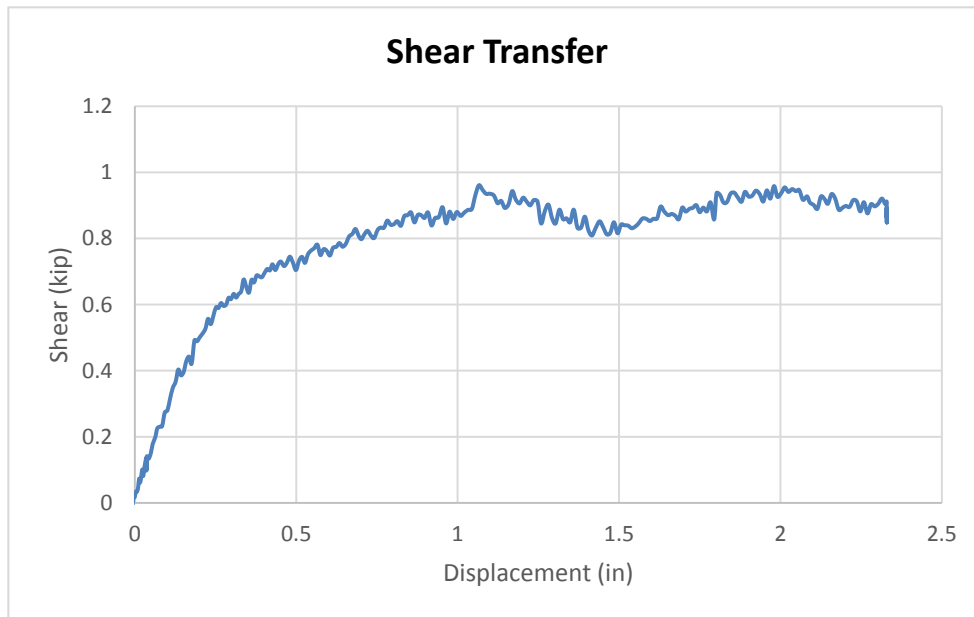


Figure 4-39 Shear transferred through a cross-frame in Test B.

4.5.2 Local Behavior

The summary of longitudinal strains at the bottom flange and top flanges of the undamaged girder (WG) along the length of the bridge are summarized in Figure 4-40 and Figure 4-41. The bottom flange strain was computed by taking average of strains at gauges 2WBF1, 2WBF2 and 2WBF3 while the average strain in top flanges was computed by taking an average of the strains measured at gauges 2WTF1 and 2WTF2. As expected, the bottom flange strain was highest at

Section 2 with 7700 $\mu\epsilon$ and lowest at Section 5 with 1880 $\mu\epsilon$. The strain in top flanges was small at mid-span, indicating the location of the plastic neutral axis was somewhere in the top flanges. This location is in a good agreement with hand calculation of the plastic neutral axis as computed earlier in Section 3.1.1.

A comparison of longitudinal strains of both girders at Section 5 is plotted in Figure 4-42. Top flanges experienced -112 $\mu\epsilon$ and -57 $\mu\epsilon$ on average in the intact girder and damaged girder, respectively. The average strain at the bottom flange of the intact girder was 1880 $\mu\epsilon$, and it was 135 $\mu\epsilon$ for the damaged girder. This suggests that some of the applied load was transferred to the damaged girder, but not that significant. Because the cross-frame force was found to be less 1 kip of load as shown previously in Figure 4-39, if some load was transferred to the damaged girder, it was mainly transferred through the deck.

The longitudinal strains measured at the top reinforcements at mid-span are shown in Figure 4-43. These gauges are located approximately 1.5 in. below the top of the deck. Gauges 2LTB1, 2LTB2, 2LTB3, and 2LTB4 are negative while gauges 2LTB5 and 2LTB6 are positive. This indicates the deck would change its deflection from concave up to concave down somewhere between gauge 2LTB4 and 2LTB5, close to the inside top flange of the damaged girder.

Figure 4-44 shows responses of top and bottom transverse reinforcements at mid-span. Gauges 2TTB1 and 2TBB1, located over the interior top flange of undamaged girder, had strains of 252 $\mu\epsilon$ and 1590 $\mu\epsilon$, respectively. Gauges 2TTB2 and 2TBB2, located at center of the deck, between two girders, had maximum strain at 24 $\mu\epsilon$ and 40 $\mu\epsilon$, respectively. Lastly, gauges 2TTB3 and 2TBB3 are located over the interior top flange of damaged girder showed strain values of 16 $\mu\epsilon$ and -142 $\mu\epsilon$. The strain data in the bottom transverse reinforcement changing from 1590 $\mu\epsilon$ to 40 $\mu\epsilon$ to -142 $\mu\epsilon$ indicates that the deck had changed its transverse deflection shape from concave up to concave down. This was consistent with the conclusion obtained from the strain data of the longitudinal reinforcements. A schematic drawing showing how the specimen deflected at mid-span is illustrated in Figure 4-45.

Cracking of the deck was recorded with three crack gauges at the top of the deck and one at the bottom face. Figure 4-46 shows that the gauge 2TTD1 experienced significantly higher strain than the others, which indicates that the cracking is largest at this location. Only gauge 2TBD1 at center bottom of the deck experienced negative value which mean the deck is in compression.

Overall, the data suggest that the specimen in this test would be likely to fail in a flexural mode. The load-carrying capacity found in this test was in a good agreement with the maximum capacity of the intact girder that was computed by hand calculation and FEA. Again the results also indicate that the contribution of the damaged girder to global behavior of the system was negligible. Lastly, if the deck was assumed to crack at $\epsilon = 160 \mu\epsilon$ ($f_R = 600$ psi with $E=3,800$ ksi), strain data from longitudinal and transverse reinforcements indicated that the deck might have been cracked at several locations at mid-span. These minor cracks in the deck were also observed after the test.

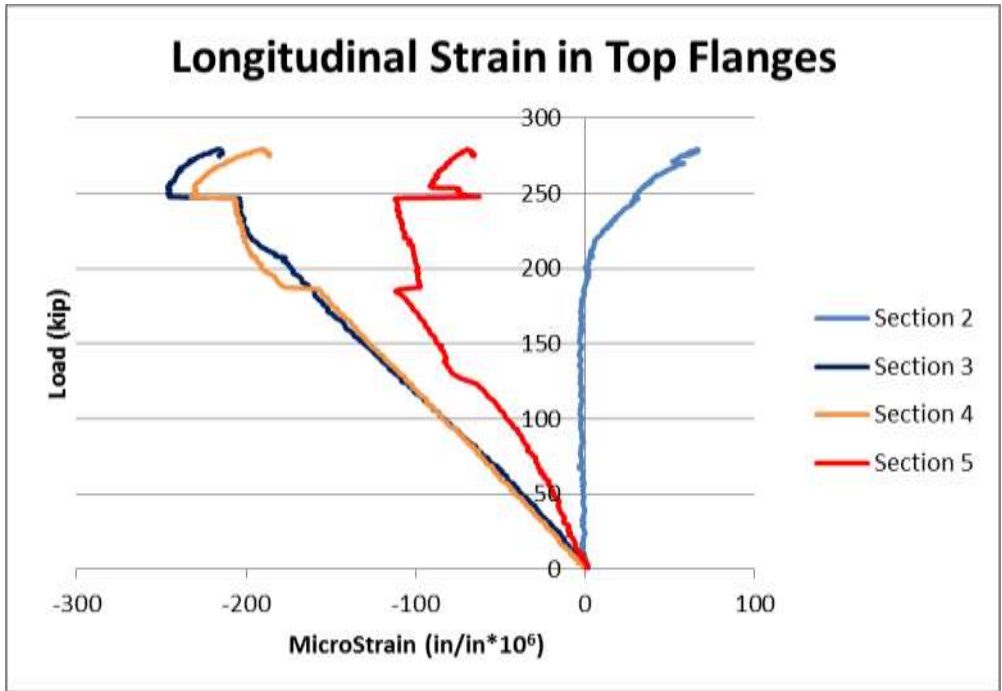


Figure 4-40 Average longitudinal strains at top flanges of the intact girder.

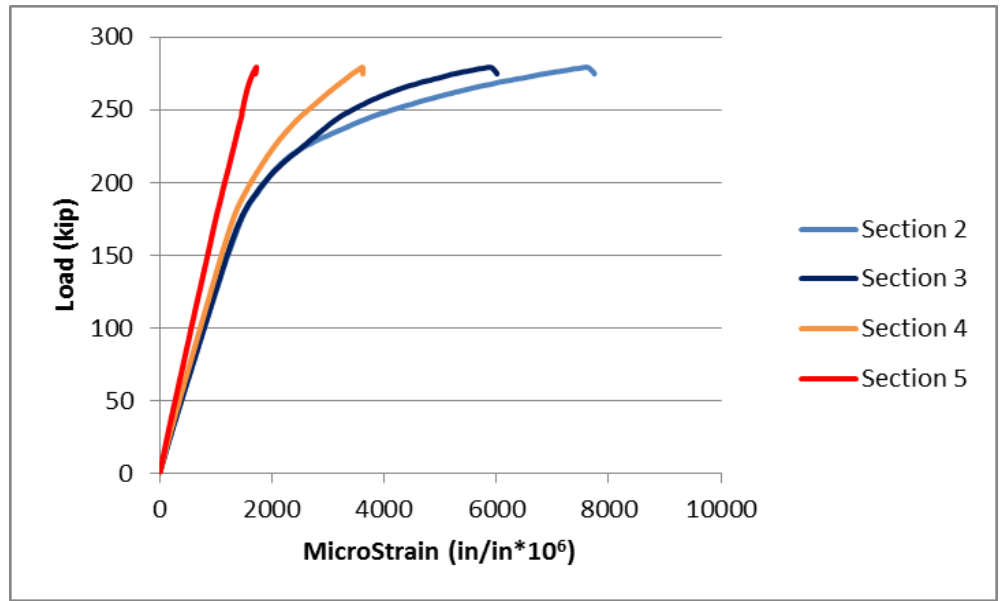


Figure 4-41 Longitudinal strains at the bottom flange of the intact girder.

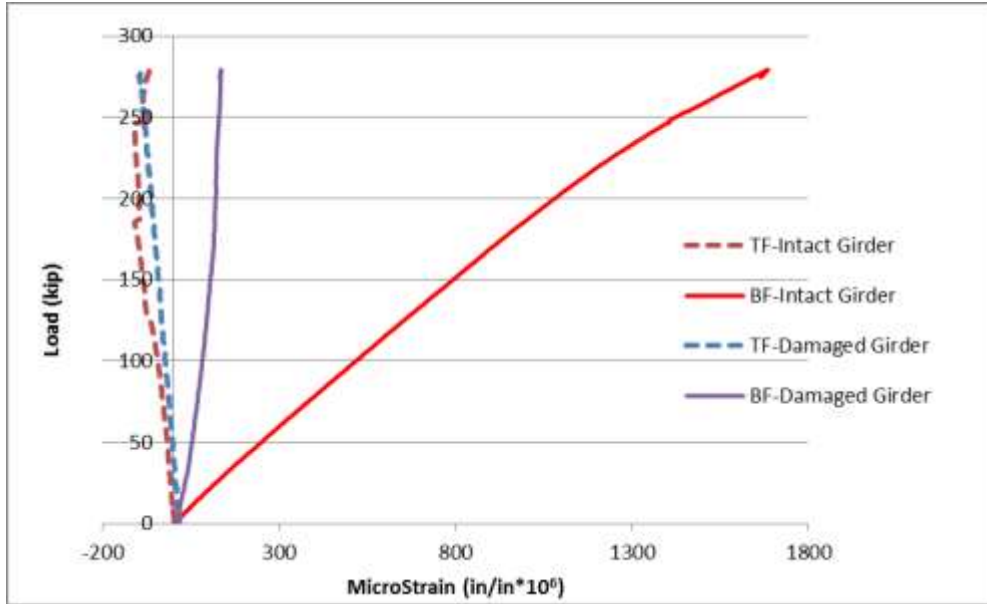


Figure 4-42 Comparison of longitudinal strains in the intact and damaged girders at Section 5.

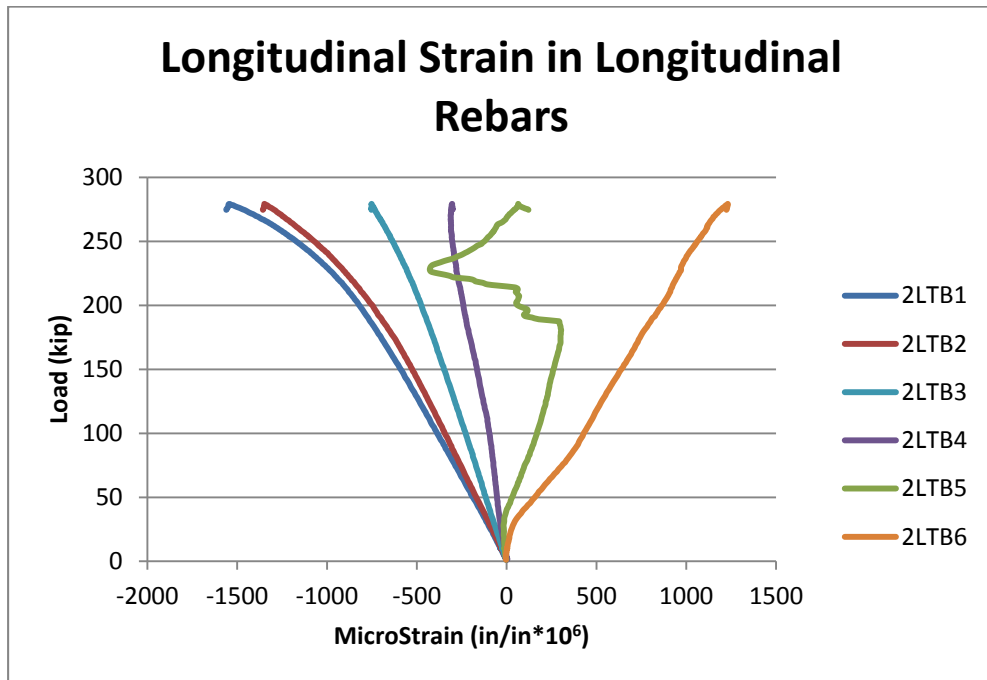


Figure 4-43 Longitudinal strain in rebars at mid-span.

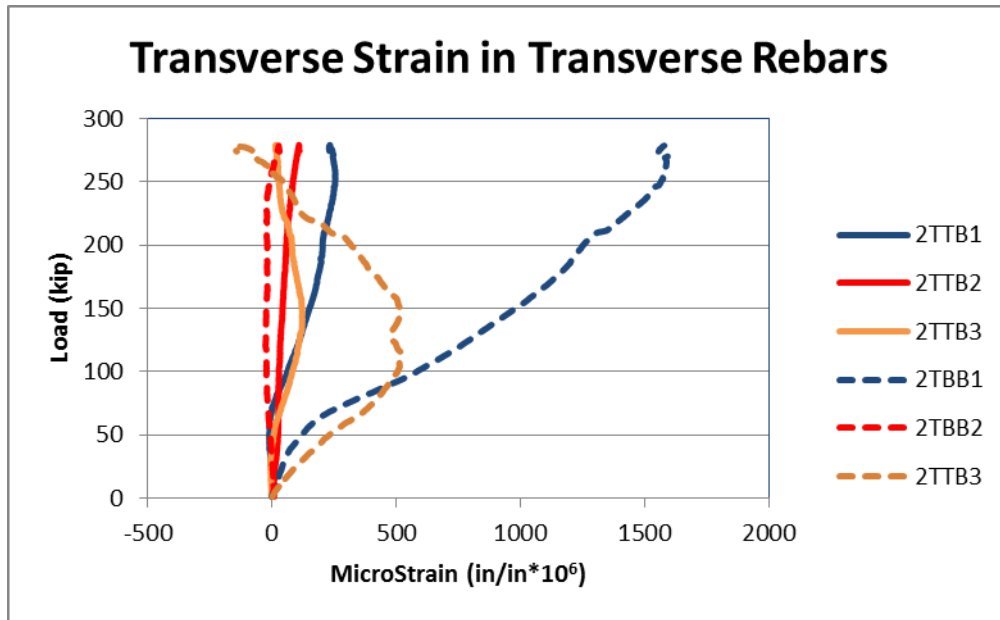


Figure 4-44 Transverse strain in rebars at mid-span.

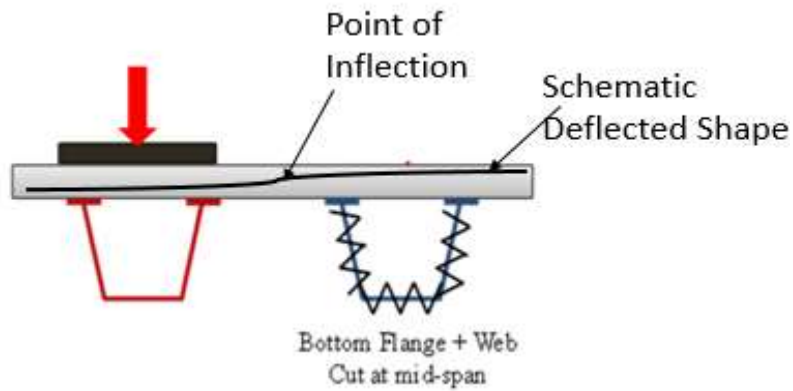


Figure 4-45 Schematic deflection shape of the deck.

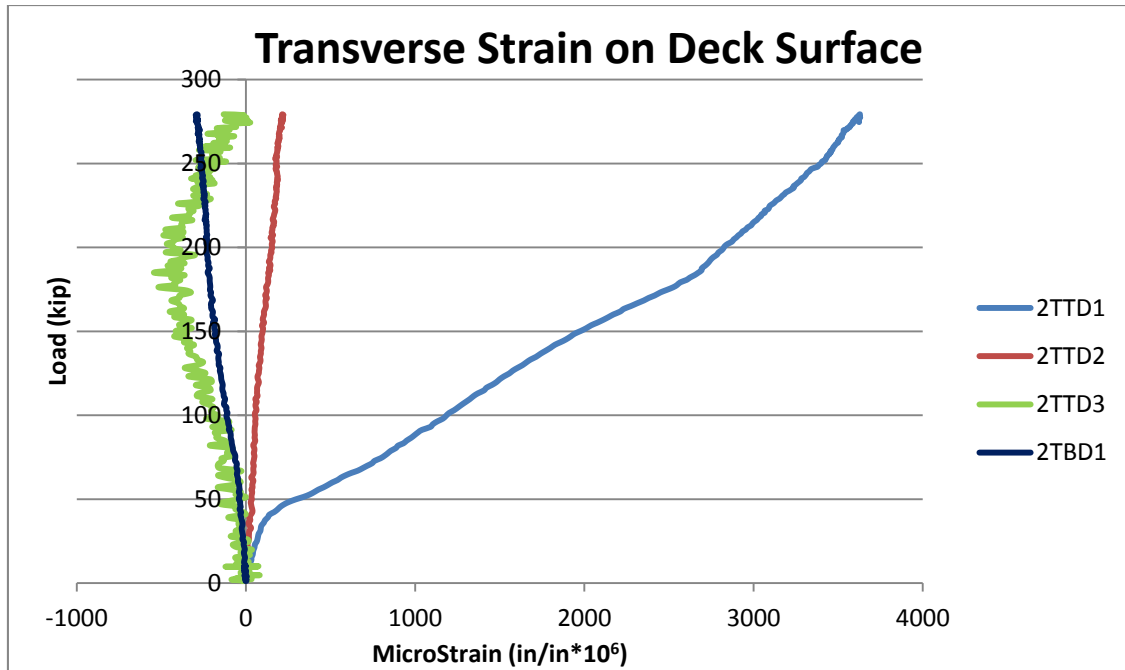


Figure 4-46 Transverse strain of the deck near mid-span.

4.6 Ultimate Test C

In ultimate Test C, the load was applied through a 10-in.-square loading pad, over the intact girder at mid-span location. The purpose of this test was to see the effect of concentrated loading configuration on the failure mode of the bridge. The schematic illustration of the test is shown in Figure 4-47. For this test, the load was applied until the specimen failed completely. It is important to note that because this test was continued after Test B without any repair, the results presented, herein, will include any permanent deformation inherited from the previous test.

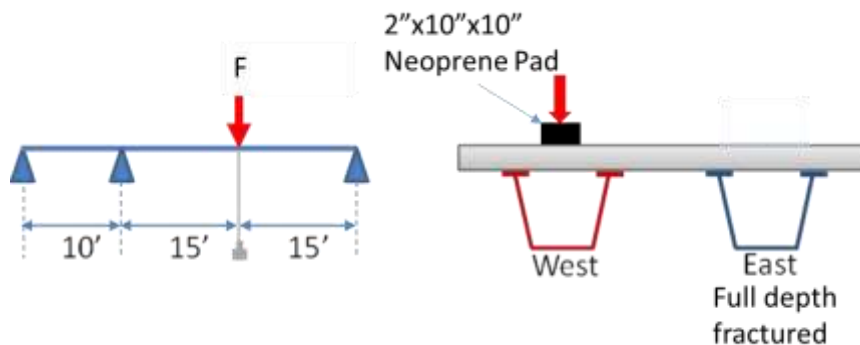
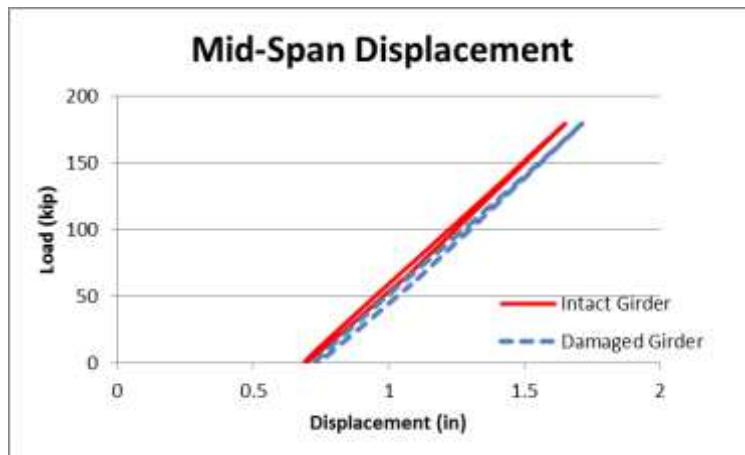


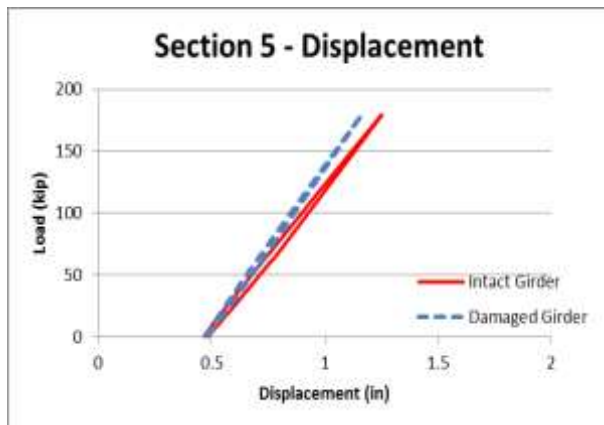
Figure 4-47 Schematic description of Test C.

4.6.1 Global Behavior

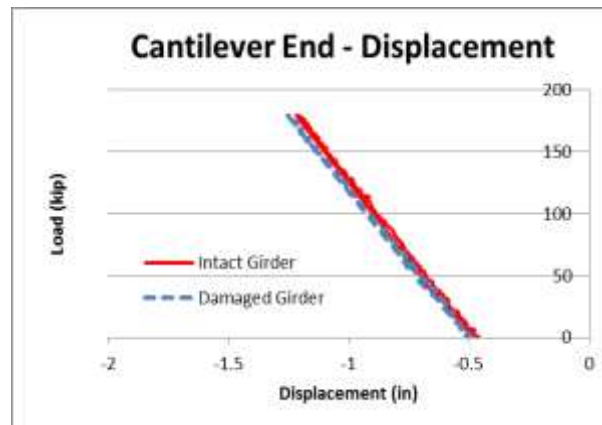
In this test, the specimen carried up to 180 kips of load before the deck was suddenly punched through by the loading pad. Load versus displacement curves of the damaged girder along its length are plotted in Figure 4-48. The specimen showed approximately 0.7 in. of permanent deformations at mid-span. The stiffness of the specimen was approximately 196 kips/in. It was similar to the data observed in Test B which was showing a stiffness of 200 kips/in. Similar to Test B, both damaged and undamaged girders experienced similar displacements along the length. The average displacements at mid span, Section 5 and cantilever end were approximately 1 in., 0.78 in. and 0.75 in., respectively. During the test, the specimen responded nearly linearly then failed abruptly without any warning. The deck was punched through by the loading pad as illustrated in Figure 4-49. Unlike ultimate Test A, no girder uplift was observed during the test and it is also illustrated in Figure 4-50 where no backward displacement was observed at the supports. The shear transferred through one of the external cross-frames is plotted in Figure 4-51. The shear force in the monitored cross-frame under this loading configuration was very small, with less than 2 kips.



(a)



(b)



(c)

Figure 4-48 Test C: Load vs. displacement curves at (a) mid-span, (b) Section 5 and (c) cantilever end.



Figure 4-49 Punching damage in test C.

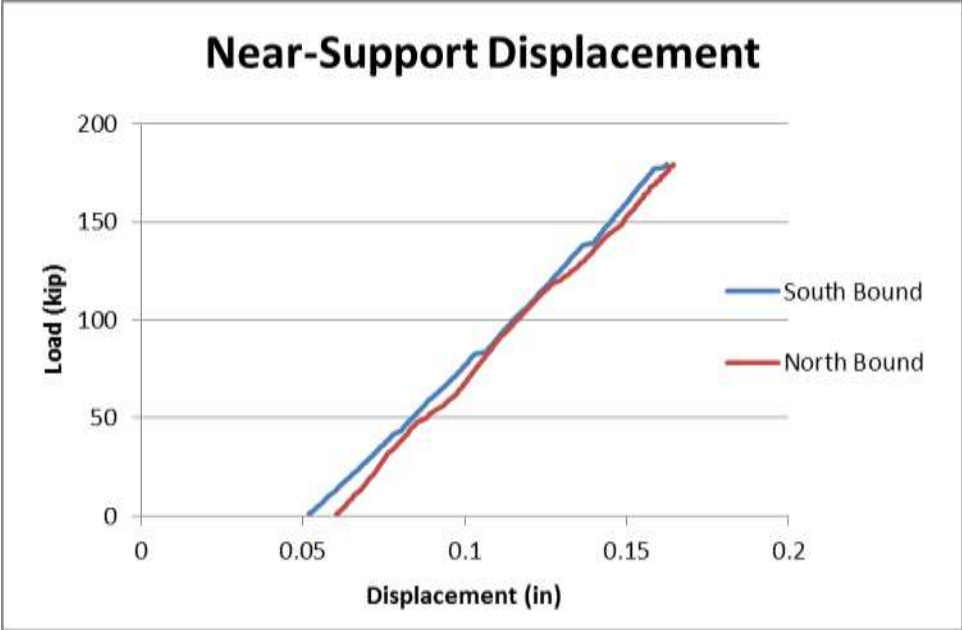


Figure 4-50 Near-support displacement.

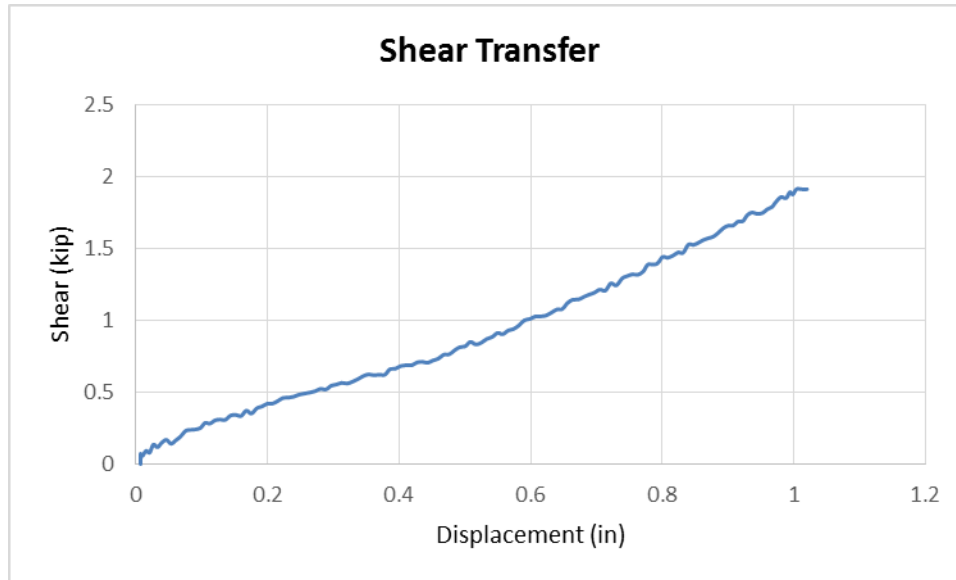


Figure 4-51 Shear transferred through a cross-frame in test C.

4.6.2 Local Behavior

It is important to note that all strains, plotted in this test and following tests, will be offset by its initial value so that the data will begin from zero. This means that any permanent deformation inherited from previous test will not be discussed here. This will allow a better comparison between experimental data and finite element analysis results, at a later time.

The comparison of strains in bottom flange and top flanges of the intact girder along the length is illustrated in Figure 4-52 and Figure 4-53, respectively. That the intact girder experienced maximum strain of $1740 \mu\epsilon$ indicated the bottom flange of intact girder just yielded. The strains in the top flanges were small and negative (compression), indicating that the neutral axis should be somewhere at the top flange. Figure 4-53 suggests that the only location that experienced a tension yielding was the bottom flange of the intact girder at the mid-span. This suggests that the moment produced in this test at mid-span should be close to the yielding capacity of the intact girder. The moment produced, in the intact girder by 180 kips of load, can be approximated by the using formula $M_n = P \times L/4$, assuming the participation of the damaged girder was negligible. This formula yields an estimated moment of 1350 kips-ft while the yield moment capacity computed by design calculation is 1366 kips-ft.

At Section 5, the bottom flanges were in tension while the top flanges were in compression for both girders. The intact girder had longitudinal strain in the bottom flange significantly higher than that of the damaged girder, as illustrated in Figure 4-54. These data are consistent with earlier findings which stated the contribution of the damaged girder to the system's capacity was very minimal.

Figure 4-55 plots strains in longitudinal rebars at mid-span. The maximum positive strain occurred at gauge 2LTB6 with $560 \mu\epsilon$ while the maximum negative one was $-840 \mu\epsilon$. All the longitudinal rebar gauges were in compression, except gauges 2LTB5 and 2LTB6. These observations were similar to what was observed in Test B.

Figure 4-56 plots strain recorded at both top and bottom transverse rebars. Changing in the strain from positive at gauge 2TBB1 to negative at gauge 2TBB2 suggested that the moment, in longitudinal direction, had changed from positive to negative. This indicates that the deck changes its transverse deflection shape from concave up to concave down. Therefore, the location of inflection point at mid-span should be located somewhere between 2TBB1 and 2TBB2. Comparing with the data obtained from Test B, this suggests that the point of inflection at mid-span section was shifted more toward to the intact girder when the loading area was decreased.

Figure 4-57 illustrates transverse strain on the deck surface. The location, closest to the loading point, has experienced the largest crack, as expected. The strains at locations 2TTD2 and 2TTD3 are very small. The fact that gauge 2TBD1 attached to the bottom of the deck surface showed a negative value suggests the deck was in compression at this location.

Overall, the recorded data were very similar to those obtained in Test B up to 180 kips of load. The data indicated that the load was mainly resisted by the intact girder. No girder uplift was observed, and cross-frame forces were negligible. However, this test had punching shear as a failure mode while Test B was likely to fail in flexural mode. The reason that this test failed much faster could be attributed to the size of the loading area. In this test, the specimen was loaded in a more concentrated manner than it was in Test B.

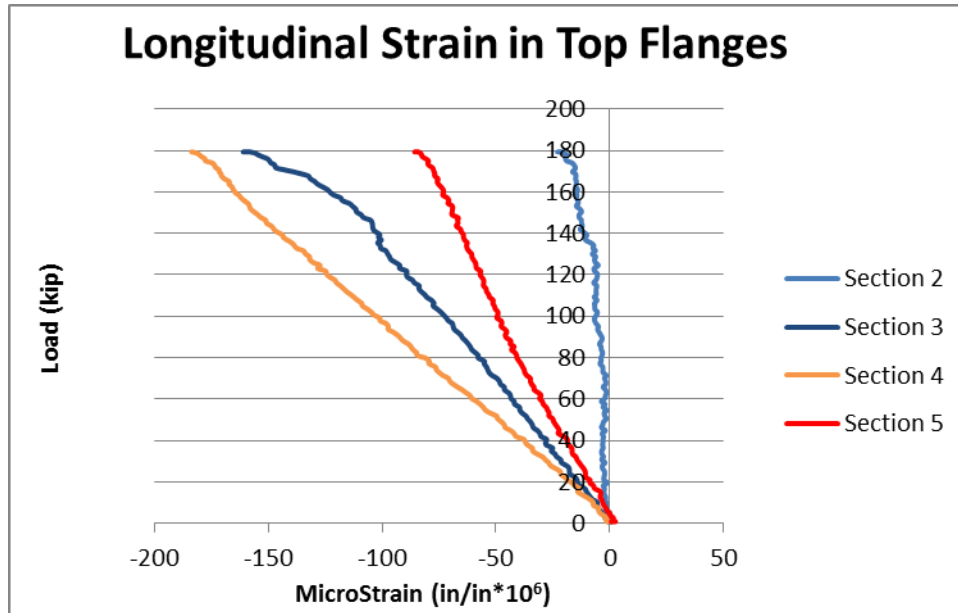


Figure 4-52 Average longitudinal strains at top flanges of the intact girder.

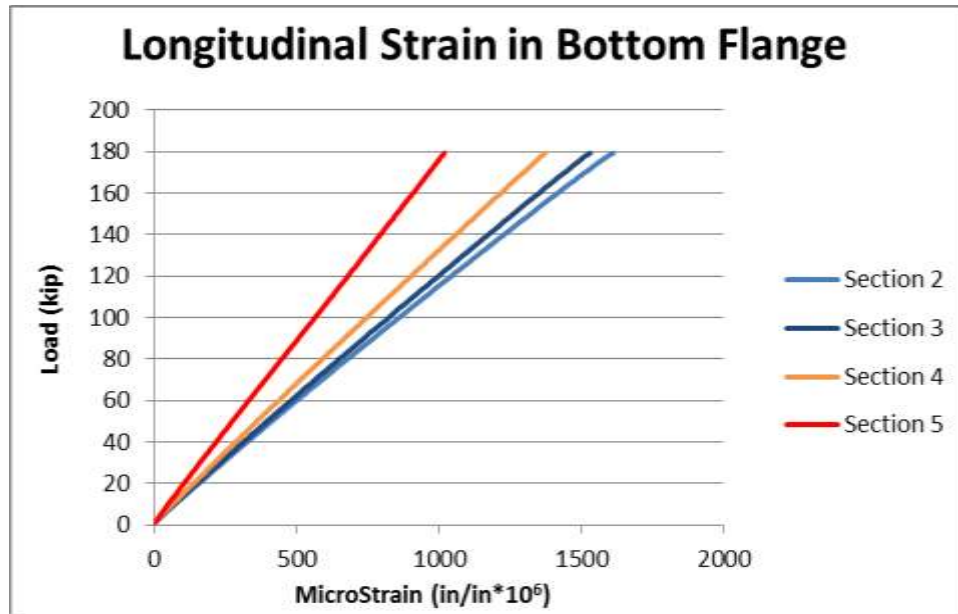


Figure 4-53 Longitudinal strains at the bottom flange of the intact girder.

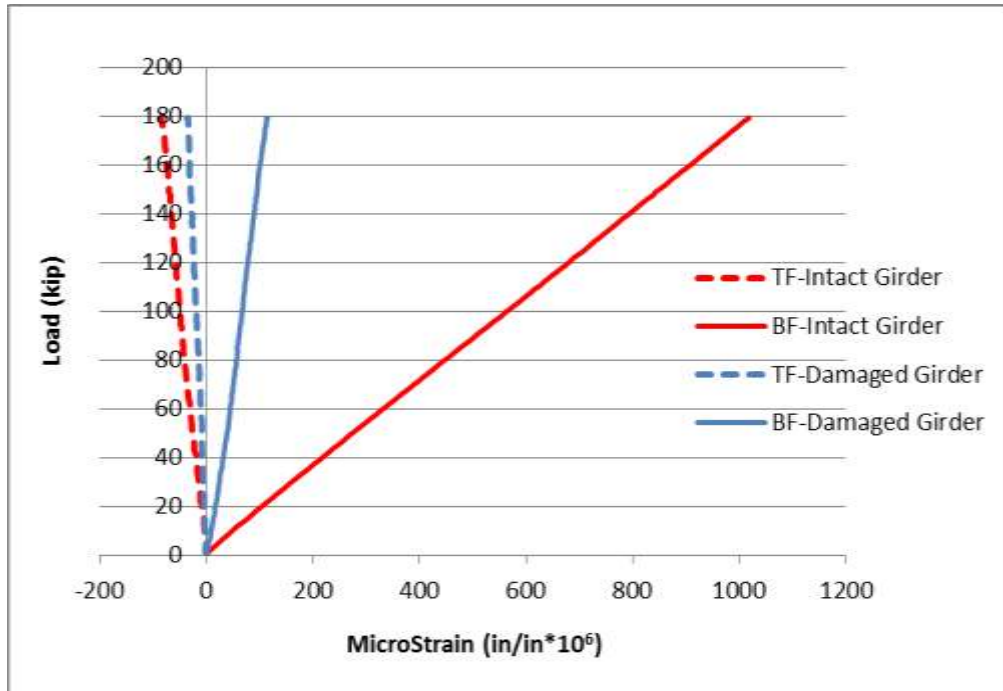


Figure 4-54 Comparison of longitudinal strains in the intact and damaged girders at Section 5.

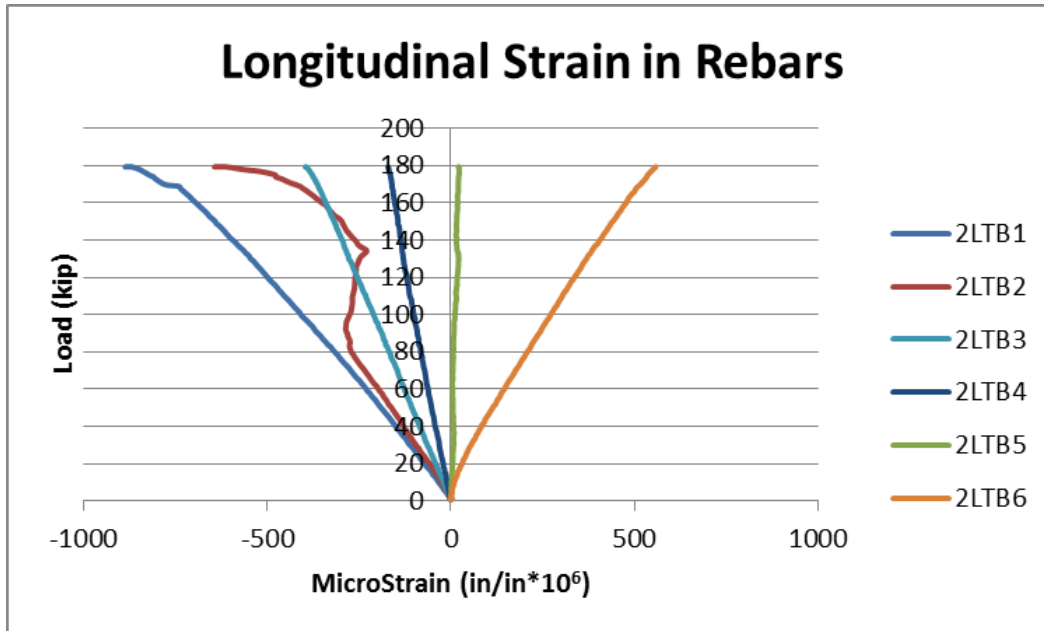


Figure 4-55 Longitudinal strain in rebars at mid-span.

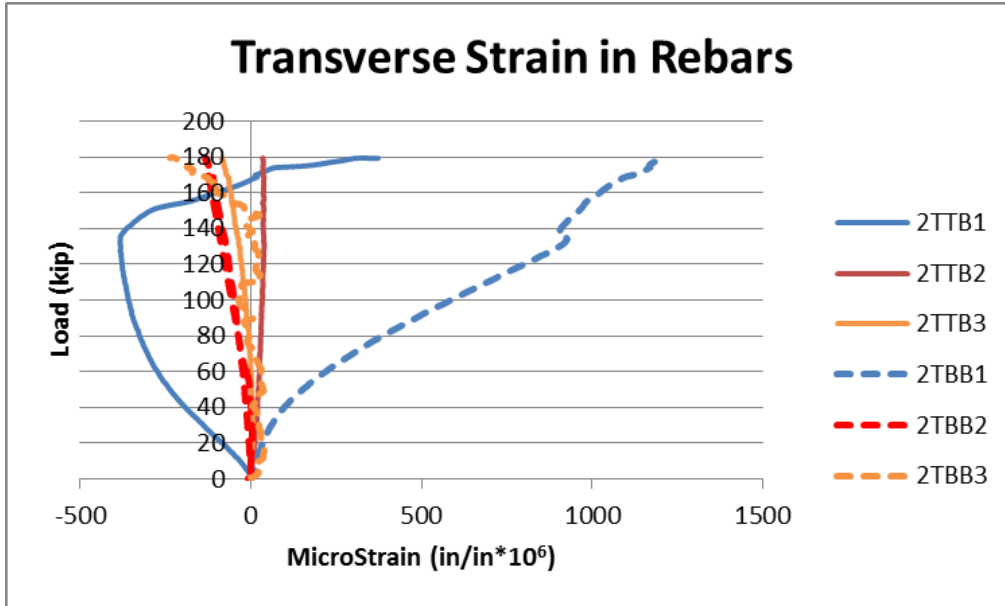


Figure 4-56 Transverse strain in rebars at mid-span.

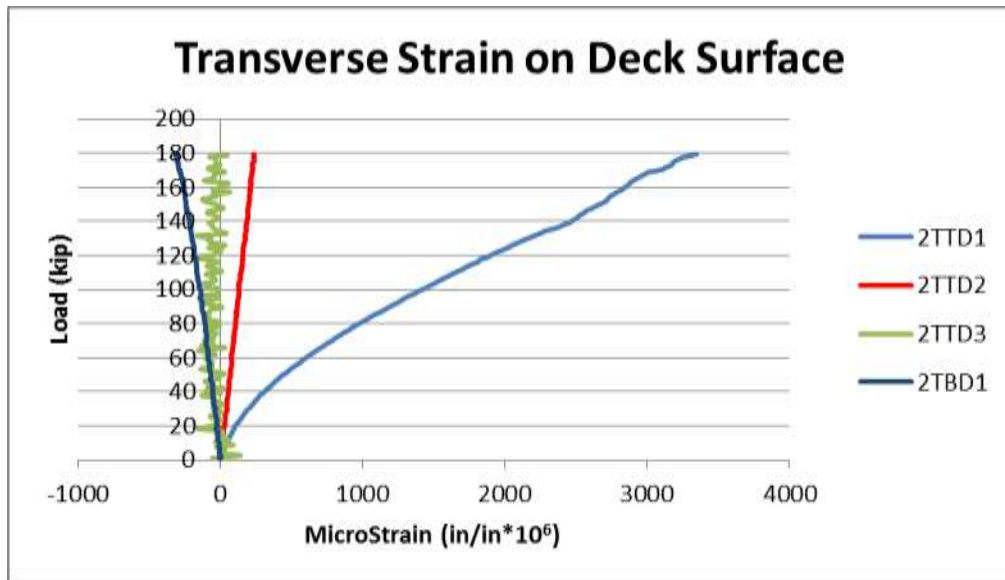


Figure 4-57 Transverse strain on the deck near mid-span.

4.7 Ultimate Test D

In this ultimate Test D, the load was applied through a 10-in.-square loading pad which was the same as in Test C, but over center of damaged girder at mid-span location. The results of this test, in addition to that of previous ultimate tests, will provide a comprehensive comparison that could explain the effects of damaged girder and loading configurations on the behaviors of the specimen. The schematic drawing of loading configuration in Test D is shown in Figure 4-58. The specimen

was loaded until failure. Since this test was continued on the same specimen without any repair, the results presented in this section will include any permanent deformation inherited from both Test B and Test C.

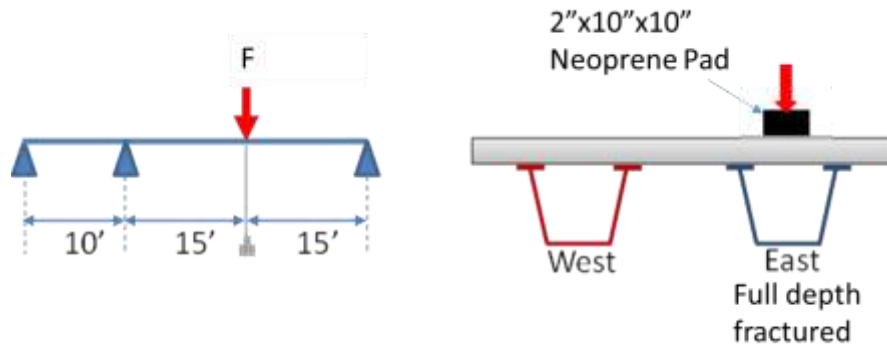


Figure 4-58 Schematic description of Test D.

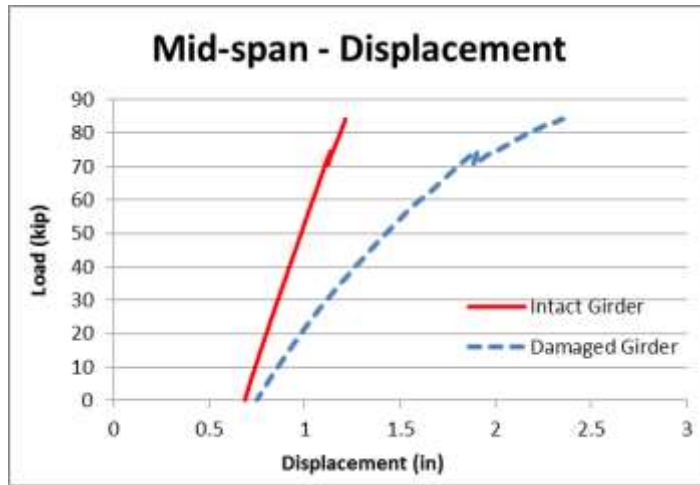
4.7.1 Global Behavior

In this test, the specimen carried up to 83 kips of load before the deck was punched through by the loading pad. The applied load versus the displacement curves of the damaged girder along its length are plotted in Figure 4-59. The specimen showed linearly elastic response up to 60 kips. Approximately 0.7 in. of permanent deformations at mid-span was observed as a result of previous tests. The initial stiffness of bridge under this loading condition was 87 kips/in and was similar to the initial stiffness obtained in Test A. However, comparing with Test B and C, the initial stiffness of the specimen was reduced an average of 55%. There was a 2-kip drop in capacity after reaching 72 kips of load due to cracks in the concrete deck. After that the specimen continued to carry up to 83 kips before it failed abruptly by punching shear. Figure 4-60 illustrates that the punching damage was confined exactly to the area of the loading pad and it was similar to the failure mode obtained in Test C.

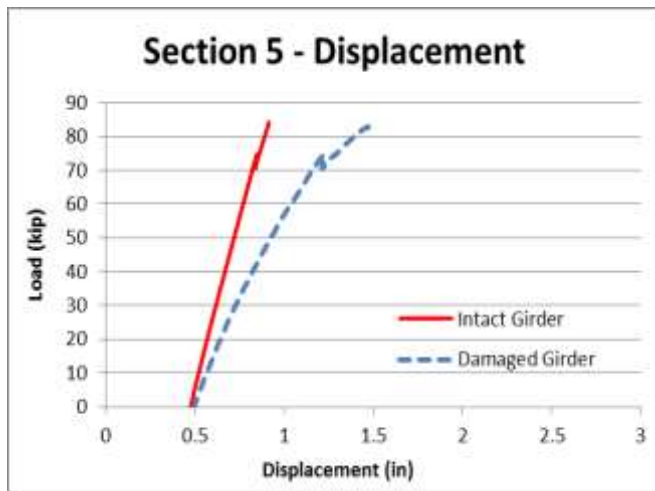
In contrast to Test B and C but similar to Test A, Figure 4-59b shows that the damaged girder experienced a significantly higher displacement than the intact girder. The displacement data at different sections suggests that the further away from mid-span, the smaller displacement difference two girders experienced as illustrated in Figure 4-59b and c. At the supports and the cantilever end, both girders experienced very similar displacements. Figure 4-61 shows that both girders displaced downward during the entire test. This suggests that no uplift occurred at the supports.

The shear transferred through one external cross-frame was less than 2 kips and is illustrated in Figure 4-62. Assuming the shear force in the other cross-frame was the same, the total shear force

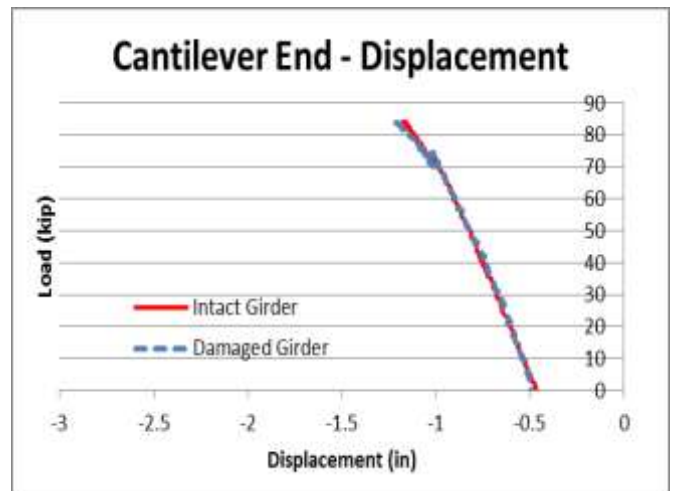
carried by all of the external cross-frames, in the main span, would be less than 4 kips. This indicates that applied load was mainly resisted and transferred to the intact girder through the deck.



(a)



(b)



(c)

Figure 4-59 Test D: Load vs. displacement curves at (a) mid-span, (b) Section 5 and (c) cantilever end.



Figure 4-60 Punching damage in Test C.

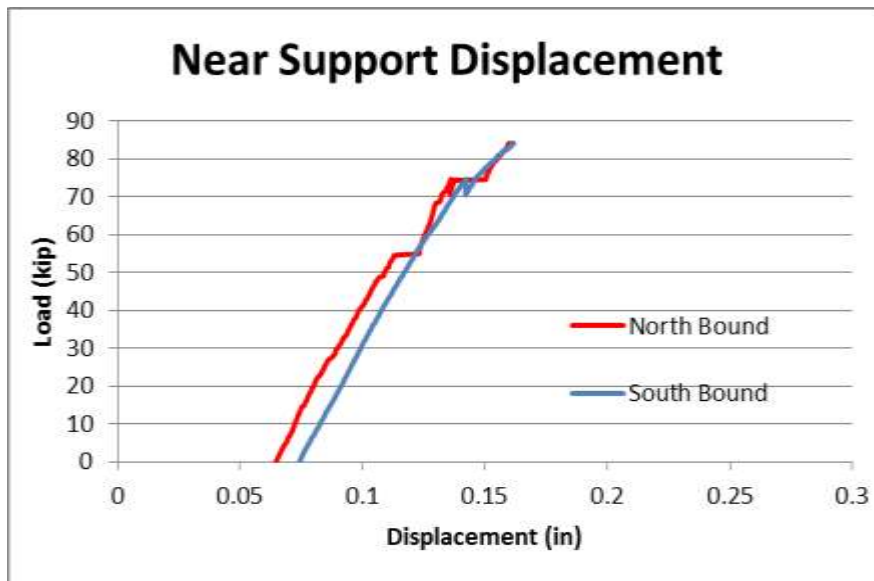


Figure 4-61 Near-support displacements.

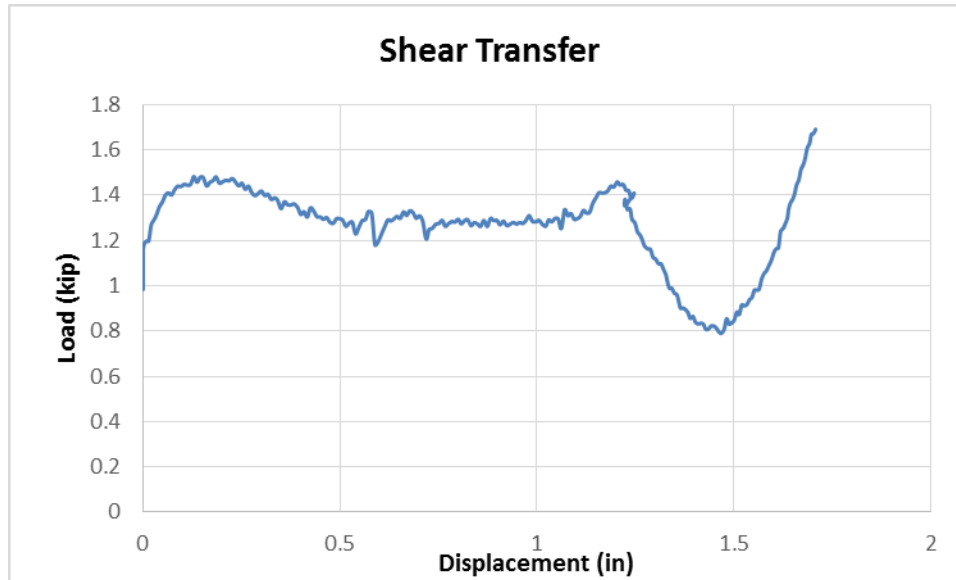


Figure 4-62 Shear transferred through a cross-frame in Test C.

4.7.2 Local Behavior

Due to the fact that the deck failed much earlier in this test than it did in other tests, the maximum strain, obtained was also smaller in a similar proportion. The average longitudinal strain in the top flanges of the intact girder is shown in Figure 4-63. The data for the bottom flange of the intact girder along the length of the bridge are illustrated in Figure 4-64. The longitudinal strains, in the bottom flange, were comparable from Section 2 to Section 5. This suggests the load that was transferred to the intact girder was distributed quite uniformly between these sections (Note that Section 2 is mid-span section and Section 5 is 5 ft away from mid-span).

Similar to Test A, the strains, obtained at Section 5, indicated that the damaged girder had the bottom flange in compression and the top flange in tension. A comparison between the intact and damaged girders is illustrated in Figure 4-65. For the intact girder, average strain was $-25 \mu\epsilon$ and $760 \mu\epsilon$ for the top flange and the bottom flange, respectively. For the damaged girder, it was $70 \mu\epsilon$ and $-280 \mu\epsilon$ for the top flange and the bottom flange, respectively.

Among six gauges installed to measure strain in the top longitudinal reinforcements, two gauges were damaged which were 2LTB1 and 2LTB2. Only gauges 2LTB5 and 2LTB6 were in tension while others were in compression. This indicates the deck would change its deflection from concave up to concave down somewhere between gauge 2LTB4 and 2LTB5. The maximum strain was $1300 \mu\epsilon$ obtained at gauge 2LTB6 over the outside top flange of the damaged girder. This indicates the top layer of longitudinal rebar have not yielded yet. Strains in top and bottom transverse rebars are plotted in Figure 4-67, indicating some of the transverse rebars yielded.

Figure 4-68 shows the transverse strains recorded on the deck surface. Gauges 2TBD1 and 2TTD3 experienced negative strains while gauges 2TTD1 and 2TTD2 had positive strains which mean the deck were in tension at these locations. Since gauges 2TTD2 and 2TTD3 are next to each other and had opposite sign of change in strain, this suggests that the point of inflection was somewhere between these two gauges. Combining this finding and the findings based on the longitudinal rebars, the point of inflection was approximately near the inside top flange of the damaged girder.

In general, the specimen showed similar behavior to what observed, in Test A, up to 83 kips of load. However, two different failure modes were observed. In this test, the load area was reduced and the specimen failed predominantly in punching shear (or two-way shear failure) without any warning while the failure was likely a combination of both one-way and two-way shear failure in Test A. The applied load was found to be transferred mainly through the deck. The fact that the deck was punched through faster in this test (83 kips) than it was in Test C (180 kips) could be attributed to the effect of the girders on supporting the deck, especially where the load was applied.

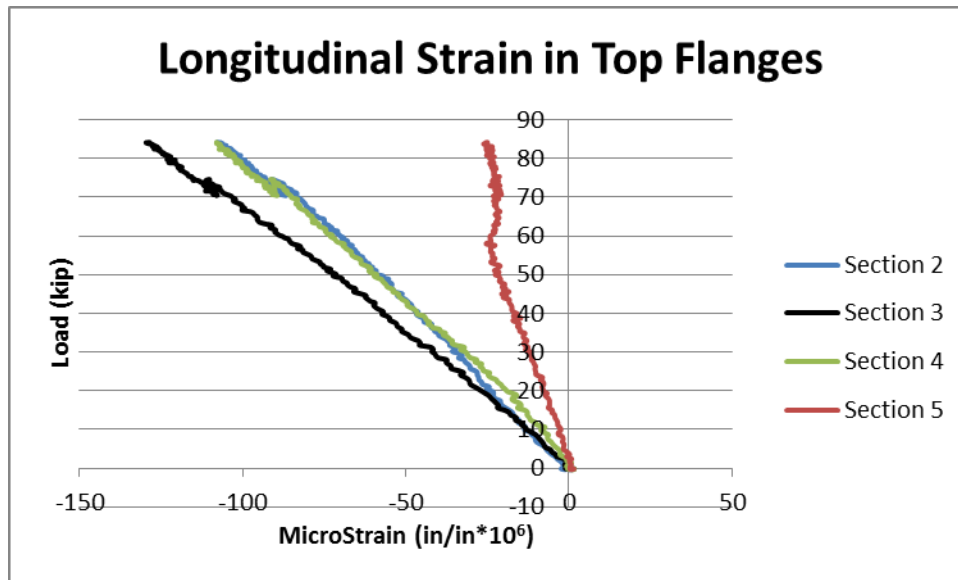


Figure 4-63 Average longitudinal strains at top flanges of the intact girder.

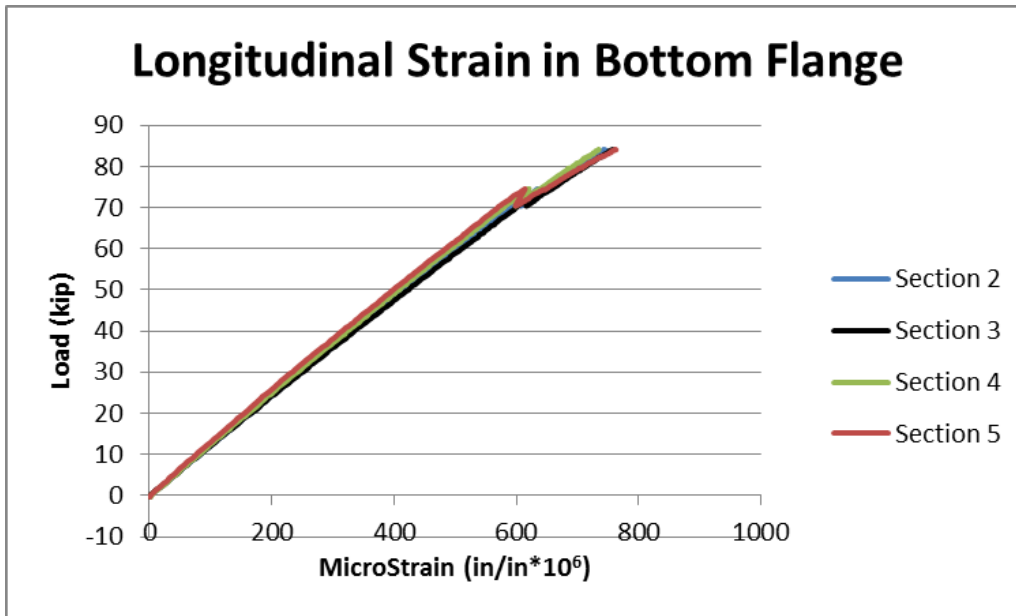


Figure 4-64 Longitudinal strains in bottom flange of the intact girder at Sections 2, 3, 4, and 5.

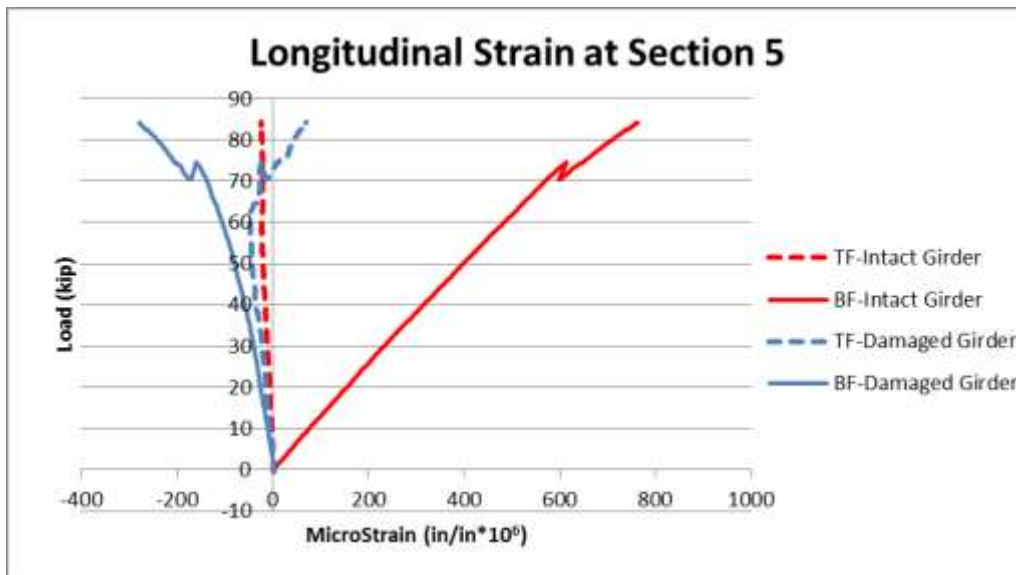


Figure 4-65 Comparison of longitudinal strains in the intact and damaged girders at Section 5.

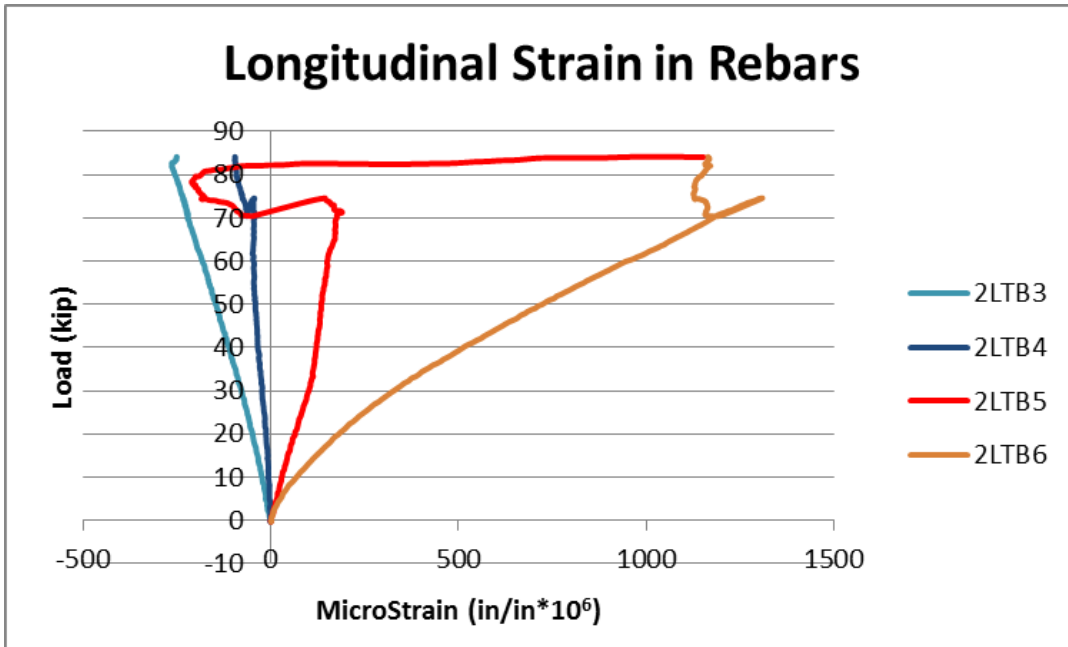


Figure 4-66 Longitudinal strain in rebars at mid-span.

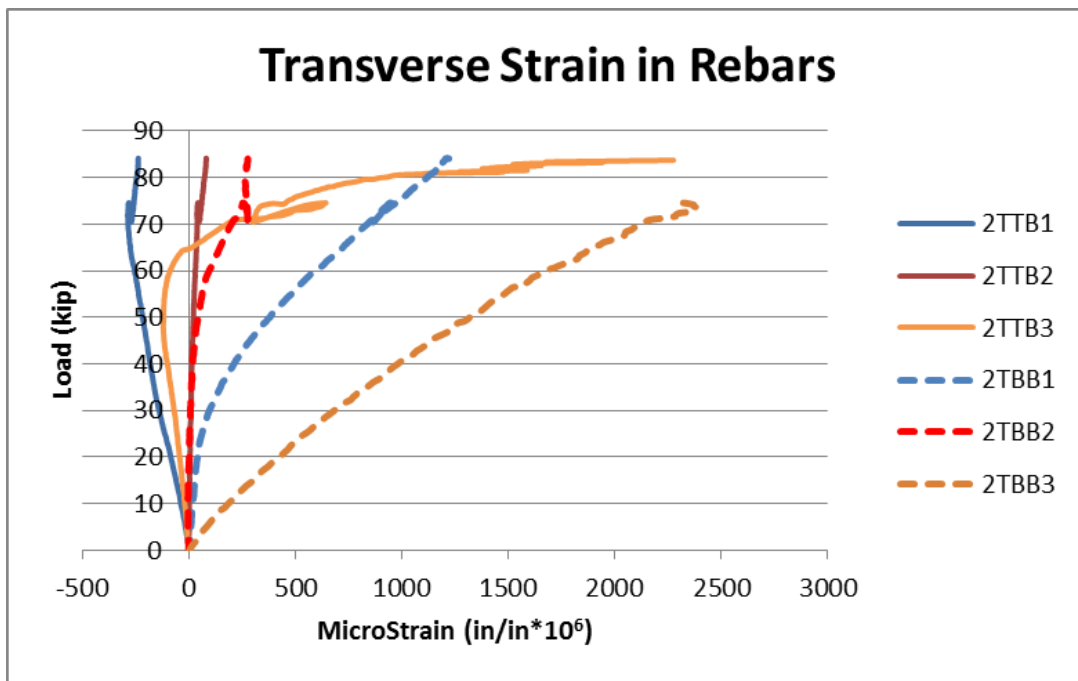


Figure 4-67 Transverse strain in rebars at mid-span.

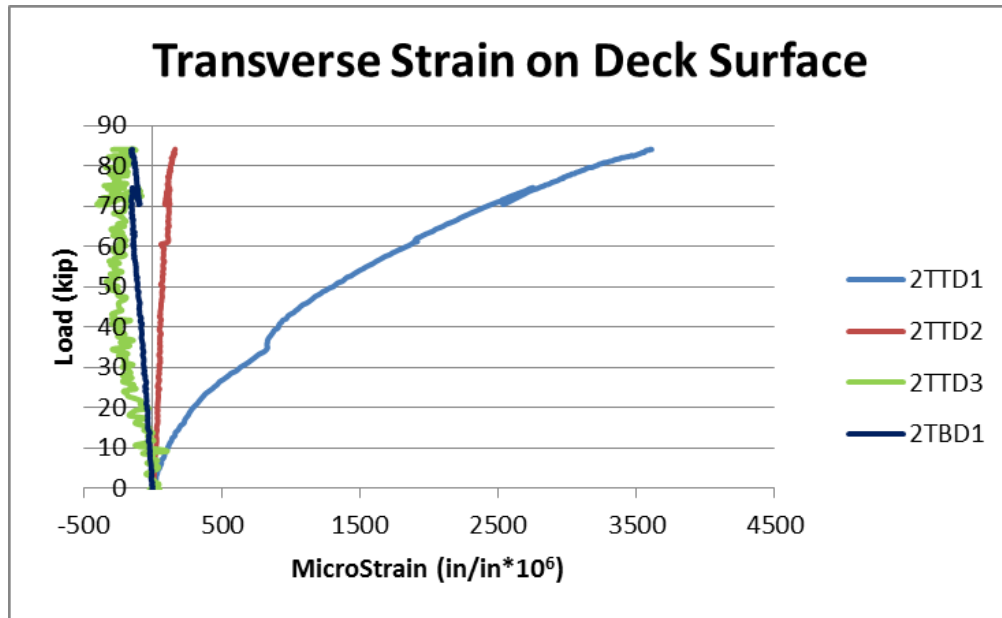


Figure 4-68 Transverse strain on the deck near mid-span.

4.8 Damage Repair

After completing Tests C and D, a decision was made to repair damage due to punching in the deck before carrying out one last ultimate test in which the specimen was loaded under a truck footprint. In order to repair these damages, first of all, spalling concrete fragments were removed around punched square holes. Then tapcons were drilled into the concrete to act as shear studs. After that, an attempt was made to get a saturated surface dry (SSD) condition in the holes. The main material used for the repair was MasterEmaco T302, a two-component polymer-modified cement-based repair mortar with an integral corrosion inhibitor. The expected compressive strength for this composition is 6,000 psi. Once the mortar mix was thoroughly mixed, the moistened concrete fragments were added in, since no pea gravel was available on hand at that time. Then, the mortar mix was poured into the holes and then vibrated in order to get the best possible penetration. Once the repair patch was troweled, moist cure bags were placed over the repair areas. Some pictures taken during the repair are shown in Figure 4-69.



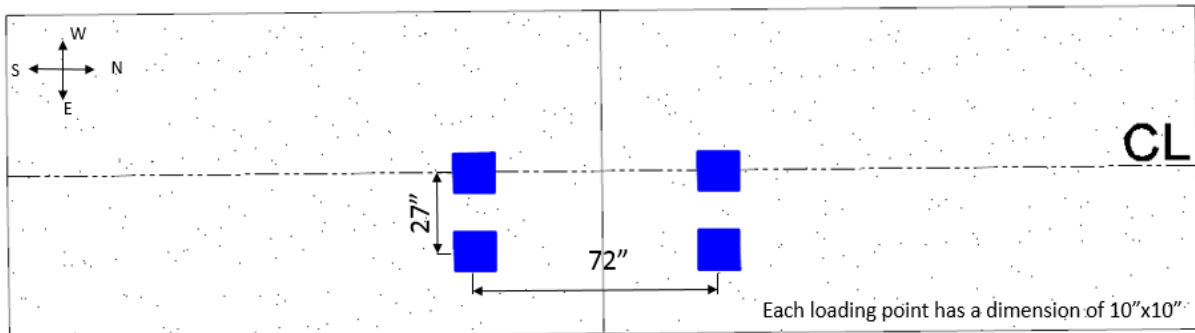
Figure 4-69 Repair of punching shear damage from Tests C and D.

4.9 Ultimate Test E

In this test, the load was applied through four loading pads in order to simulate the truck footprints. The loading pads were the same as in previous tests with a dimension of 10 in. x 10 in. The distance between north wheels and south wheels was 72 in., while the distance between west wheels and east wheels was 27 in. from center to center. The west wheels were placed at the center of cross-section while the east wheels were at the center of damaged girder. The schematic description of Test E loading set up is shown in Figure 4-70. The purpose of this test was to investigate whether the same failure mode of punching shear will be obtained, under truck-load configuration.



(a)



(b)

Figure 4-70 (a) Test setup for Test E and (b) schematic locations of loading foot prints.

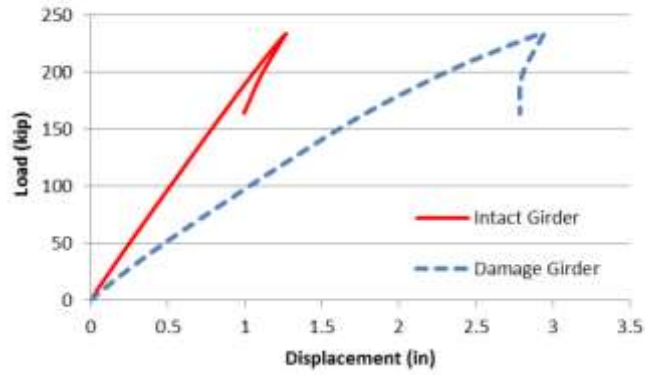
4.9.1 Global Behavior

In this test, the specimen carried up to 235 kips of load before it failed abruptly as shown in Figure 4-71a-c. The load vs. deflection curve indicates the specimen had its stiffness reduced gradually from the beginning. The initial stiffness of bridge under this loading condition was approximately 103 kips/in which was similar to its initial stiffness under Tests A and D. Significant damages on the deck are illustrated in Figure 4-72 a-d. The deck was cracked and crushed heavily along its center, especially where the west wheels were placed. Figure 4-72d shows these cracks

extended from these west wheels toward the inside top flange of the intact girder. Figure 4-73 illustrated that the concrete deck at the ends was cracked and almost ripped off, similar to what was observed in Test A. The reasons this happened was explained previously in Test A. By assuming the participation of the damaged girder in resisting the applied load is negligible, this test is similar to the case studied by Natario (2014), where the slab is linearly supported by the undamaged box girder and subjected to concentrated loads. Overall, the crack and damage pattern suggest that the specimen failed predominantly in one-way shear failure.

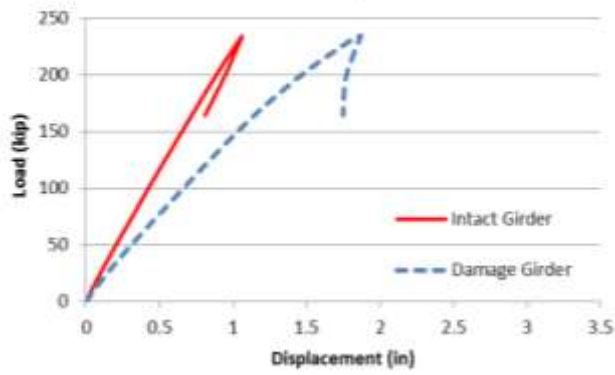
The displacements at Section 5 and at cantilever end are plotted in Figure 4-71b-c. The displacements measured at the cantilever end were about the same for both girders up to 150 kips of load. This suggests that the shear cracks, illustrated in Figure 4-73, might begin at this point of time causing the differential displacement between two girders. The displacements monitored near the supports increased during the entire test as illustrated in Figure 4-74. This indicates no uplift occurred in this test. Shear force captured in the cross-frame at Section 5 was only 7 kips as shown in Figure 4-75. This indicates that the contribution of cross-frame under this loading configuration was also negligible and the applied load was transferred to the intact girder mainly through the deck. The reason that the specimen experienced a different failure mode in this test than in previous tests and the load was transferred to the intact girder mainly through deck is attributed to the loading configuration that was used in the test. In this test, the specimen was loaded with four points, instead of one, and the loads were placed much closer to the intact girder so that it facilitated transferring the load to the intact girder in both longitudinal and transverse directions.

Mid-Span - Displacement



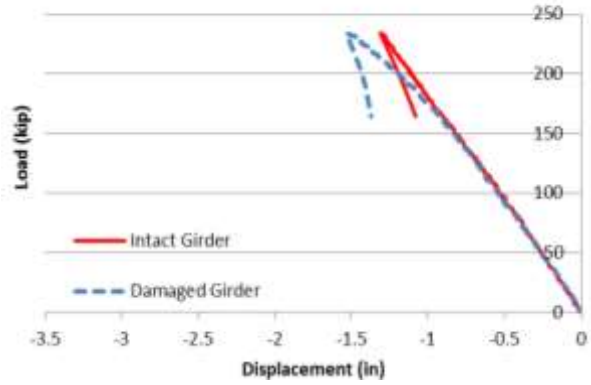
(a)

Section 5 - Displacement



(b)

Cantilever End- Displacement

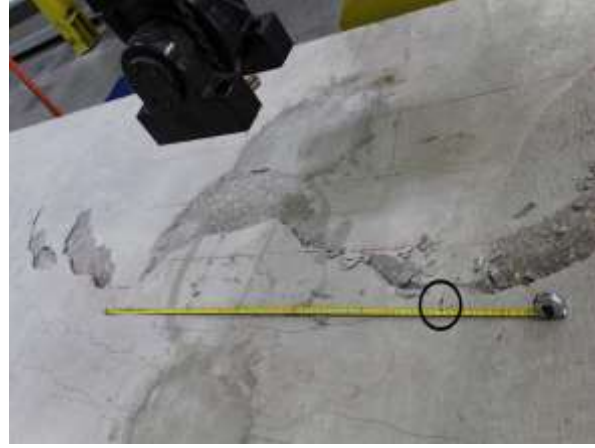


(c)

Figure 4-71 Test E: Load vs displacement curves at (a) mid-span, (b) Section 5 and (c) cantilever end.



(a)



(b)

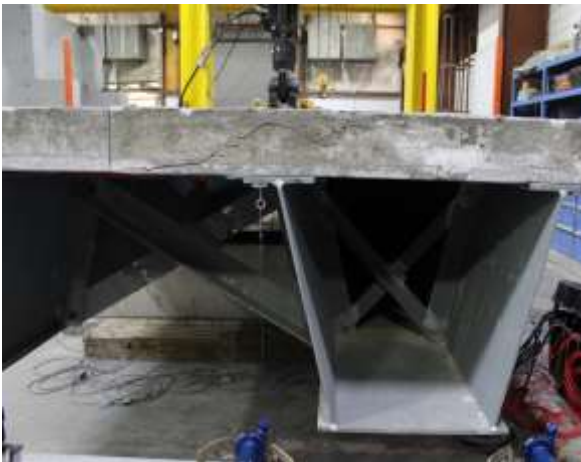


(c)



(d)

Figure 4-72 Damage in Test E.



(a)



(b)

Figure 4-73 Shear damage at ends in Test E.

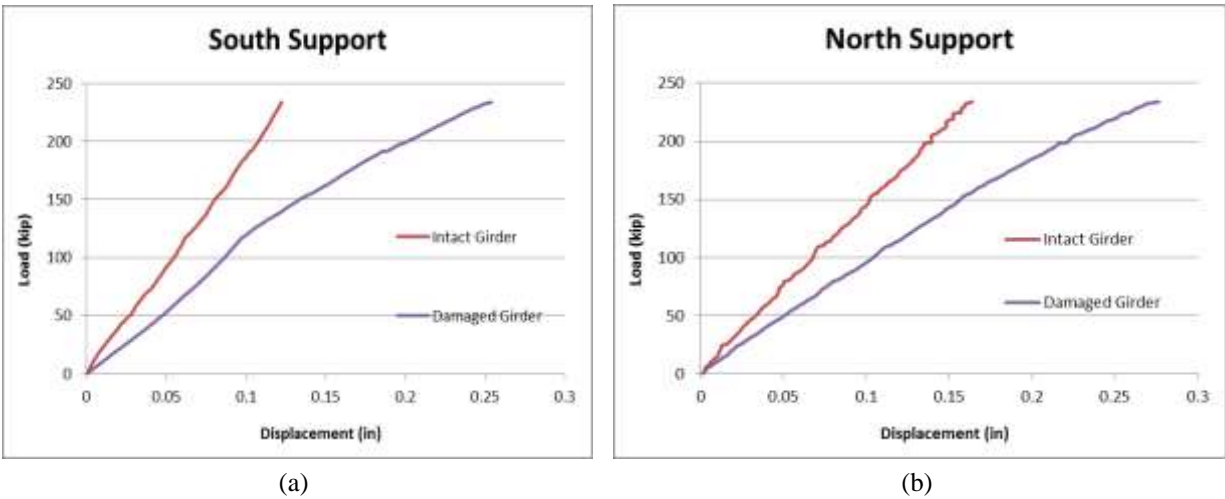


Figure 4-74 Near-support displacement.



Figure 4-75 Shear transferred through a cross-frame in Test E.

4.9.2 Local Behavior

The top flange longitudinal strains of the intact girder are plotted in Figure 4-76. These were average strains of both top flanges. The average longitudinal strains in the top flanges were $-240 \mu\epsilon$, $-270 \mu\epsilon$, $-250 \mu\epsilon$ and $-107 \mu\epsilon$ respectively for Sections 2, 3, 4, 5. Longitudinal strains, obtained in the bottom flange were also averaged and are illustrated in Figure 4-77. They were $1717 \mu\epsilon$, $1740 \mu\epsilon$, $1683 \mu\epsilon$ and $1846 \mu\epsilon$ for Sections 2, 3, 4, and 5, respectively. These longitudinal strains in the top flanges and bottom flange at Sections 2, 3, 4 and 5 indicated the load was distributed

more uniformly than it was in other tests with single concentrated load. These strains also indicate the bottom flange just yielded at these sections. At Section 5, the bottom flange experienced slightly larger strain than other sections. It could be due to the fact that, the loading pads were positioned closer to that section. The data from the intact girder and damaged girder is compared in Figure 4-78. The bottom flange of the damaged girder was in compression while it was in tension for the intact girder.

The longitudinal strains in the rebars are shown in Figure 4-79. Three gauges were damaged as results of previous tests. All gauges in the transverse rebars were damaged; therefore, not reported here. The crack gauges on the top and bottom of the deck also had similar trends as they was observed in Tests A and D. Gauge 2TTD1 had significantly high tensile strain, indicating the major crack occurred over the inside top flange of the intact girder. Gauges 2TTD2 and 2TBD1 were very small. This indicates the point of inflection was at center of the bridge cross-section. While the center of gravity of the load was right at the center of the damaged girder in Test A and D, in this test with truck-load configuration, the center of gravity of the load was shifted closer to the intact girder. This was the reason why the point of inflection was also shifted toward to the intact girder.

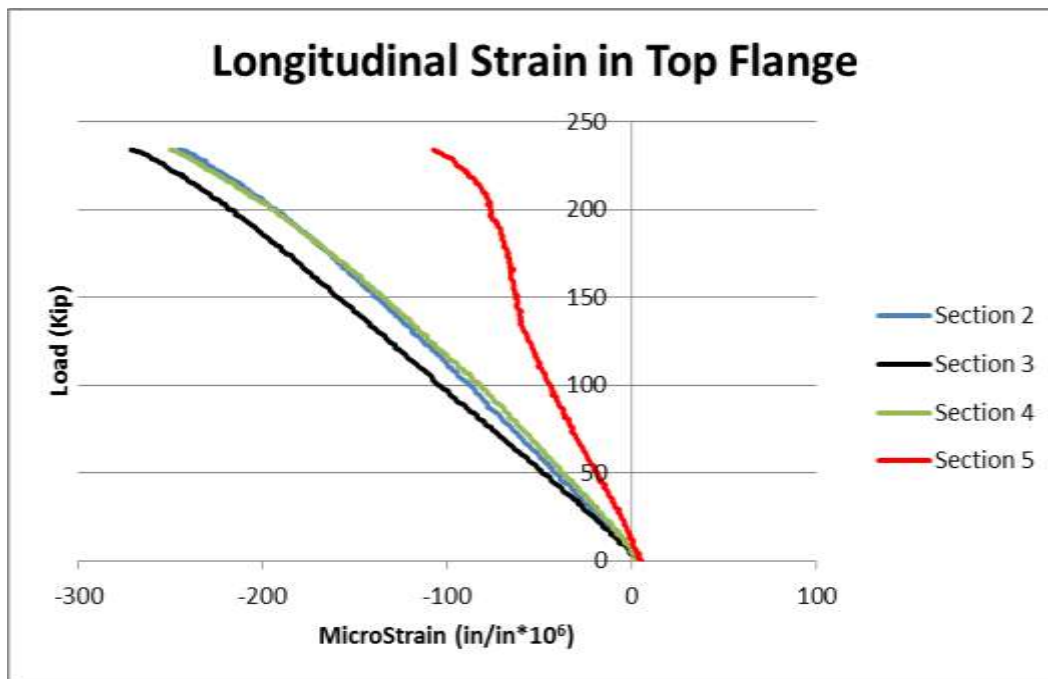


Figure 4-76 Average longitudinal strains at top flanges of the intact girder.

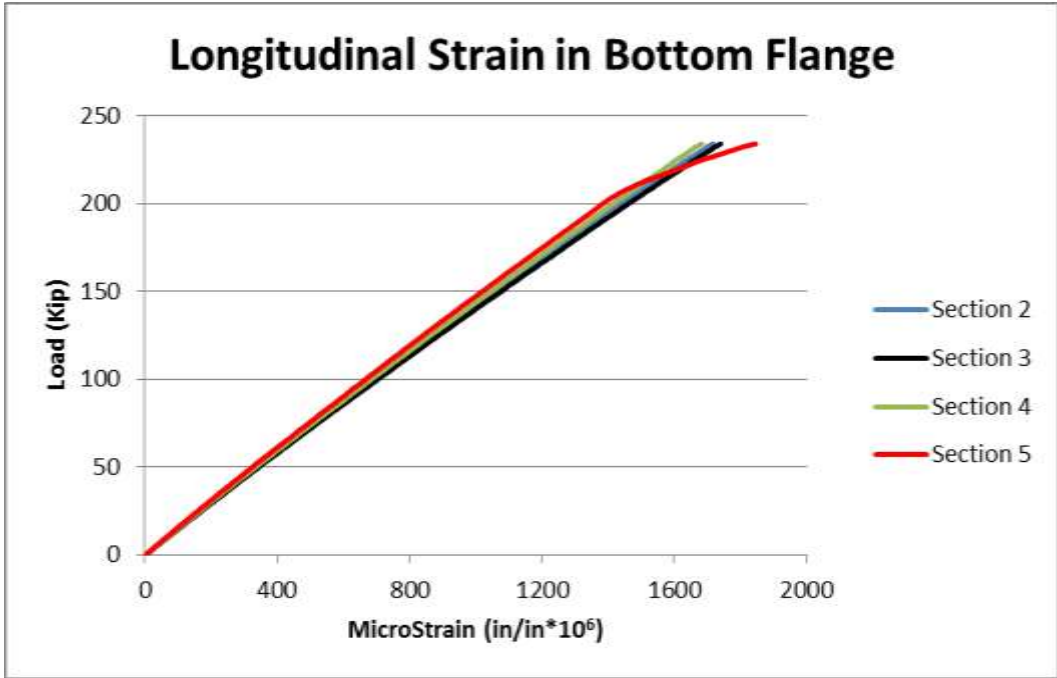


Figure 4-77 Longitudinal strains at the bottom flange of the intact girder.

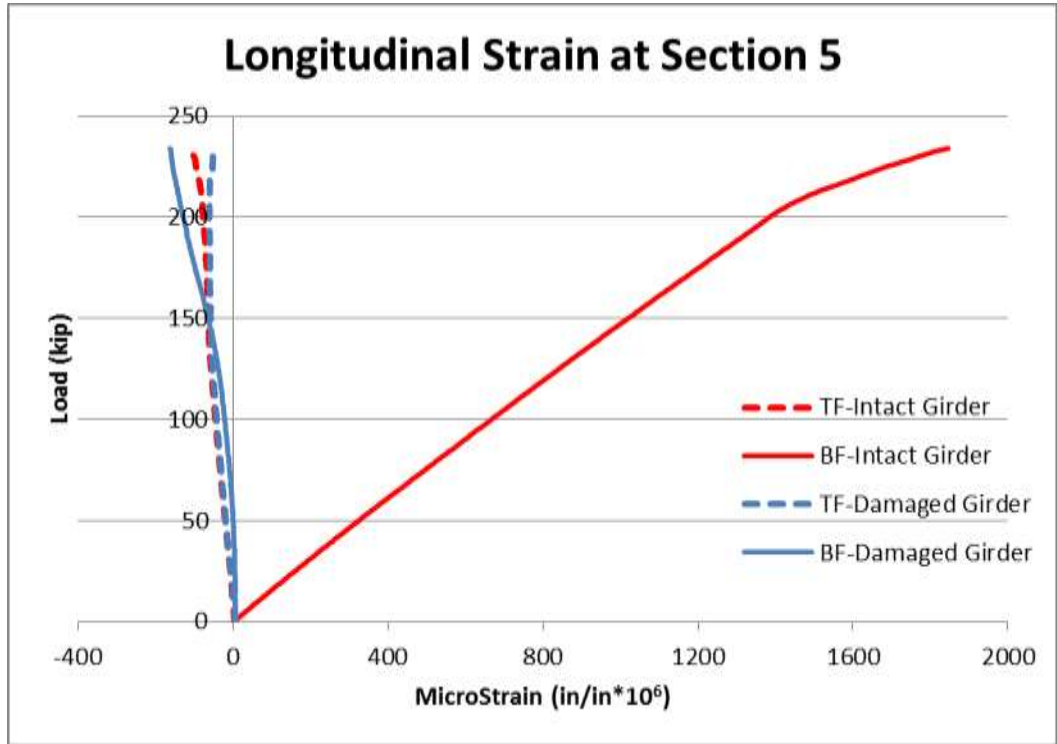


Figure 4-78 Comparison of longitudinal strains in the intact and damaged girders at Section 5.

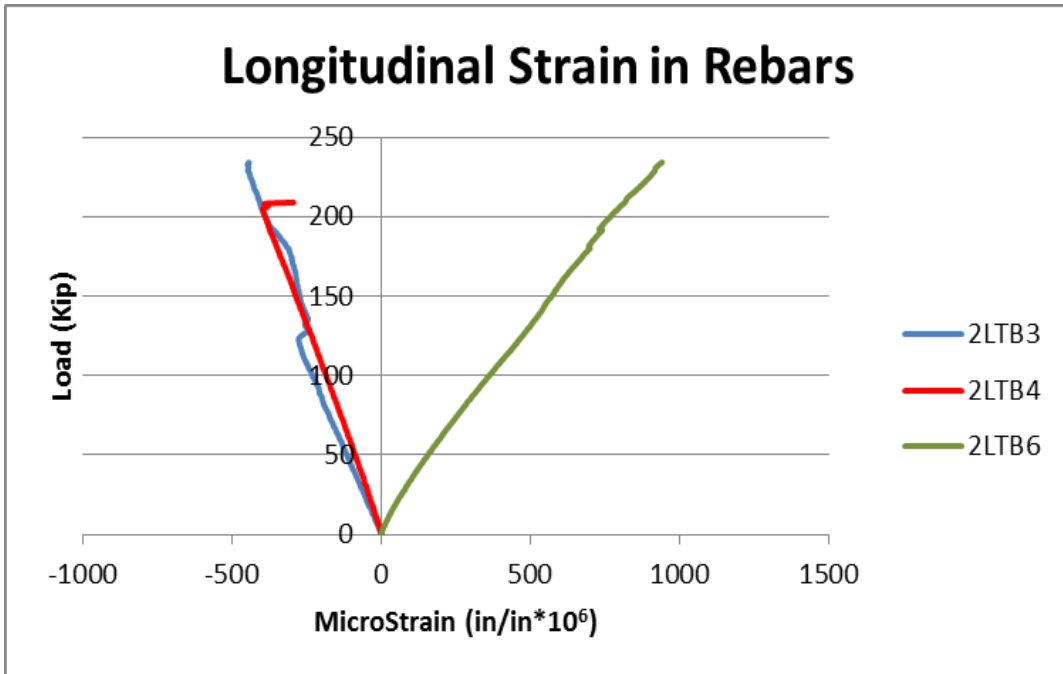


Figure 4-79 Longitudinal strain of rebars at mid-span.

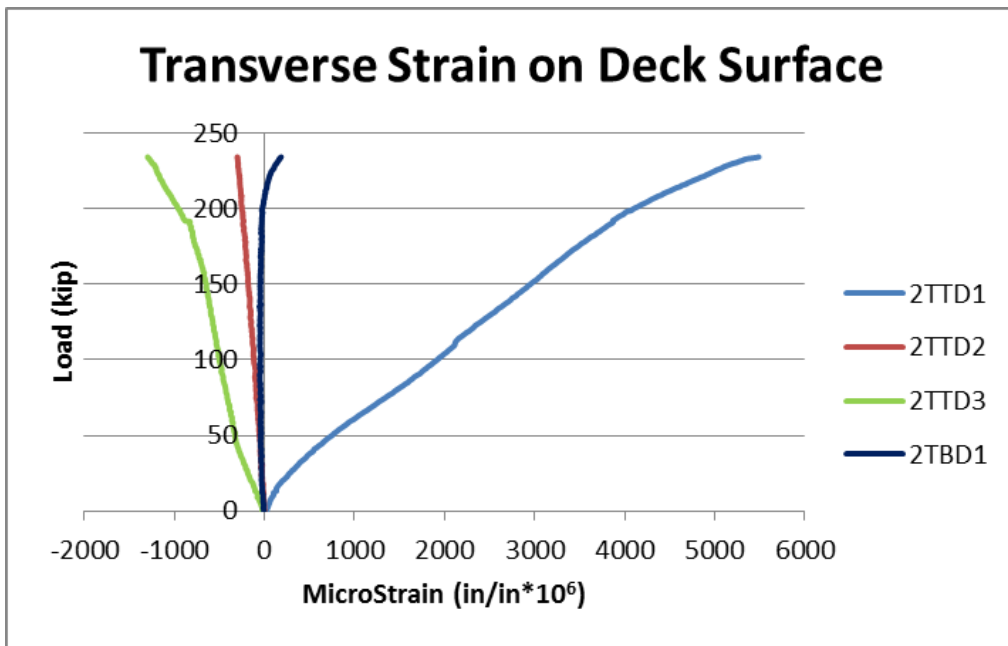


Figure 4-80 Transverse strain on the deck near mid-span.

Chapter 5 Finite Element Modeling — Procedures and Verification

ANSYS, a finite element modeling software package, was utilized in this research to predict and capture the behavior of the bridge specimen that couldn't be captured in the laboratory testing. Material nonlinearities were taken into account when modeling both steel and concrete behavior. The steel materials were assumed to have multi-linear isotropic hardening responses. The concrete was also modeled as a multi-linear isotropic hardening material but with cracking and crushing capabilities enabled. The cracking and crushing characteristics of concrete are usually neglected or simplified in other research because they generally increase the analysis time significantly and cause convergence issues. The contact areas between the steel girder or the deck and pads were also taken into consideration in modeling. The contacts between girder bottom flange and supporting bearing pads were modeled to capture any uplift incident while the contact between loading pads and concrete deck was also modeled to simulate any slippage occurrence. The details of the numerical model are described in the following sections.

5.1 FEM of Bridge Specimen

The steel box-girder bridge was modeled to represent the test specimen as realistically as possible. The steel plate girder was modeled using 4-node shell element, SHELL181 with six degrees of freedom at each node. This shell element is well suited for linear, larger rotation and large strain nonlinear application and will therefore reduce non-convergence issue. For the same reasons, the stiffeners and the interior diaphragm were also modeled by SHELL181 elements. However, the interior and exterior cross-frames and lateral bracings were modeled by using 2-node beam elements, BEAM188 with six degrees of freedom at each node. BEAM188 element is based on Timoshenko beam theory with shear deformation effects included. This element is suitable for analyzing slender structures such as cross-frames and bracings. The concrete deck and rail were modeled using 8-node solid elements, SOLID65 with three translational degrees of freedom at each node. This element is typically used for three-dimensional modeling of solids with or without reinforcing bars. Specially, this particular element has additional cracking and crushing capabilities making it a perfect element for concrete modeling. Figure 5-1 illustrates the complete model of the bridge in ANSYS.

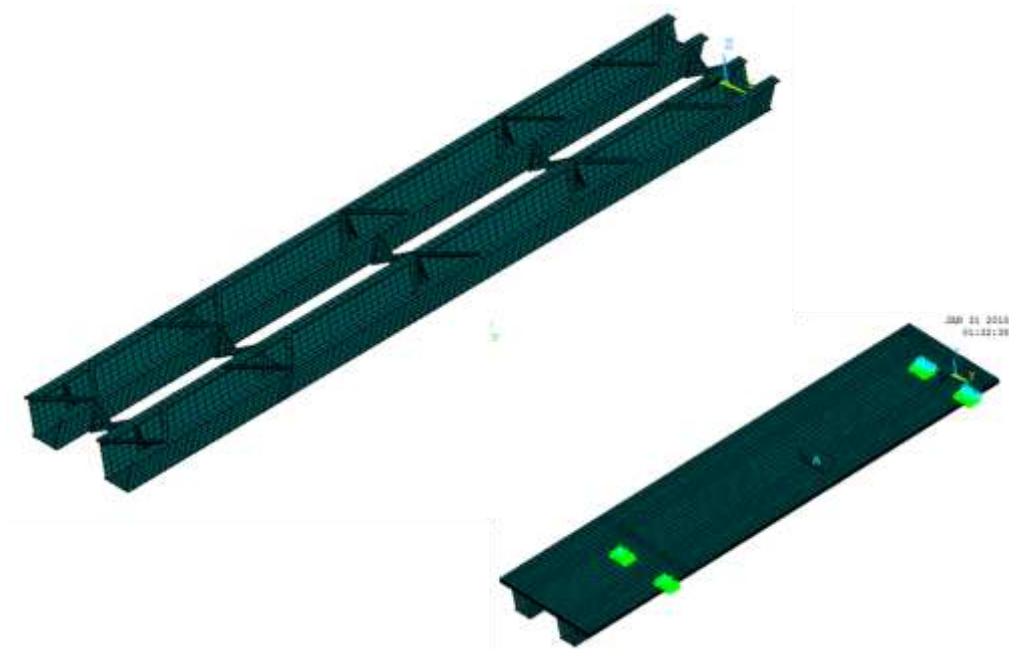


Figure 5-1 Finite element bridge model.

5.2 Fracture Damage and Connection Modeling

Basically, there are two approaches to simulate fracture/crack condition in the girder. The first and the simplest approach is removing or deleting the selected elements at fractured location. The second approach is separating the coincident nodes in the bottom flange and webs, at fracture location before merging all other coincident nodes. Although both approaches provided similar results in general, the later one was eventually chosen because it was the best representation of how the fracture was induced in the experiment.

The process to simulate the fractured condition is described as illustrated in Figure 5-2a-d. Note that two nodes plotted next to each other are coincident nodes with the same location. First, node at fractured location is selected as shown by red dot in Figure 5-2a. The selected node is then separated from its companion node by shifting to the right a small distance as illustrated in Figure 5-2b. Once separated, all other coincident nodes are merged together as shown in Figure 5-2c. In the last step, the separated node is brought back to the original location as shown in Figure 5-2d. The final simulation of full-web fracture condition is illustrated in Figure 5-3. It should be noted that two fractured segments still are connected together by sharing the same nodes at the top flanges.

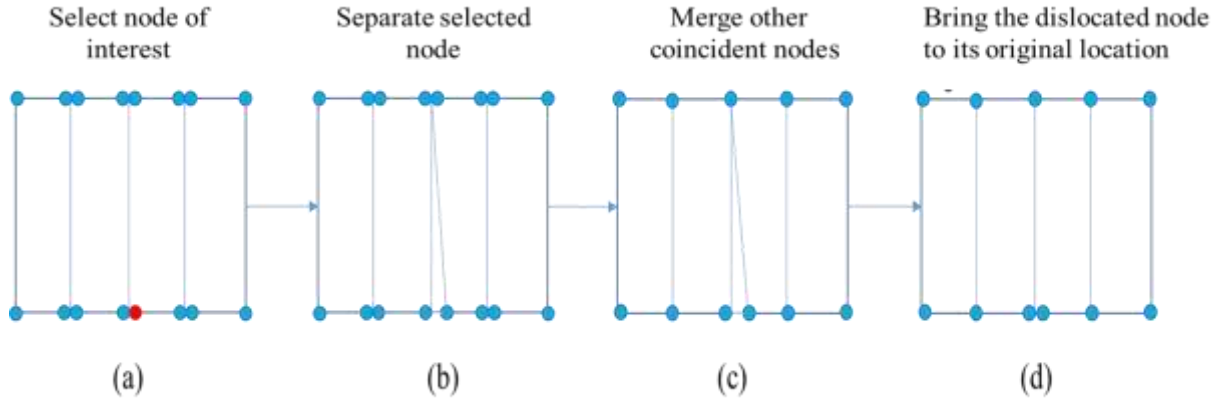


Figure 5-2 Process to simulate a fracture condition.

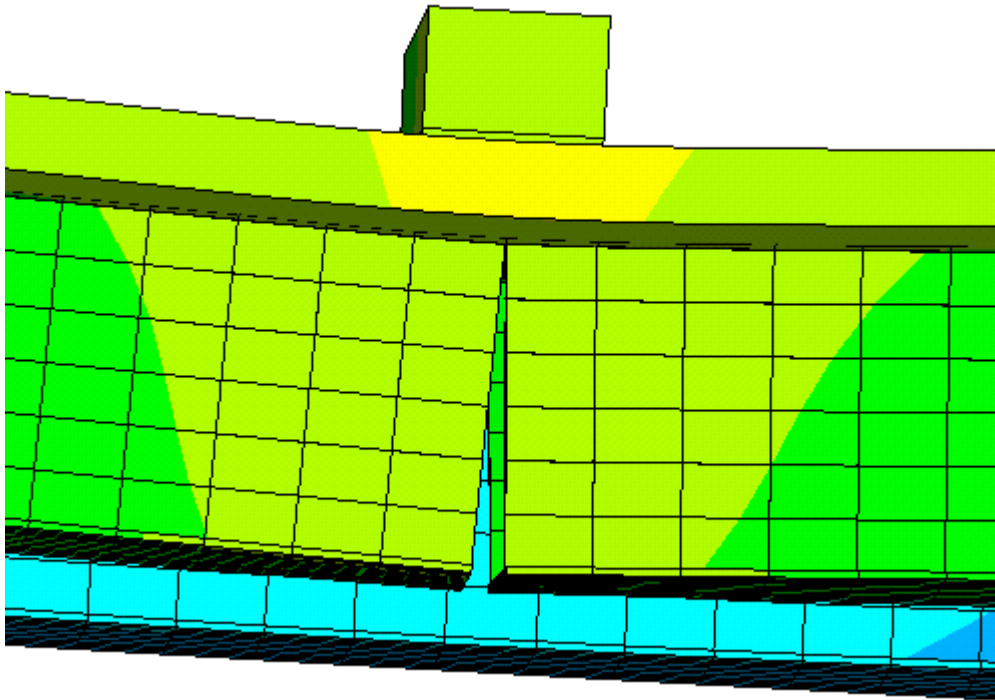


Figure 5-3 Finite element model with full-web fracture condition.

Since the subject of this study only focused on the inelastic behavior of the twin steel box-girder bridge under the worst-damage condition, which is full-web fracture condition, the need to simulate the crack propagation was eliminated.

5.3 Steel Behavior Modeling

The inelastic behaviors of steel plates, steel brace members, and steel reinforcement were modeled as a multi-linear inelastic model with isotropic hardening (Dassault Systemes, 2007). Von Mises plasticity was incorporated, which means the material was assumed to yield when the

equivalent stress exceeded the von Mises yield criterion, and the perfectly plastic behavior was assumed when the stress exceeded yield stress. This research used available data rather than testing to verify the steel material properties and behavior. The steel plates and bracing members used to construct this small-scaled specimen were A709 Grade 50 steel while the steel reinforcement bars were A706 Grade 60 reinforcement. The stress-strain curves of the steel plates and rebars shown in Figure 5-4 are approximations of typical stress-strain curves of A709 Grade 50 steel and A706 Grade 60 steel reinforcements under uniaxial tension load.

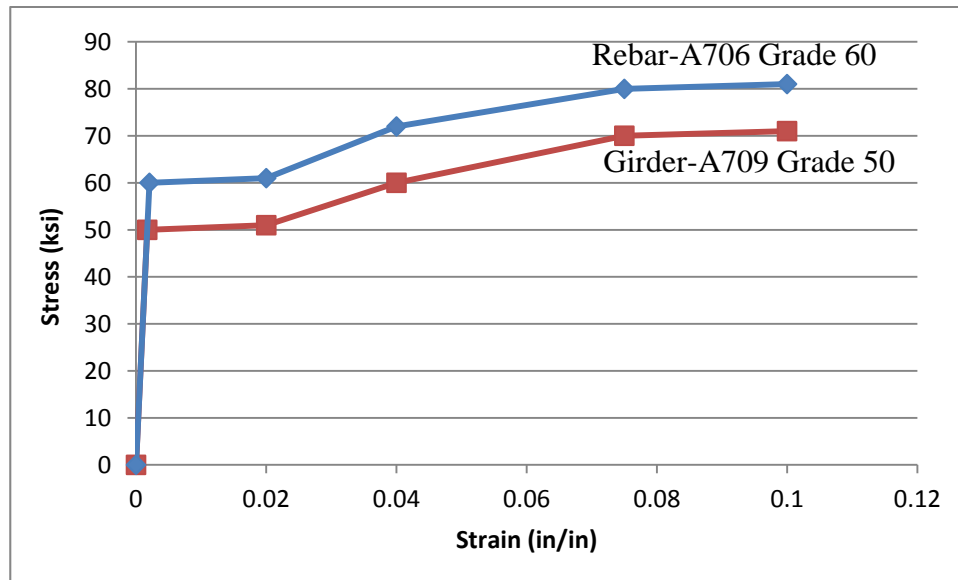


Figure 5-4 Stress-strain behavior of steel girder and rebars.

All the bolts that were used for connections in external and internal cross-frames are A325 Type 1 steel with 5/8-in. diameter. These bolts are supposed to have a minimum yield strength of 92 ksi and a minimum tensile strength of 120 ksi according to ASTM A325-14. To simplify the model, these bolt connections were modeled assuming full connections. This assumption was reasonable as the failure modes observed in the laboratory tests indicated that the failure of cross-frame connections did not significantly affect the capacity of the specimen.

5.4 Concrete Material Properties

FDOT uses Class II concrete mix with 28-day strength of 4,500 psi, 3-in. slump and ¾-in. maximum aggregate size. This is also the concrete that was used for the deck of bridge in this project. The concrete cylinder strengths were tested for the first specimen as well as the reconstructed specimen. The results of concrete compressive strengths for the first specimen are summarized in Table 5-1. The average of all concrete cylinder tests was 7,829 psi, and this is the final value used in respective simulated finite element models.

Table 5-1 Concrete Cylinder Strengths for First Specimen

Specimen ID	Date Poured	Specimen Age (days)	Avg. Diameter (in)	Avg. Length (in)	Weight (lb)	Ultimate Load (lb)	Strength (psi)
C1-1	7/29/13	120	5 ¹⁵ / ₁₆	11 ⁷ / ₈	27.44	218560	7893
C1-2	7/29/13	120	5 ¹⁵ / ₁₆	11 ⁷ / ₈	27.50	203850	7361
C1-3	7/29/13	120	5 ¹⁵ / ₁₆	11 ⁷ / ₈	27.32	216480	7818
C1-4	7/29/13	120	5 ¹⁵ / ₁₆	11 ¹³ / ₁₆	27.32	221220	7989
C1-5	7/29/13	150	5 ¹⁵ / ₁₆	11 ⁵ / ₈	26.74	226110	7997
C1-6	7/29/13	150	5 ¹⁵ / ₁₆	11 ¹¹ / ₁₆	26.96	217050	7677
C1-7	7/29/13	150	5 ¹⁵ / ₁₆	11 ⁹ / ₁₆	26.92	228090	8067
Average							7829

The reconstructed specimen used the same concrete mix as mentioned above. The concrete cylinder strengths at test day are summarized below in Table 5-2. Please note that in the first four cylinder tests, the average diameter and length of the cylinders were assumed to be 6” and 12” respectively, because the measurements were not taken that day. The average concrete compressive strength for the reconstructed specimen was approximately 7,135 psi.

Table 5-2 Concrete Cylinder Strengths for Reconstructed Specimen

Specimen ID	Date Poured	Specimen Age (days)	Avg. Diameter (in)	Avg. Length (in)	Weight (lb)	Ultimate Load (lb)	Strength (psi)
C2-1	12/22/14	49	6	12	28.56	207530	7340
C2-2	12/22/14	49	6	12	28.54	199120	7043
C2-3	12/22/14	49	6	12	28.58	201270	7118
C2-4	12/22/14	49	6	12	28.54	199220	7046
C2-5	12/22/14	52	5 ¹⁵ / ₁₆	11 ⁵ / ₈	27.04	197780	7143
C2-6	12/22/14	52	5 ⁷ / ₈	11 ¹¹ / ₁₆	27.26	193030	7121
Average							7135

A tensile splitting test were also performed on two concrete cylinders. The cylinders were loaded at a rate of 106 psi/min and the results are shown below in Table 5-3. The average tensile strength of concrete was found to be 545 psi. Although this tensile strength might be slightly different for the first specimen, this value was used for all finite element models.

Table 5-3 Concrete Tensile Strengths for Reconstructed Specimen

Specimen ID	Date Poured	Specimen Age (days)	Avg. Diameter (in)	Avg. Length (in)	Weight (lb)	Ultimate Load (lb)	Strength (psi)
T2-1	12/22/14	49	5 ¹⁵ / ₁₆	11 ¹⁵ / ₁₆	27.04	58885	529
T2-2	12/22/14	49	5 ¹⁵ / ₁₆	11 ¹⁵ / ₁₆	27.08	62340	560
Average							545

In this study, concrete was modeled using a multi-linear isotropic hardening material. Concrete compressive behavior was constructed using EQ 5-1 as suggested by Hognestad (1951). With the ultimate strain ($\epsilon_0=0.003$) and concrete compressive strength that was found earlier from concrete cylinder tests, the stress-strain curve of concrete under uniaxial compressive force is graphically illustrated in Figure 5-5. On the tension side of the stress-strain curve, the concrete is assumed to

have the same initial stiffness as it has initially for the compression strength under uniaxial force as mentioned in finite element software package such as ANSYS or ABAQUS.

$$f_c = f'_c * \left(2 * \frac{\varepsilon}{\varepsilon_0} - \left(\frac{\varepsilon}{\varepsilon_0} \right)^2 \right) \quad \text{EQ 5-1}$$

where f_c = concrete compressive stress at given strain (ksi)

f'_c = concrete compressive strength (ksi)

ε_0 = ultimate strain (in/in)

ε = strain (in/in)

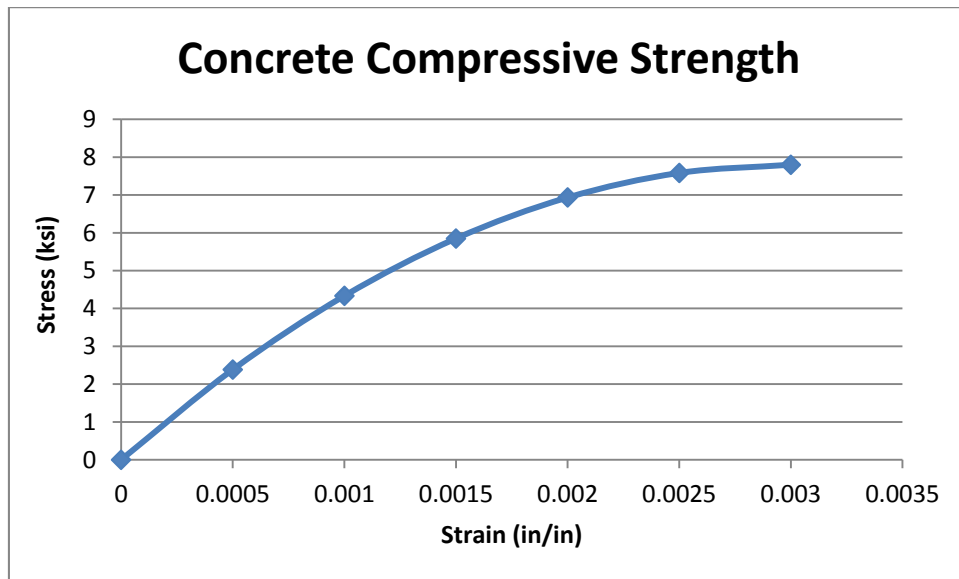


Figure 5-5 Stress-strain curve of concrete in compression.

5.5 Concrete and Reinforcement Behavior Modeling

Concrete was modeled in ANSYS by SOLID65, a three dimensional eight-node isotropic solid element as shown in Figure 5-6. The SOLID65 element is capable of plastic deformation, creep, cracking in three orthogonal directions, and crushing. SOLID65 has one solid element and up to three rebar materials. Rebar specifications are input as real constants, including material properties, volume ratio with respect to the solid element volume, and the orientations as denoted by θ and Φ in Figure 5-6. The material properties of the steel reinforcement bars are discussed in the section above. The steel bars are capable of tension, compression but no shear. The reinforcement bars are modeled to be “smeared” throughout the elements. Figure 5-7 shows the smeared steel reinforcement inside the SOLID65 elements. In this specimen, the concrete is reinforced in both longitudinal and transverse directions.

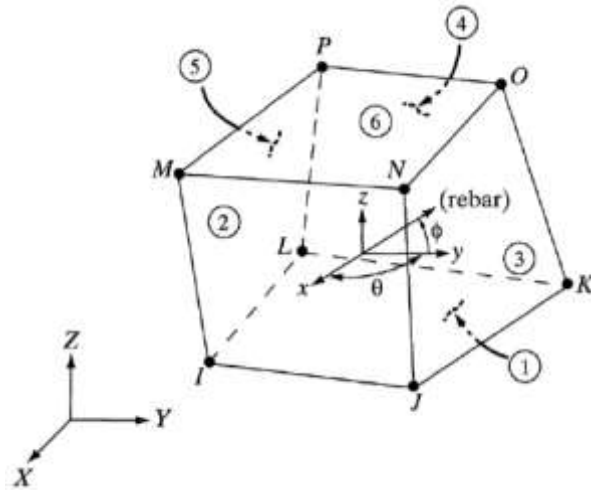


Figure 5-6 Solid65 concrete element in ANSYS.

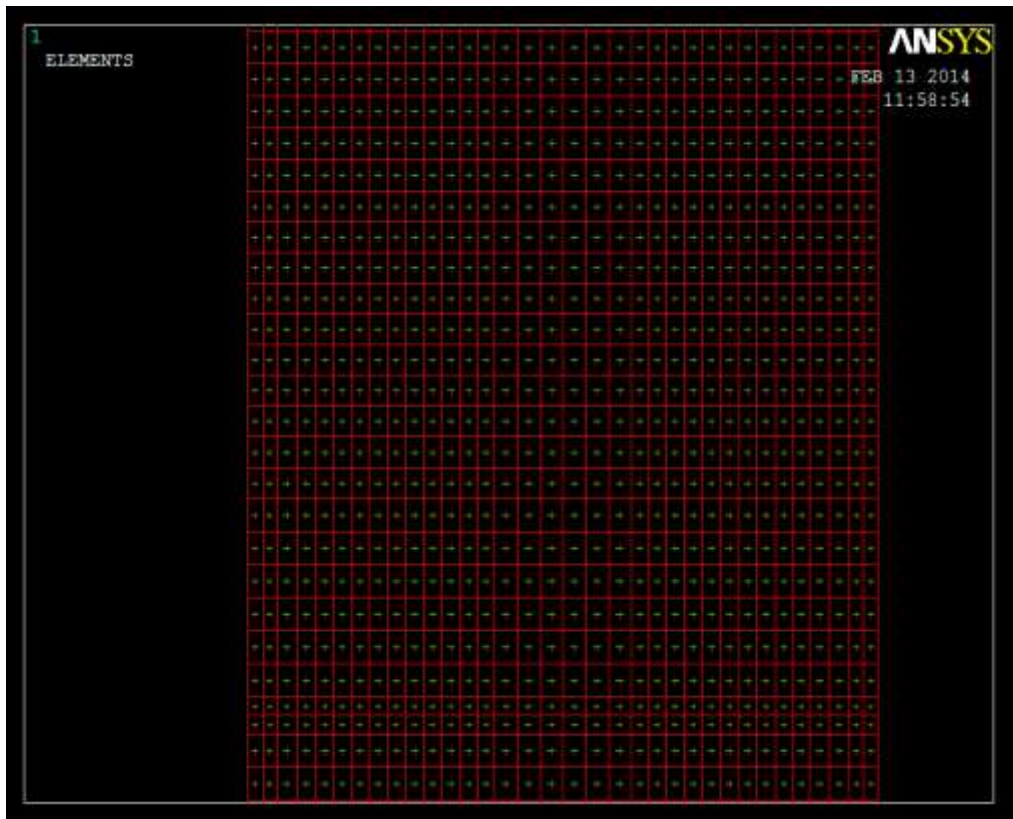


Figure 5-7 Smeared reinforcement bars.

Concrete material data are input through nine constants, which are summarized in Table 5-4, for SOLID65 elements. The first two constants are shear transfer coefficients for open and closed cracks. These shear transfer coefficients can vary from zero to one. Zero represents a smooth crack with no shear transfer and one represents a rough crack with full shear transfer. Previous studies have shown that if the shear transfer coefficient for an open crack is below 0.2 (Kachlakev et al.,

2001), the model might face convergence issues. In this study, only the first four constants are input while the last five constants are left at their default values. In this study, the shear transfer coefficients are assumed to be 0.35 for an open crack and 1.0 for a closed crack. The uniaxial tensile cracking stress limit, which corresponds to the constant number 3, is assumed to be 0.55 ksi based on the results of cylinder splitting tests. The uniaxial crushing stress limit is assumed to be the same with the average concrete cylinder compressive strength that were found from concrete cylinder tests.

Table 5-4 Input Parameters for Properties of Concrete Materials

Constant	Meaning
1	Shear transfer coefficients for an open crack.
2	Shear transfer coefficients for a closed crack.
3	Uniaxial tensile cracking stress.
4	Uniaxial crushing stress (positive).
5	Biaxial crushing stress (positive).
6	Ambient hydrostatic stress state for use with constants 7 and 8.
7	Biaxial crushing stress (positive) under the ambient hydrostatic stress state (constant 6).
8	Uniaxial crushing stress (positive) under the ambient hydrostatic stress state (constant 6).
9	Stiffness multiplier for cracked tensile condition, used if KEYOPT(7) = 1 (defaults to 0.6).

The Willam and Warnke (1975) yield criterion was used to define a failure surface of concrete material. The biaxial and triaxial failure surfaces of concrete material are illustrated in Figure 5-8. In this model, the concrete element is defined as cracked when a principal stress exceeds the ultimate tensile strength. The cracking plane is perpendicular to the direction of principal stress which tensile stress exceeded. The crack can occur in all three principal directions. If the material at an integration point fails in uniaxial, biaxial, or tri-axial compression, the material is assumed to crush at that point. This means the concrete is assumed to be crushed when one or all principal stresses lie outside the failure surface. When crushing occurs, strength of concrete is assumed to

degrade to an extent such that the contribution to the stiffness of an element at the integration point in question can be ignored.

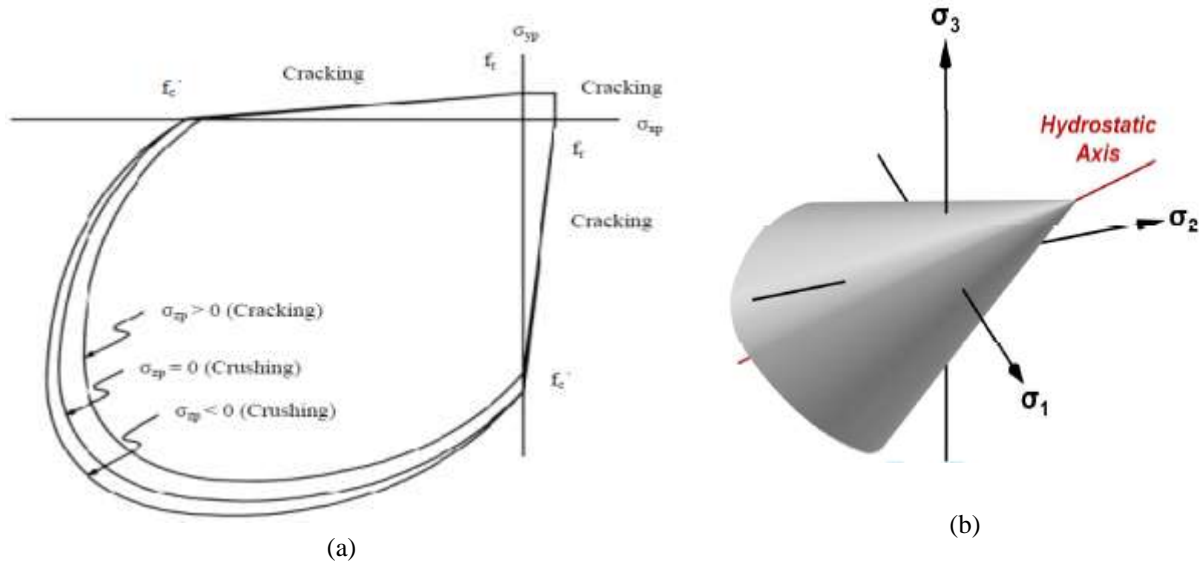


Figure 5-8 Failure surfaces of concrete under (a) biaxial and (b) triaxial loading states (Willam and Warnke, 1975).

This concrete model is known to be sensitive to mesh density, especially at contact surfaces (Dassault Systemes, 2007). Material properties and the element size through thickness of the deck were also found to affect the convergence of the simulated models.

5.6 Bearing Pads Modeling

The bearing pads that were used in this experiment were steel reinforced elastomeric pads with a durometer hardness range of 50. The dimension of the bearing pads was 1 in. x 24 in. x 2 in. Based on the provided durometer hardness, the shear modulus of the pads, at room temperature, can range anywhere from 85 psi to 110 psi, according to FDOT Structure Specifications for Road and Bridge Construction, or 95 psi to 130 psi according to AASHTO Bridge Design Specification. In this study, the shear modulus was assumed to be 100 psi. According to Lee (1994), the bulk modulus for 50 Shore hardness elastomeric bearings is assumed to be 2,060 MPa, which is equivalent to 290 ksi. The typical Young's modulus for 50 Shore hardness is approximately 320 psi. Young's modulus of elastomeric bearings for different Shore hardness was provided by Podolny and Muller (1982). The typical stress-strain curve for steel reinforced bearing pads based on the hardness and the shape factor is shown in Figure 5-9.

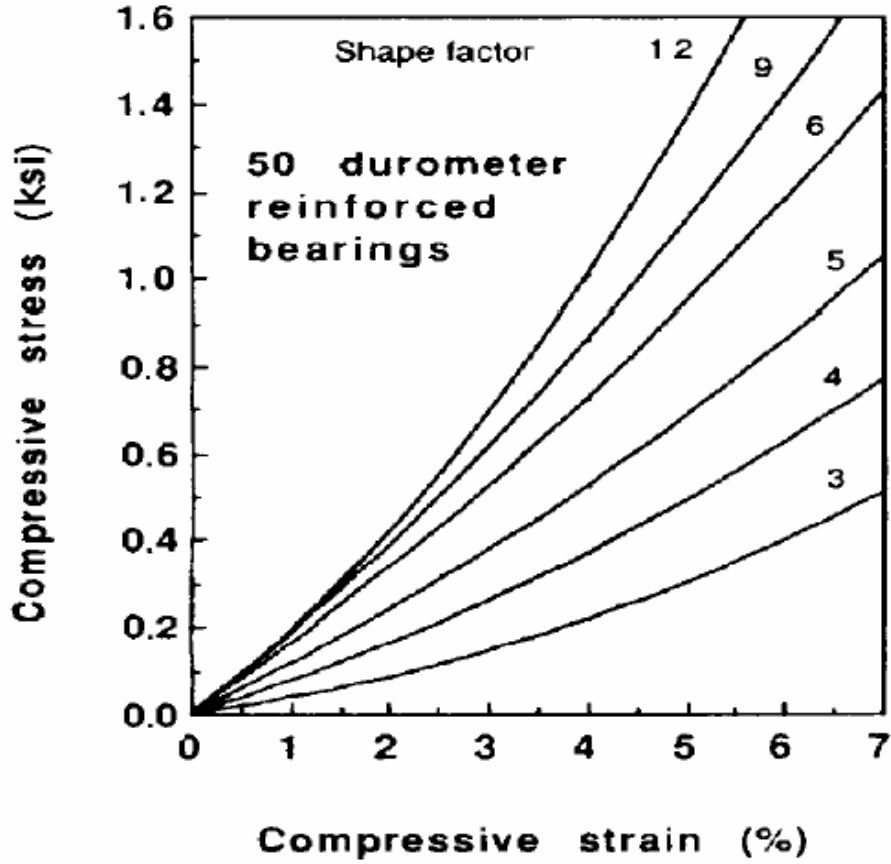


Figure 5-9 Typical stress-strain curve for steel-reinforced bearings (AASHTO-C14.7.6.3.3-1).

These bearing pads were simulated using SOLID185 elements. The material nonlinearity of the pads was modeled using three-parameter Mooney-Rivlin hyper-elastic material model. The input data for Mooney-Rivlin model requires three parameters, which are C_{10} , C_{01} and C_{11} . These three parameters are material constants characterizing the deviatoric deformation of the material. These constants are usually determined by curve-fitting the experimental data. It was suggested to use 0.044, 0.011 for the first two parameters for 50 shore hardness bearings (Altidis and Adams, 2005). The third parameter C_{11} was determined to be 100 based on parametric studies. This parameter will take into account the fact that as compression is increased, the effective shear modulus also increases. Figure 5-10 compares between mid-span displacements, before and after the bearing pads were modeled, and the actual displacements in experimental testing. This illustrates that the bearing pad deflection contributed a significant portion to the total displacement of the bridge.

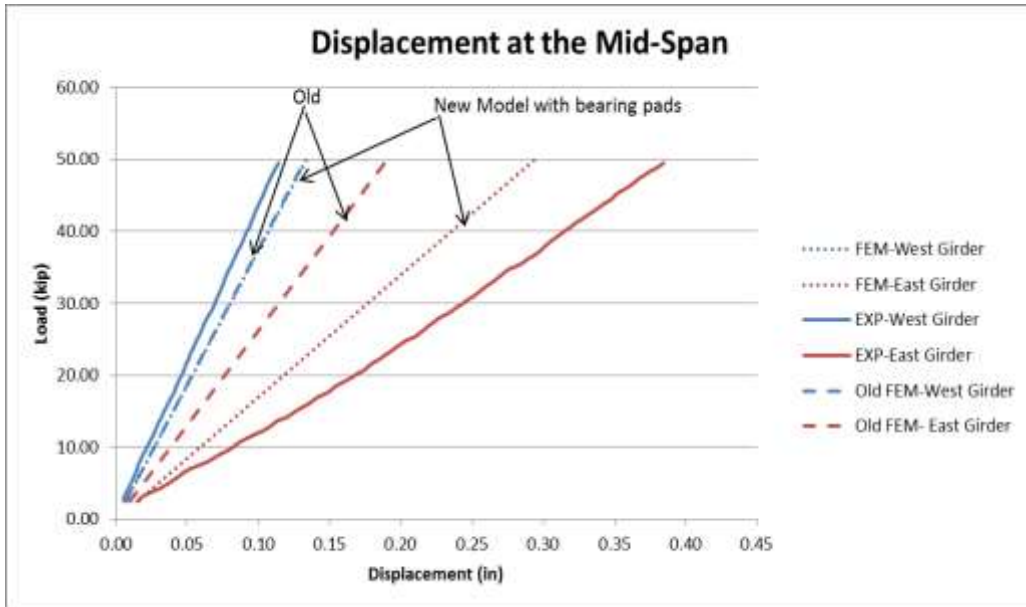


Figure 5-10 Mid-span displacement before and after modeling the bearing pads.

In addition to the bearing pad models, the contact surfaces between the bearing pads and bottom flange of the girders, or the between the loading pads and concrete deck were also simulated to capture any occurrence of uplift or slippage as illustrated in Figure 5-11. The contact surface was modeled using a combination of TARGE170 element and CONTA173 element. TARGE170 element is used to model a 3-D target surface where the contact occurs while CONTA173 is surface-to-surface contact element which is used to model contact and sliding between target surface and a deformable body. The target surface is paired with its associated contact surface via a shared real constant set. As illustrated in the figure, the target area could be larger than the contact area. It should be noted that modeling contact surface might make the FE model more prone to non-convergence issues. The results from this study suggest that refining mesh density and reducing time step are possible solutions for this problem.

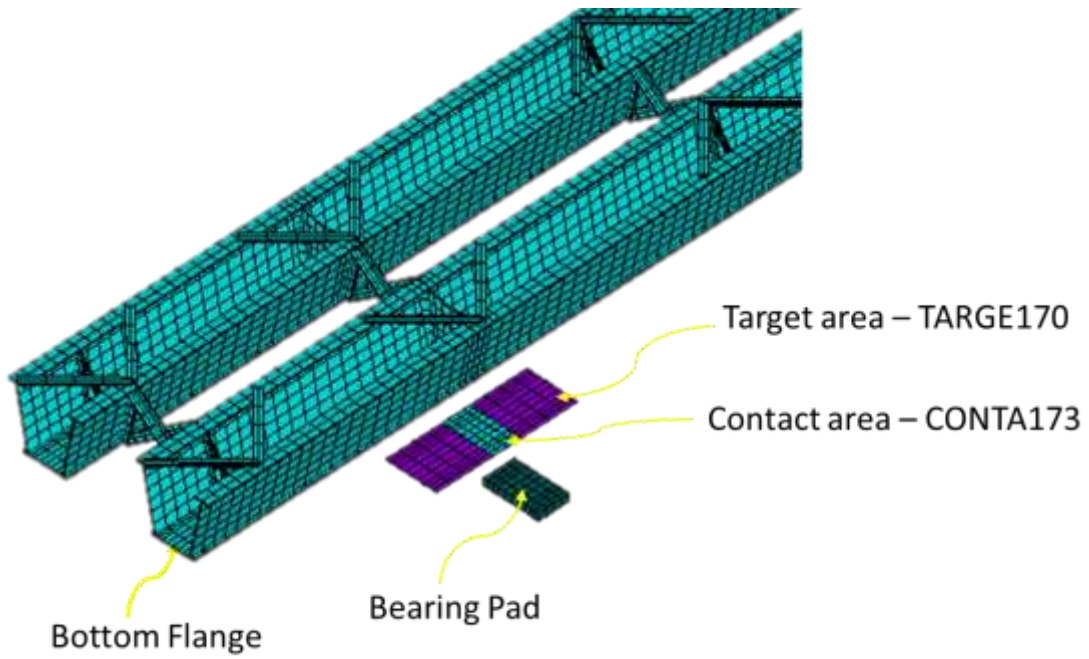


Figure 5-11 Contact surface between the bearing pad and bottom flange of girder.

Chapter 6 Validating FE Models with Experimental Data

For verification purposes, the finite element analysis results are compared to the experimental data on selected tests. The verifications will be made in both elastic and inelastic ranges. Due to a high number of elastic tests carried out, only a few tests are selected for the comparison purposes for each damage condition. The experiment data used for the comparison purposes in Section 6.1, 6.2 and 6.3 was extracted from the third ramp in the loading history. Although data from third loading cycle is expected to present the most accurate behavior of the specimen, the specimen might not be completely unloaded at the beginning of the third loading cycle as illustrated in Figure 3-23. That is the reason, the experimental data might not start from zero in some comparison plots.

6.1 Undamaged Bridge Specimen

For the undamaged specimen, the comparison between experimental data and finite element analysis results were made for Test 1, 2, and 3 and presented in the following sections. The comparison includes the longitudinal strain and displacement, at the mid-span section.

6.1.1 Test 1 - No Rail, No Continuity, Symmetric Loading (NNS)

The first test had NNS characteristics. Figure 6-1 provides a schematic description of the test.

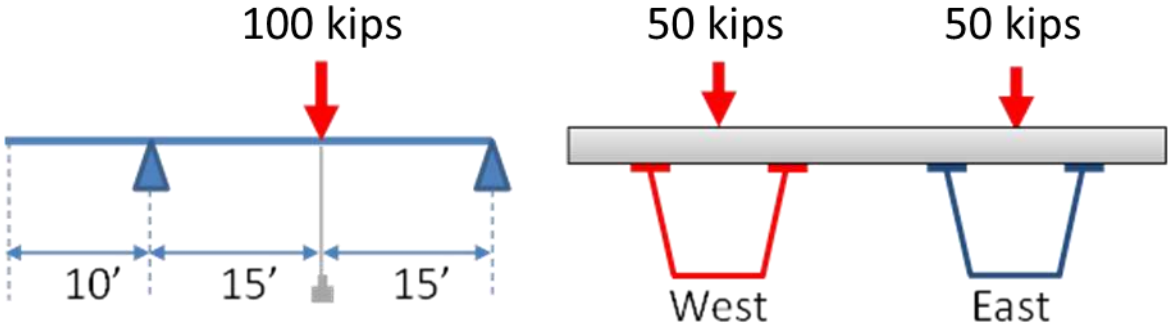


Figure 6-1 Schematic description of Test 1.

The vertical displacements at the center of the bottom flange of both girders at the mid-span section are compared with those obtained from FEM in Figure 6-2. The longitudinal strains in the bottom flange and top flange at the mid-span section are compared in Figure 6-3 and Figure 6-4, respectively. In Figure 6-4, only the exterior top flange of EG and the interior top flange of WG were compared, and the same comparison was made in subsequent tests.

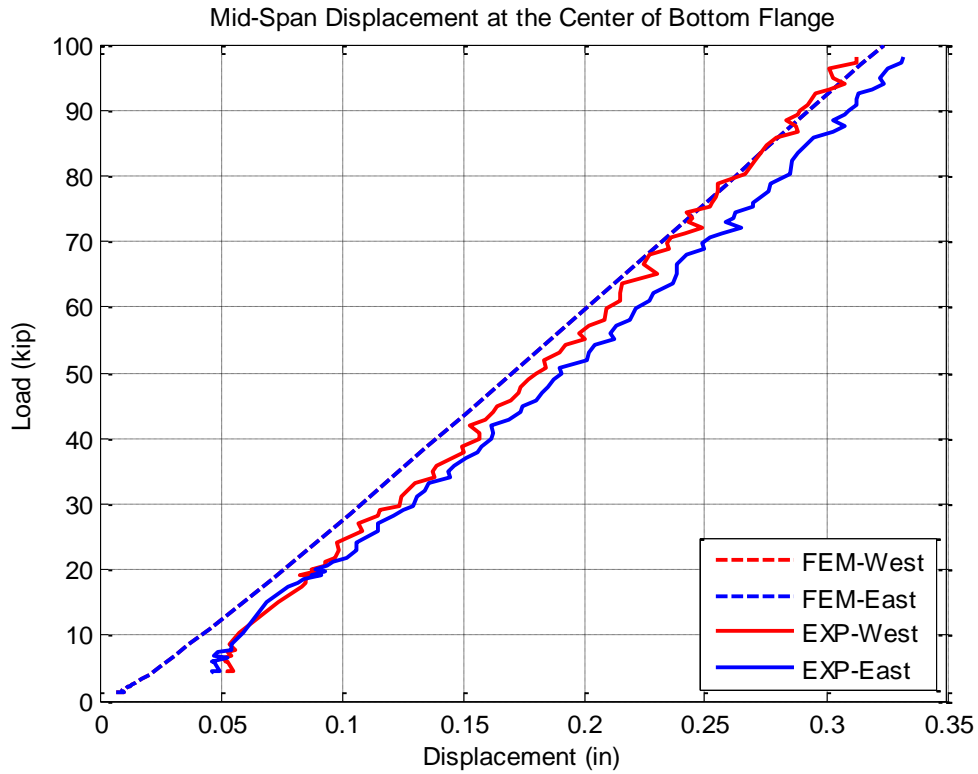


Figure 6-2 Comparison of vertical displacement at the bottom flange of each girder in Test 1.

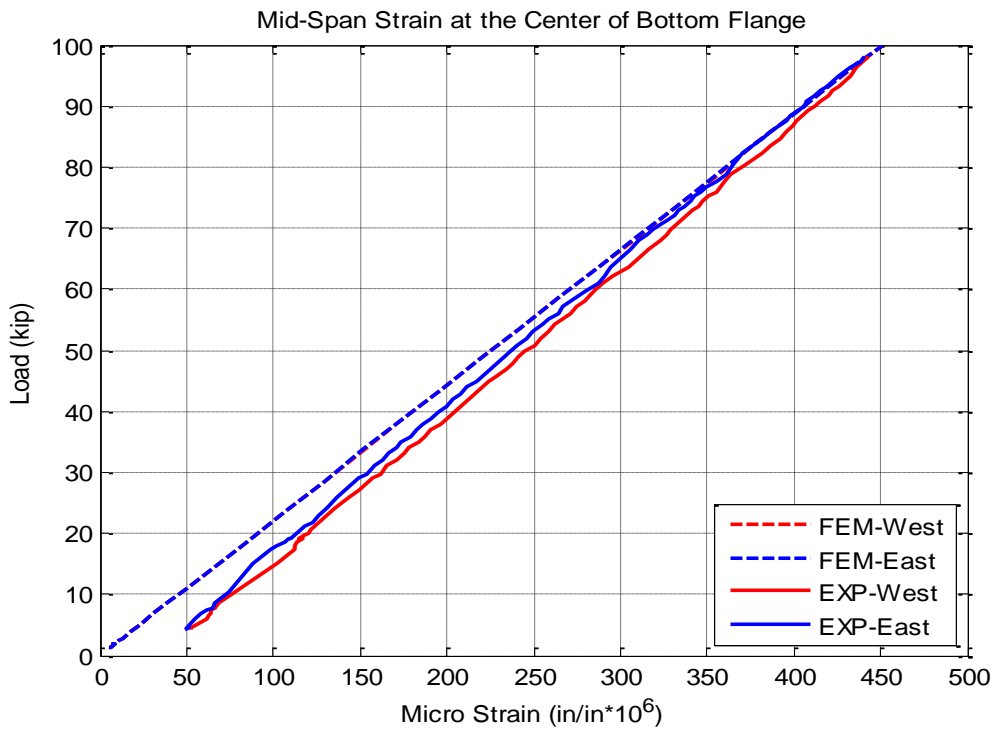


Figure 6-3 Comparison of longitudinal strain at the bottom flange of each girder in Test 1.

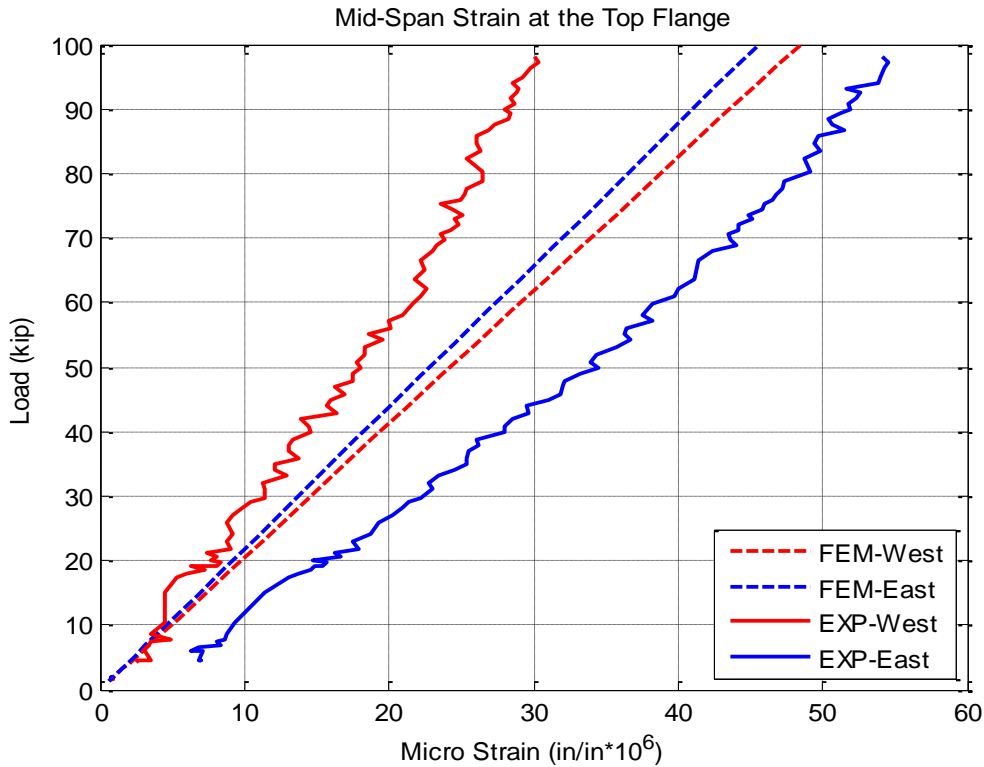


Figure 6-4 Comparison of longitudinal strain at the top flange of each girder in Test 1.

6.1.2 Test 2 - No Rail, No Continuity, Unsymmetrical Loading (NNU)

Test 2 NNU was carried out without railing and continuity installed. Schematic drawing of the test is shown in Figure 6-5.

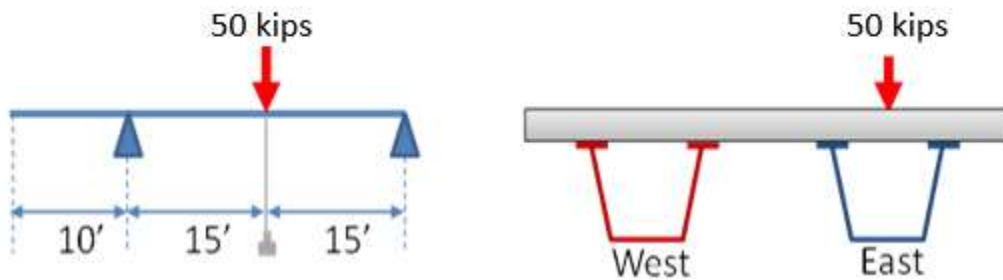


Figure 6-5 Schematic description of Test 2.

Figure 6-6 compares the vertical displacement measured at the center of bottom flange of each girder at mid-span to the one obtained from results of FEA. Figure 6-7 provides a comparison of

measured and calculated longitudinal strains at the center of the bottom flange at the mid-span section, while Figure 6-8 compares measured and calculated longitudinal strains in the top flanges.

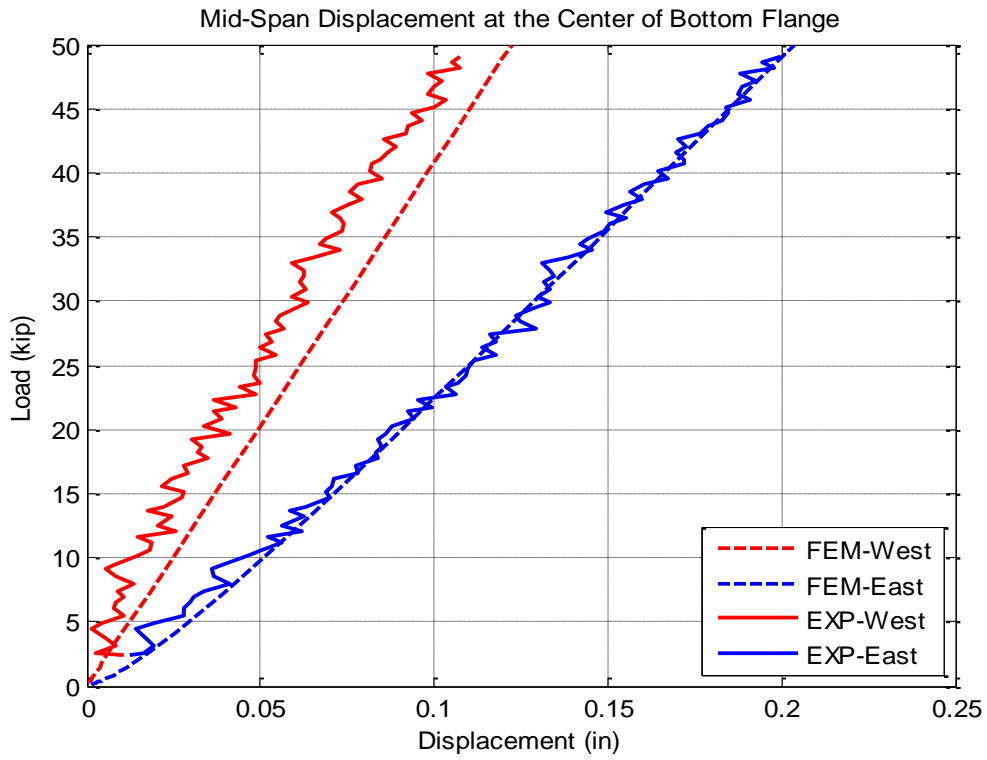


Figure 6-6 Comparison of vertical displacement at the bottom flange of each girder in Test 2.

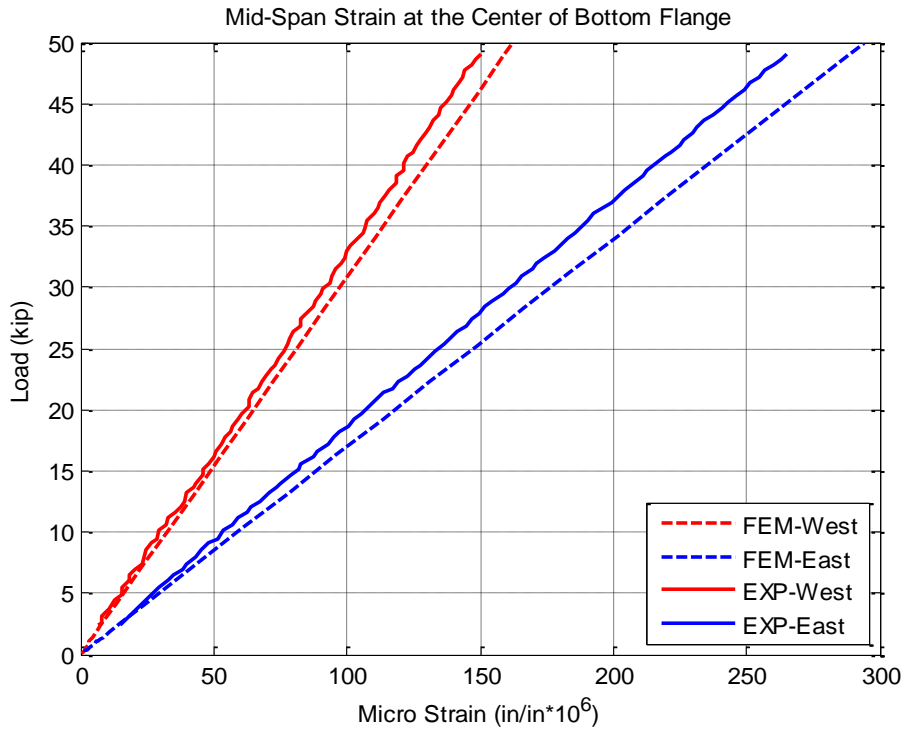


Figure 6-7 Comparison of longitudinal strain at the bottom flange of each girder in Test 2.

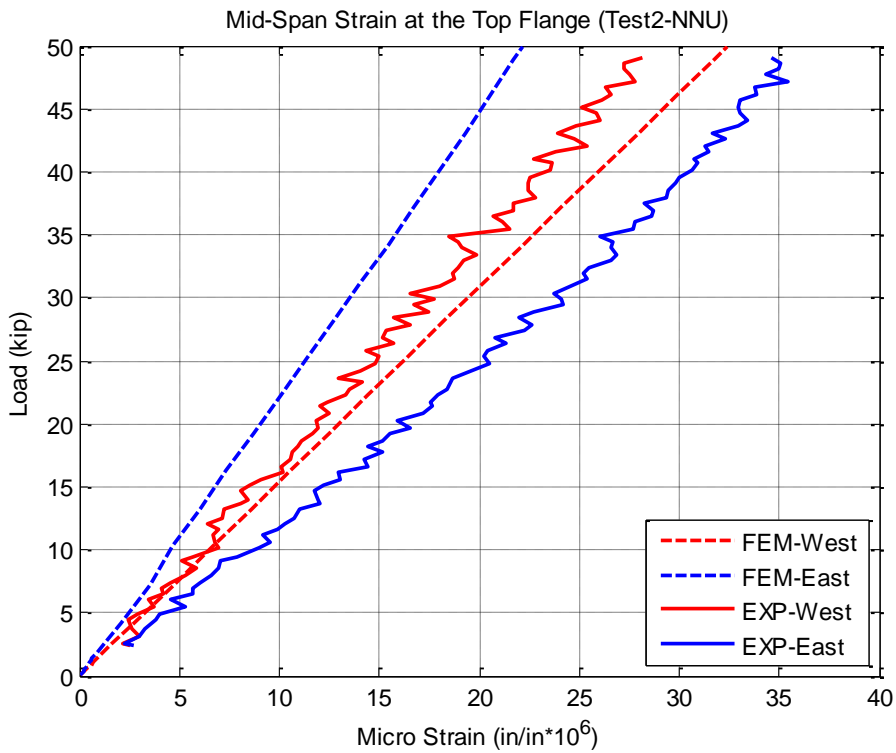


Figure 6-8 Comparison of longitudinal strain at the top flange of each girder in Test 2.

6.1.3 Test 3 - No Rail, with Continuity, Unsymmetrical Loading (NYU)

In Test 3 NYU, the cantilever end was restrained from moving up vertically to provide continuity effect. Its schematic description is shown in Figure 6-9.

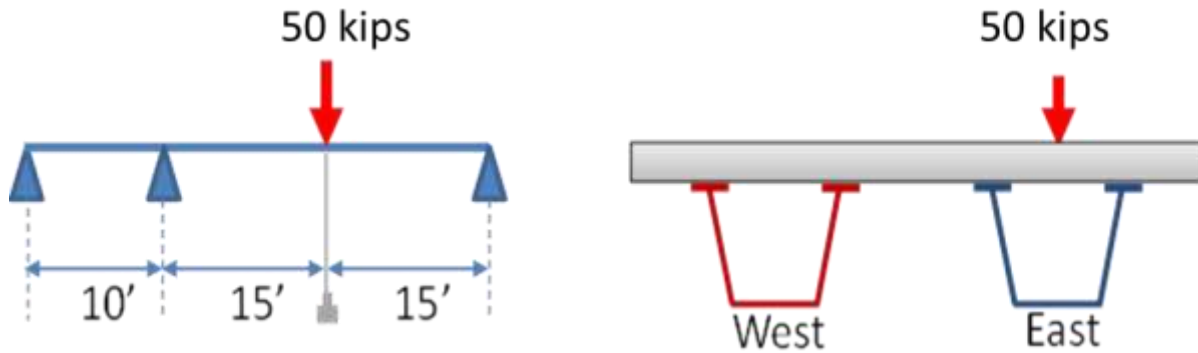


Figure 6-9 Schematic description of Test 3.

The vertical displacements of the center of the bottom flange of both girders at the mid-span obtained from the experiment and FEA are compared in Figure 6-10. Similarly, the longitudinal strains in bottom flange and top flange at the mid-span section are compared in Figure 6-11 and Figure 6-12, respectively.

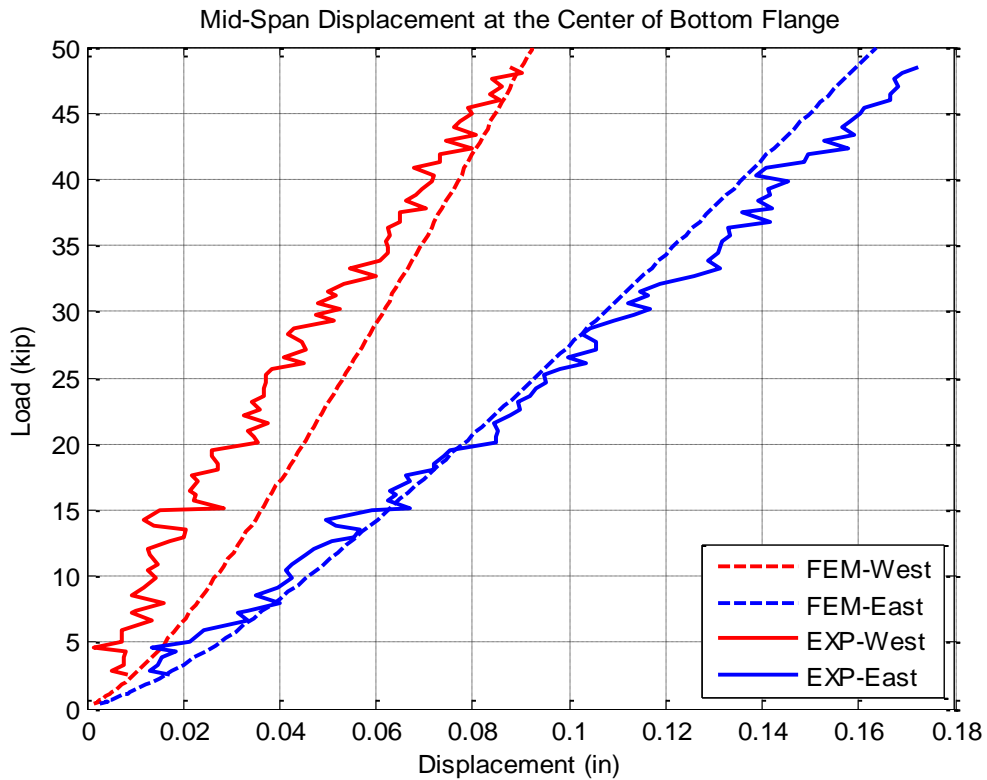


Figure 6-10 Comparison of vertical displacement at the bottom flange of each girder in Test 3.

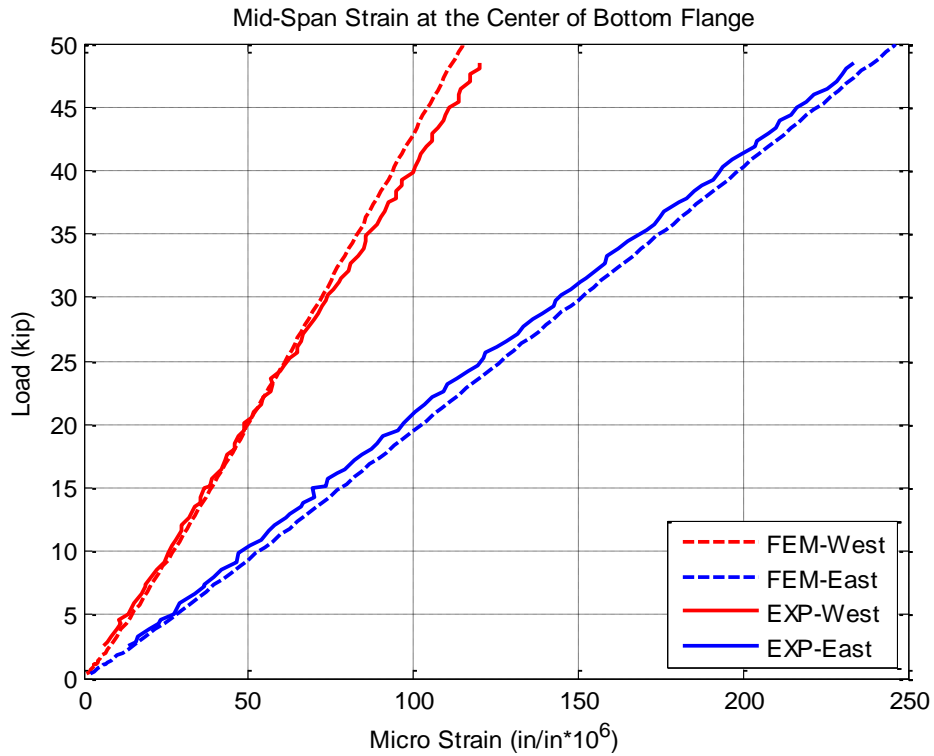


Figure 6-11 Comparison of longitudinal strain at the bottom flange of each girder in Test 3.

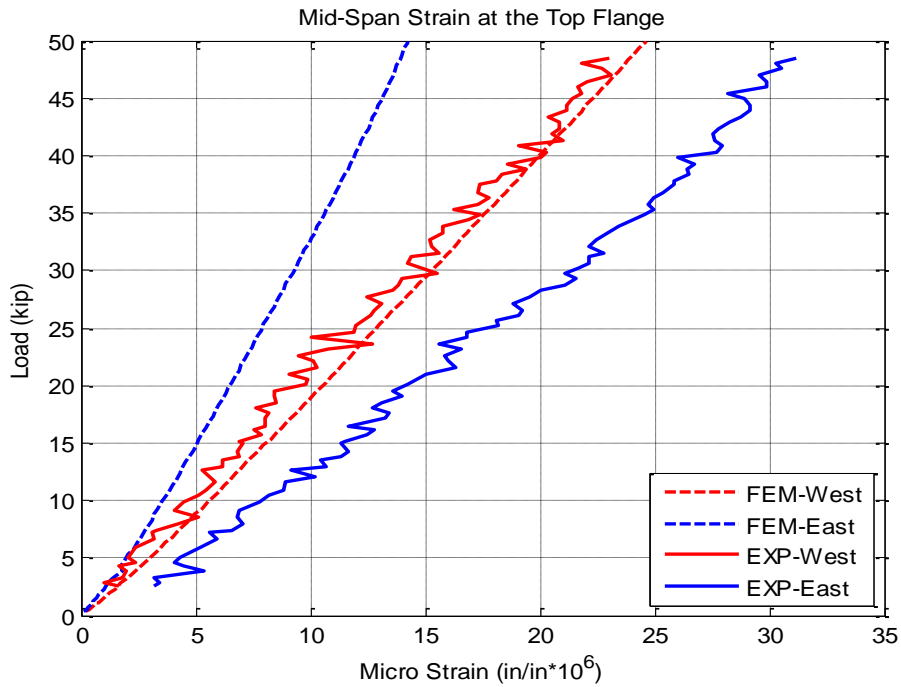


Figure 6-12 Comparison of longitudinal strain at the top flange of each girder in Test 3.

In general, the FEA results showed reasonable agreement with the experimental data for the tests on undamaged specimen, especially in the bottom flanges. In Test 3, the top flange strains showed some discrepancy between FEA and experiment.

6.2 Bridge Specimen with Bottom Flange Fractured in One Girder

FEA results and experimental data for Test 9 and Test 10 are compared to verify the FE modeling techniques for the series of tests with the bottom flange fractured in one girder.

6.2.1 Test 9 - with Rail, No Continuity, Unsymmetrical Loading (YNU)

Test 9 was YNU with bottom flange fractured in EG as illustrated in Figure 6-13.

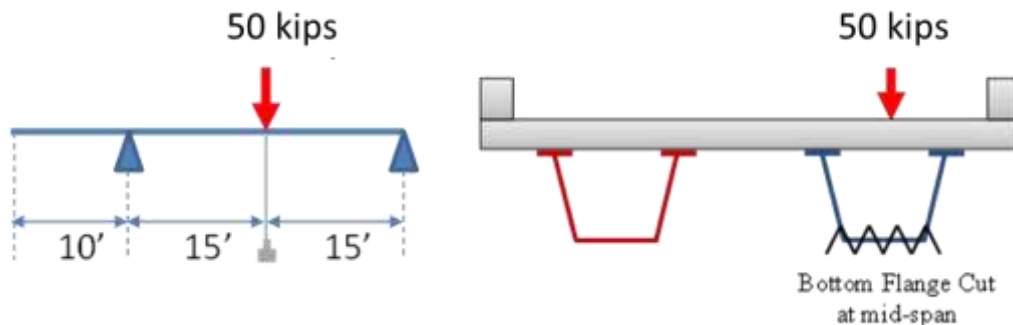


Figure 6-13 Schematic description of Test 9.

The mid-span vertical displacements at the center of bottom flange of both girders from the experiment and FEA are compared in Figure 6-14. The longitudinal strains in bottom flange and top flange at mid-span section are compared in Figure 6-15 and Figure 6-16, respectively.

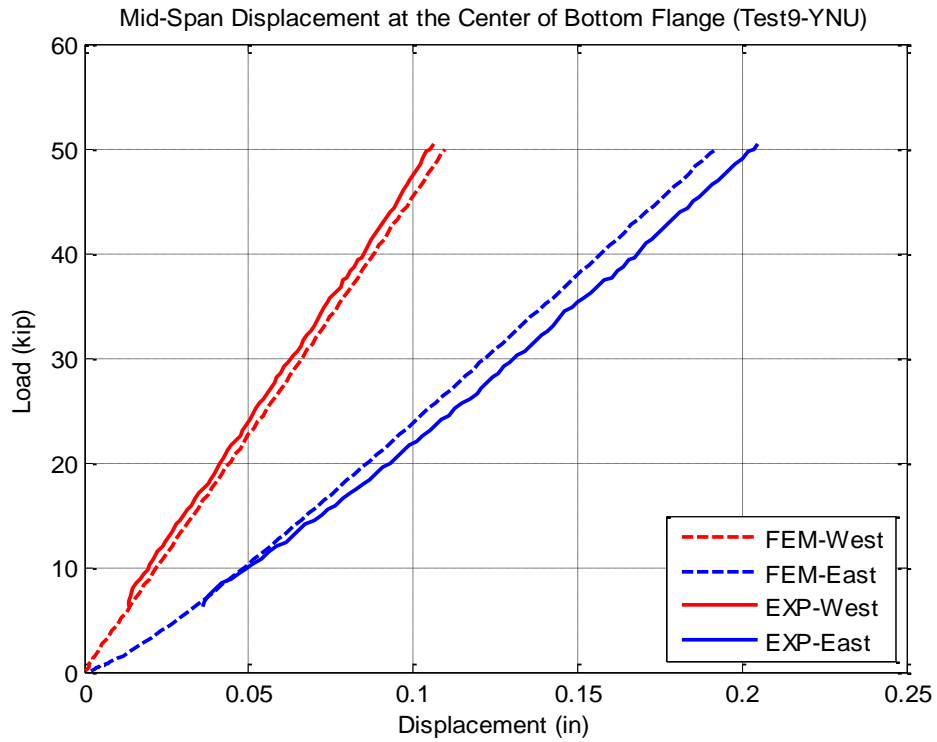


Figure 6-14 Comparison of vertical displacement at the bottom flange of each girder in Test 9.

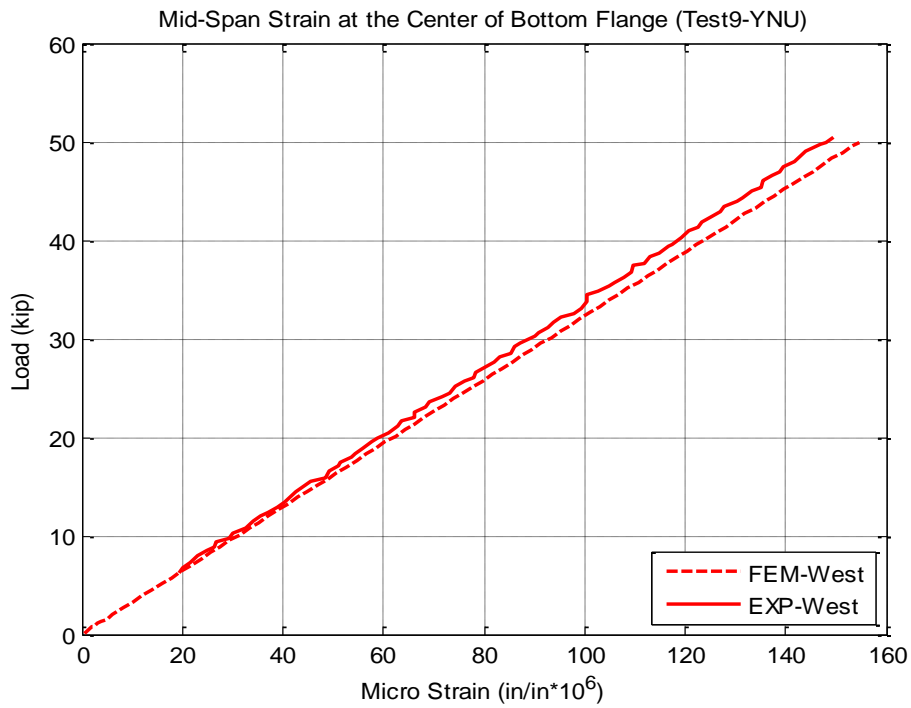


Figure 6-15 Comparison of longitudinal strain at the bottom flange of each girder in Test 9.

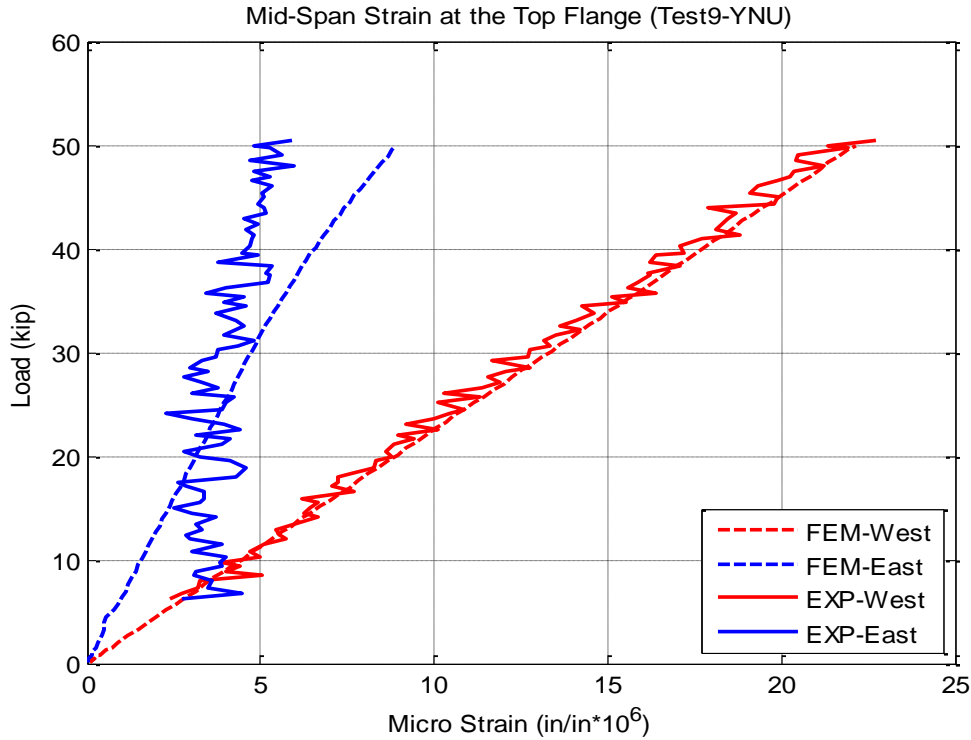


Figure 6-16 Comparison of longitudinal strain at the top flange of each girder in Test 9.

6.2.2 Test 10 - No Rail, No Continuity, Symmetric Loading (NNS)

Test 10 was carried out without rail, without continuity and symmetrical load applied and is illustrated in Figure 6-17.

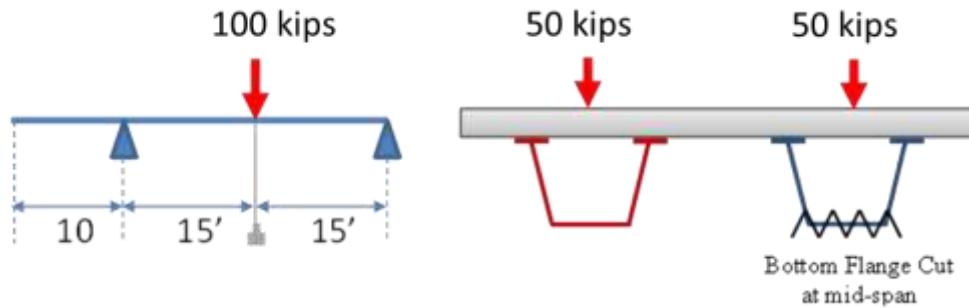


Figure 6-17 Schematic description of Test 10.

The vertical displacements of the center of bottom flange at mid-span from the experimental data and FEA are compared in Figure 6-18. Similarly, the longitudinal strains in the bottom flange and top flanges at the mid-span section are compared in Figure 6-19 and Figure 6-20, respectively.

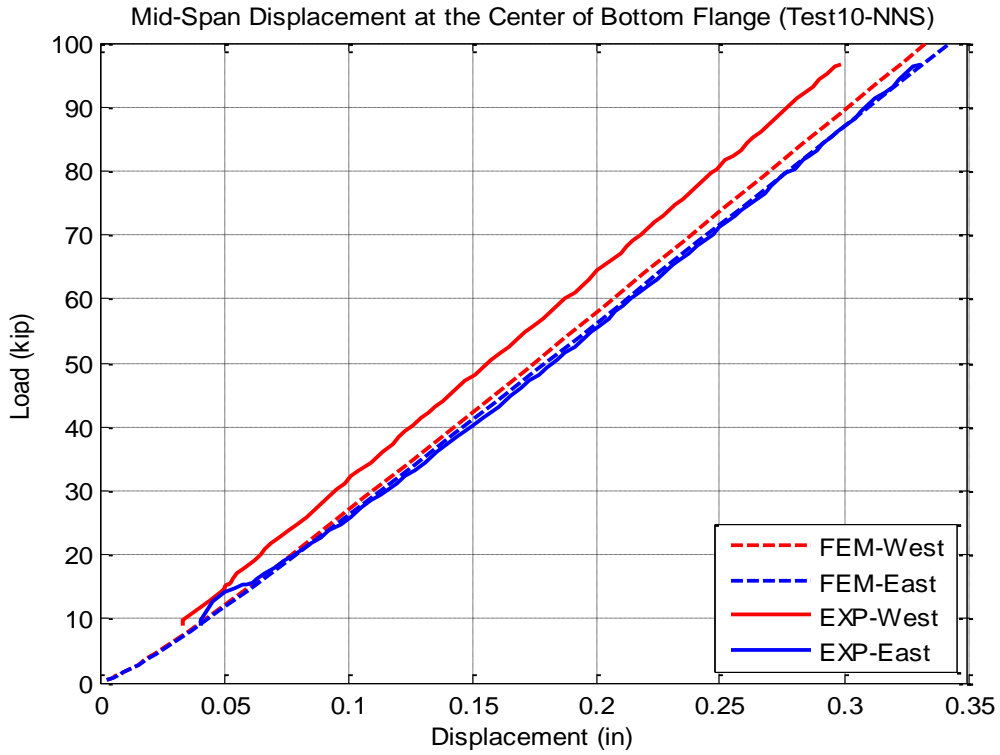


Figure 6-18 Comparison of vertical displacement at the bottom flange of each girder in Test 10.

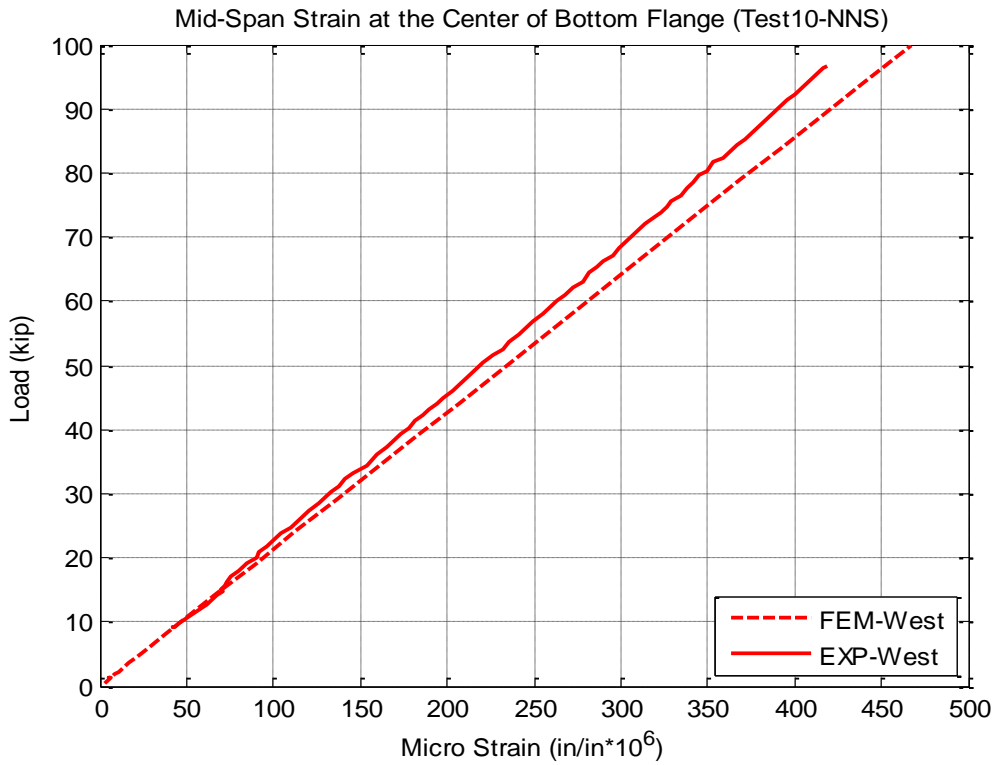


Figure 6-19 Comparison of longitudinal strain at the bottom flange of each girder in Test 10.

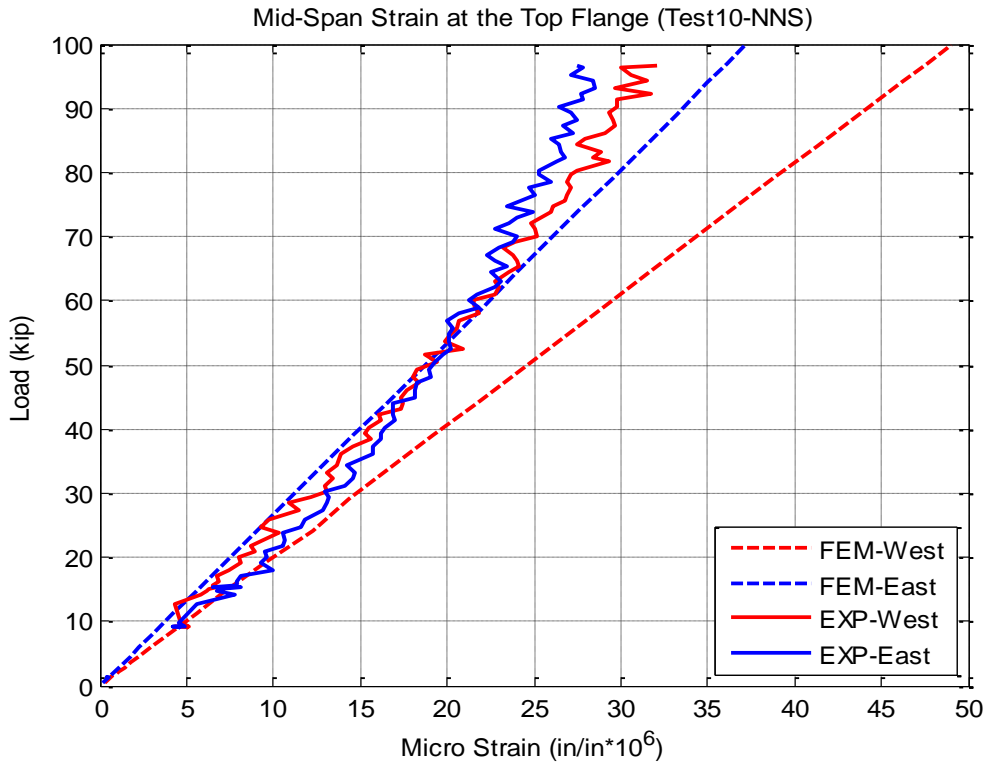


Figure 6-20 Comparison of longitudinal strain at the top flange of each girder in Test 10.

For bottom flange fractured specimen, the FEM results showed reasonable agreement with the experimental data in both local and global responses.

6.3 Bridge Specimen with Full-Web Fractured in One Girder

With the web and bottom flange completely fractured in one girder, the FEA results from Test 16 and Test 17 are compared to the experimental data. Test 16 and Test 17 have characteristics similar to Test 9 and Test 10 except the web in EG was now fractured in addition to the bottom flange.

6.3.1 Test 16 - with Rail, No Continuity, Unsymmetrical Loading (YNU)

The specimen was tested with the railings but no continuity, and 50 kips of load was applied to the damaged girder. A schematic of Test 16 is shown in Figure 6-21.

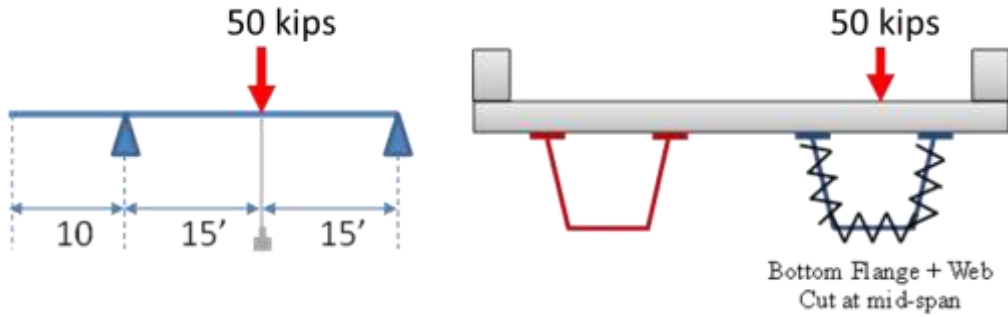


Figure 6-21 Schematic description of Test 16.

The vertical displacements of center of bottom flange at the mid-span from the experimental data and FEA are compared in Figure 6-22. Similarly, the longitudinal strain comparison in bottom flange at mid-span section is plotted in Figure 6-23. Both sets of data showed similar slopes. However, the experimental data showed bottom flange had some initial strains because the specimen wasn't completely unloaded in the third loading cycle.

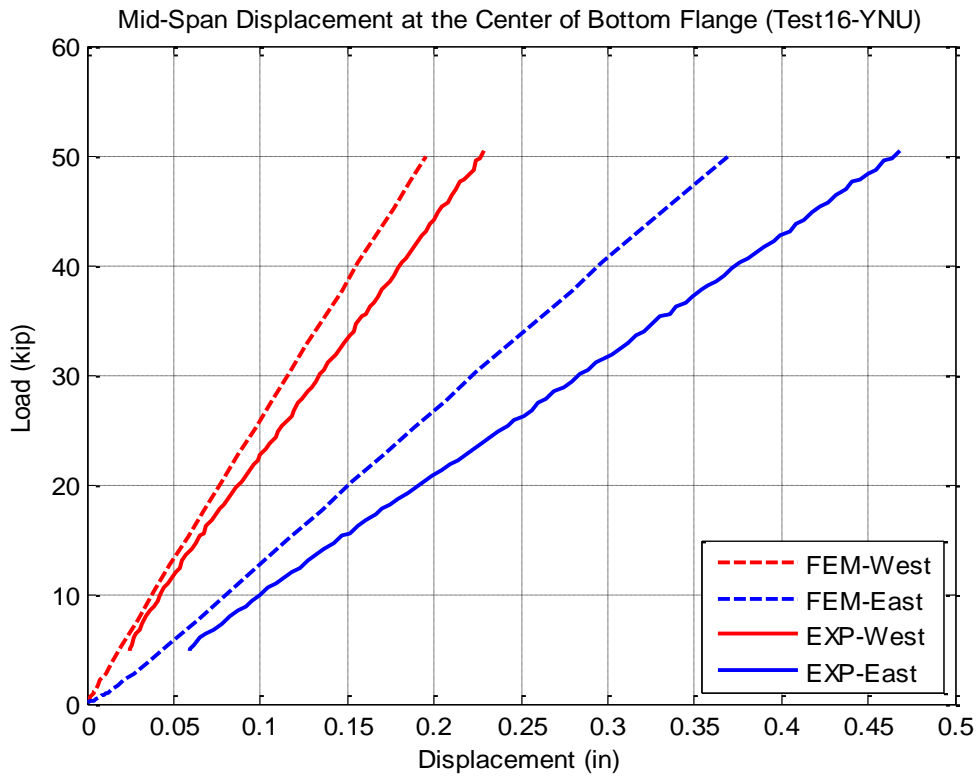


Figure 6-22 Comparison of vertical displacement at the bottom flange of each girder in Test 16.

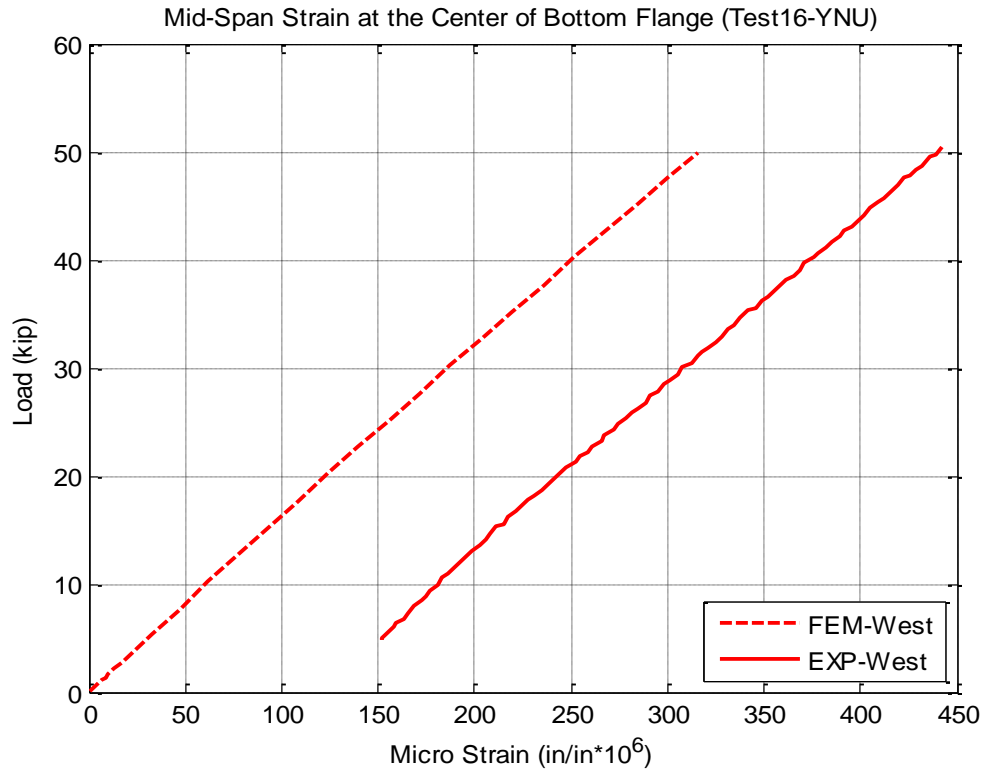


Figure 6-23 Comparison of longitudinal strain at the bottom flange of undamaged Girder in Test 16.

6.3.2 Test 17 - No Rail, No Continuity, Symmetric Loading (NNS)

In Test 17, the bridge was tested without rail and continuity and under symmetrical loading. A schematic of Test 17 is shown in Figure 6-24.

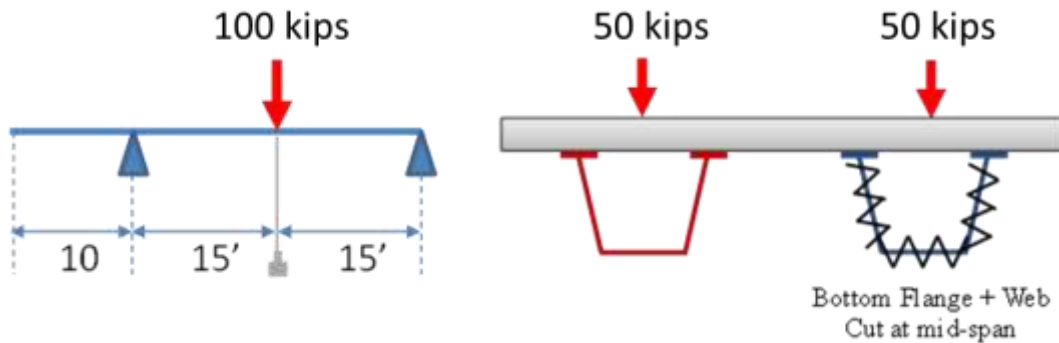


Figure 6-24 Schematic description of Test 17.

The vertical displacements of the center of the bottom flange at the mid-span obtained from the experimental data and FEM analysis are compared in Figure 6-25. Similarly, the longitudinal strain in the bottom flange at the mid-span section is compared in Figure 6-26.

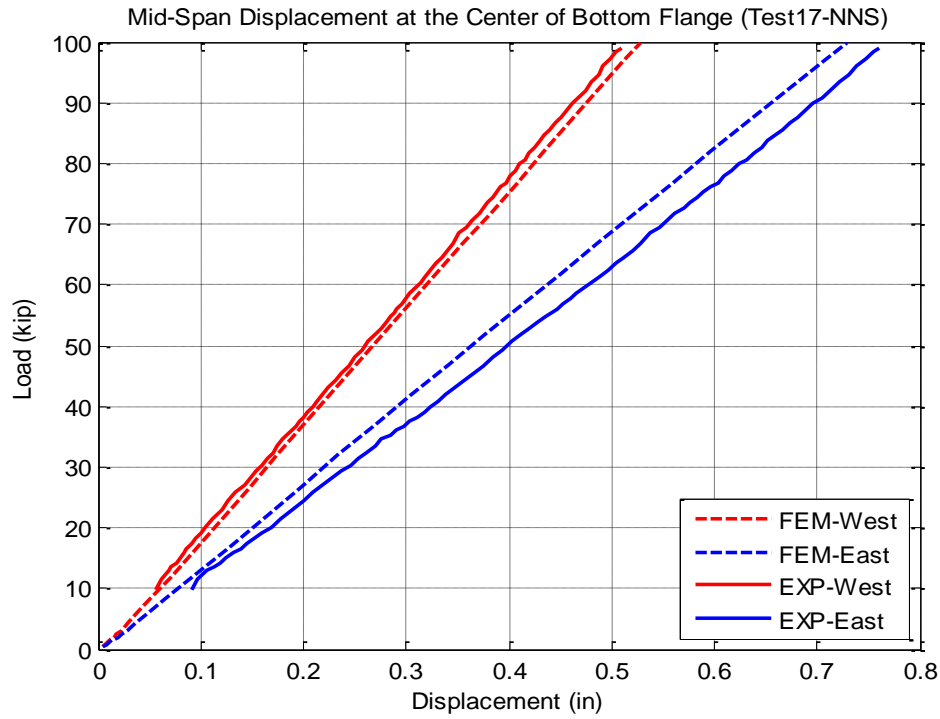


Figure 6-25 Comparison of vertical displacement at the bottom flange of each girder in Test 17.

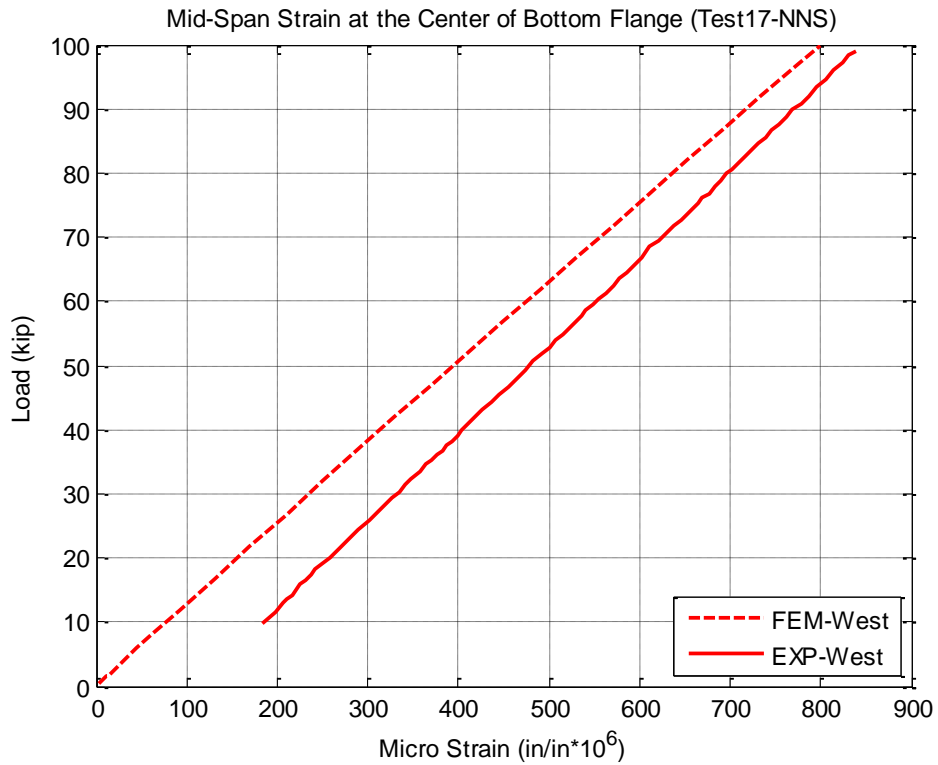


Figure 6-26 Comparison of longitudinal strain at the bottom flange of undamaged girder in Test 17.

In general, the finite element model is capable of reasonably predicting the linear responses of the specimen under the full-web fracture damage condition.

6.4 Verification of FEMs with Ultimate Test A

Both load-control and displacement control approaches were utilized to predict the ultimate load capacity of the specimen. The ultimate capacity of the specimen was predicted to be between 143 kips and 153 kips from FEA using the displacement-control method, for 7.8 ksi and 8.0 ksi concrete compressive strength, respectively, as a lower bound and upper bound. This method allows us to capture the capacity drop in the bridge after crushing of the concrete, as shown in Figure 6-27. The ultimate load, predicted from FEA using the load-control method, was 148 kips with concrete compressive strength of 7.8 ksi and was 163 kips with concrete compressive strength of 8.0 ksi. In FEA with load control method, after the ultimate capacity was reached, that load value then held nearly constant with increasing displacement for a short increment until the analysis was automatically terminated by the program, which can be seen in Figure 6-28. Since the ultimate capacity of the specimen in ultimate Test A was 156 kips, this suggests that the FE models provided good estimations of the ultimate capacity of tested specimen in either approach. Moreover, the FE models showed good agreements with experimental data on predicting when the ultimate capacity of the specimen will be reached.

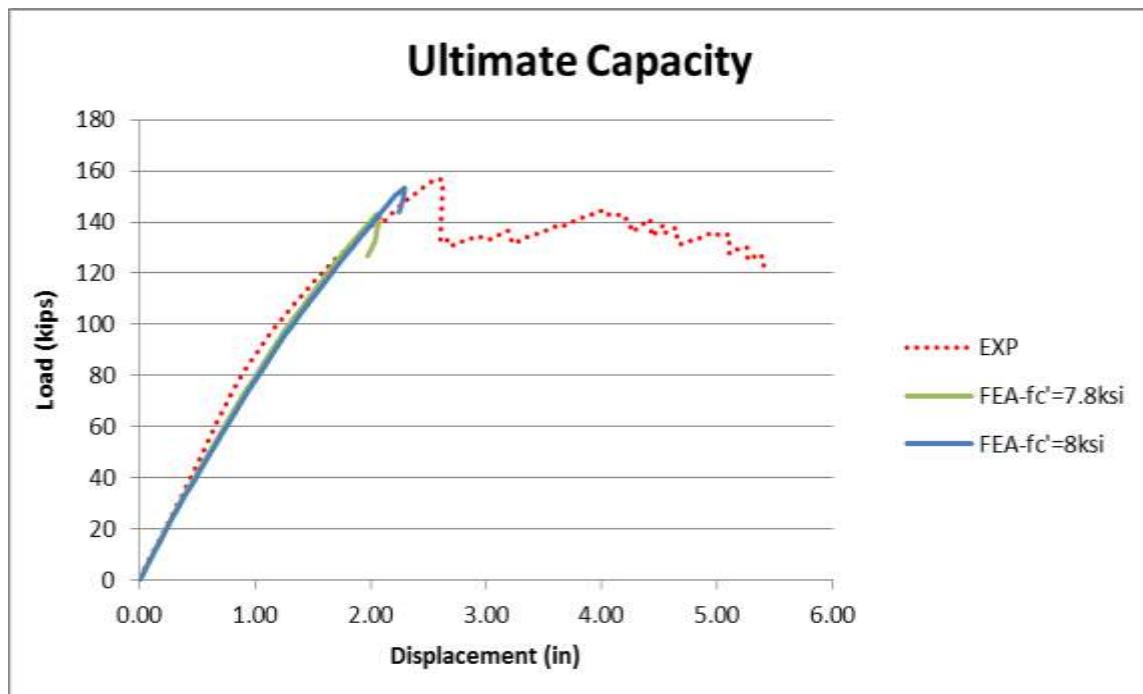


Figure 6-27 Comparison of load vs. vertical deflection curves using displacement-control analysis.

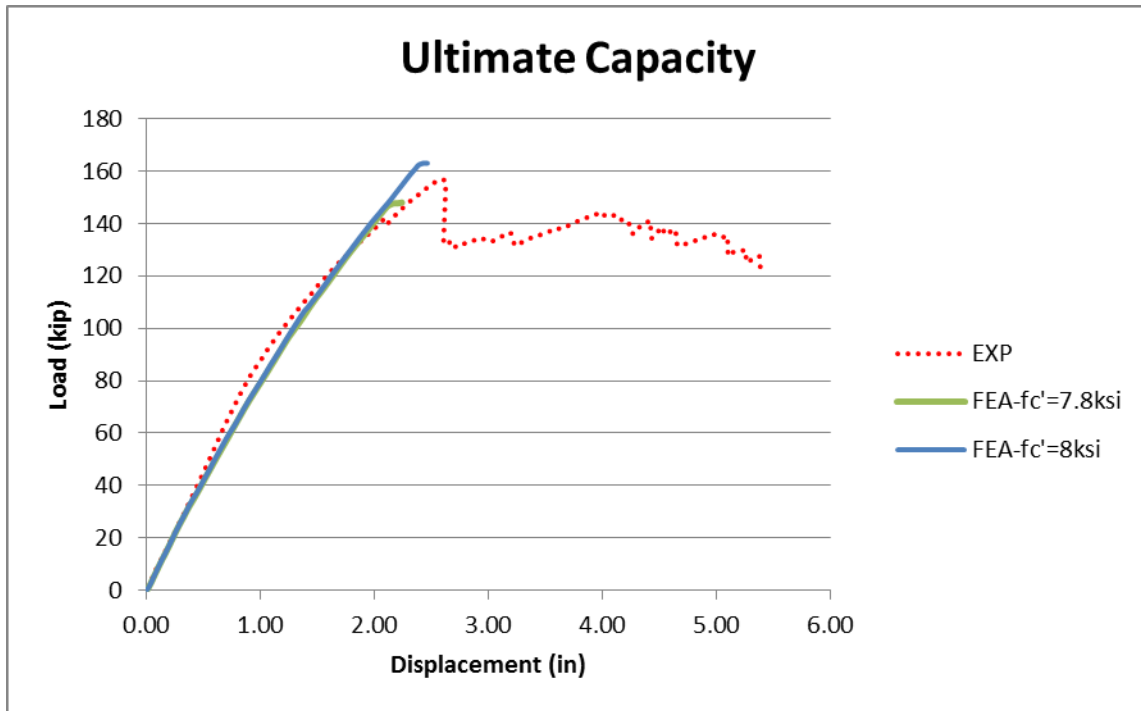


Figure 6-28 Comparison of load vs. vertical deflection curve using load-control analysis.

The capability of the FE models in capturing the behavior of the concrete deck and steel girders is also verified below.

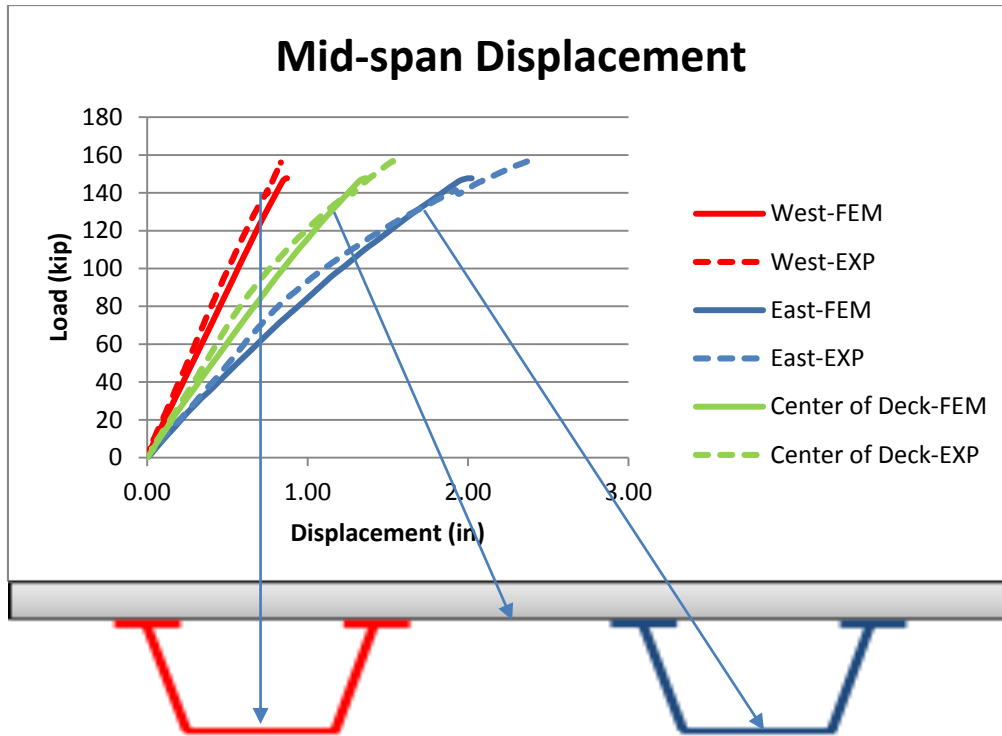


Figure 6-29 Vertical displacements at the bottom flange of each girder and at center of the deck at mid-span.

The FE models predicted very well the displacement of the laboratory specimen at mid-span, the most critical section, as shown in Figure 6-29. The difference between FEM and experimental data for mid-span displacement was less than 5%. In addition, the FE models well predict the uplift of the bridge that occurred in experiment. Figure 6-30a-b indicate that the WG was the only one that experienced uplifting in the experiment. This uplift occurred at the south support location when the applied load was around 80 kips (the blue dot in Figure 6-31a represents where and when the uplift occurred). The curve also shows that the uplift of the undamaged girder at the south support location might not have lifted completely until after the ultimate capacity was reached.

By using contact elements to model the interface between the supports and the bottom flanges, the FEM was also able to capture correctly the support location that will have uplift as shown in Figure 6-31. With negative reaction, the south-west support location was predicted as the location, which will experience uplifting. It is important to note that tolerance in the contact algorithm and deviation of contact normal at large deflections allow us to capture the apparent small negative reaction force.

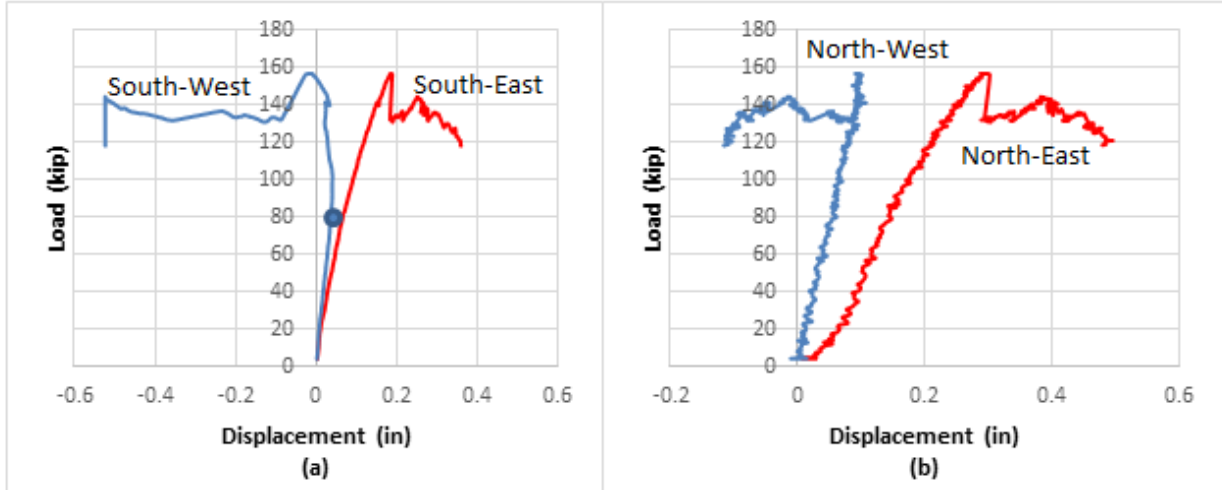


Figure 6-30 Reactions vs. EG vertical displacement.

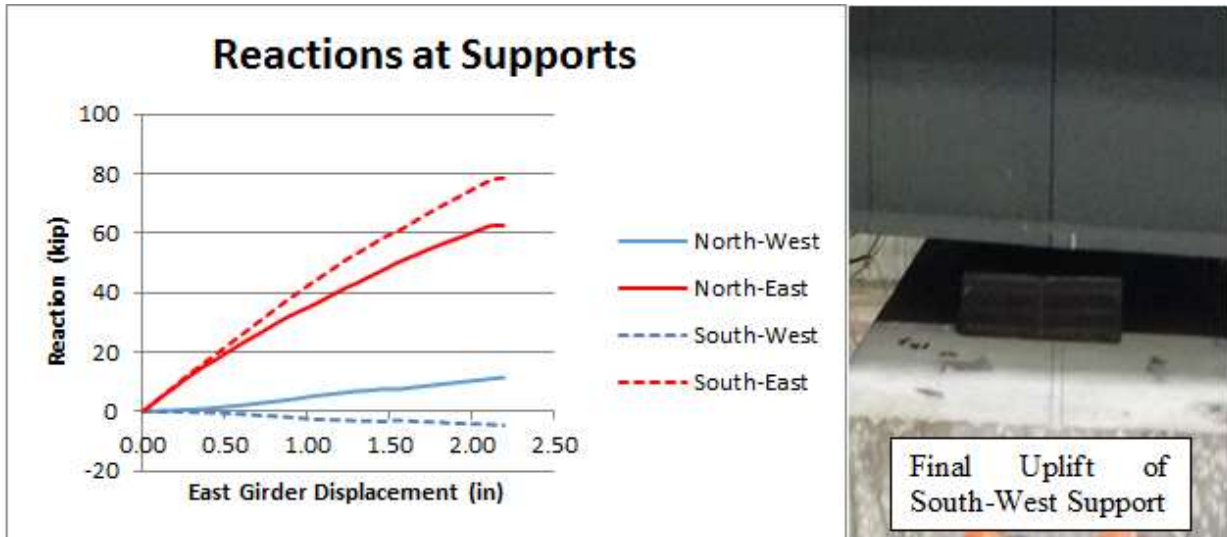


Figure 6-31 Prediction of uplift in finite element analysis.

Local behaviors of both the steel girders and deck were validated. Comparisons of longitudinal strain of top flanges and bottom flange of the undamaged WG, between FEA results and experimental data, are illustrated in Figure 6-32 and Figure 6-33, respectively. The transverse strains in the deck are verified in Figure 6-34.

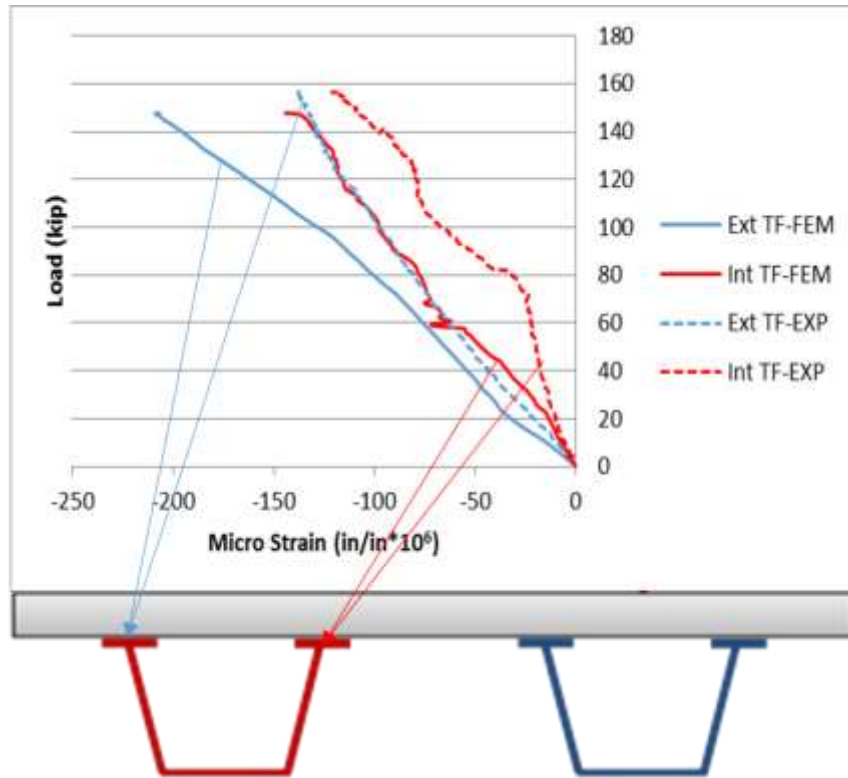


Figure 6-32 Comparison of longitudinal strains at the top flange of WG at mid-span.

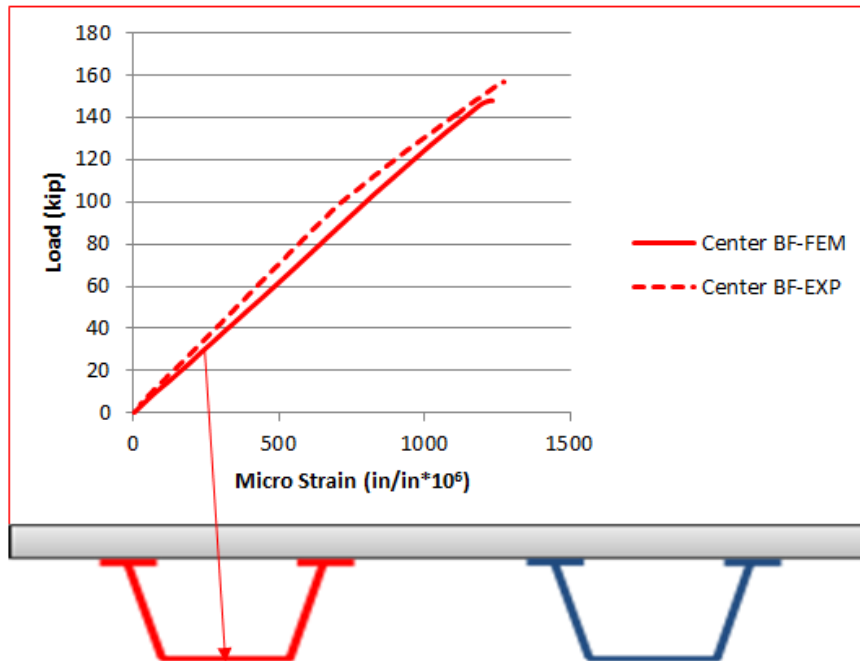


Figure 6-33 Comparison of longitudinal strain at bottom flange at mid-span.

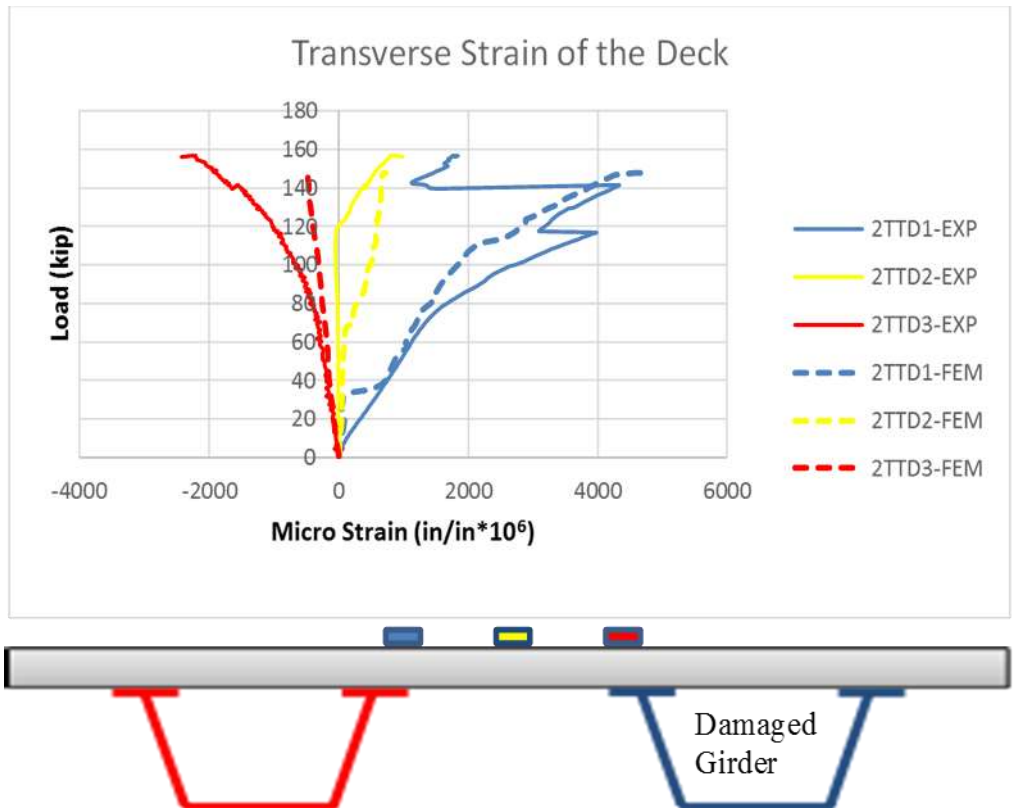


Figure 6-34 Comparison of transverse strain on the top of deck.

The FEM models provided a good prediction of the location where concrete crushing would occur. Figure 6-35 compares the location of concrete crushing in the analytical model and experiment. Figure 6-36 compared experimental results to finite element analysis results regarding cracks at the ends of specimen. Finite element analysis results in Figure 6-36 predicted the shear cracks and tensile cracks would occur at the ends of the bridge.

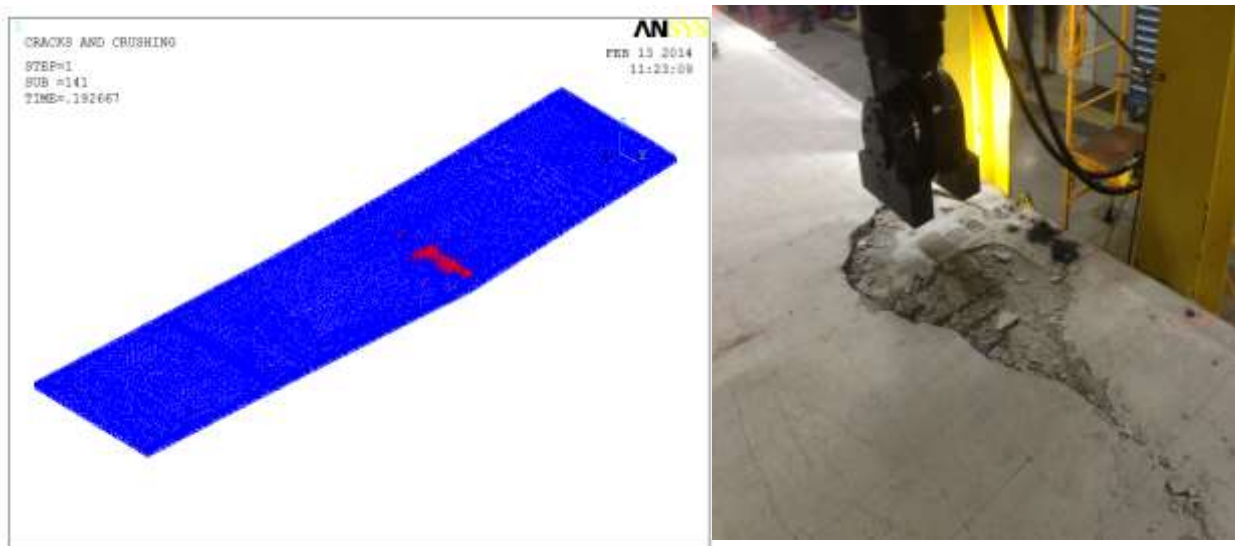


Figure 6-35 Location of concrete crushing in FEA and in experiment.

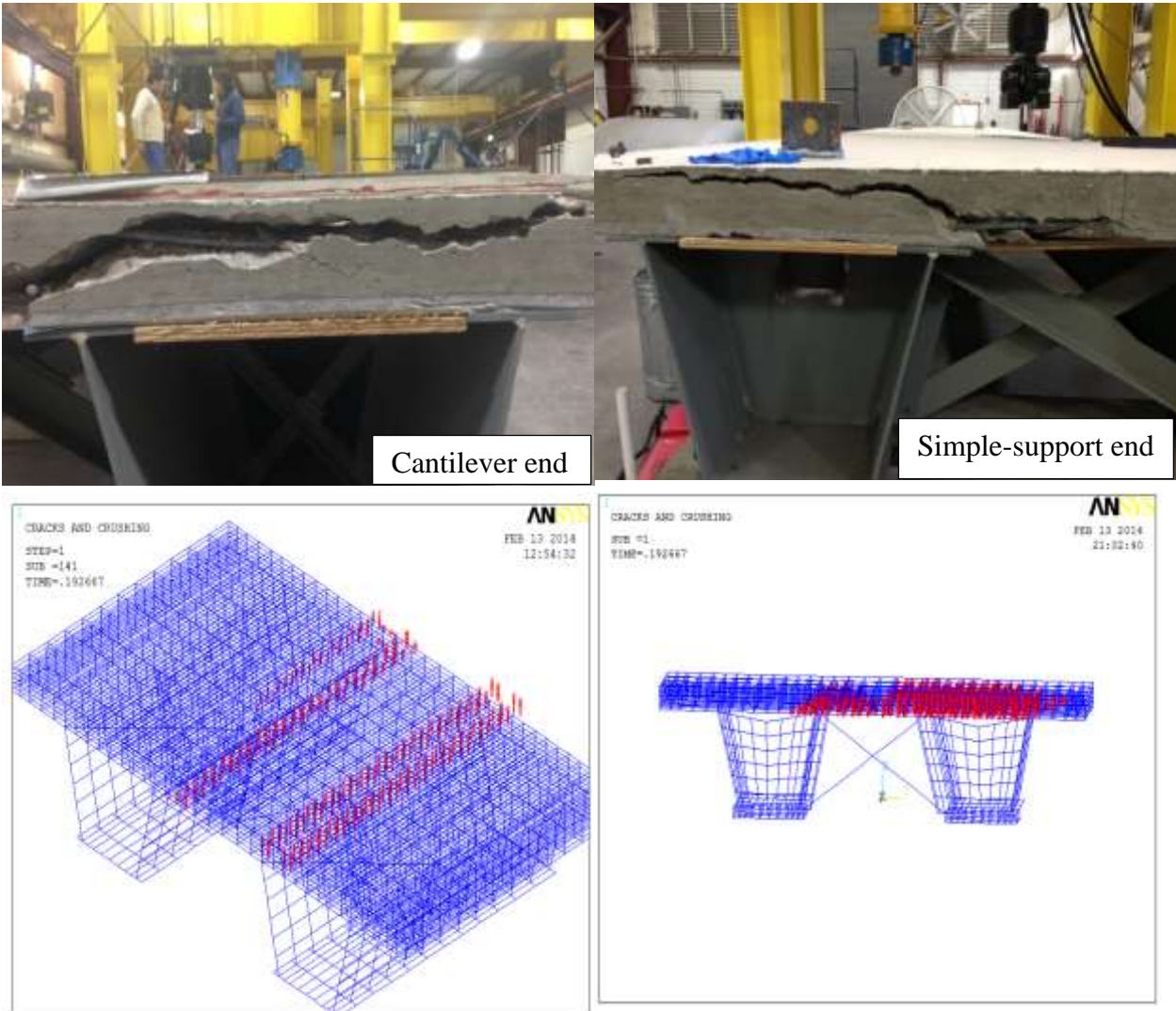


Figure 6-36 Shear cracking in south (left) and north (right) supports.

Figure 6-37 shows that the maximum von Mises stress in the steel girder was around 48 ksi, which was less than 50 ksi, the assumed yielded stress of the material. In other words, the steel girder had not yet yielded when the ultimate capacity of the model was reached and this matches with what was observed from the experimental data. The FEA results also showed a similarity with experimental tests in the stress distribution along the length of both intact and damaged girders.

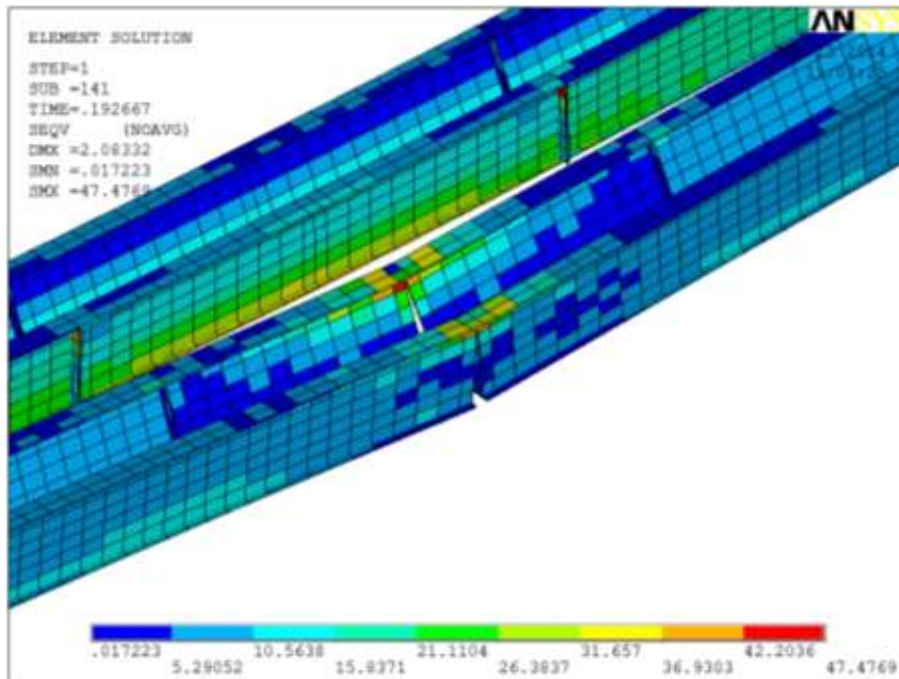
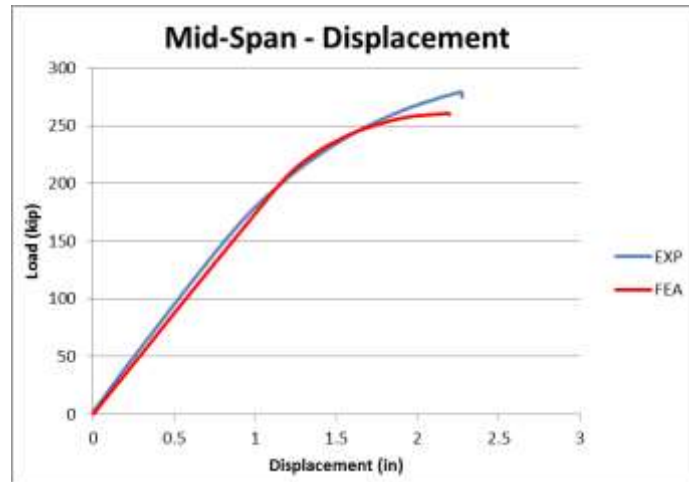


Figure 6-37 Stress contour at mid-span in the steel girders.

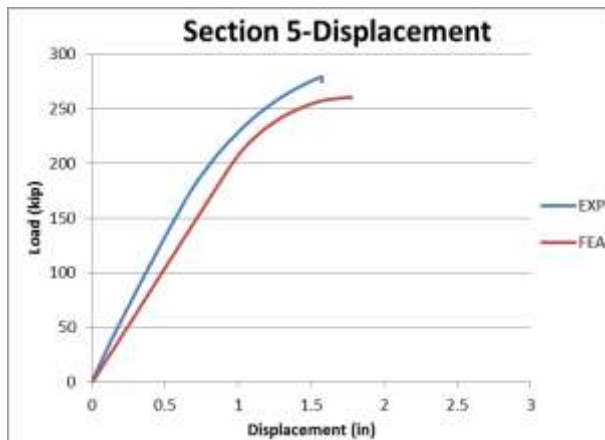
Overall, the FE model was able to capture behavior of concrete, steel girder, and major damages that were observed during the test such as shear failures of concrete deck at the loading point and at both ends as well as the uplift of the intact girder.

6.5 Verification of FEMs with Ultimate Test B

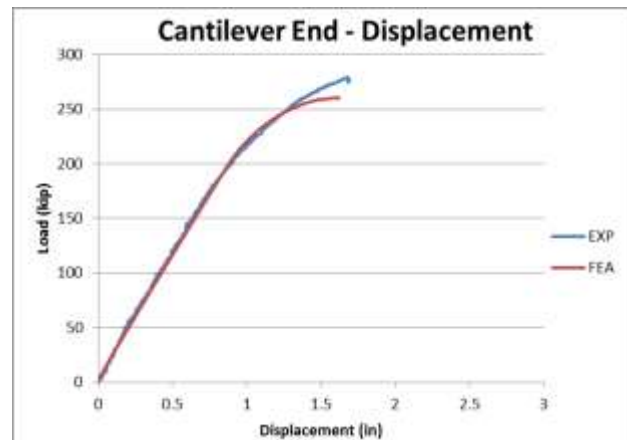
Since both girders experienced similar displacements as illustrated in Section 4.5, the average vertical displacements are used to present the displacement of both girders. The average vertical displacements of both girders along the length of the specimen were compared in Figure 6-38. In this figure, the agreements were observed not only in the vertical displacements of the girders along the length but also in the capacity of the specimen. The capacity obtained from the test was 275 kips while the capacity obtained from FEA as 260 kips.



(a)



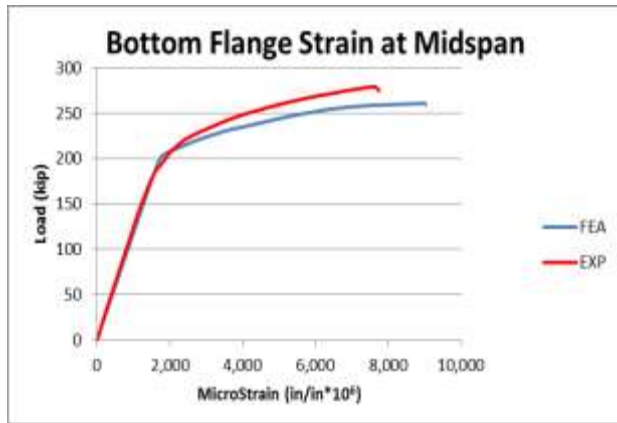
(b)



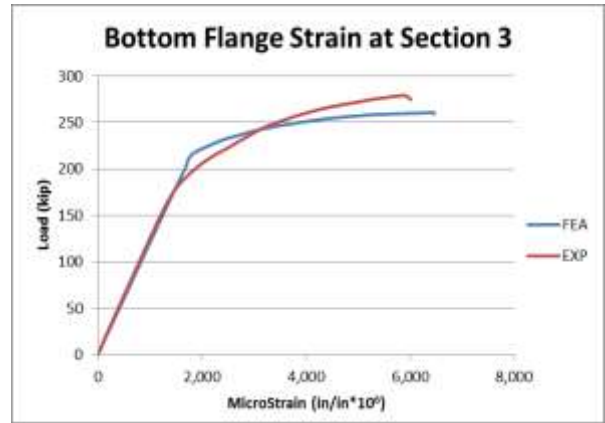
(c)

Figure 6-38 Load vs average vertical displacements at (a) mid-span, (b) Section 5, and (c) cantilever end.

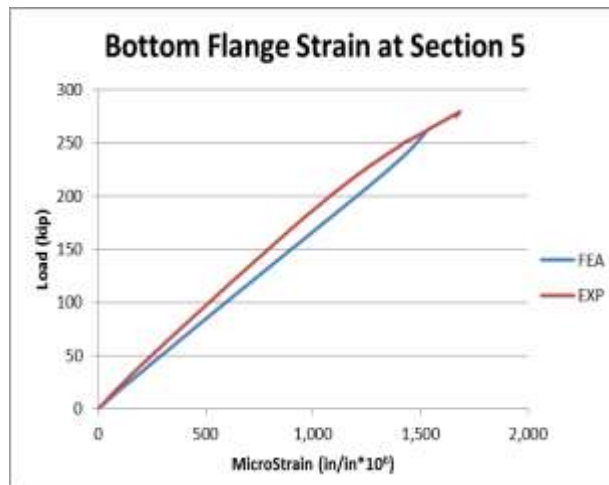
In addition, Figure 6-39 and Figure 6-40 compare test data and FEA results on longitudinal strains of the intact girder and on the transverse strain of the deck at mid-span. The comparison indicates that the FEMs were to predict and capture the behavior of both deck and steel girder. However, the comparison on steel girders had better agreement than it was on the deck. This could be due to several assumptions that was made when modeling the concrete, such as stress-strain material model, crushing stress, cracking stress and shear transfer coefficients.



(a)



(b)



(c)

Figure 6-39 Comparison of longitudinal strains at the bottom flange of the intact girder at (a) mid-span, (b) Section 3, and (c) Section 5.

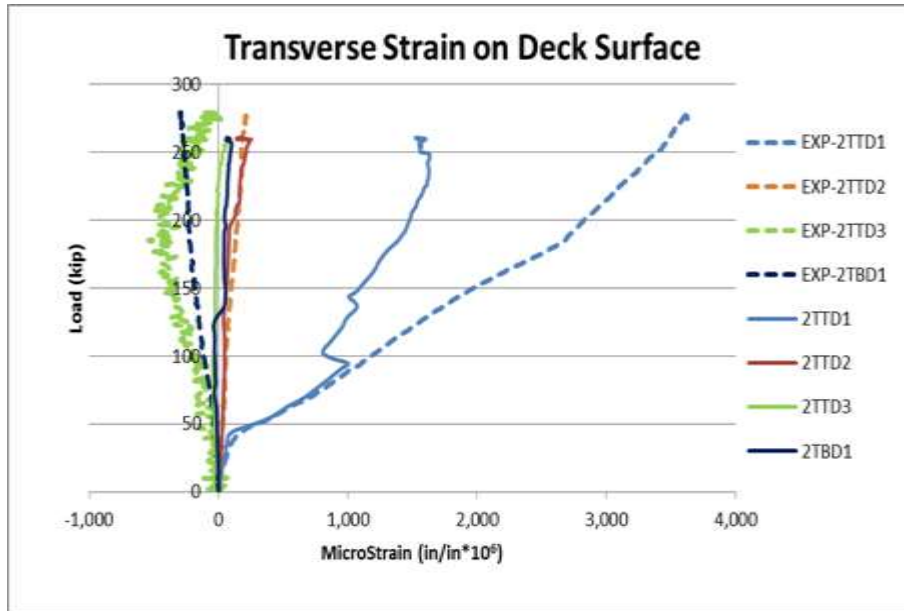


Figure 6-40 Transverse strain on the deck at mid-span.

Overall, the capacity and displacements produced by the FEM were in good agreement with those observed in the test. The FEM was also able to predict the responses in both steel girders and the concrete deck.

6.6 Summary

Overall, the predictions from finite element analyses were in good agreement with experimental data in both elastic and inelastic ranges. The maximum vertical displacements in each elastic test obtained from experimental data and FEM analysis results are listed in Table 6-1. Percentage difference in the last column of the table is calculated by dividing the difference of experimental and FEM deflection with the experimental deflection and multiplying by 100. The percentage differences between FEM analysis results and test data was 5.1% on average ranging from 0.03% for Test 2 (NNU) on undamaged system to 19.8% for Test 16 (YNU) on damaged system.

It should be noted that the high percentage of difference resulted primarily from the tests that have the rail system. This could be because the connection between the rail and the deck was assumed to be a full connection in the finite element models and the contact area between rail segments weren't modeled. Since in all ultimate tests, the specimen was tested without the rail, these assumptions were made to simplify the finite element modeling, and it was expected that they would not affect findings of this study.

From ultimate Tests A and B, it can be concluded that the finite element models were able to capture the inelastic responses of the specimen. For example, the finite element models were able to predict the modes of failure, the maximum capacity as well as damages observed in the

experiment such as uplift of the intact girder, deck cracks at both ends and shear damage on the deck in ultimate Test A.

A good agreement between finite element analyses and experimental data in both elastic and inelastic ranges for several experiments indicates that the finite element models used in this study have been fully calibrated.

Table 6-1 Comparison of Displacement between FEA Results and all Elastic Tests.

Test #	Characteristics	Experimental Deflection (in)	FEM Deflection (in)	% Difference
1	NNS	0.333	0.324	2.7
2	NNU	0.203	0.203	0.03
3	NYU	0.179	0.189	5.8
4	YNS	0.303	0.285	6.0
5	YYU	0.174	0.171	1.6
6	YNU	0.194	0.182	6.2
7	YNS	0.337	0.300	11.1
8	YYU	0.180	0.180	0.2
9	YNU	0.206	0.192	6.7
10	NNS	0.337	0.342	1.6
11	NNU	0.218	0.215	1.3
12	NYU	0.188	0.200	6.1
14	YNS	0.573	0.575	0.3
15	YYU	0.378	0.330	12.8
16	YNU	0.460	0.369	19.8
17	NNS	0.741	0.730	1.6
18	NNU	0.503	0.465	7.6
19	NYU	0.401	0.403	0.7
Avg Difference =				5.1

Chapter 7 Field Testing of Ft. Lauderdale Twin Box-Girder Bridge 860600

Florida International University (FIU) contracted Bridge Diagnostics, Inc. (BDI) to conduct a field test on Ramp Bridge 860600 located in Ft. Lauderdale, Florida. This structure is a multiple-span bridge and the test was performed on the north module, which is a three-span continuous bridge. The bridge has two separate superstructures. Each superstructure consists of two steel box-girders composite with a concrete deck. In this project, only the west superstructure that provides the access ramp from SW 1st street to I-95 South was tested. Figure 7-1 and Figure 7-2 show the pictures of the first two spans of the bridge.

Tasks began on May 22, 2012, when FIU staff began preliminary work on the bridge including marking the exact spot for each instrument and preparing the surface of the steel box-girders for installation of instruments. That task was completed on May 23, 2012, and then BDI started its job on the bridge site on May 30, 2012. The BDI services included providing testing equipment and instruments, installation, data collection and preliminary data processing. Loading trucks were provided by FDOT District 4 and were weighed at a nearby certified scale. The loading started around 9:00 p.m. on May 30, 2012. Eight different moving load scenarios were applied and testing finished at 11:30 p.m. that night. After that, removing the instruments, wiring and equipment, and restoring the instrumentation spots on the steel girders to their initial state, including cleaning, sanding, zinc coating and painting was done until 3:00 am on May 31, 2012 when the field job was accomplished.

The acquired data was first reviewed and analyzed by BDI, which showed the structure was behaving in a linear elastic manner. A slight thermal drift was detected during the test, which is typical for long-duration tests. The drift was corrected with a linear offset. BDI reported the overall data to be of good quality.

FIU analyzed the data provided by BDI using finite element analysis of the bridge under different loading scenarios. In general, the deflection results match with the test data with good precision. The collected strain data are also in good agreement with the finite element analysis results. A partial fixity in the abutment of the bridge is observed from the strain data compared to ideal finite element model, which is in agreement to observations of past researchers. This partial fixity causes slightly greater stresses in the superstructure close to the abutment and reduces the magnitude of stresses in the mid-span region to some extent.

This chapter provides details regarding the instrumentation, load test procedures and response plots. The processed data from each path has been formatted as a function of longitudinal truck position. In general, the good match of the analysis results and test data verifies the accuracy of the finite element models that FIU researchers have constructed to study the behavior of twin box-girder bridges.

It should be noted that the test results presented in this chapter correspond to the properties of the structure at the time of testing. Any further structural aging, degradation, damage, or retrofits must be taken into account for future analysis or rating purposes.



Figure 7-1 First two spans of the ramp bridge - underneath view.



Figure 7-2 First span of the ramp bridge 860600 - elevation view from west.

7.1 Objective

The main goal of this field testing was to calibrate the finite element models and verify the accuracy of the modeling techniques that are used in the redundancy analysis of twin box-girder bridges in elastic range. Another target was to observe the behavior of an existing two girder bridge under actual truck loading.

7.2 Bridge Configuration

The Ft. Lauderdale Ramp Bridge 860600 has a twin box-girder superstructure that is continuous over three spans. The lengths of the spans are 144, 163 and 148 ft and the bridge total length is 455 ft. Figure 7-3 shows the elevation view of the bridge.

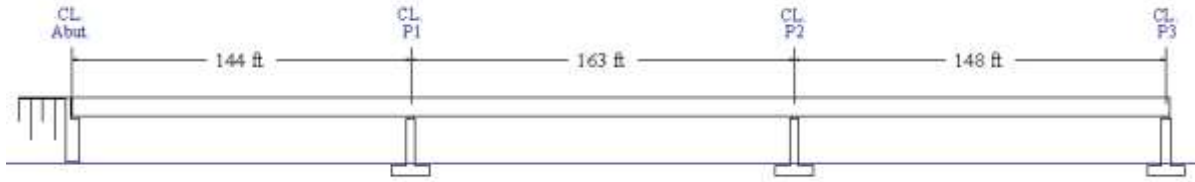


Figure 7-3 Elevation view of the bridge.

The box-girders of the superstructure are composite with a concrete deck of 8-in thickness. The depth of the box-girders is 6 ft - 4 in. The width of the roadway is 28ft and there are two railings with a width of 1 ft - 6.5 in. at each side of the roadway. Figure 7-4 shows the bridge superstructure cross-section.

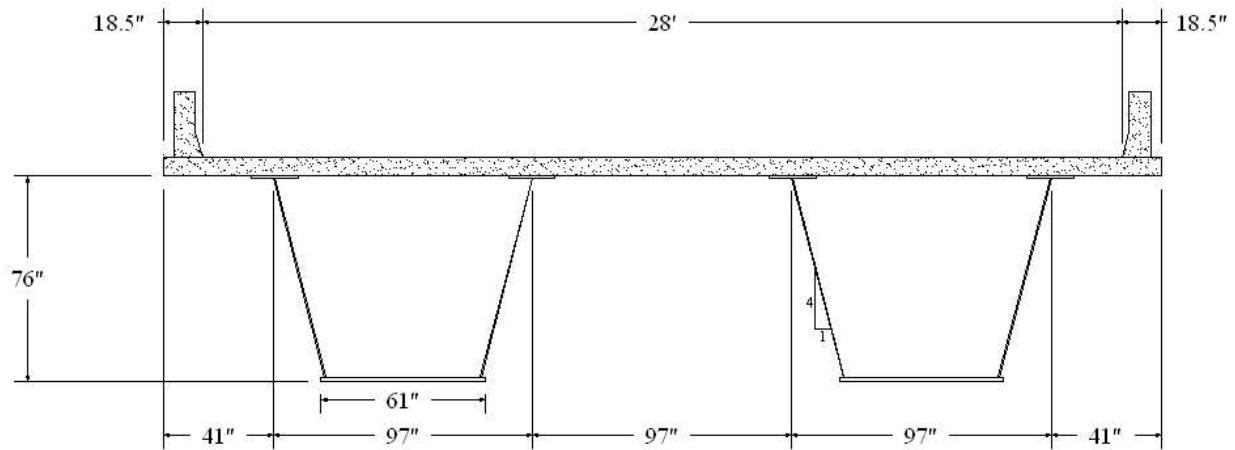


Figure 7-4 Cross-section of the Ft. Lauderdale bridge 860600.

The width of the bottom flange of each box-girder is 5 ft and 1 in. and the center-to-center distance of the top flanges is 8 ft and 1 in. The thickness of girder webs is equal to 0.6875 in. and they are inclined with a slope of 4:1. The width of the top flange and the thickness of the top and bottom flanges of the girders are changing throughout the length of the girders and are tabulated in Table 7-1.

Table 7-1 Thickness of Top and Bottom Flanges of the Bridge Girders

Plate #	Plate Length	Top Flange		Bottom Flange	
	(ft)	Width (in.)	Thickness (in.)	Width (in.)	Thickness (in.)
1	128.5	12	1	61	5/8
2	25	16	15/8	61	9/8
3	40	16	1	61	7/8
4	72	12	1	61	5/8
5	22.5	12	5/4	61	7/8
6	45	24	2	61	13/8
7	31	16	1.5	61	7/8
8	72.5	16	1.5	61	5/8
9	17.5	12	5/4	61	5/8

The internal bracing of the box-girders are made of an L5x5x3/8 angle for the top chord and an inverted V bracing with L3.5x3.5x1/2 sections for each leg. These elements are connected to the box-girder by means of web transverse stiffeners with 5-in. width and 0.5-in. thickness. There are 11, 13 and 12 of such internal braces in the first, second and third spans, respectively. These braces are approximately equally spaced in each span. Figure 7-5 depicts the internal braces that are used in the box-girders.

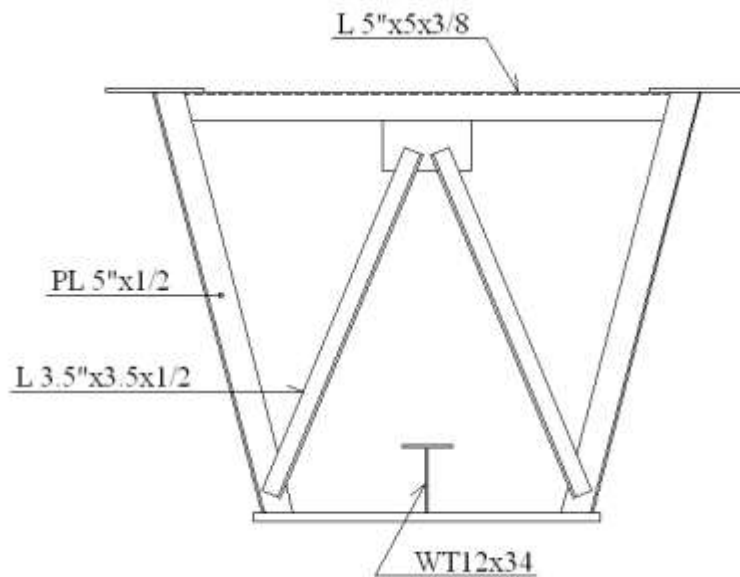


Figure 7-5 Internal bracing of superstructure girders.

Table 7-2 presents some general information about the bridge and the testing procedure.

Table 7-2 General Structure and Testing Specifications

ITEM	DESCRIPTION
STRUCTURE NAME	Park and Ride Outbound Ramp to Southbound I-95
CITY/STATE	Ft. Lauderdale, FL
TESTING DATE	May 22 to 31, 2012
CLIENT'S STRUCTURE ID #	Ramp Bridge 860600
STRUCTURE TYPE	Steel Twin Box-girder
TOTAL NUMBER OF SPANS TESTED	2
SPAN LENGTH(S)	Span 1: 144'-0" , Span 2: 163'-0"
ROADWAY WIDTH	28'-0"
SKEW	0
WEARING SURFACE	Concrete
SPANS TESTED	2
TEST REFERENCE LOCATION (X=0,Y=0) - BOW	CL of North Abutment at the inside face of the East Parapet
NUMBER/TYPE OF SENSORS	Strain Transducers – 28, Displacement Sensors – 8
SAMPLE RATE	40 Hz – Semi-Static and Normal Speed
NUMBER OF TEST VEHICLES	2
STRUCTURE ACCESS TYPE	Bucket Truck
STRUCTURE ACCESS PROVIDED BY	FDOT
TRAFFIC CONTROL PROVIDED BY	FDOT
TOTAL FIELD TESTING TIME	4 Days

7.3 Instrumentation

The instrumentation of the bridge was performed using the BDI wireless structural testing system. In this system, the transducers are connected to a wireless data acquisition device which collects the structure response data at a predefined frequency. In this project, the bridge is instrumented in two locations to gather the displacement data and in three sections for strain data. The following two subsections describe the details of the instrumentation at each section.

7.3.1 Potentiometers (Displacement Sensors)

To measure the deflections of the bridge under live load, eight potentiometers are installed below the superstructure of the bridge at two locations, named locations 1 and 2. A side view of the bridge showing these two locations is illustrated in Figure 7-6.

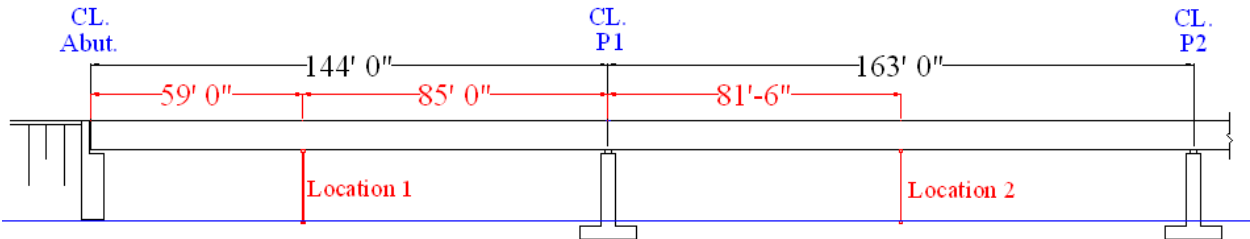


Figure 7-6 Locations of potentiometers in the first two spans.

Location 1 is in the first span at a distance of 85 ft from the first pier. At this location, there are four potentiometers, two of them below the edges of the bottom flange of the west box-girder, one in middle of the concrete deck between the steel girders and the other one below the west edge of the EG. Figure 7-7 displays the arrangement of the potentiometers in the first span. The gauge and channel ID's (in parentheses) of these displacement sensors are shown in Figure 7-8. A typical photo of the assembly of these displacement sensors is in Figure 7-9. As stated earlier to measure the displacement of the concrete deck between the girders, a sensor is attached to it. As the structural insulated panel (SIP) is used for the concrete, the transducer should be attached to the SIP form instead of the concrete face. Figure 7-10 shows the transducer attached to formwork below the concrete slab.

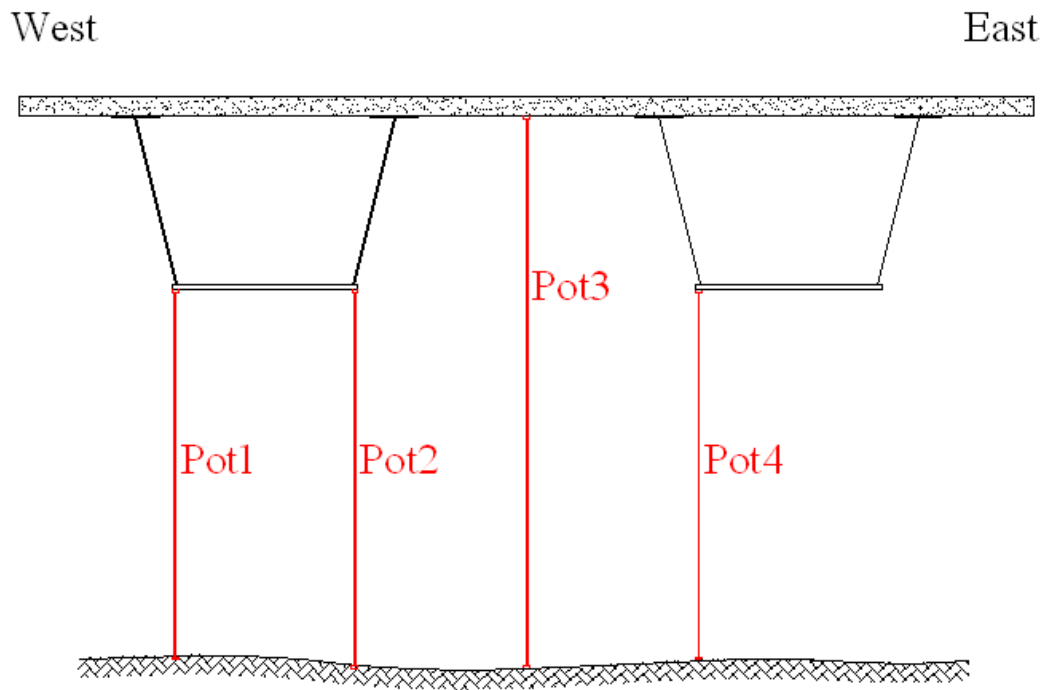


Figure 7-7 Arrangement of potentiometers at Location 1 in the first span.

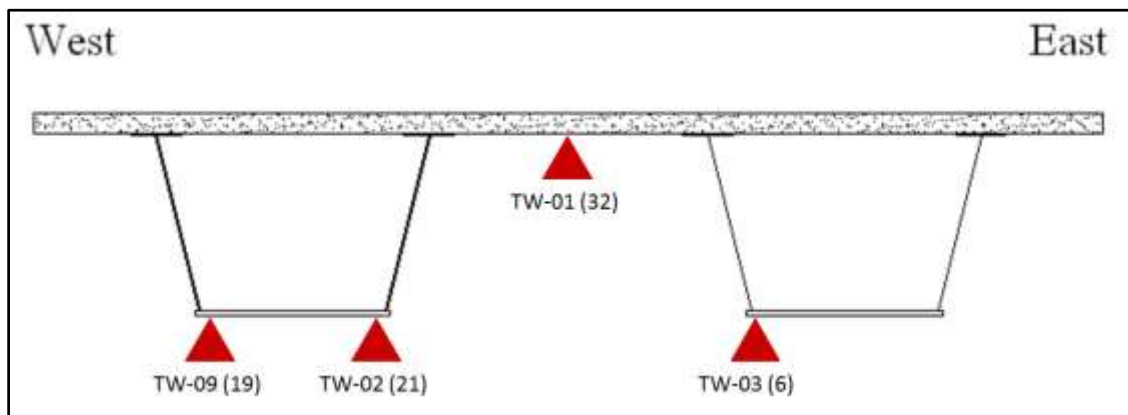


Figure 7-8 Gauge and channel ID of first span displacement sensors.



Figure 7-9 Displacement sensor beneath bottom flange of box-girder (typical).



Figure 7-10 Displacement sensor on SIP form below concrete deck.

In the second span, four potentiometers are installed in the middle of the span which has a distance of 81'-6" from the adjacent piers. At this location, one potentiometer is attached to each edge of the bottom flange of each box-girder. Figure 7-11 shows the configuration of the potentiometers at middle of the second span. The gauge and channel ID's (in parentheses) of these potentiometers are indicated in Figure 7-12.

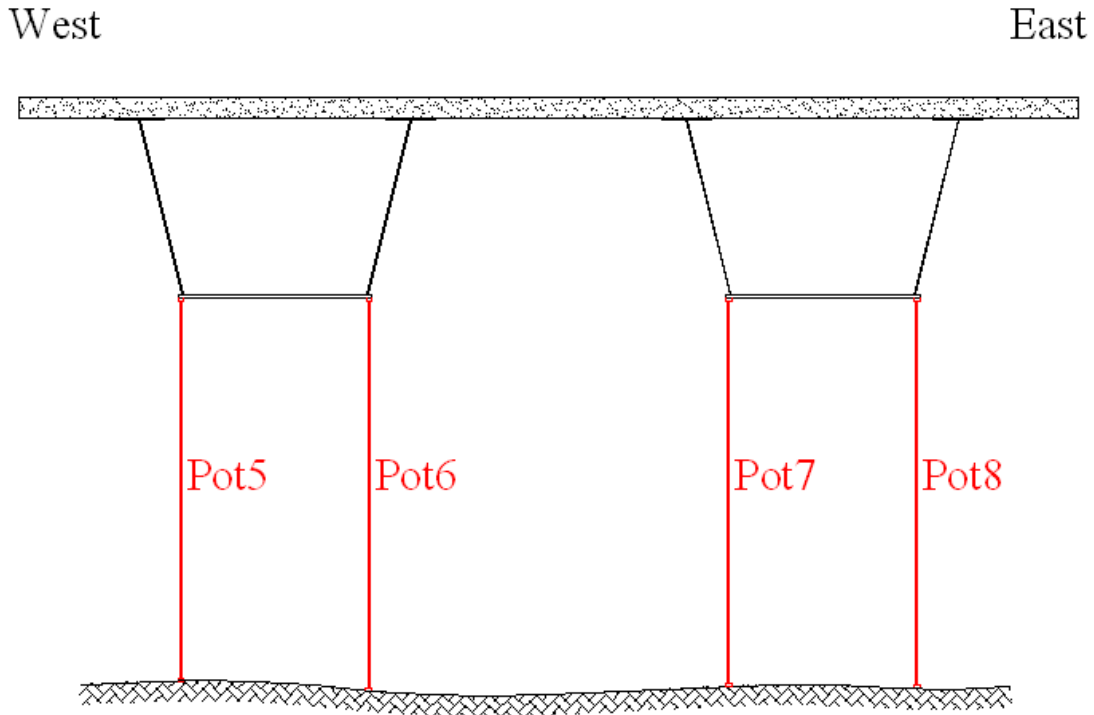


Figure 7-11 Arrangement of the potentiometers at Location 2 in the second span.

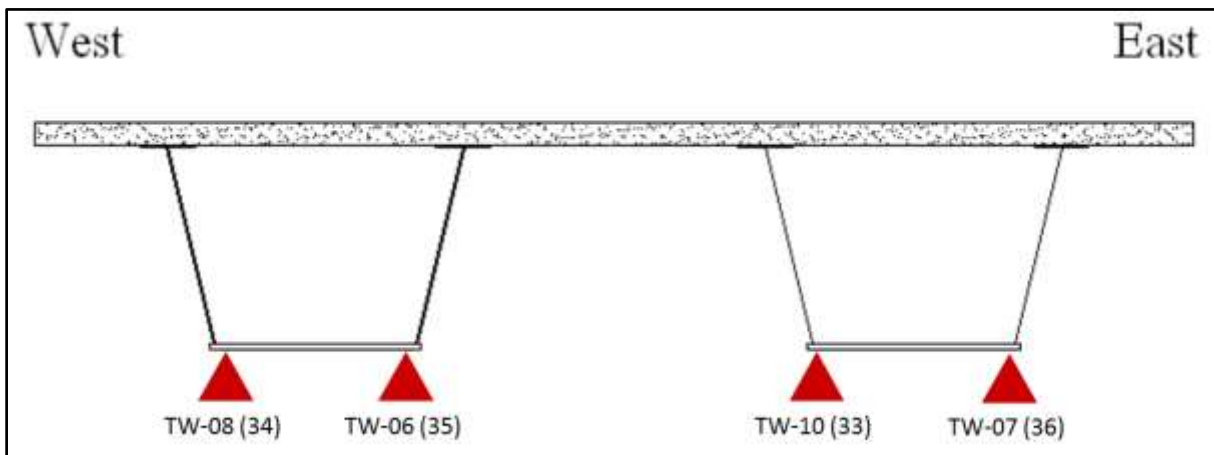


Figure 7-12 Gauge and channel ID of displacement sensors at Location 2.

7.3.2 Strain Gauges

In order to measure longitudinal strains in the steel girders of the bridge superstructure under live load, 28 strain gauges are installed in the first span of the bridge at three sections, named sections 1, 2, and 3. The distances of these sections from the end of the superstructure are 6, 58 and 138 ft, respectively. Figure 7-13 shows the location of these sections in an elevation view of the bridge. The strain gauges are attached to the outer surface of the steel box-girders at different places of each section. Figure 7-14 shows two pictures of typical strain transducers attached for the steel girders in this project.

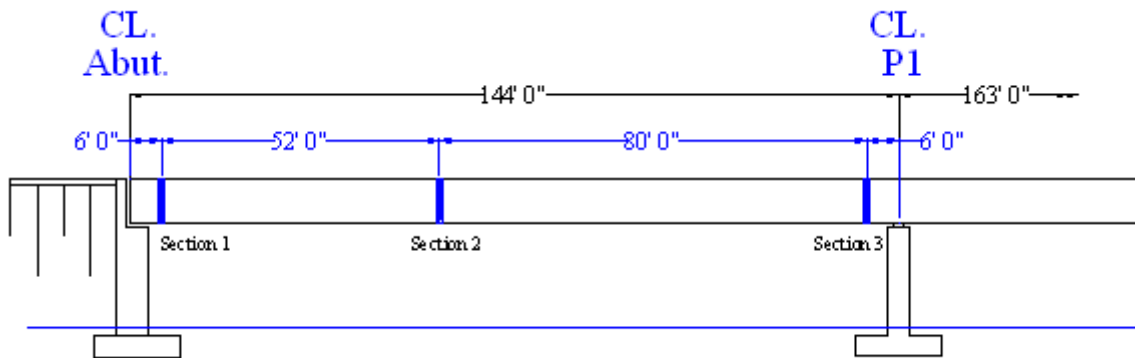


Figure 7-13 Locations of strain gauges in the first span.

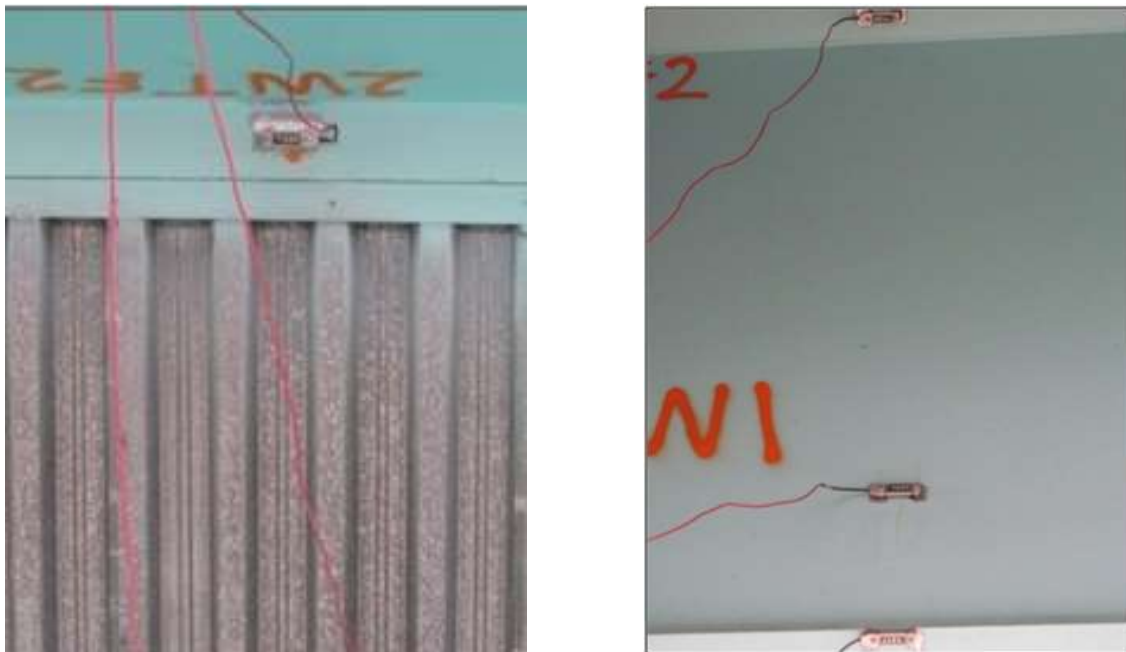


Figure 7-14 Strain transducers on box-girders (typical).

In section 1, nine strain gauges are installed on the girders. The WG has one strain gauge attached to the lower surfaces of its east top flange. That strain gauge is placed in the middle of the outstanding length of the top flange. This girder has one strain gauge installed on its west web, 15 in. above the bottom flange. The bottom flange has two strain gauges, 2 in. from the flange edges. The WG has a total of four strain gauges.

At this section, the EG has five strain gauges, two of them on the lower surface of its top flanges, similar to that of the WG. The west web of the EG has one strain gauge attached to its outer surface, 10 in. below the top of flange. The bottom flange of this girder has two strain gauges located 2 in. away from the edges. Figure 7-15 shows the arrangement of the strain gauges at this section of the bridge.

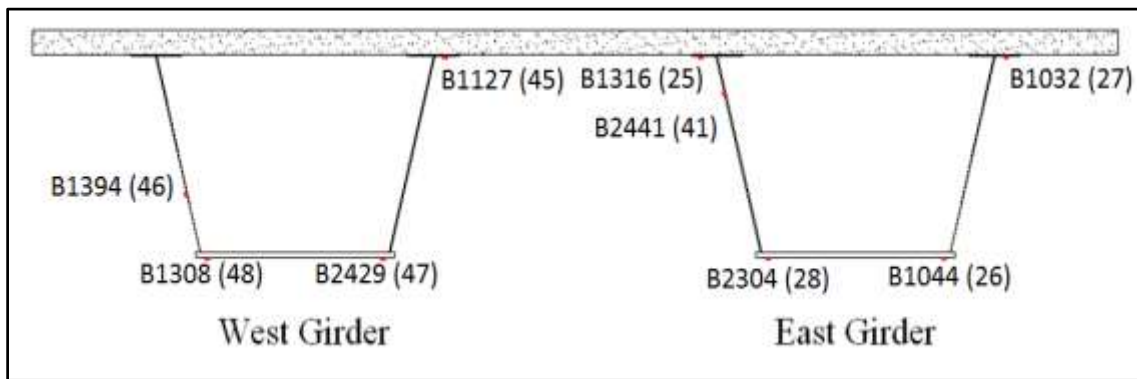


Figure 7-15 Gauge and channel ID's of strain gauges at Section 1.

Section 2, which is located 58 ft from the abutment, has nine strain gauges, five of them installed on the WG and four of them on the EG. In this section, both girders have one strain gauge under the lower surface of the top flanges, and two strain gauges at the edges of the bottom flange. The WG has one strain gauge on the east web, 10 in. above the bottom flange. Figure 7-16 displays the arrangement of the strain gauges at Section 2.

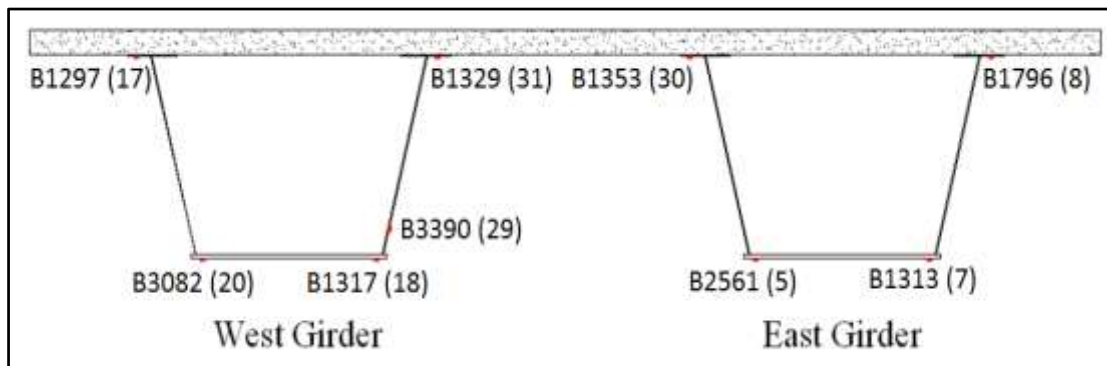


Figure 7-16 Gauge and channel ID's of strain gauges at Section 2.

Section 3, which is located 6 ft from the center line of the first pier (or 138 ft from the abutment) has ten strain gauges, five of them installed on the WG and the other five on the EG. In this section, both of the girders have a strain gauge under each of their top flanges. In addition, both have two strain gauges at the edges of their bottom flanges. The east web of the WG and the west web of EG have one strain gauge, 12 in. above the bottom flange. Figure 7-17 displays the arrangement of the strain gauges at section 3.

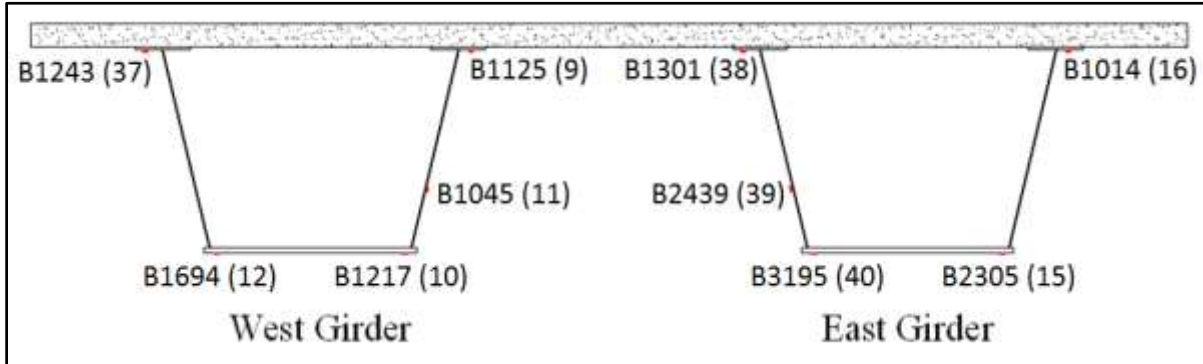


Figure 7-17 Gauge and channel ID's of strain gauges at Section 3.

7.4 Loading

Loading of the bridge was done by two trucks which were provided by District 4 of the Florida DOT. Those 10-wheel trucks, named Truck-1 and Truck-2, were weighed in a certified weigh station close to the bridge site about an hour before the testing. The weights of Truck-1 and Truck-2 were 62560 and 59940 pounds, respectively. Other specifications of the test trucks are tabulated in Table 7-3 and Table 7-4. In addition, the spacing of the axles of these trucks is illustrated in Figure 7-18 and Figure 7-19.

Table 7-3 Test Truck-1 Specifications

VEHICLE TYPE	TANDEM REAR AXLE DUMP TRUCK	
GROSS VEHICLE WEIGHT (GVW)	62,560 lbs	
WEIGHT/WIDTH - AXLE 1	13,320 lbs	7'-2"
WEIGHT/WIDTH – AXLE 2 – REAR TANDEM PAIR	49,240 lbs	7'-2"
SPACING: AXLE 1 - AXLE 2	13'-3"	
SPACING: AXLE 2 – AXLE 3	4'-8"	
WEIGHTS PROVIDED BY	Certified Weight Station	
AUTOCLICKER POSITION	Driver – 3 rd axle	
WHEEL ROLLOUT 5 REVS	53'-0"	
WHEEL CIRCUMFERENCE	10.6'	
# SEMI-STATIC PASSES	10	
# NORMAL SPEED PASSES	1	
VEHICLE PROVIDED BY	FDOT	

Table 7-4 Test Truck-2 Specifications

VEHICLE TYPE	TANDEM REAR AXLE DUMP TRUCK	
GROSS VEHICLE WEIGHT (GVW)	59,940 lbs	
WEIGHT/WIDTH - AXLE 1	11,380 lbs	7'-2"
WEIGHT/WIDTH - AXLE 2 - REAR TANDEM PAIR	48,560 lbs	7'-2"
SPACING: AXLE 1 - AXLE 2	12'-8"	
SPACING: AXLE 2 - AXLE 3	4'-6"	
WEIGHTS PROVIDED BY	Certified Weight Station	
AUTOClicker POSITION	Driver - 3 rd axle	
WHEEL ROLLOUT 5 REVS	52'-7"	
WHEEL CIRCUMFERENCE	10.52'	
# SEMI-STATIC PASSES	4	
# NORMAL SPEED PASSES	0	
VEHICLE PROVIDED BY	FDOT	

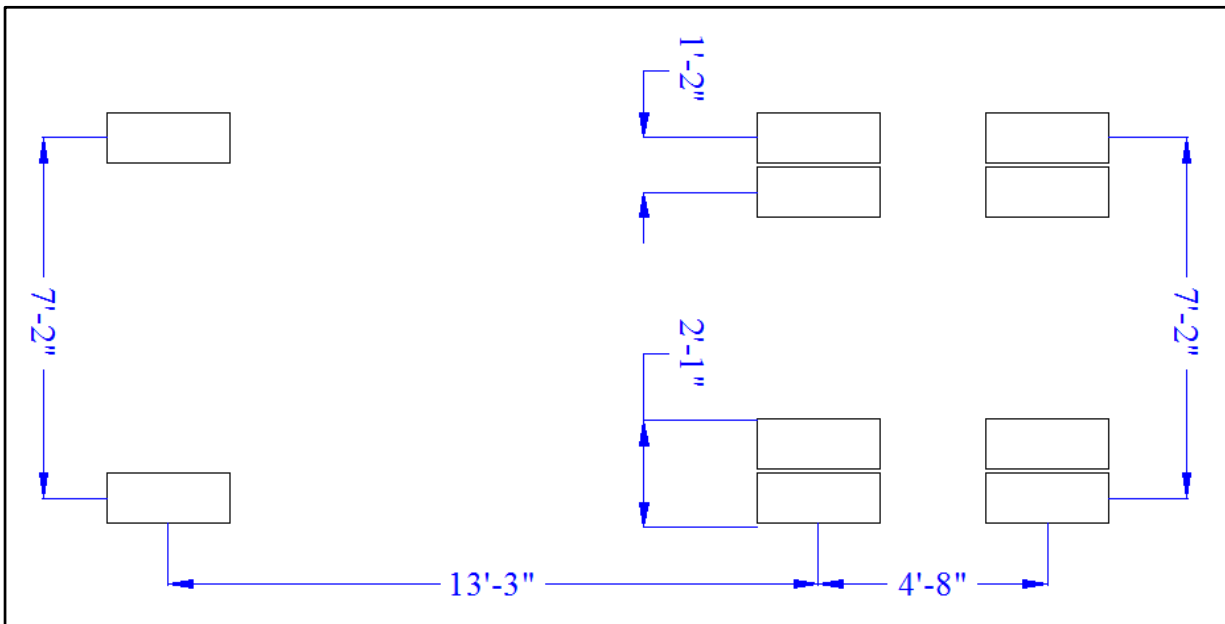


Figure 7-18 Test Truck-1 axle spacing.

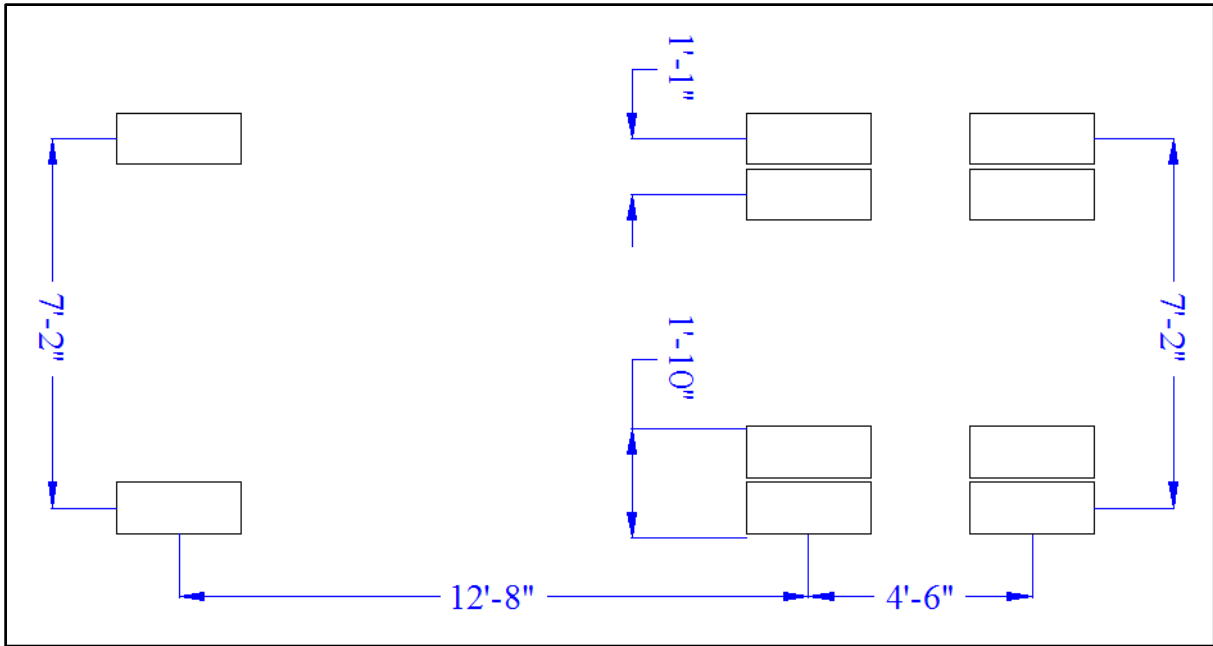


Figure 7-19 Test Truck-2 axle spacing.

Trucks were moved along three paths over the bridge. Each path is defined based on the distance of the driver side wheels from the inner face of the east railing of the bridge. This distance was equal to 2 ft, 10 ft - 5 in. and 18 ft -10 in. for the three paths. These loading paths are defined in Figure 7-20 and Table 7-5.

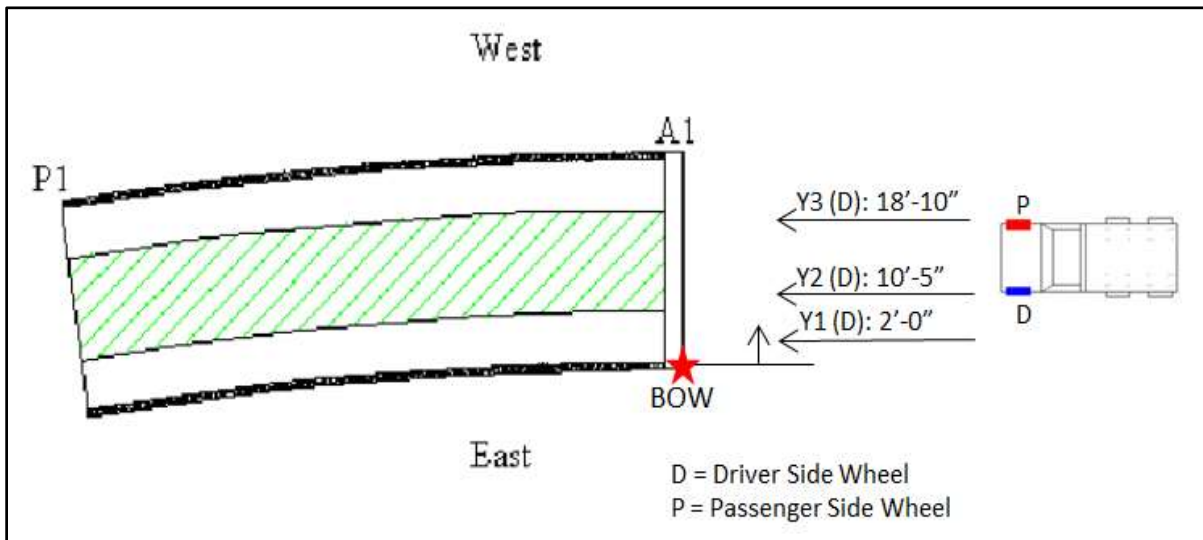


Figure 7-20 Test truck path locations.

Table 7-5 Loading Path Definitions

TEST VEHICLE DIRECTION	From North to South
TEST BEGINNING POINT	Front axle at X = ~21'-3"($\pm 1'$)
LATERAL LOAD POSITIONS (PERPENDICULAR TO ROADWAY)	Y1 (D) = 2'-0" Y2 (D) = 10'-5" Y3 (D) = 18'-10"

The loading was done in eight different scenarios. In scenarios 1, 2, and 3, Truck-1 was run over path-1, path-2 and path-3, respectively with a slow (crawling) speed. In scenario-4, Truck-2 moved along path-1. In scenario-5, Truck-1 and Truck-2 traveled side by side on path-3 and path-1, respectively. In scenario-6, Truck-1 ran on path-2 with a speed of 30 MPH. In scenarios 7 and 8, Truck-1 followed by Truck-2 moved along path-1 and path-2, respectively. Therefore, the only high speed loading was at scenario-6 while all other loading scenarios conducted in a very low speed.

Table 7-6 Loading Scenario Definitions

TEST SCENARIO	LOADING CONFIGURATION	<i>LATERAL POSITION</i>
1	Truck-1	Y1
		Y1
2		Y2
		Y2
3		Y3
		Y3
4	Truck-2	Y1
5	Truck-2 (Y1), Truck-1 (Y3)	Y1 & Y3
6	Truck-1 (Y2) Roadway Speed Test	Y2
7	Truck-1 followed by Truck-2	Y1
8	Truck-1 followed by Truck-2	Y2
	Truck-1 followed by Truck-2	Y2
ADDITIONAL COMMENTS		Weather: High 70's, humid

7.5 Finite Element Modeling

The main objective of this field testing was to calibrate the finite element models. These calibrated finite element models are required for further understanding of the behavior of twin box-girder bridges. Therefore, the finite element model of the Bridge 860600 is used to evaluate the responses of the bridge under the defined loading scenarios. The ABAQUS FEA software package is used for this purpose. The results of the analyses are compared with the field testing data.

An attempt was made to include all possible details in the finite element model. Therefore, the top flange, web, and bottom flange of the box-girders, web transverse stiffeners, internal and external diaphragms, concrete deck, and railings of the bridge are modeled using shell elements. The only elements that are modeled using beam elements are the internal bracings of the girders. Then, the footprints of the trucks in each loading scenario are applied to the concrete deck of the

bridge. This is done using surface pressure feature in Abaqus FEA. Figure 7-21 shows the model with and without the concrete deck, so that the modeling details can be more visible. The meshed model shows meshing of the cracked zone of a damaged girder.

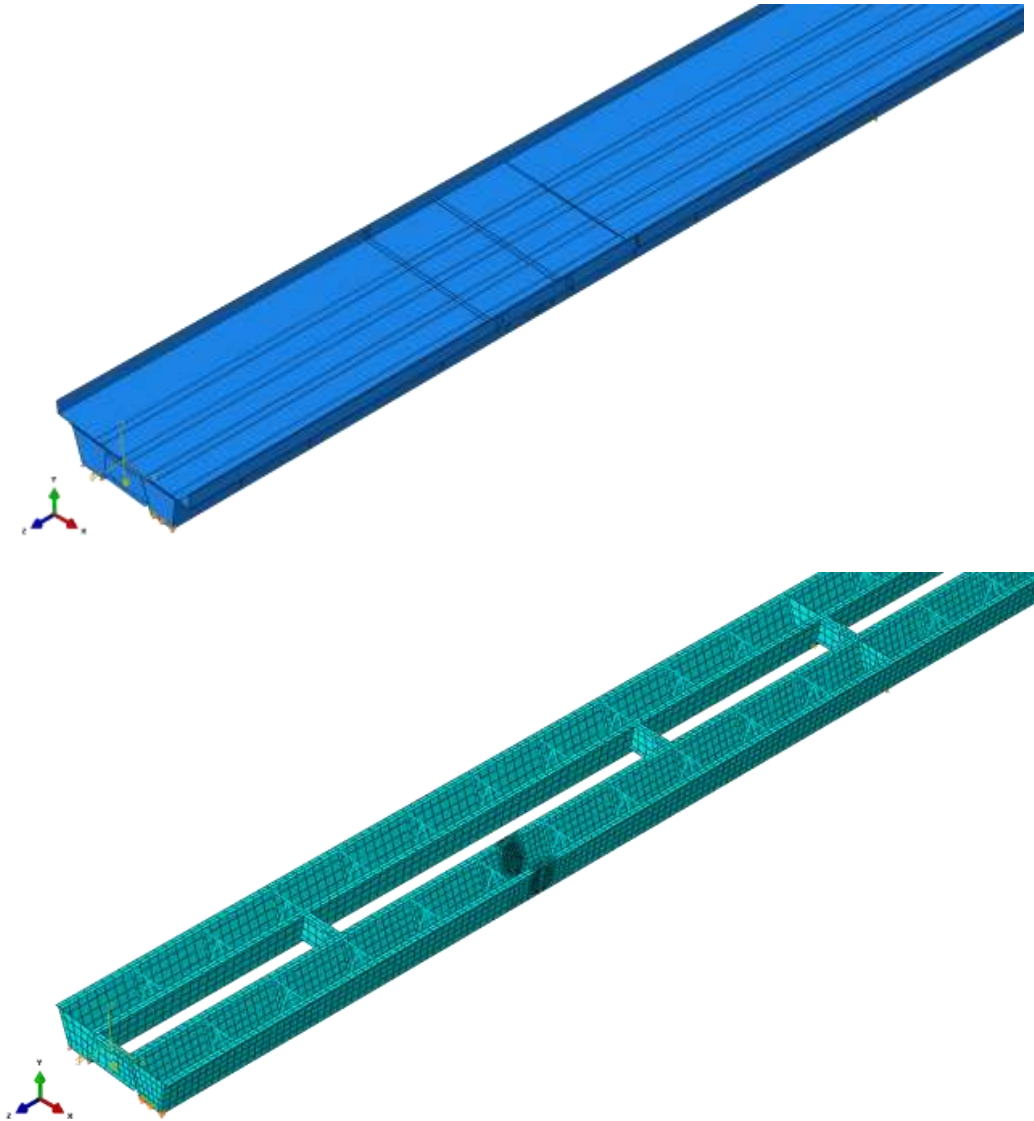


Figure 7-21 Finite element model of the first span of Ft. Lauderdale bridge 860600.

7.6 Qualitative Review of Test Data

Field data was examined graphically first by BDI and then by FIU to determine its quality and usefulness for analytical comparisons. Some of the typical indicators of data quality include reproducibility between identical truck crossings, elastic behavior (strains returning to zero after truck crossing), and observation of any unusual responses that might indicate possible gauge malfunctions.

Responses as a Function of Load Position:

Data recorded from the wireless truck position indicator (BDI Autoclicker) was processed so that all of the corresponding response data could be presented as a function of vehicle position. This was done so that during analytical modeling, important measurement responses could be directly related to a specific load location rather than an arbitrary point in time.

Reproducibility and Linearity:

Responses from identical truck passes were very reproducible, as shown in Figure 7-22 and Figure 7-23. In addition, all response data was linear with respect to load magnitude and truck position. Note that the majority of responses returned to zero (barring thermal drift for strains – see next item), indicating elastic behavior. All of the response histories had a similar degree of reproducibility and linearity, indicating that the data collected was of good quality.

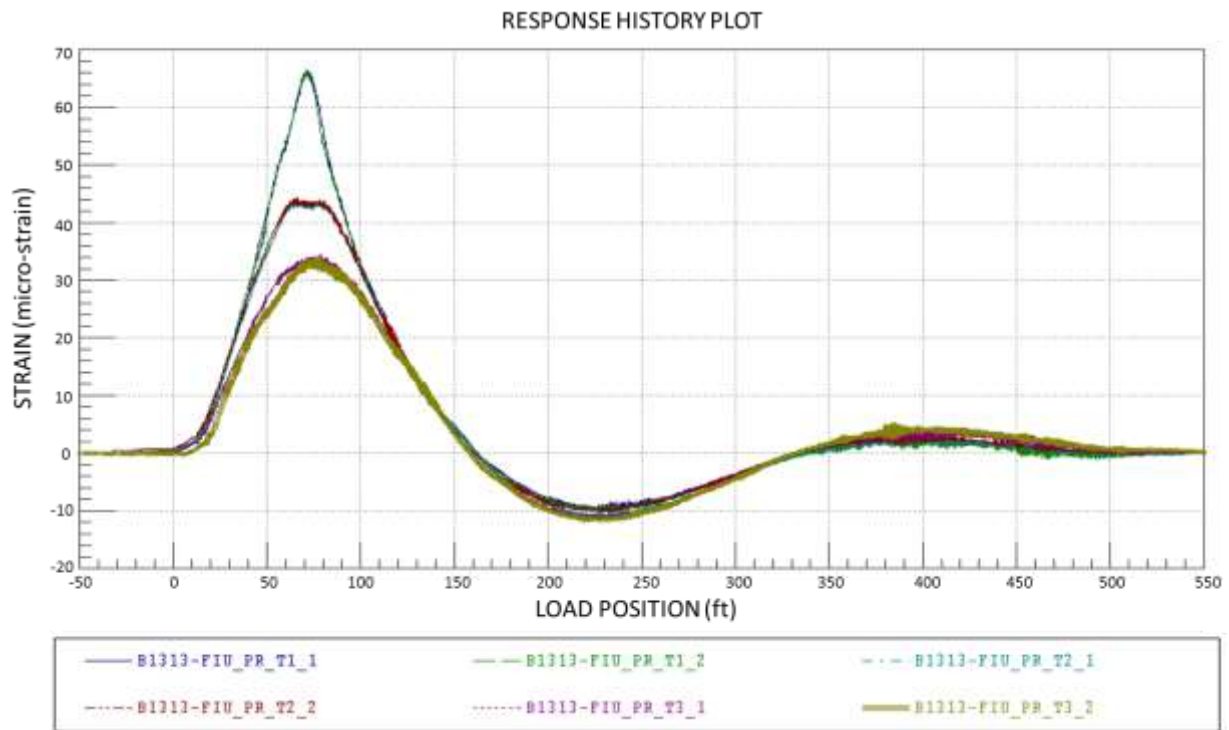


Figure 7-22 Reproducibility of strain response histories (typical).

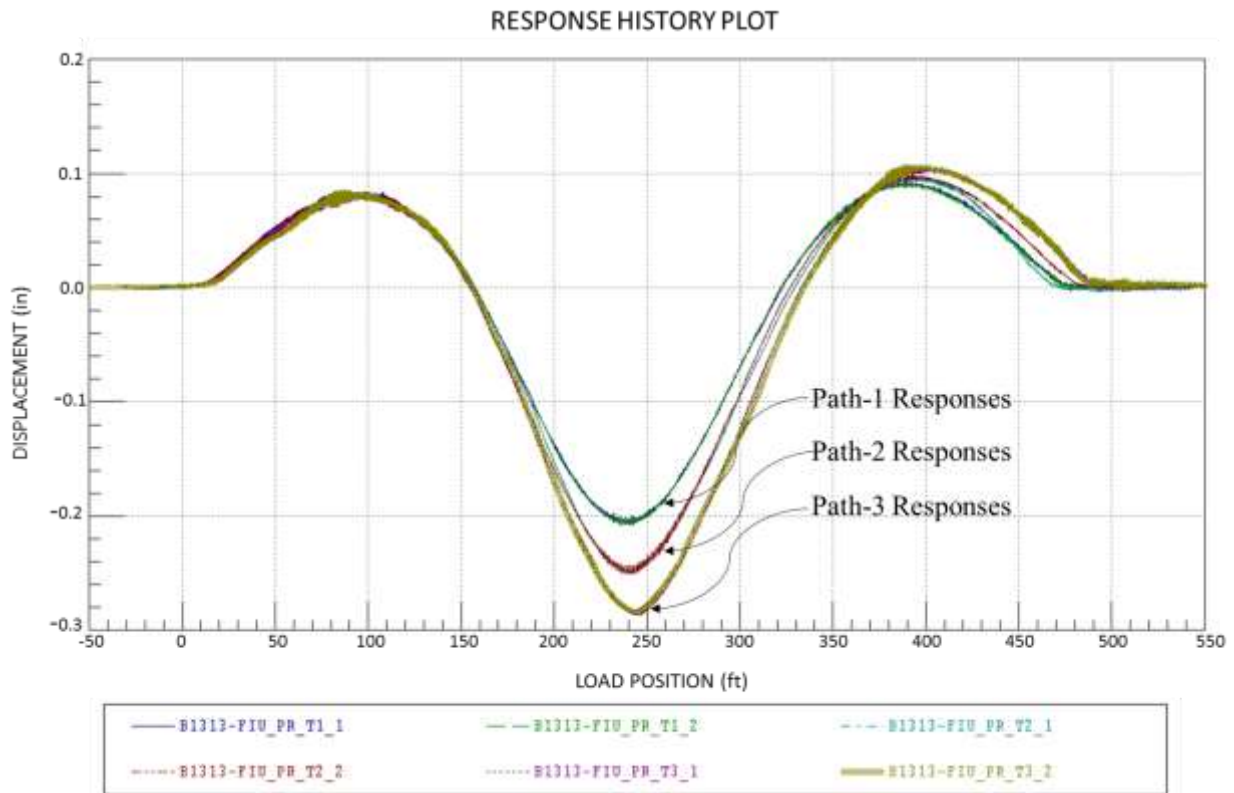


Figure 7-23 Reproducibility of displacement response histories (typical).

Thermal Drift:

During the initial data investigation, it was observed that the majority of the strain response data tended to drift throughout the load tests, as shown in Figure 7-24. This is a common occurrence with strain transducers since they have very little mass and react to temperature changes very rapidly compared to the structure to which they are attached to. Generally, temperature drift is not a concern for short duration load tests because the magnitude of the drift is very small compared to the live-load responses. However, due to the extended duration of the tests (greater than 4 minutes) some of the strain measurements were able to drift by as much as $6 \mu\epsilon$. To account for the drift, a linear offset was assumed for the duration of each load test and subtracted from each sensors' output. This is illustrated in Figure 7-25, where the raw response and corrected response for Truck-1 load along path-1 are shown on the same plot.

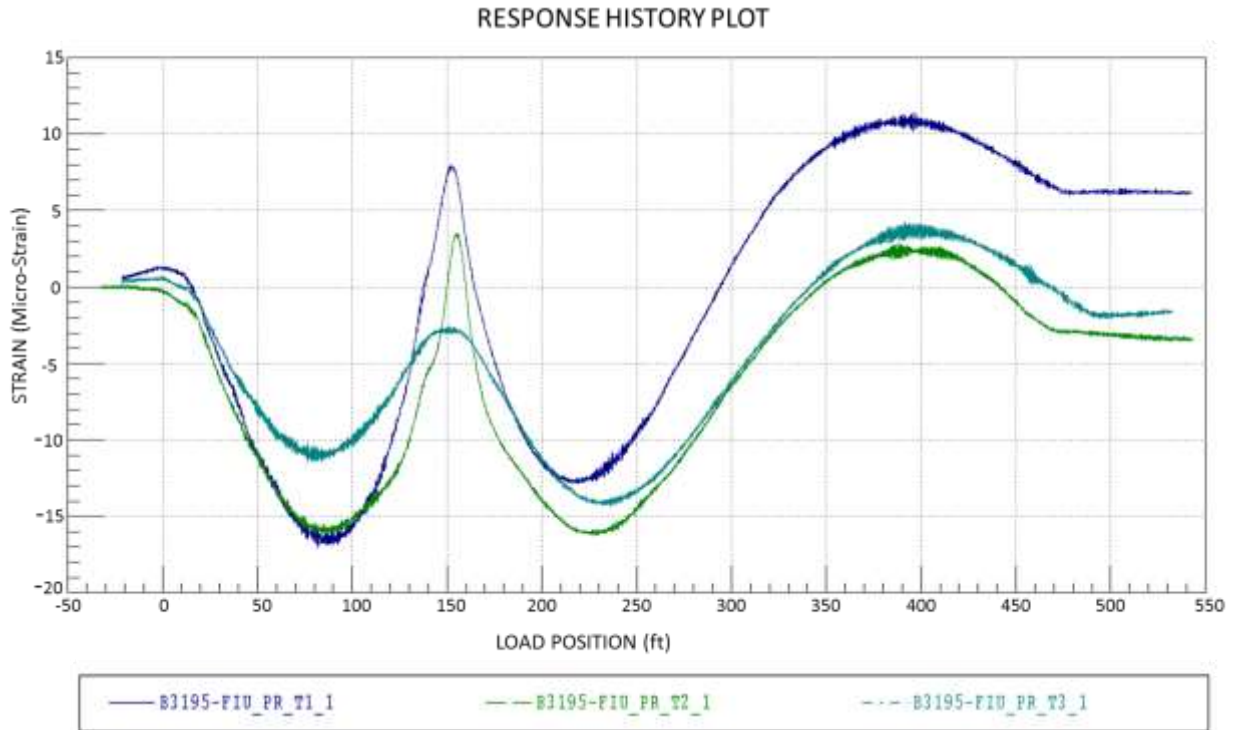


Figure 7-24 Example of variable thermal drift observed during testing.

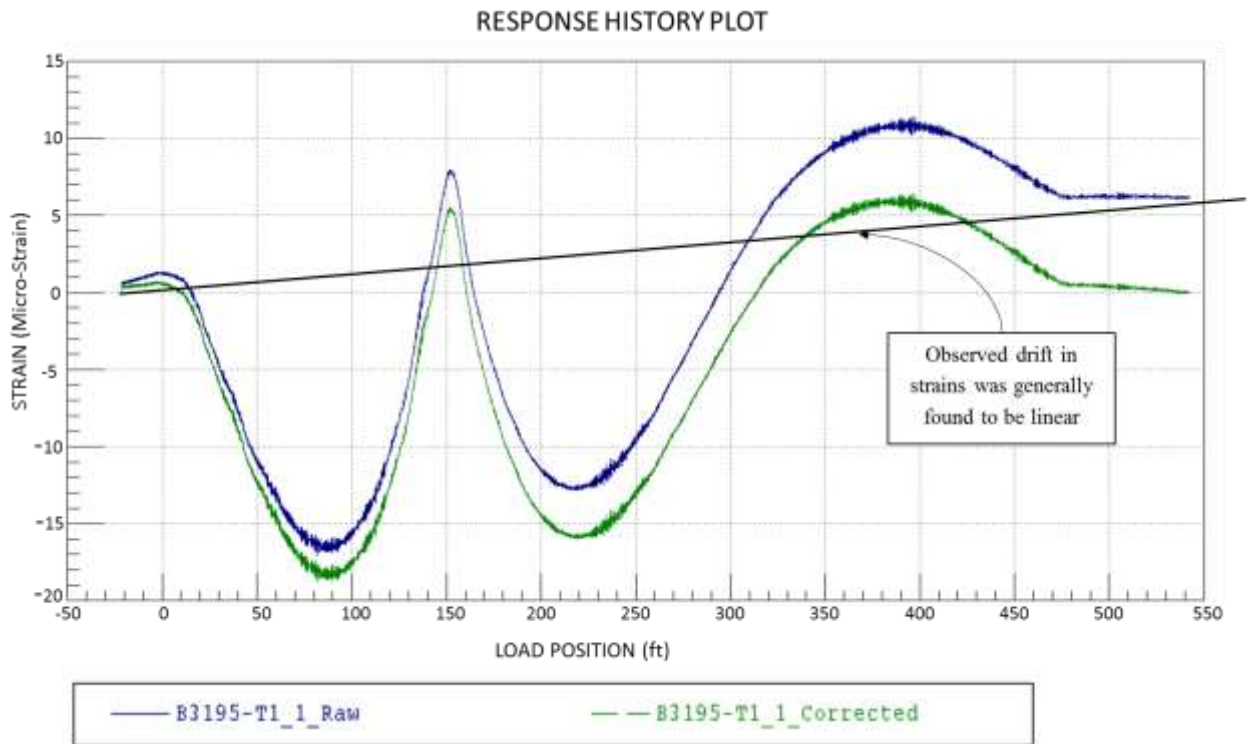


Figure 7-25 Comparison of raw and thermally corrected strain data.

Dynamic Component of Response:

Tests at both crawl speed (~3 mph) and roadway speed (~30 mph) were performed along path-2 using test Truck-1. When comparing strain responses from the two different tests, a fairly significant dynamic effect was observed in the roadway speed test as compared to the crawl speed test, seen in Figure 7-26. In this figure the blue response is from the crawl speed test while the green response is from the roadway speed test. Comparing with the crawl speed test, the roadway speed test saw a dynamic effect of approximately 12%. It is important to note that this impact factor is less than the impact factor of 33% specified in AASHTO *LRFD Bridge Design Specifications* due to dynamic loading. This difference is because the dynamic impact factor specified in AASHTO *LRFD Bridge Design Specifications* is defined as the ratio of peak response to static response, while the dynamic effect found here are calculated based on the peak responses between two dynamic loading tests.

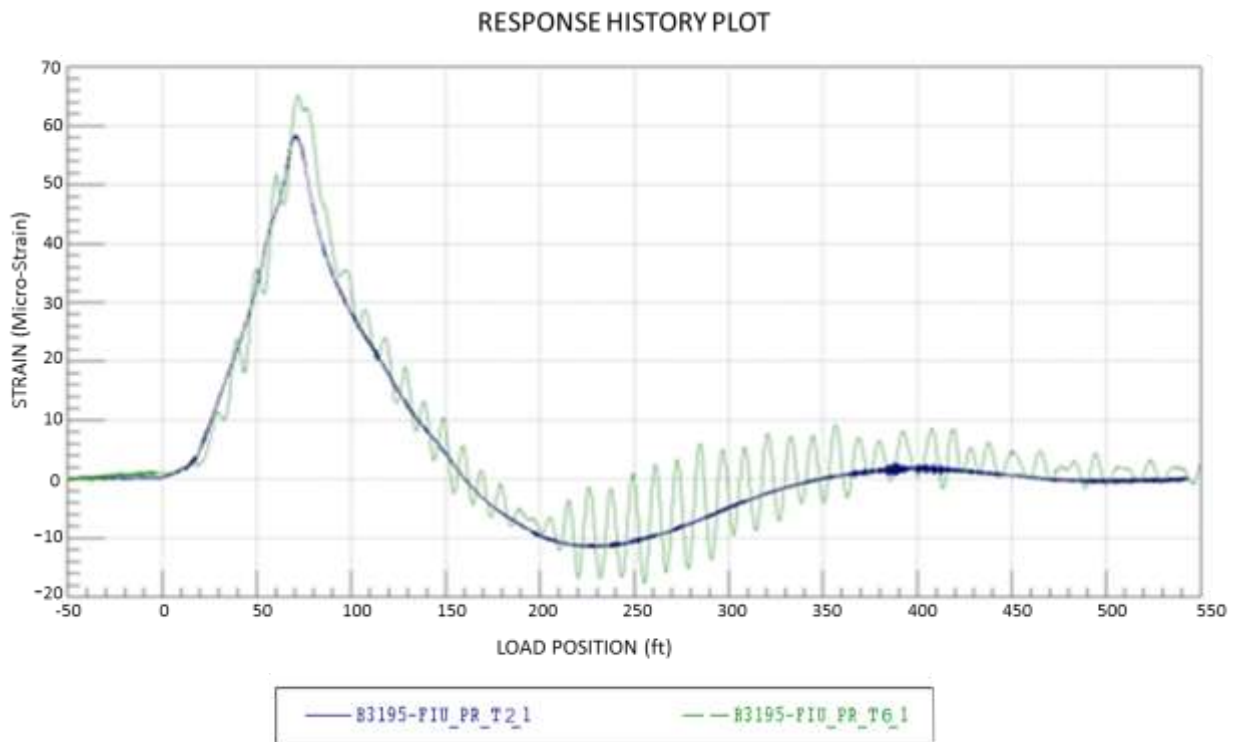


Figure 7-26 Strain history comparison – crawl speed vs. roadway speed at Section 2.

7.7 Comparison of Field Test Data and FEA Results

In general, the results of field testing were in good agreement with the results of finite element analysis. In this section, some of the results of finite element analysis of the bridge under loading scenarios are compared to the field test data. The selected loading scenarios include scenario-3 which has Truck-1 on path-3, scenario-5 which has Truck-2 on path-1 and Truck-1 on path-3 and

loading scenario-7 which has Truck-1 followed by Truck-2 on path-1. Figure 7-27 through Figure 7-32 compare the deflection of the girders in first and second spans due to application of selected loading scenarios.

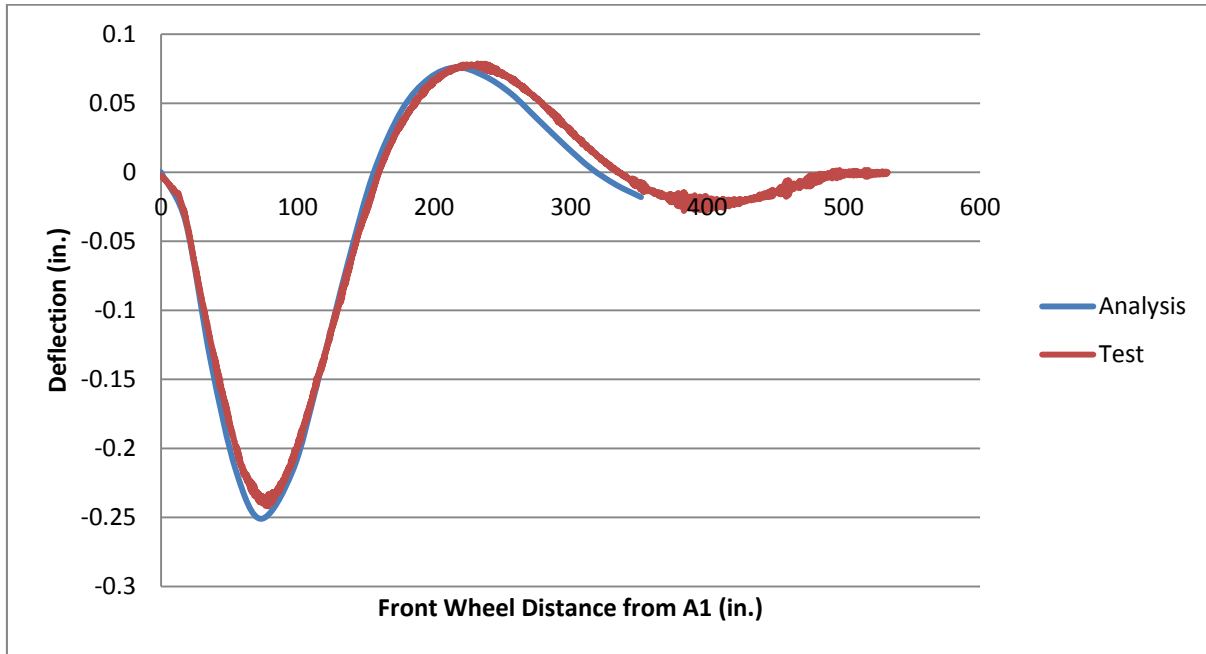


Figure 7-27 Vertical deflection of west edge of WG: 59 ft from north abutment, Truck-1 on path-3.

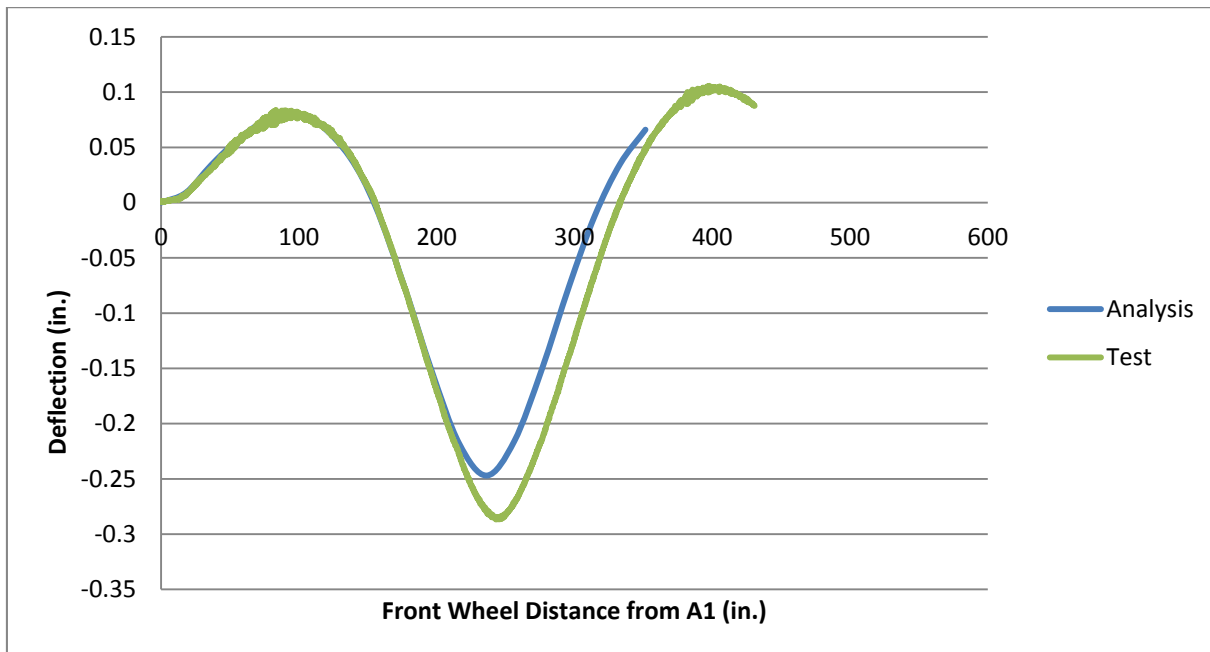


Figure 7-28 Vertical deflection of west edge of WG: 225.5 ft from north abutment, Truck-1 on path-3.

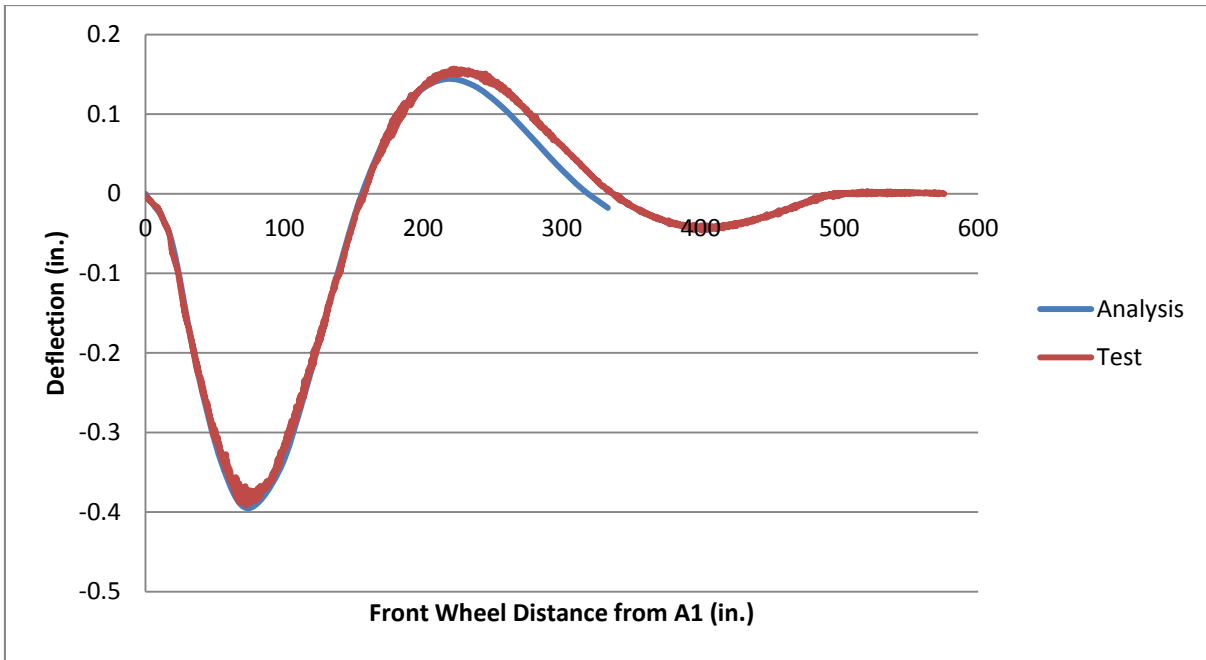


Figure 7-29 Vertical deflection of west edge of EG: 59 ft from north abutment, Truck-1 on path-3 and Truck-2 on path-1.

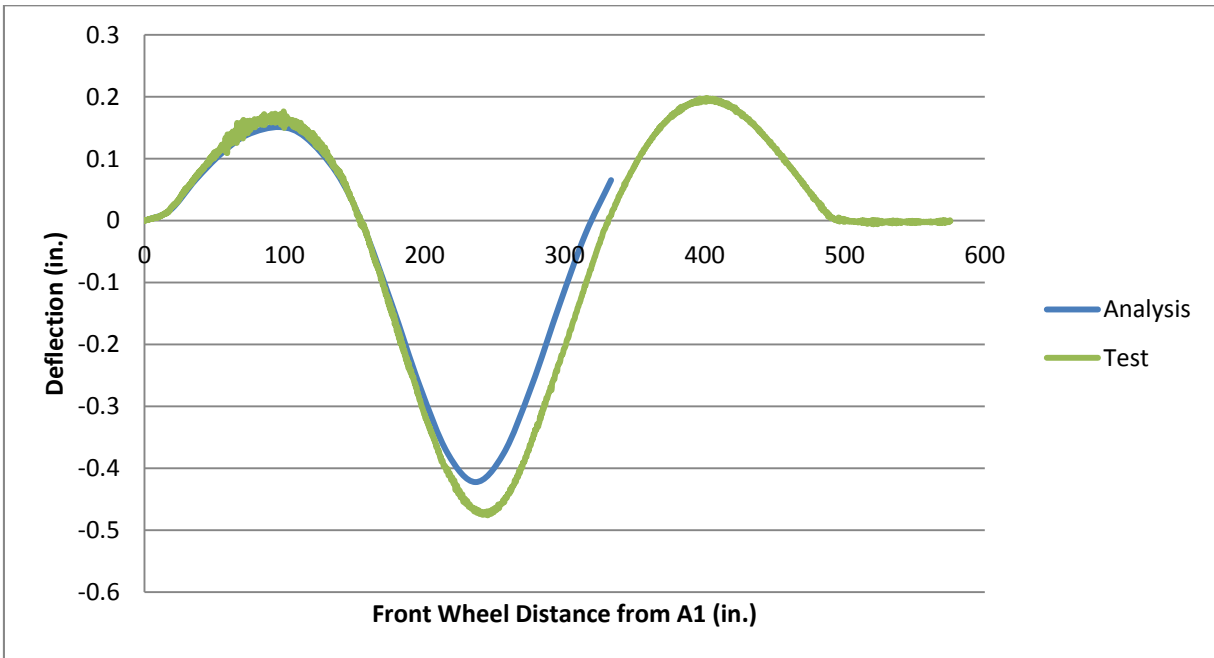


Figure 7-30 Vertical deflection of west edge of WG: 225.5 ft from north abutment, Truck-1 on path-3 and Truck-2 on path-1.

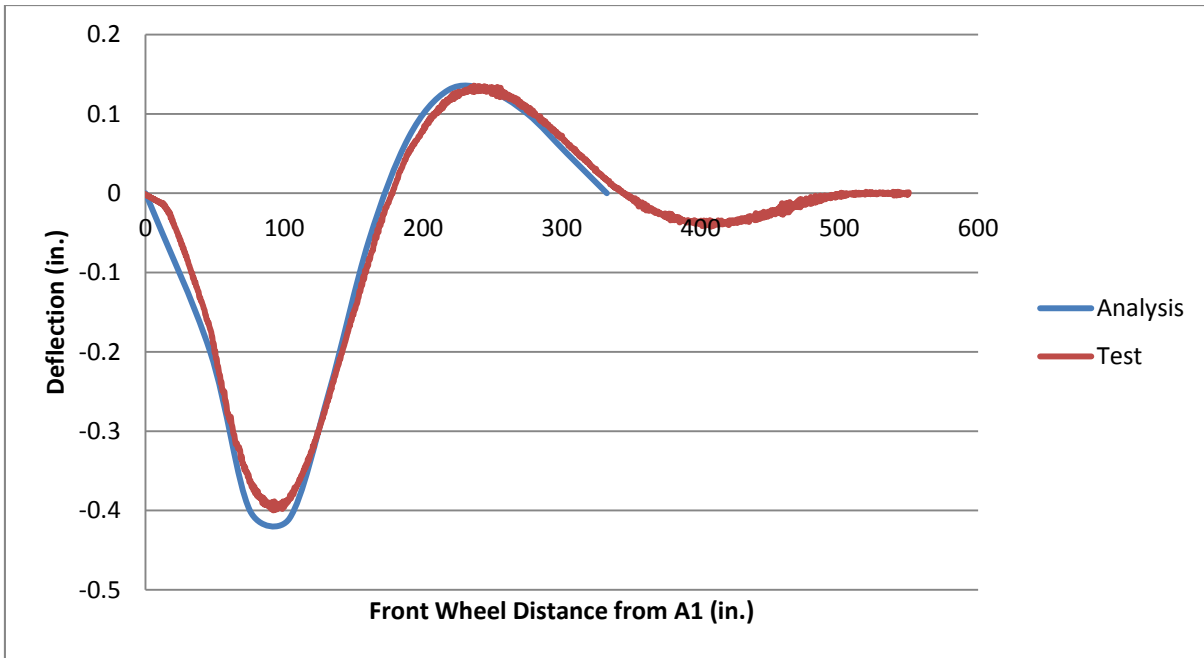


Figure 7-31 Vertical deflection of west edge of EG: 59 ft from north abutment, Truck-1 followed by Truck-2 on path-1.

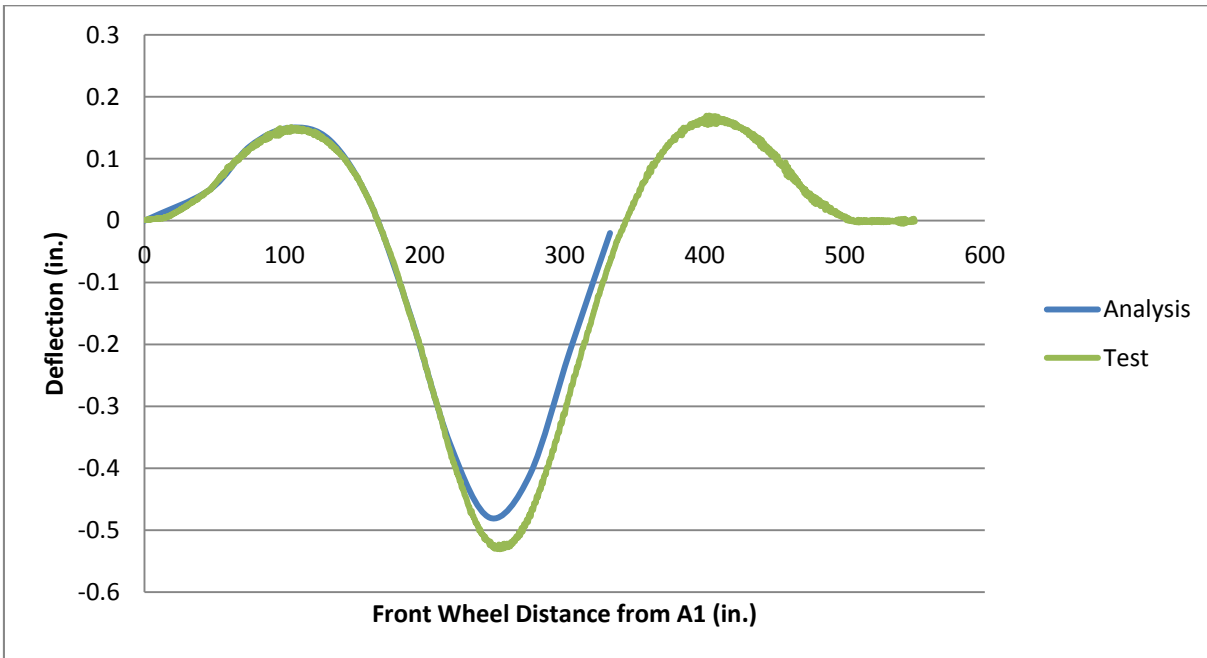


Figure 7-32 Vertical deflection of east edge of EG: 225.5 ft from north abutment, Truck-1 followed by Truck-2 on path-1.

It is observed that the field test deflections are in agreement with computer model deflections. Figure 7-33 through Figure 7-38 illustrate the longitudinal stresses of the bottom flange of the box-girders due to application of loading scenario-3 to the bridge.

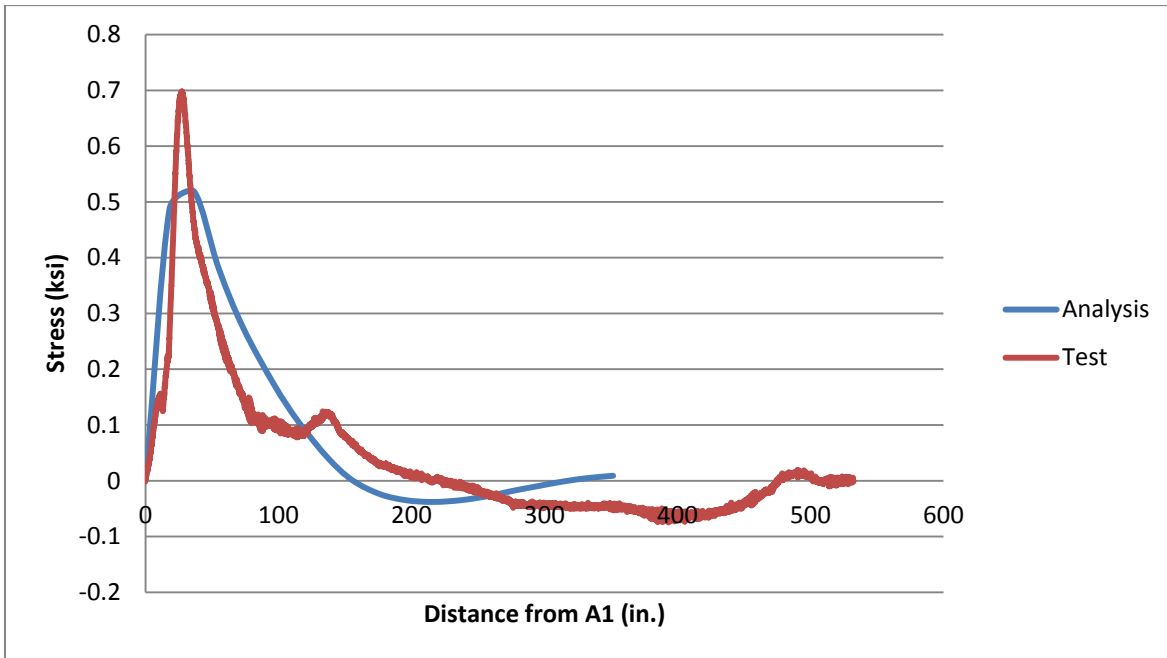


Figure 7-33 Longitudinal stress at 6 ft from north abutment in the west edge of bottom flange of WG: Truck-1 on Path-3.

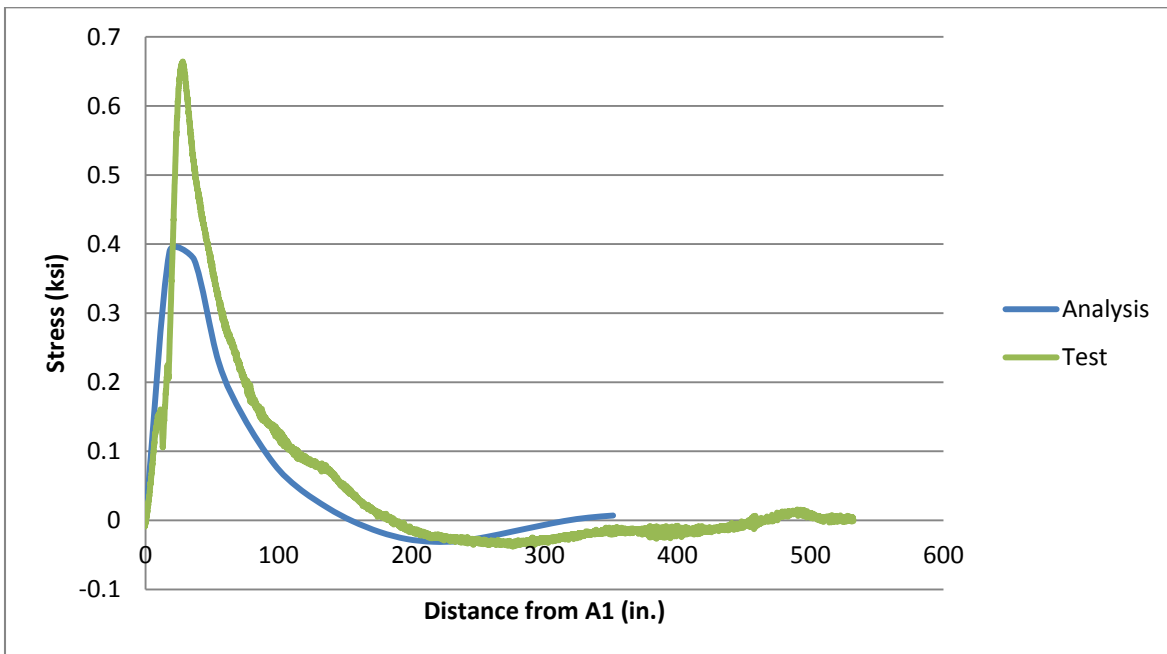


Figure 7-34 Longitudinal stress at 6 ft from North Abutment in the west edge of bottom flange of EG: Truck-1 on path-3.

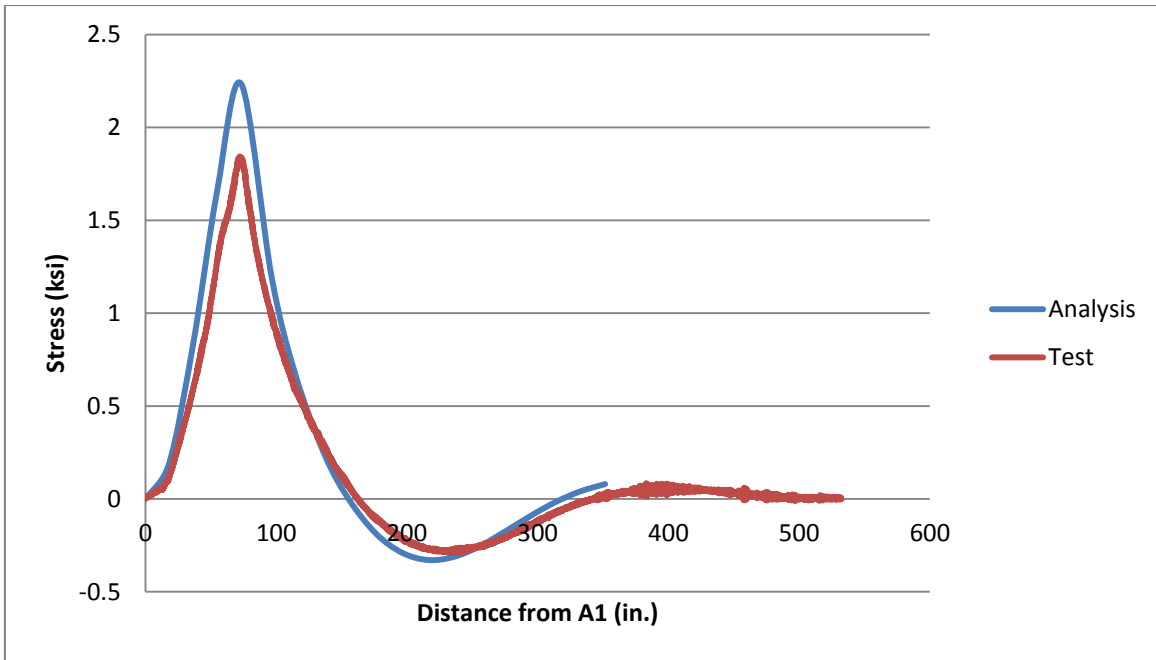


Figure 7-35 Longitudinal stress at 58 ft from north abutment in the west edge of bottom flange of WG: Truck-1 on path-3.

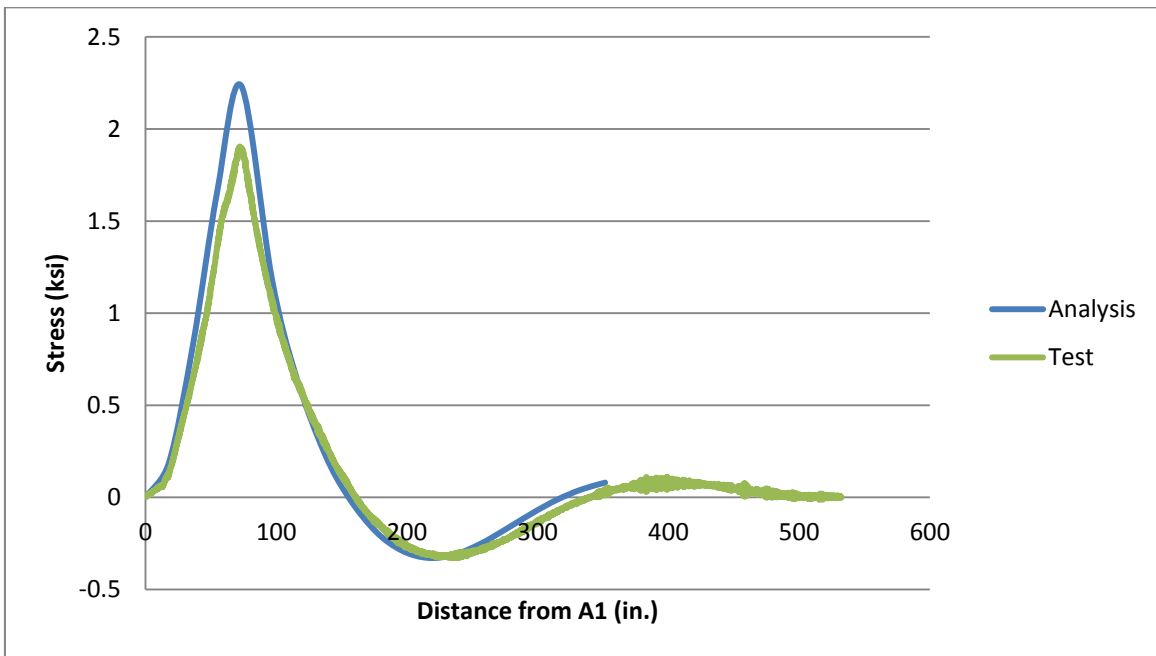


Figure 7-36 Longitudinal stress at 58 ft from north abutment in the east edge of bottom flange of WG: Truck-1 on path-3.

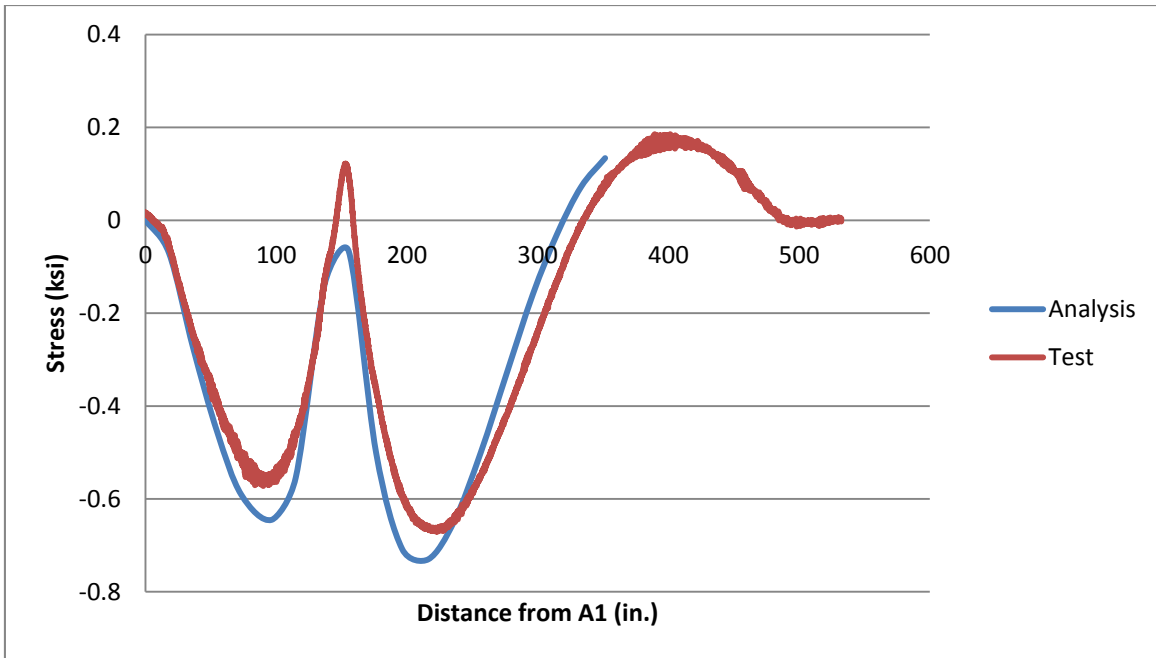


Figure 7-37 Longitudinal stress at 138 ft from north abutment in the west edge of bottom flange of WG: Truck-1 on path-3.

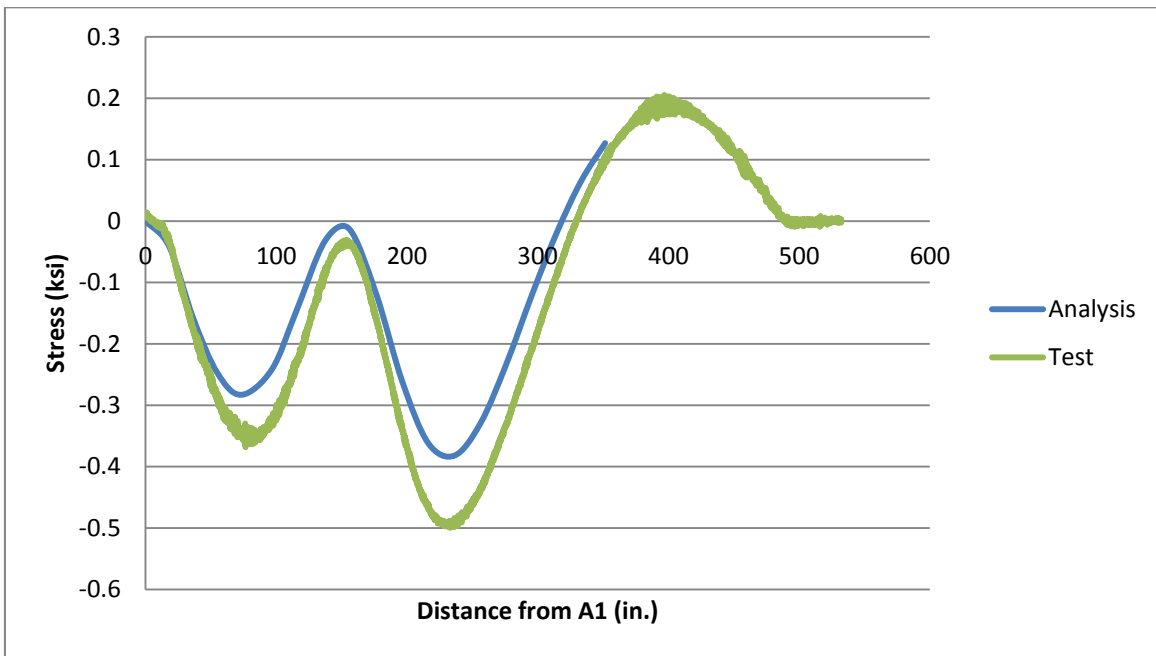


Figure 7-38 Longitudinal stress at 138 ft from north abutment in the east edge of bottom flange of WG: Truck-1 on path-3.

Figure 7-39 through Figure 7-44 compare the longitudinal stresses of the bottom flange of the box-girders due to application of loading scenario-5 to the bridge.

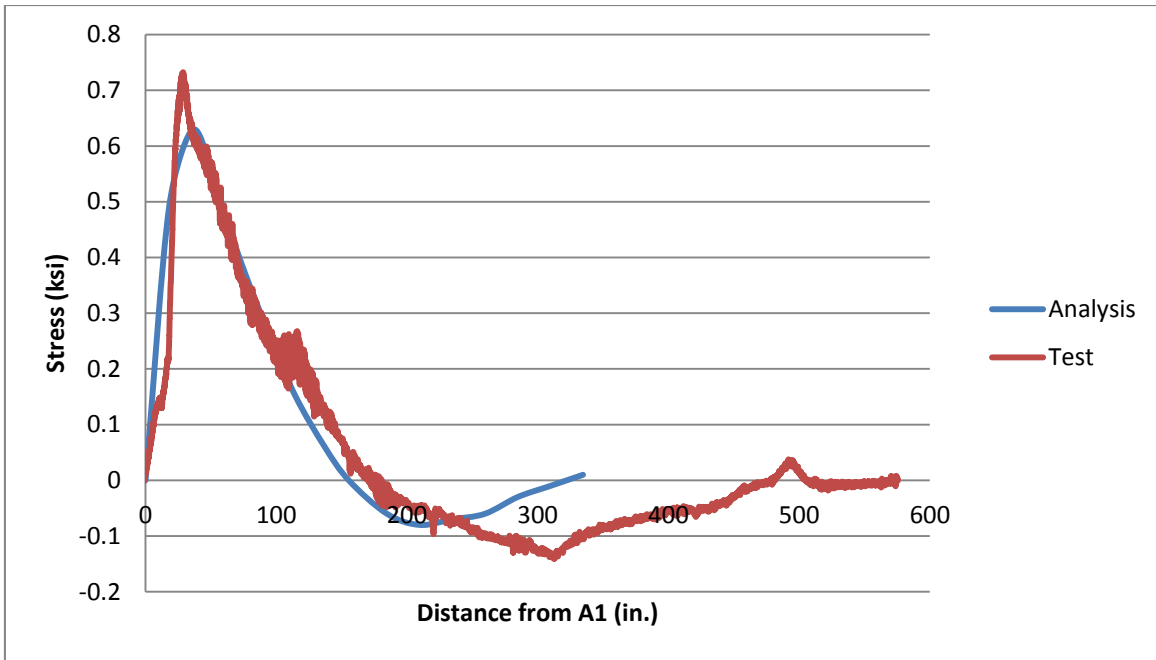


Figure 7-39 Longitudinal stress at 6 ft from north abutment in the west edge of bottom flange of WG: loading scenario-5.

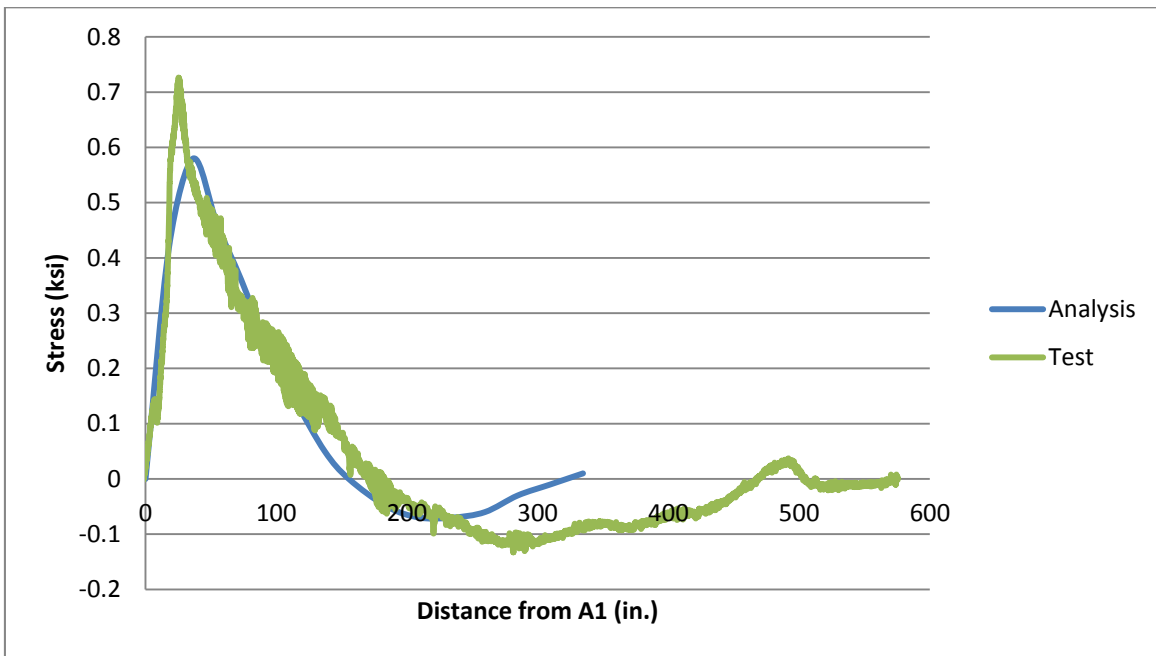


Figure 7-40 Longitudinal stress at 6 ft from north abutment in the west edge of bottom flange of EG: loading scenario-5.

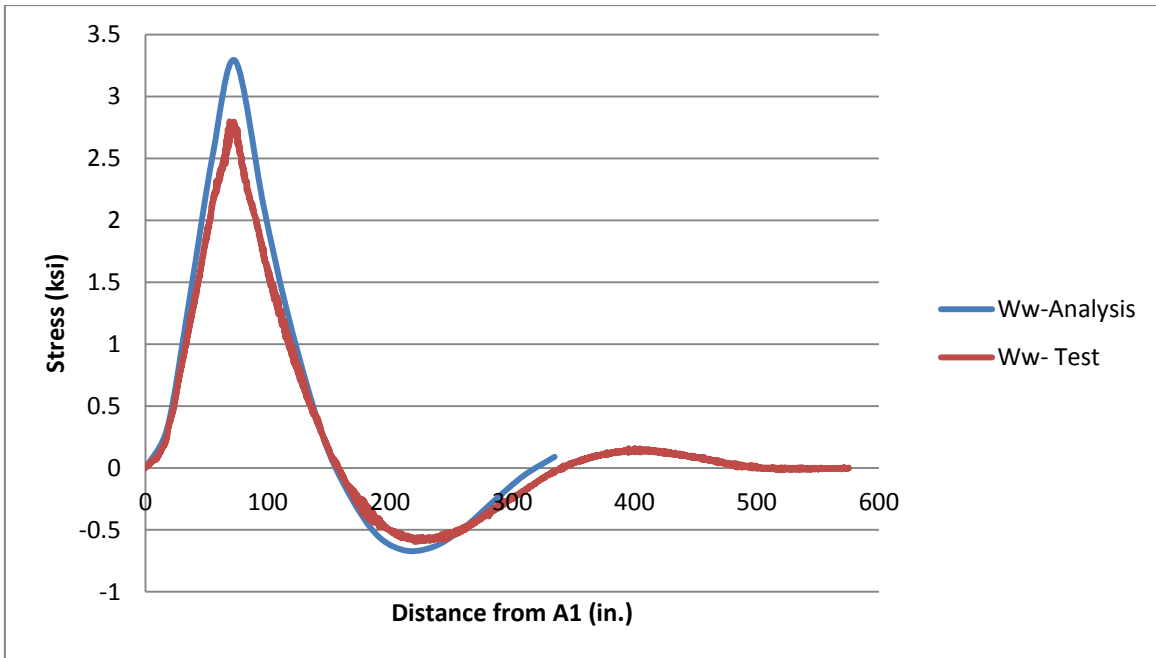


Figure 7-41 Longitudinal stress at 58 ft from north abutment in the west edge of bottom flange of WG: loading scenario-5.

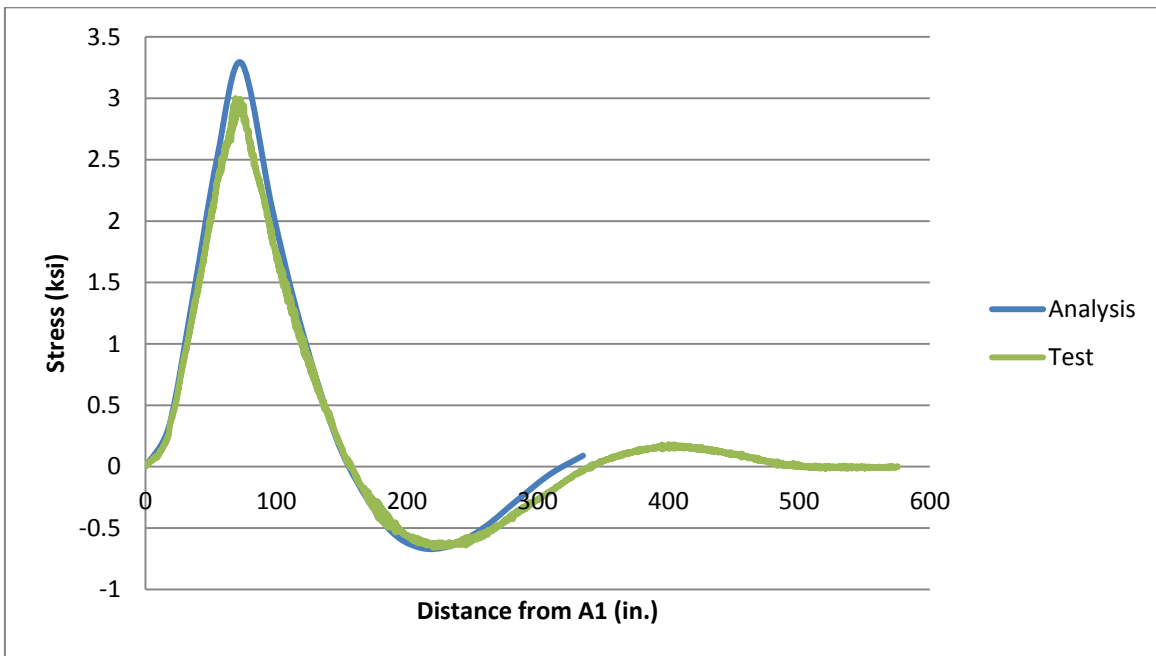


Figure 7-42 Longitudinal stress at 58 ft from north abutment in the east edge of bottom flange of WG: loading scenario-5.

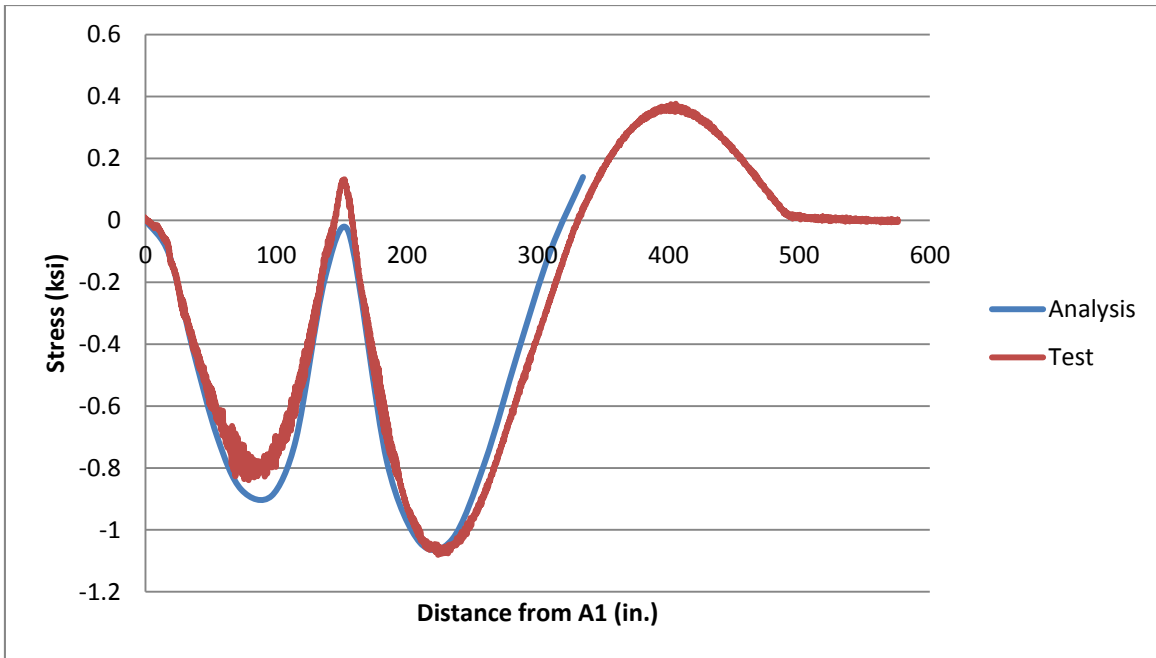


Figure 7-43 Longitudinal stress at 138 ft from north abutment in the west edge of bottom flange of WG: loading scenario-5.

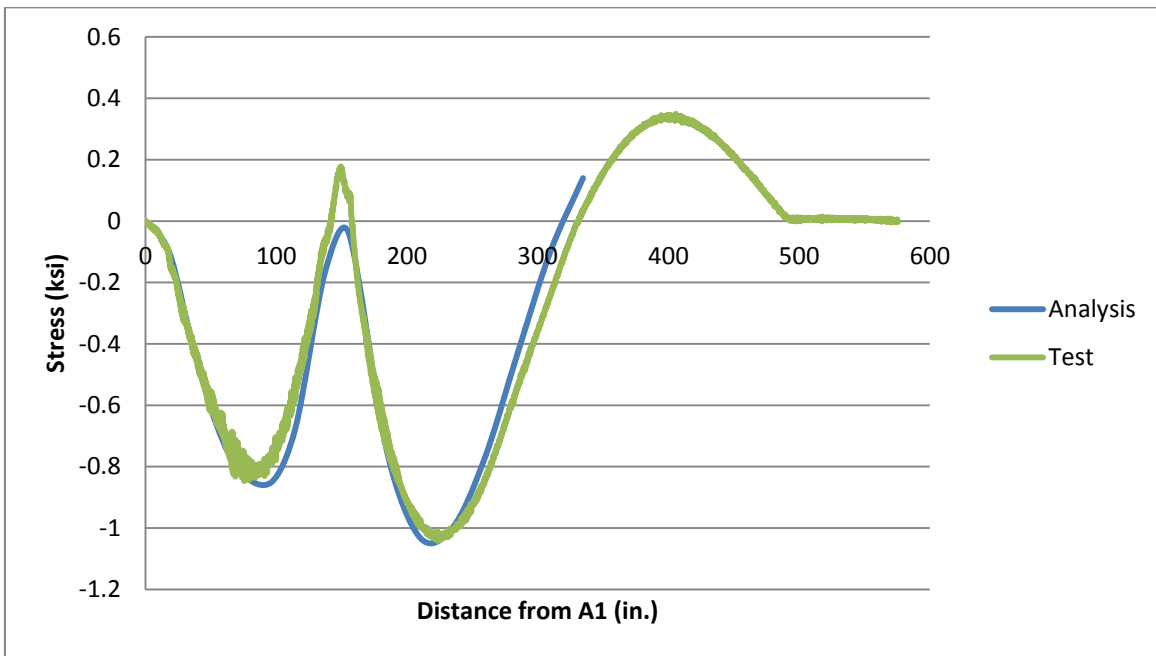


Figure 7-44 Longitudinal stress at 138 ft from north abutment in the east edge of bottom flange of WG: loading scenario-5.

In Figure 7-45 to Figure 7-50, the longitudinal stress of the bottom flange of the box-girders that resulted from finite element analysis of loading scenario-7 are compared to the test data.

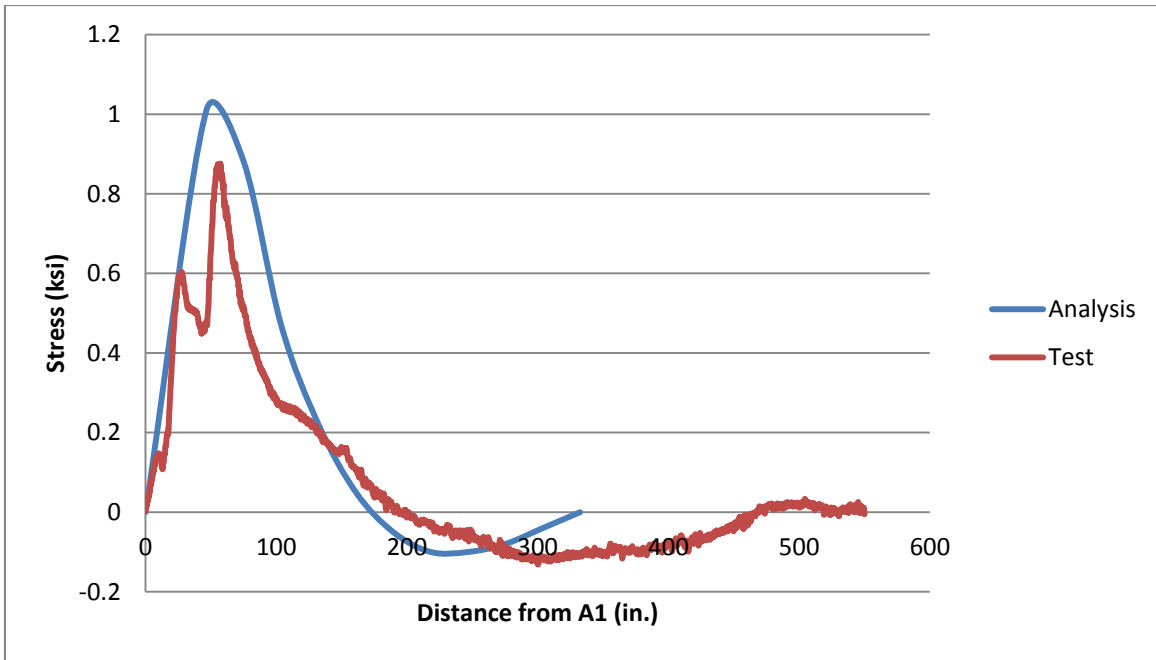


Figure 7-45 Longitudinal stress at 6 ft from north abutment in the west edge of bottom flange of EG - Truck-1 followed by Truck-2 on path-1.

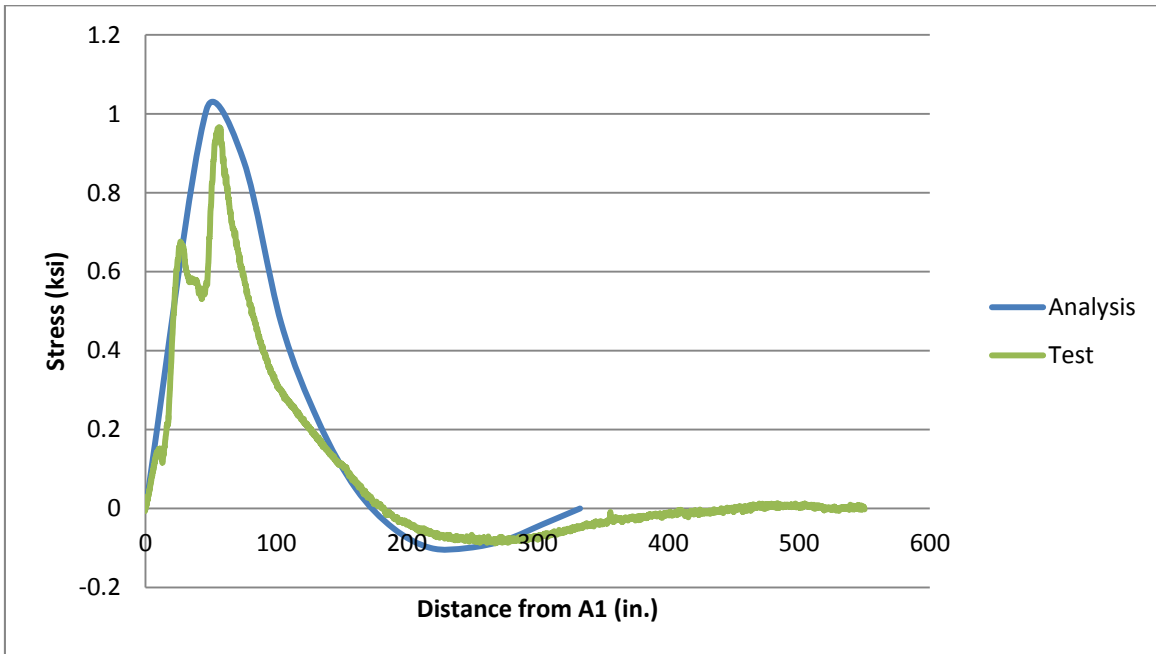


Figure 7-46 Longitudinal stress at 6 ft from north abutment in the east edge of bottom flange of EG: Truck-1 followed by Truck-2 on path-1.

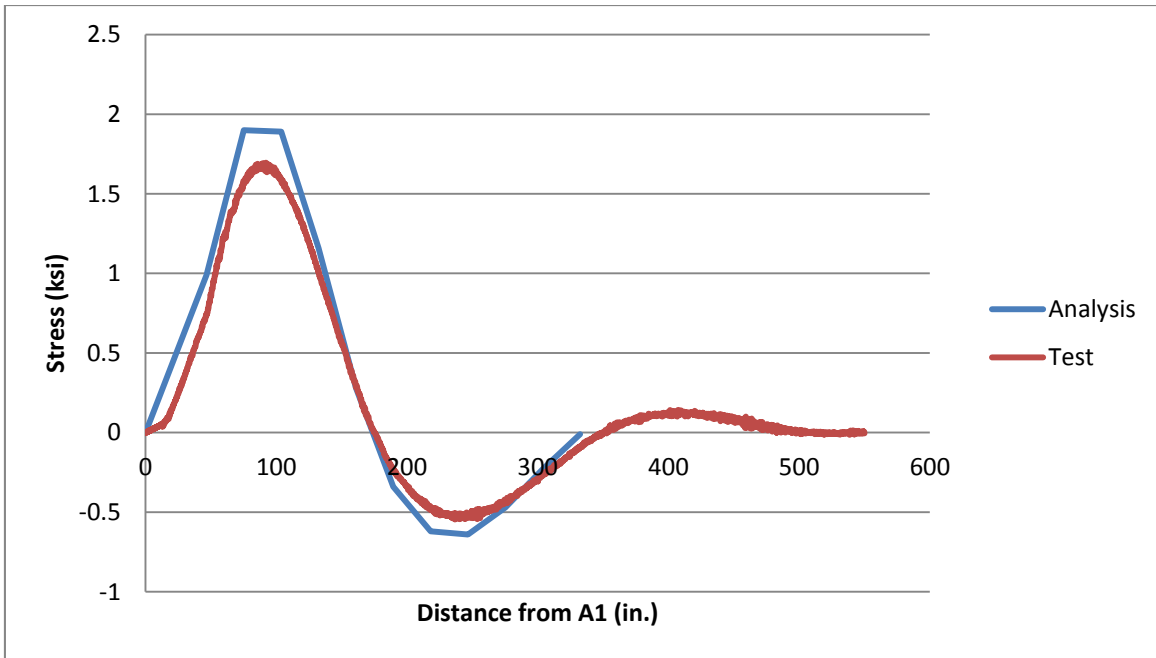


Figure 7-47 Longitudinal stress at 58 ft from north abutment in the west edge of bottom flange of EG: Truck-1 followed by Truck-2 on path-1.

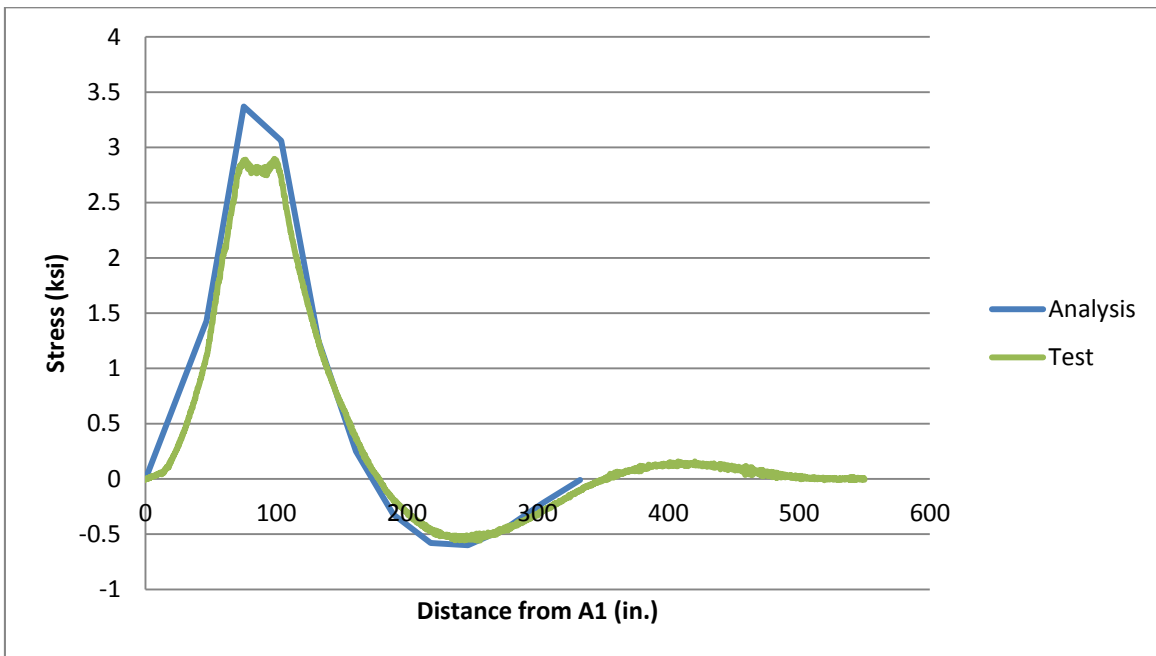


Figure 7-48 Longitudinal stress at 58 ft from north abutment in the east edge of bottom flange of EG: Truck-1 followed by Truck-2 on path-1.

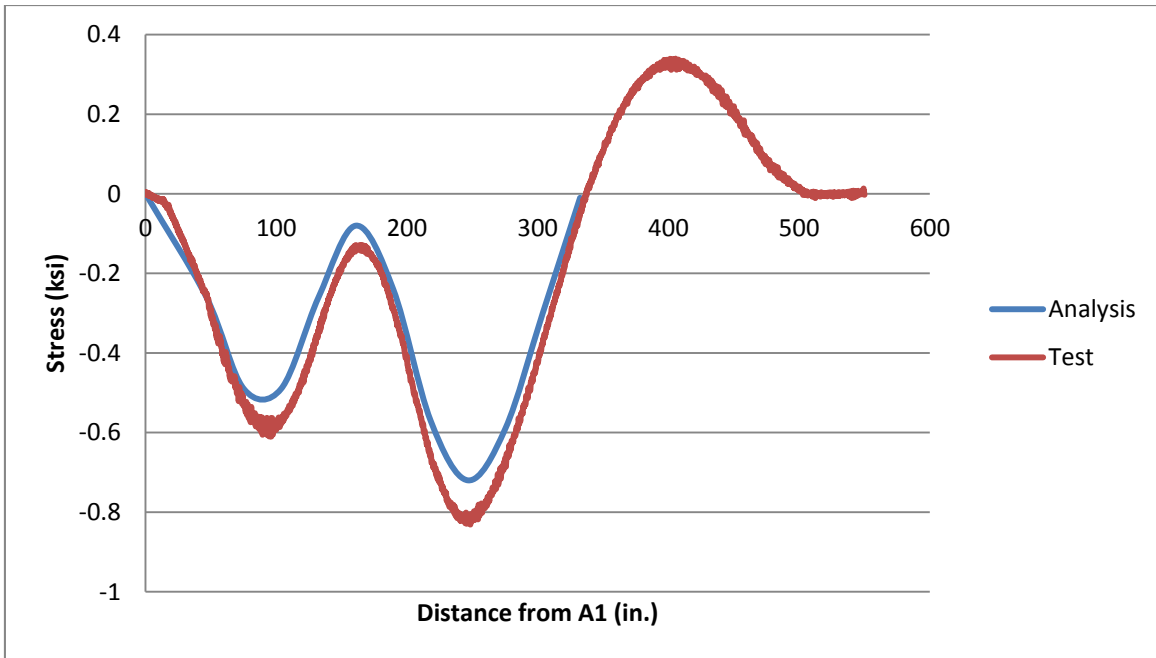


Figure 7-49 Longitudinal stress at 138 ft from north abutment in the west edge of bottom flange of WG: Truck-1 followed by Truck-2 on path-1.

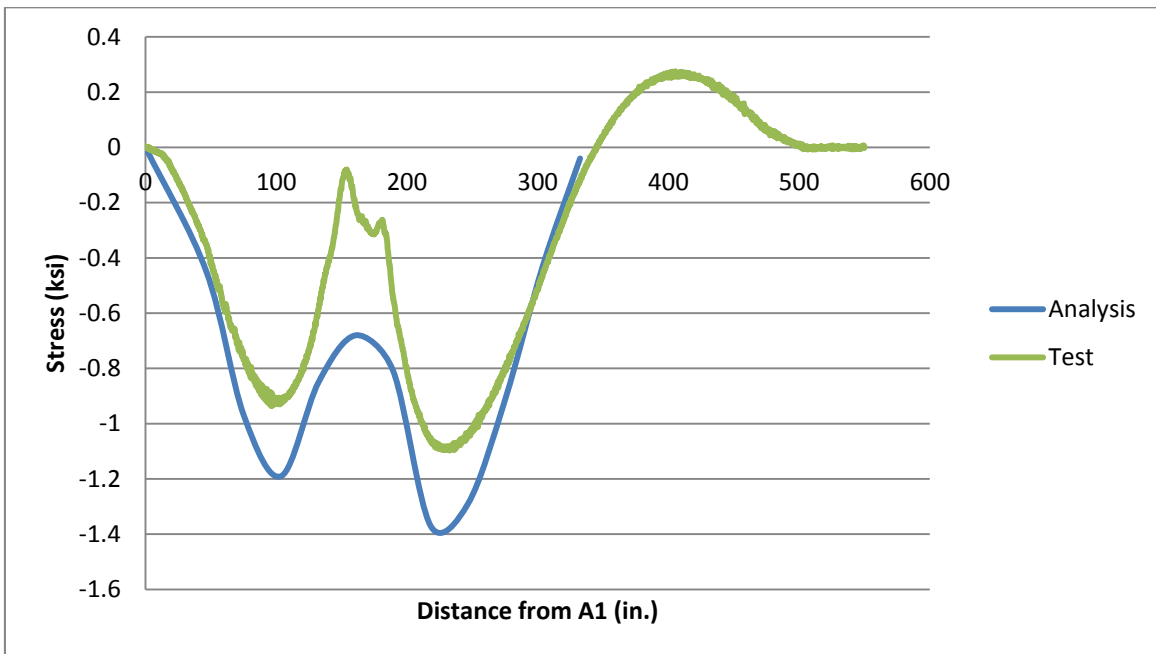


Figure 7-50 Longitudinal stress at 138 ft from north abutment in the east edge of bottom flange of EG: Truck-1 followed by Truck-2 on path-1.

It is observed from the stress results that the analytic and observed stresses match each other in most of the points of the curve. The maximum tensile stresses from finite element analysis in the section close to north abutment (Section-1) are greater than the field test maximum stresses. This

can be attributed to the partial fixity over the abutment in the real life structure compared to that of the computer model which assumes a perfect pin in the abutments. That is why the finite element stresses at the section 58ft from the north abutment are smaller than those of field test.

Chapter 8 Redundancy Analysis of Ft. Lauderdale Twin Box-Girder Bridge 860600

In this chapter, the redundancy of Ft. Lauderdale twin box-girder bridge which was discussed earlier in Chapter 7 will be assessed using direct analysis approach that was proposed by Ghosn and Moses in NCHRP Report 406. Please refer to Section 1.3.1 for the overview description of this approach and to Chapter 7 for the detailed information on the bridge geometry and configuration.

8.1 Bridge Girder Flexural Capacity

The first needed parameter for redundancy analysis of the bridge is the flexural capacity of the composite box-girder section. A summary of the dimensions of the composite section at the middle of the span is shown in Figure 8-1.

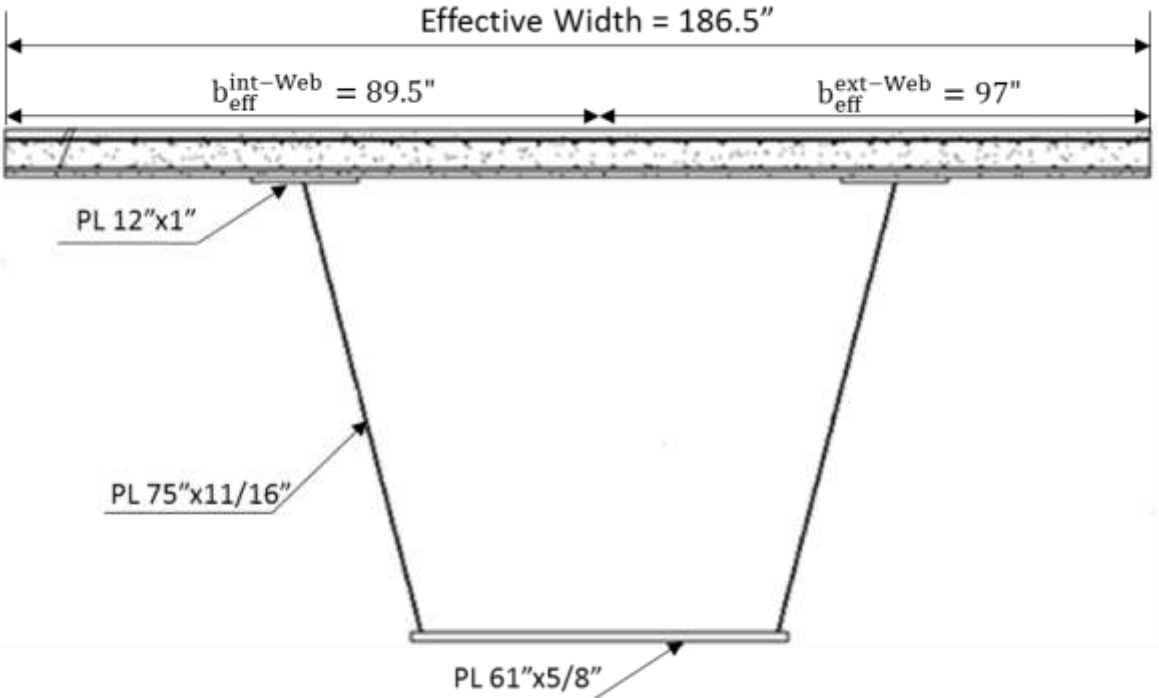


Figure 8-1 Box-girder composite section, Ft Lauderdale bridge.

8.1.1 Effective Width of Concrete Deck

Based on the provisions of AASHTO *LRFD Specifications*, the effective width of concrete deck for the composite action of each girder of a two-girder bridge can be calculated as follows:

$$b_{\text{eff}} = b_{\text{eff}}^{\text{int-Web}} + b_{\text{eff}}^{\text{ext-Web}}$$

Where:

$b_{\text{eff}}^{\text{int-Web}}$ = Effective concrete deck width for an interior web

$b_{\text{eff}}^{\text{ext-Web}}$ = Effective concrete deck width for an exterior web

And the effective width of concrete deck for the interior web of the girder is calculated as the minimum of the following three values:

$$12t_s + \frac{1}{2}b_{\text{TF}} = 12 \times 8 + \frac{1}{2} \times 12 = 102 \text{ in}$$

$$\frac{\text{Span Length}}{4} = \frac{1716}{4} = 429 \text{ in}$$

$$\text{Avg. Girder Spacing} = 97 \text{ in}$$

Therefore, the effective width of concrete deck for the interior web of the girder is equal to 97 in. For the exterior web of the girder, the effective width of concrete deck will be equal to half of the effective width for the interior web plus the minimum of the following three values:

$$6t_s + \frac{1}{4}b_{\text{TF}} = 6 \times 8 + \frac{1}{4} \times 12 = 51 \text{ in}$$

$$\frac{\text{Span Length}}{8} = \frac{1716}{8} = 214.5 \text{ in}$$

$$\text{Overhang length} = 41 \text{ in.}$$

Hence

$$b_{\text{eff}}^{\text{ext-Web}} = \frac{97}{2} + 41 = 89.5 \text{ in}$$

And

$$b_{\text{eff}}^{\text{Box}} = b_{\text{eff}}^{\text{int-Web}} + b_{\text{eff}}^{\text{ext-Web}} = 97" + 89.5 = 186.5 \text{ in}$$

Therefore, it is concluded that the effective width for each girder is one-half of the total width of the concrete deck.

8.1.2 Section Compactness

Based on AASHTO *LRFD Bridge Design Specifications*, the following criteria should be met so that the girder section can be considered a compact section.

1. Web and flanges yield stress:

$$F_{yf} = F_{yw} = 50 \text{ ksi} < 70 \text{ ksi}$$

2. For webs without longitudinal stiffener (AASHTO LRFD 6.11.2.1.2):

$$\frac{D}{t_w} = \frac{77}{\frac{11}{16}} = 112 < 150$$

3. Top flange width limit (AASHTO LRFD 6.11.1.1):

$$b_f = 12 \text{ in.} < \frac{\text{Span Length}}{5} = \frac{143 \text{ ft}}{5} = 343.2 \text{ in}$$

4. Limit for depth of web in compression at plastic moment:

$$\frac{2D_{cp}}{t_w} \leq 3.76 \sqrt{\frac{E}{F_y}}$$

8.1.3 Nominal Moment Capacity

The nominal moment capacity of the composite section is obtained as follows:

$$M_n = M_p \left(1.07 - 0.7 \frac{D}{D_t} \right) \leq 1.3M_y \quad \text{EQ 8.1}$$

Where:

M_p = Plastic moment capacity

M_y = Yield moment

D = Distance from top fiber of the composite section to the plastic moment neutral axis

D_t = Total depth of the composite section

8.1.3.1 Plastic Moment

To calculate the plastic moment capacity, first the location of the neutral axis when the section bears the plastic moment should be determined. Based on the cross-section shown in Figure 8-1

and the details shown in Figure 8-2, the forces of each element of the section under plastic moment are calculated as follows:

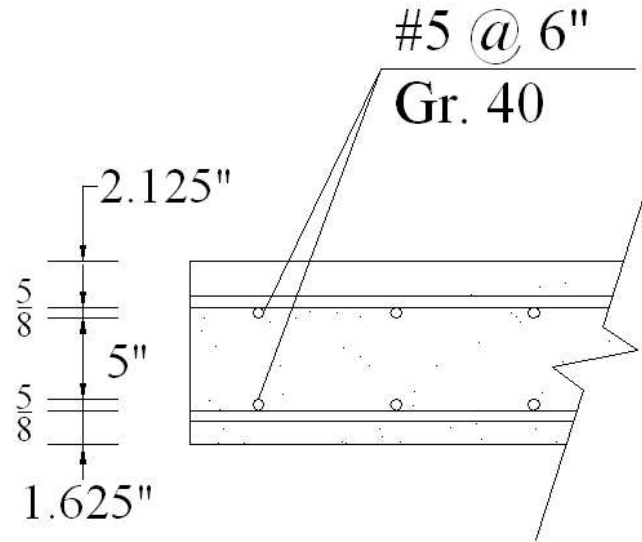


Figure 8-2 Rebar layout in concrete slab.

$$f'_c = 4.5 \text{ ksi}$$

$$F_y = 60 \text{ ksi}$$

$$A_{\text{rebar}} = \frac{186}{6} \times \frac{\pi}{4} \times \left(\frac{4}{8}\right)^2 = 6.09 \text{ in}^2$$

$$P_{rt} = 60 \times 6.09 = 365.4 \text{ kips (Top layer of rebar)}$$

$$P_c = 0.85 \times 4.5 \times 186.5 \times 8 = 5,707 \text{ kips (Concrete)}$$

$$P_{rb} = 60 \times 6.09 = 365.4 \text{ kips (Bottom layer of rebar)}$$

$$P_b = 2 \times 12 \times 1 \times 50 \text{ ksi} = 1,200 \text{ kips (Bottom flange of girder)}$$

$$P_w = 2 \times \frac{78 \times 11}{16} \times 50 \text{ ksi} = 5,363 \text{ kips (Webs of girder)}$$

$$P_t = \frac{61 \times 5}{8} \times 50 \text{ ksi} = 1,906 \text{ kips (Top flanges of girder)}$$

And

$$P_t + P_w + P_s = 8,469 \text{ kips} > P_{rb} + P_c + P_{rt} = 6,438 \text{ kips}$$

Therefore, the neutral axis under plastic moment is located in the top flange of the steel girder and its distance to the top fiber of the steel girder is calculated using the following equation:

$$\bar{Y} = \frac{t_c}{2} \times \left(\frac{P_t + P_w - P_c - P_{rt} - P_{rb}}{P_s} + 1 \right) = 0.846 \text{ in}$$

It can also be concluded that total web depth would be in tension at plastic moment and so the depth of web in compression would be equal to zero:

$$D_{cp} = 0$$

$$\frac{2D_{cp}}{t_w} = 0 < 3.76 \sqrt{\frac{E}{F_y}}$$

So the section under consideration is compact and the nominal moment capacity is calculated using the EQ 8.1 and the plastic moment is calculated as follows:

$$M_p = \frac{P_c}{2t_c} \times [\bar{Y}^2 + (t_c - \bar{Y})^2] + \sum P_i d_i \quad \text{EQ 8.2}$$

The value of the plastic moment from the previous equation will be equal to:

$$M_p = 381,524 \text{ kips} \cdot \text{in}$$

8.1.3.2 Yield Moment

To calculate the yield moment, M_y , the composite section, shown in Figure 8-1 is analyzed to find the location of the neutral axis for the elastic flexural member, and therefore to find the yielding moment. For the elastic analysis, the concrete material is transformed to its steel equivalent. The modular ratio is found as follows:

$$n = \frac{E_s}{E_c} = \frac{29,000}{1822\sqrt{4.5}} = 7.5$$

And so the equivalent width of the concrete slab and also the rebars for each girder will be:

$$b_{\text{eff,conc}} = \frac{186.5}{7.5} = 24.87 \text{ in}$$

$$b_{\text{eff,rebar}} = \frac{186.5}{6} \times \left(\frac{\pi}{4} \times 0.5^2 \right) \times \frac{6.5}{7.5} = 10.66 \text{ in}$$

The result of this elastic analysis indicates that the neutral axis and moment of inertia of the section will be equal to:

$$\bar{Y}_{\text{top}} = 24.62 \text{ in}$$

$$I_x = 340,968 \text{ in}^4$$

The steel material yield stress is equal to 50 ksi and the maximum stress capacity of concrete material is 4.5 ksi. Setting the values of stresses in the top fiber of the concrete equal to the

maximum stress and in the top and bottom flanges of steel box-girder equal to yield stress gives three values for the moment which the minimum of those three moments is the yielding moment of the section. This analysis results in a yielding moment equal to 280,217 k-in.

$$M_y = 279,421 \text{ kips} - \text{in}$$

Based on the calculated plastic and yield moment capacities for the composite section, the nominal flexural capacity will be equal to

$$\begin{aligned} M_n &= 381,524 \left(1.07 - 0.7 \frac{8.846''}{85.46''} \right) = 380,587 \text{ kips} - \text{in} > 1.3M_y \\ &= 1.3 \times 280,217 = 364,282 \text{ kips} - \text{in} \end{aligned}$$

Hence,

$$M_n = 364,282 \text{ kips} - \text{in}$$

8.2 Linear Elastic Analysis of the Bridge

In this redundancy analysis study, two different cases for the Ft. Lauderdale bridge are considered. In one case, just the first span of the bridge is studied and in the other case, the continuous three-span bridge is investigated. For this purpose, in addition to the moment capacity of the composite girder obtained in the previous section, the maximum moment in the girders due to dead load and HS-20 truck load using a linear elastic analysis is needed.

First, the single span bridge is modeled and analyzed using SAP2000 structural analysis software. For live load analysis, two HS-20 trucks are placed so that the moments in one of the girders are maximized. In order to generate the maximum moment in one girder, both trucks should be placed as close to that girder as possible. The most severe loading condition to create the maximum moment in one of the girders is shown in Figure 8-3.

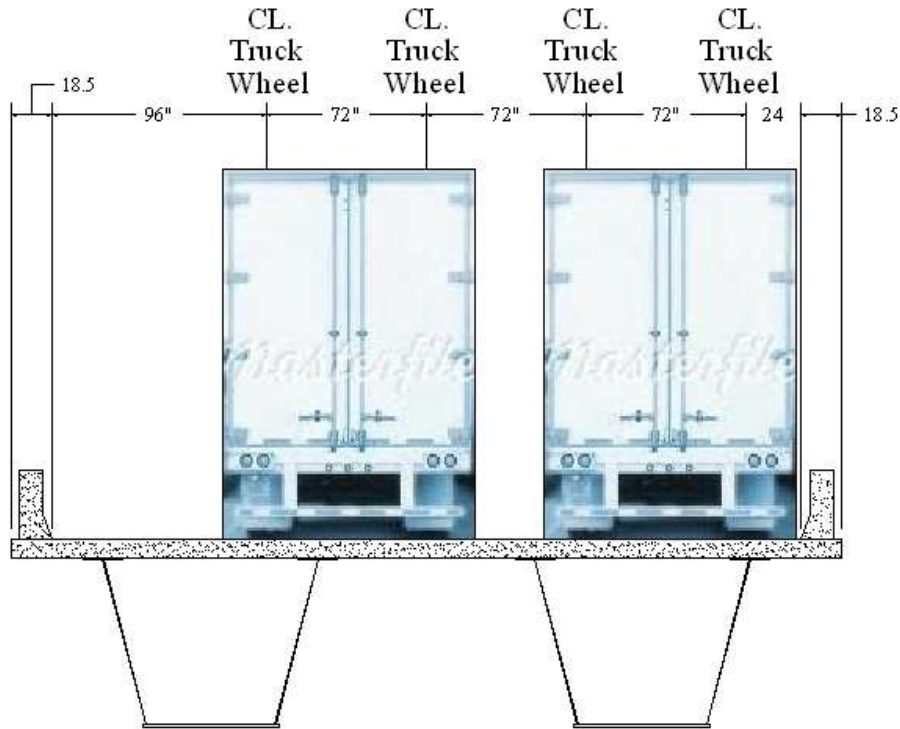


Figure 8-3 Worst case scenario for HS-20 loading of the bridge.

The results of a linear elastic analysis in SAP2000 show that the maximum flexural moment in the girders of the single-span bridge is equal to 34,637 kips-in. To verify the results of SAP2000 analysis, the maximum bending moment in the composite girders of the bridge is approximated by hand calculations. For this purpose, two trucks with unit weight are applied to a 2D model of the bridge cross-section to find the transverse distribution of loads between the girders. Figure 8-4 shows the point loads representing the truck wheels applied to the bridge deck.

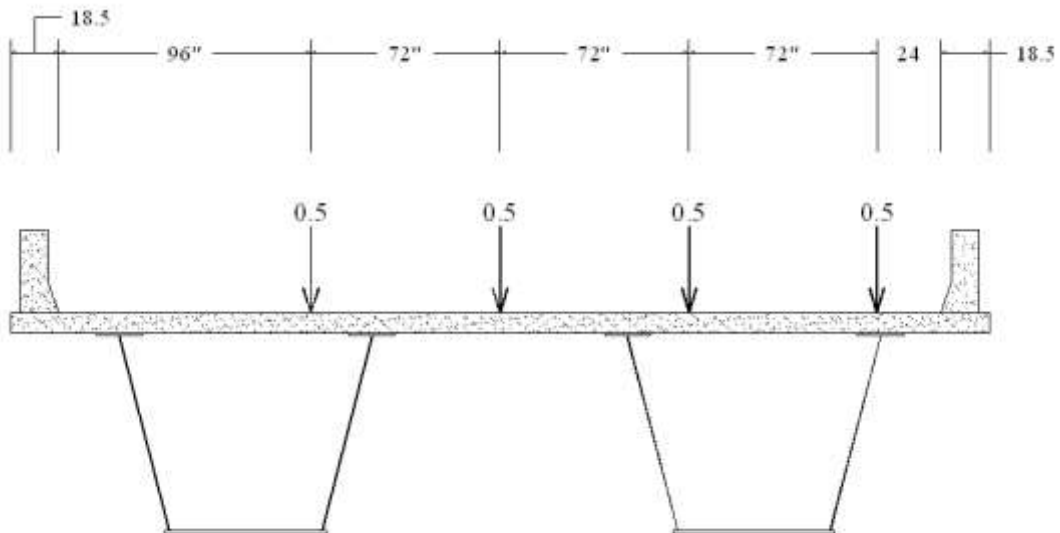


Figure 8-4 Worst case scenario of loading for two trucks with unit weight.

Assuming the webs of the girders act like a pin support for the concrete deck, the reactions of the supports are found through 2D analysis of the continuous deck. Figure 8-5 shows the reaction forces that are developed in the girder webs.

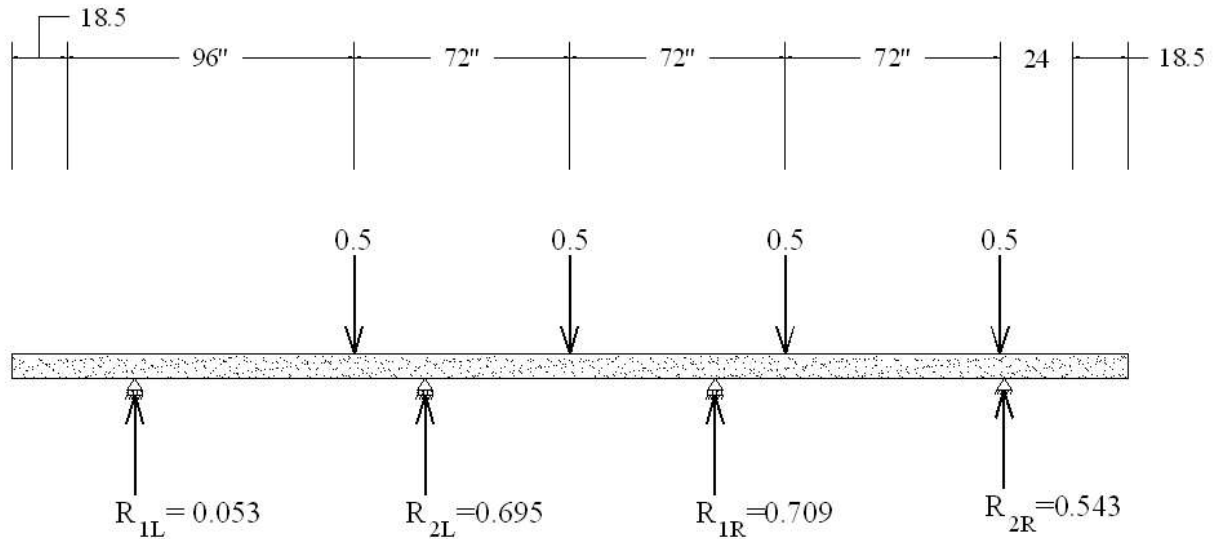


Figure 8-5 Web reactions due to application of two trucks with unit weight.

Therefore, the maximum reaction force which is developed in the right girder will be equal to:

$$R_R = R_{1R} + R_{2R} = 1.252$$

And it can be concluded that due to positioning of two HS-20 trucks on the bridge in the most severe location, 1.252 times of the weight of one of the trucks is carried by one of the girders. At this point, the girder should be analyzed in the longitudinal direction, so that the maximum moment in the girder is obtained. If the distance of the front axle of the truck and the support is set equal to the unknown parameter, x , maximizing the girder moment, which would be a function of x , shows that the value of x equal to 55 ft results in the maximum moment in the girder. The position of the truck, which creates the maximum moment is illustrated in Figure 8-6. This maximum moment is equal to 27,564 kips-in. due to one HS-20 truck. Based on the transverse analysis results that showed one of the girders may carry up to 1.252 times the truck weight, it is concluded that the maximum moment in the composite girders due to weight of two HS-20 trucks will be equal to 34,510 kips-in. This maximum moment is in agreement with the maximum moment obtained from SAP2000 linear elastic analysis which was equal to 34,637 kips-in. Therefore, the maximum moment in the girders due to application of two HS-20 trucks is chosen to be equal to 34,637 kips-in.

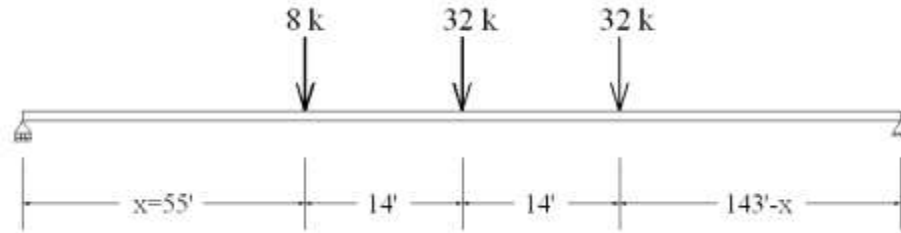


Figure 8-6 Position of the HS-20 truck for maximum moment in girders.

The other parameter needed for the redundancy analysis of the bridge is the moment due to dead weight of the bridge in single span and continuous bridge and also live load moment in the continuous structure. The results of SAP2000 analysis show that the dead load moments are equal to 83,676 and 49,780 kips-in. in single span and continuous bridges, respectively. The moment due to HS-20 loading in the continuous bridge is equal to 27,765 kips-in. With the moments produced by dead and live loads and the nominal moment capacity of the bridge, the only remaining part of the analysis is the nonlinear finite element analysis of the bridge in different limit states.

8.3 Nonlinear Finite Element Analysis

For redundancy analysis of the bridge, the live load capacity of the structure in three different limit states is required: the ultimate capacity of the undamaged bridge, the capacity of the damaged structure, and the capacity of the bridge corresponding to a live load deflection equal to the span length/100. To find these load carrying capacities, the single span and continuous bridges are modeled. Figure 8-7 and Figure 8-8 show the state of the von Mises stresses in the single-span bridge under maximum bending moment in undamaged and full-web cracked conditions, respectively. Figure 8-9 shows the load-deflection curves of the single-span and three-span bridges under different conditions.

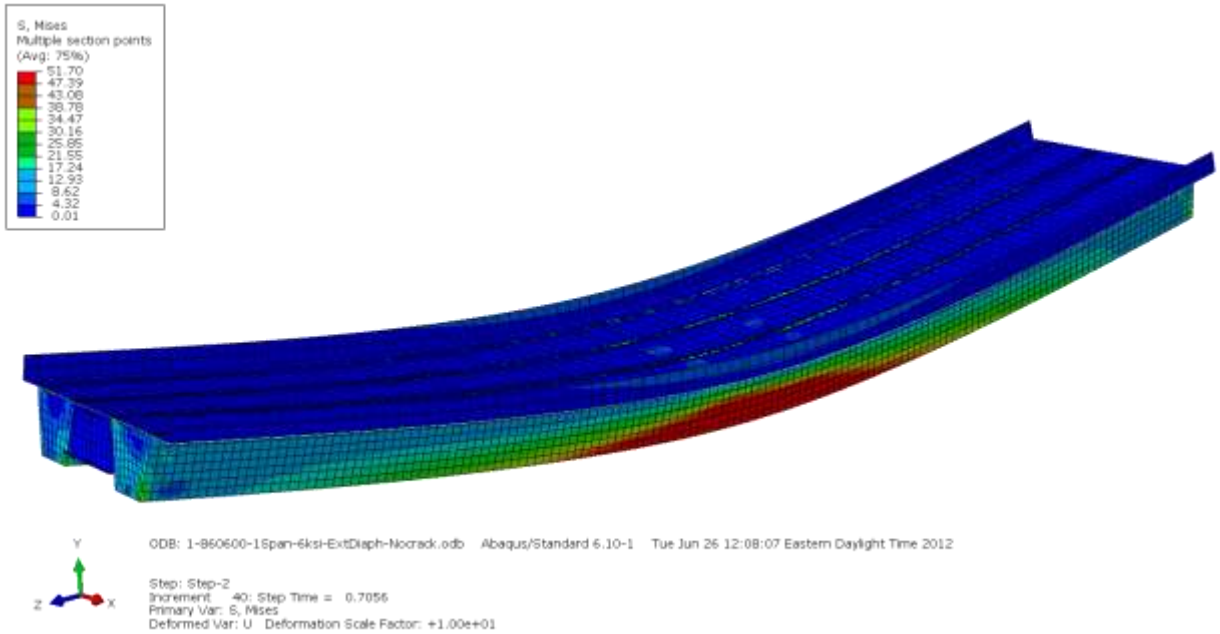


Figure 8-7 Von Mises stresses in single-span bridge under maximum moment, undamaged condition.

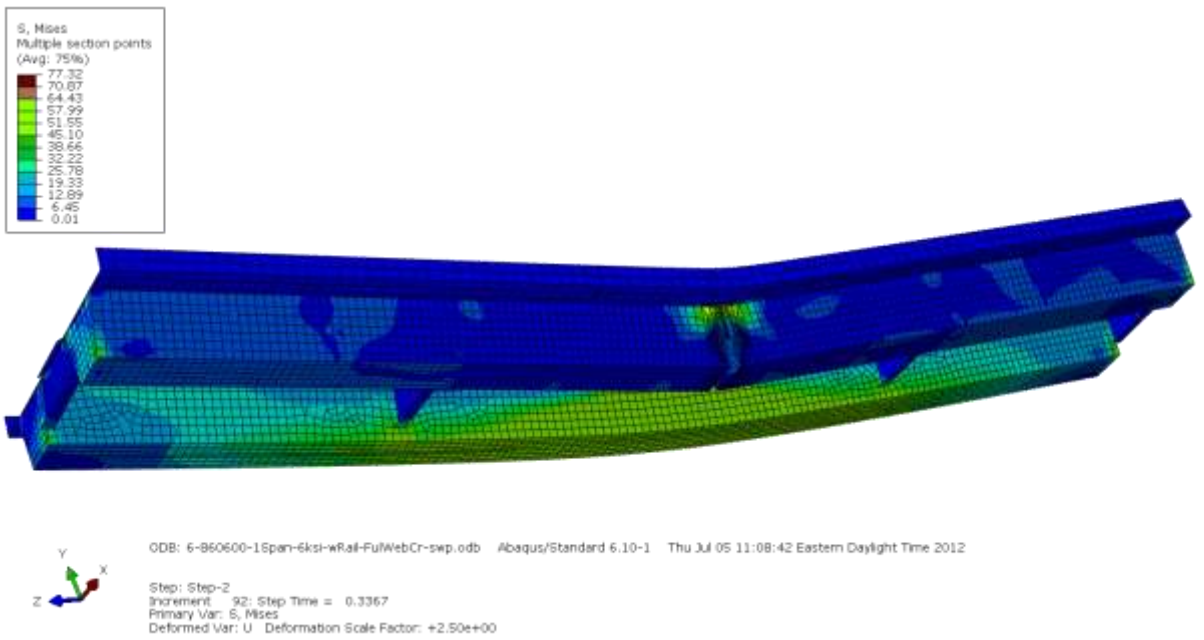


Figure 8-8 Von Mises stresses in single-span bridge under maximum moment, full-web cracked condition.

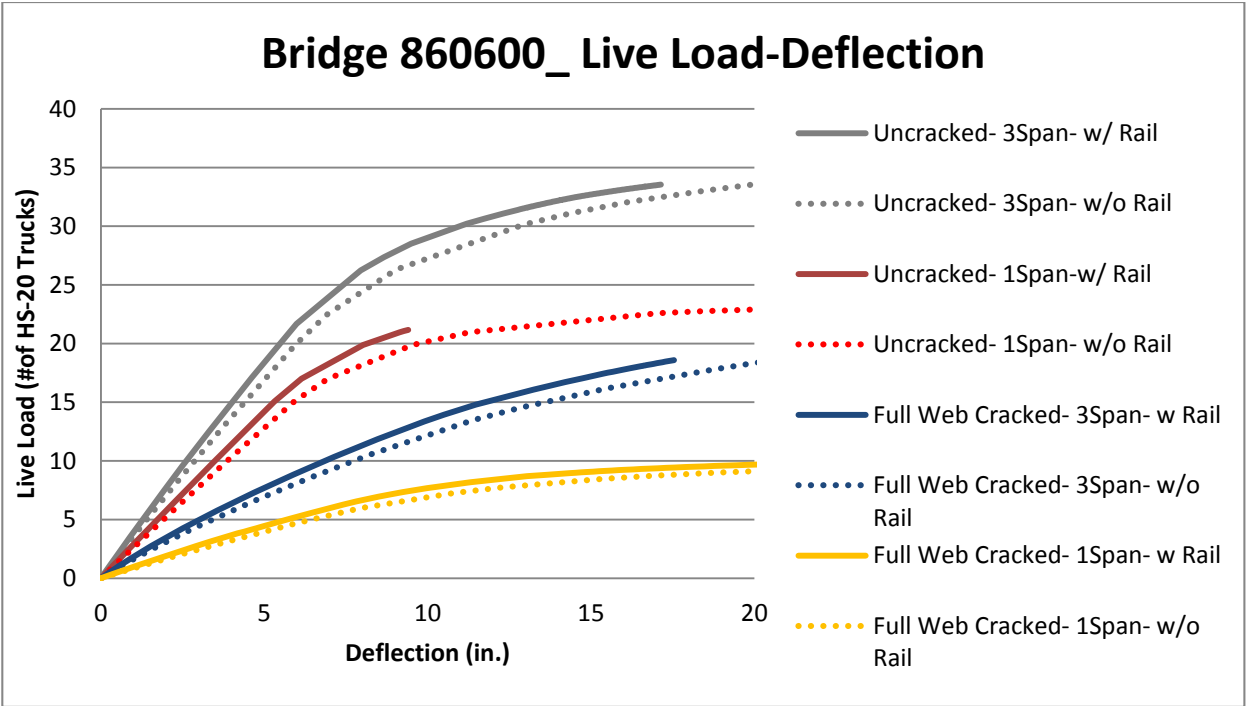


Figure 8-9 Load vs. vertical deflection of single- and three-span bridges with different conditions.

The live load capacities from nonlinear finite element analysis of the undamaged and cracked bridges in different limit states are tabulated in Table 8-1. As seen in Figure 8-9, the Ft. Lauderdale bridge is predicted to fail in flexural mode in all the cases under the HS-20 loading configuration. However, it is important to note that the finite element model that was used to analyze the Ft. Lauderdale bridge was only calibrated in the linear range, plus the crushing capabilities of concrete wasn't activated.

Table 8-1 Live Load Capacity of the Bridge as a Multiplier of HS-20 Trucks

	Undamaged	Full-Web Cracked	Corresponding to $d=L/100$
Single Span Bridge	22.68	9.90	9.55
Continuous 3-Span Bridge	33.54	18.60	18.39

The other factor that is studied in the finite element analyses is the effect of the railing. Both single- and three-span bridges in undamaged and damaged conditions are analyzed under live loads with and without railing. The results show that the existence of a concrete railing, integrally connected to the superstructure deck, will not change the capacity of the structure drastically. From the load deflection curves, it is observed that the ductility of the bridge is reduced due to existence of such railings. However, it should not be a major concern because after brittle failure of the railing at mid-span under compression, the bridge behavior tends to be similar to a bridge without railing.

8.4 Redundancy Analysis

Using the results of the linear elastic analysis for dead and live loads, the nonlinear finite element analysis of live load and the calculated flexural capacity of the bridge composite girders, the system redundancy factors of the bridge are obtained using the direct analysis approach. For that purpose, first the load factors recommended by NCHRP Report 406 are evaluated as follows.

8.4.1 Member Failure (LF_1)

Member failure limit state is a check of individual member safety using elastic analysis or the capacity of the structure to resist its first member failure.

$$LF_1 = \frac{R - D}{L} \leftarrow \text{Linear Elastic Analysis} \quad \text{EQ 8.3}$$

Where:

- R = Resistance
- D = Dead load effects
- L = Live load effects

If moment values are implemented in EQ 8.3, it will convert to:

$$LF_1 = \frac{M_n - M_{DL}}{M_{LL,2HS-20}} \leftarrow \text{Linear Elastic Analysis}$$

Where:

- M_n = Nominal moment capacity based on AASHTO LRFD
- M_{DL} = Dead load moment
- $M_{LL,2HS-20}$ = Live load moments due to two HS-20 trucks

For single span bridge, the LF_1 will be equal to:

$$LF_{1, \text{single-span}} = \frac{364,282 - 83,676}{34,637} = 8.10$$

And for the continuous three-span bridge the load factor will be equal to:

$$LF_{1, \text{three-span}} = \frac{364,282 - 49,780}{27,780} = 11.32$$

8.4.2 Ultimate Limit State (LF_u)

Ultimate limit state factor is defined as the ultimate capacity of the undamaged bridge system or the load required for the formation of a collapse mechanism in the bridge system divided by the weight of two HS-20 trucks. In mathematical format, this definition yields in:

$$LF_u = \frac{\text{Ultimate Load Capacity of Undamaged Bridge from Nonlinear FEA}}{2 \times 72 \text{ kips}} \quad \text{EQ 8.4}$$

Where:

72 kips = Weight of one HS-20 Trucks

Based on the results of the conducted finite element analysis, the capacities of the undamaged single-span and three-span bridges are equal to 22.68 and 33.54 time HS-20, respectively. Therefore, the ultimate limit state load factors for single span bridge will be equal to:

$$LF_{u, \text{single-span}} = \frac{22.68 \times 72 \text{ kips}}{2 \times 72 \text{ kips}} = 11.34$$

And this load factor for the three-span bridge will be:

$$LF_{u, \text{three-span}} = \frac{33.54 \times 72 \text{ kips}}{2 \times 72 \text{ kips}} = 16.77$$

The redundancy reserve ratio for the undamaged condition is defined as the ratio of the ultimate limit state load factor and the member failure factor. This factor for the single span bridge will be as follows:

$$R_{u, \text{single-span}} = \frac{LF_u}{LF_1} = \frac{11.34}{8.10} = 1.40 > 1.30$$

So, the capacity of the single span bridge in its ultimate limit state is satisfactory. For the three span bridge, the redundancy reserve ratio will be evaluated as follows:

$$R_{u, \text{three-span}} = \frac{LF_u}{LF_1} = \frac{16.77}{11.32} = 1.48 > 1.30$$

Therefore, the three-span bridge is also passing the redundancy criterion in the undamaged condition.

8.4.3 Damage Condition Limit State (LF_d)

Damage condition limit state is defined as the ultimate capacity of the bridge system after removal or cracking of one load carrying component from the structure model.

$$LF_d = \frac{\text{Ultimate Load Capacity of Damaged Bridge}}{2 \times 72 \text{ kips}} \quad \text{EQ 8.5}$$

The limiting value for the redundancy reserve ratio in this limit state is defined as follows:

$$R_d = \frac{LF_d}{LF_1} \geq 0.50$$

This factor and the relevant criterion for single- and three-span bridges are evaluated as follows:

$$LF_{d,single-span} = \frac{9.9 \times 72 \text{ kips}}{2 \times 72 \text{ kips}} = 4.95$$

$$R_{d,single-span} = \frac{LF_d}{LF_1} = \frac{4.95}{8.10} = 0.61 > 0.50$$

$$LF_{d,three-span} = \frac{18.60 \times 72 \text{ kips}}{2 \times 72 \text{ kips}} = 9.30$$

$$R_{d,three-span} = \frac{LF_d}{LF_1} = \frac{9.30}{11.32} = 0.82 > 0.50$$

It is observed that both single- and three-span bridges meet the redundancy criterion in their damaged conditions.

8.4.4 Functionality Limit State (LF_f)

Functionality limit state is defined as the capacity of the structure to resist a live load displacement in a main longitudinal member equal to the span length/100. The functionality limit state load factor is obtained from dividing this capacity by the weight of two HS-20 trucks.

$$LF_f = \frac{\text{Load Capacity corresponding to } \frac{L}{100} \text{ deflection}}{2 \times 72 \text{ kips}} \quad \text{EQ 8.6}$$

And the reserve ratio criterion for this limit state is:

$$R_f = \frac{LF_f}{LF_1} \geq 1.10$$

This factor and the relevant criterion for single- and three-span bridges are evaluated as follows:

$$LF_{f,single-span} = \frac{9.55 \times 72 \text{ kips}}{2 \times 72 \text{ kips}} = 4.78$$

$$R_{f,single-span} = \frac{LF_f}{LF_1} = \frac{4.78}{8.10} = 0.59 < 1.10$$

$$LF_{f,three-span} = \frac{18.39 \times 72 \text{ kips}}{2 \times 72 \text{ kips}} = 9.20$$

$$R_{f,three-span} = \frac{LF_f}{LF_1} = \frac{9.20}{11.32} = 0.81 < 1.10$$

It is observed that neither single-span bridge nor three-span one meets the functionality redundancy criterion in their damaged condition.

8.5 Summary

The redundancy analysis results for the Ft Lauderdale twin steel box-girder bridge is summarized in Table 8-2. The results indicate that both the single-span and three-span bridge satisfy the redundancy criteria for the ultimate limit state and damaged limit state, but not for the functionality limit state. This suggests that the bridge has enough ultimate capacity to be classified as redundant; however, the intensive deformation that the bridge will experience makes the bridge unsafe to use even at loads lower than the ultimate capacity. The continuity was observed to improve the redundancy of the bridge significantly.

Table 8-2 Summary of Redundancy Analysis Results on the Ft. Lauderdale Bridge

Models	$R_u = \frac{LF_u}{LF_1} (1.30)$	$R_d = \frac{LF_d}{LF_1} (0.5)$	$R_f = \frac{LF_f}{LF_1} (1.10)$
Simple Span	1.40 (OK)	0.61 (OK)	0.59 (NG)
3-Span	1.48 (OK)	0.82 (OK)	0.81 (NG)

Chapter 9 Parameters Affecting Load-Carrying Capacity of Bridge

In order to investigate the sensitivity of the research findings to variations in some of the key parameters, several finite element simulations and analyses were performed. Parameters investigated in this study include span length, railings, and degree of structural indeterminacy and presence of cross-frames.

The parametric study was carried out under the same loading configuration that was used in Test D, assuming this was the worst loading scenario. The purpose of this parametric study was to investigate whether variations of these parameters would affect the failure mode and capacity of the specimen under concentrated loading configuration. In this parametric study, only post-fracture behavior was considered. The load was incrementally applied until collapse was detected.

9.1 Cross-frames

As demonstrated in Test D, the contribution of cross-frame to the load-carrying capacity wasn't significant. It is interesting to check how much the capacity of the specimen will change if all external cross-frames connecting two girders are removed. As illustrated in Figure 9-1, removing the external cross-frames reduces the specimen's load-carrying capacity only slightly from 104 kips to 94 kips. Once the cross-frames were removed, the intact girder retained almost the same stiffness and displacement as before, while the deflection of the fractured girder increased significantly. This indicates that the external cross-frames play important roles in controlling the relative deflection between the girders in the damaged bridge. However, both models had punching shear failure in the concrete deck as the failure mode.

It is also important to note that under different loading configurations, the effect of external cross-frames will vary. For example, in Test A, the contribution of external cross-frames was observed to be larger than it was in Test D. This was because in Test A, the load was applied directly over the top flanges of the damaged girder, and hence more load was distributed to the damaged girder than it was in Test D, where the load is applied only over a small portion of the deck at the center of the damaged girder. Note that the load resisted by the damaged girder should be transferred to the intact girder by means of the external cross-frames and the deck; therefore, as more load is applied to the damaged girder, the more load will be resisted by the cross-frames.

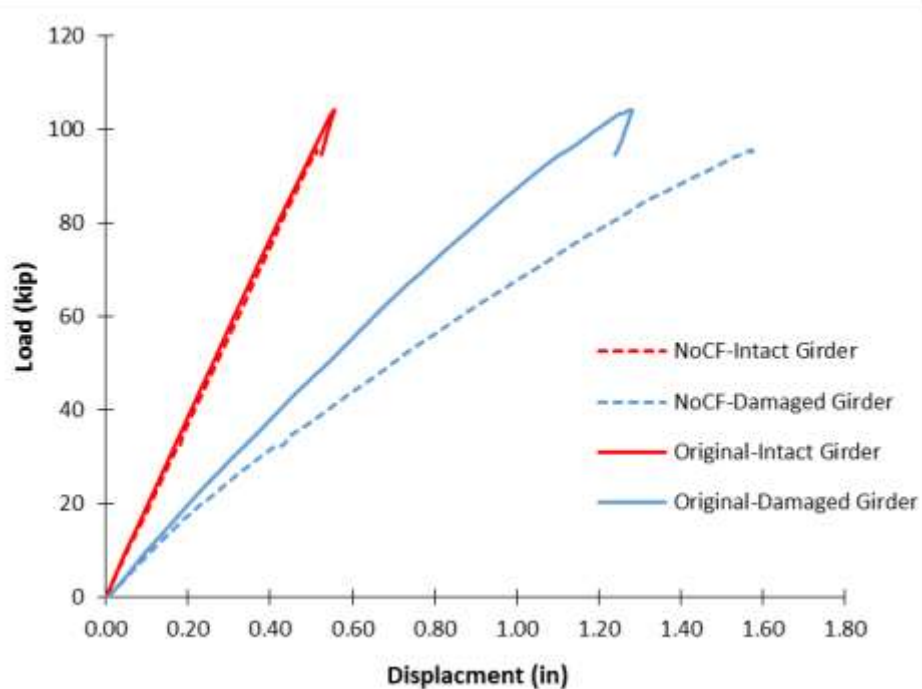


Figure 9-1 Effects of cross-frames.

9.2 Railing

The deflection and capacity of the specimen with and without presence of the railing system is shown in Figure 9-2. Since the railing system was poured using the same concrete mix used to cast the deck, it was modeled to have the same nonlinear properties as the deck. The reinforcement was modeled using smeared-reinforcement approach as the concrete deck and the geometry of the railing can be referred in Figure 3-3. However, the expansion joints between the railing segments were neglected in the model for simplification. Moreover, the model assumed the full connection between the rail and concrete deck.

As expected, the model with the railing system deflected less than the model without the railing in both girders. The additional railing also increased the capacity of the specimen because when engaged it acted as deep beam on the edge of the deck and increased bending stiffness of the deck. The capacity of specimen was increased from 104 kips to 134 kips with the presence of the railing. Furthermore, that fact that concrete deck under the loading pad was crushed in both cases indicates that the specimen failed in punching shear whether with or without the presence of the railing.

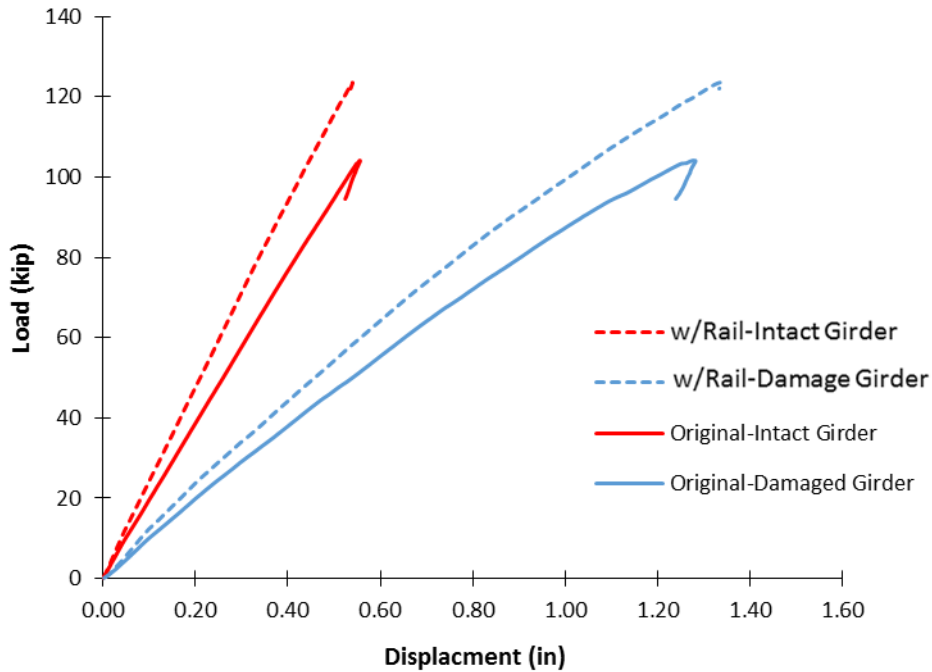


Figure 9-2 Effects of railing system.

9.3 Structural Indeterminacy and Cantilever End

Similarly to the railing system, bridges with continuous spans possess higher stiffness than the simply-supported bridge as demonstrated in elastic tests. The structural indeterminacy and continuity was found to provide additional sources of redundancy for the bridge system. In the event that one girder is fully fractured, the load applied to the fractured girder can be redistributed to the intact girder as well as neighboring spans; therefore, chance of collapse can be reduced significantly in multi-span bridges.

The continuity was modeled by simply introducing two vertical restraints at the center of each girder, additional to the original model. This approach is similar to the way it was setup in the elastic tests, which are shown in Figure 3-20. The comparison of both models is illustrated in Figure 9-3. The specimen with two spans had better performance than the simply-supported model in both displacement and capacity aspects. Similar to other cases above, the simulation was terminated due to the excessive crushing of concrete deck near the loading area. This suggests that shear failure was still a potential mode of failure of the specimen under this concentrated loading configuration.

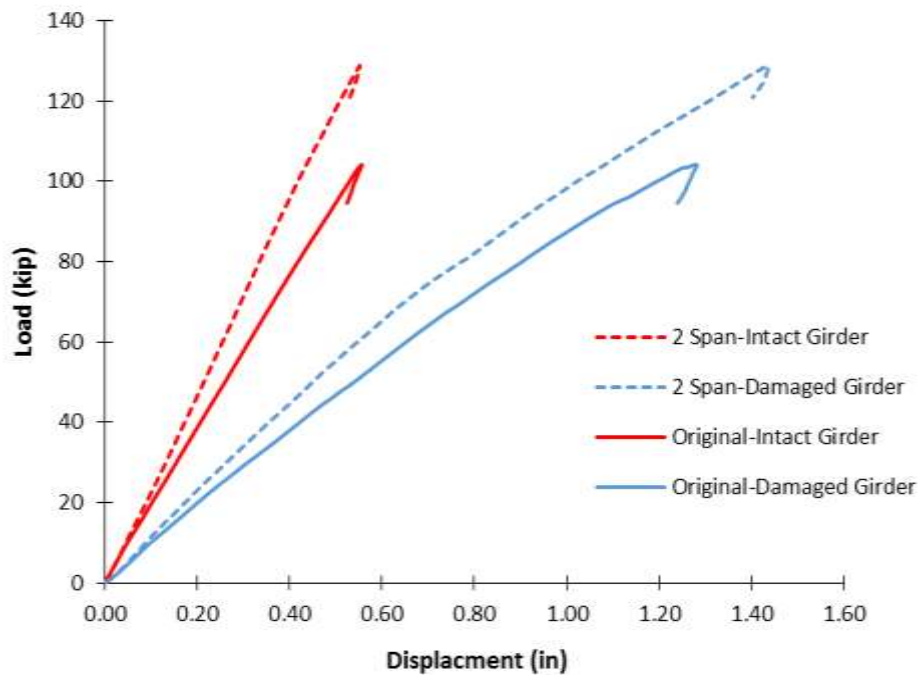


Figure 9-3 Effects of continuity.

9.4 Bridge Span Length

This small-scale model with different span lengths was analyzed to investigate the potential effects of span length on the behavior of bridges. In order to isolate and study only the effect of span length, the external cross-frames and the cantilever end were removed in these analyses. Table 9-1 compares capacity and girder displacements for different specimens with different length. In this case, span lengths will be used because all models had the same girder dimension. In case that the girder dimensions are different, the ratio of span length to girder depth will be a better criteria to use.

Table 9-1 Effects of Span Length on the Bridge Performance.

Length (ft)	Capacity (kip)	Intact Girder Displacement (in)	Damaged Girder Displacement (in)
30	80	0.33	1.67
22	70	0.1	1.19
18	75	0.05	1.10
12	74	0.008	0.65

As illustrated, the variation of span length did not significantly influence either the capacity of the specimen or the failure modes. However, as the length of span (or ratio of span length to girder depth) got smaller, the bending stiffness of the bridge increased. Therefore, it reduced the

displacement of both girders significantly. The models again failed due to the crushing of concrete deck underneath of loading area.

9.5 Summary

The effects of the external cross-frames, railing, structural indeterminacy, and span length on the capacity of the bridge specimen were investigated, under a concentrated loading. Overall, the presence of cross-frames and railings and additional continuity were found to increase the stiffness of structure and improve the capacity of the bridge. The capacity improvement can be seen clearly when adding the railing or continuity. It is also found that varying the span length of the specimen does not affect much the capacity of the bridge.

It is also important to note that these effects may vary under different loading configuration. For instance, if the load is applied in a more distributed manner, the effects of external cross-frames, railings and structural indeterminacy might increase and varying the length of specimen might also affect the capacity of the bridge.

Chapter 10 Summary and Future Considerations

10.1 Research Summary

According to AASHTO *LRFD Bridge Design Specifications*, twin steel box-girder bridges are currently classified as bridges with fracture critical members (FCMs), in which a failure of a tension member leads to a collapse of the bridge. However, there are several evidences indicating that twin steel box-girder bridges are redundant and still able to carry a significant amount of traffic load with little noticeable change to their global behavior. The main objectives of this current FDOT-sponsored research study, presented in this report, are to provide an understanding of the behavior of twin steel box-girder bridges and to develop complete methodology and associated tools that can be used to evaluate performance of these bridges after damage and remove them from the fracture critical list, where possible.

The suggested methodology is a two-step process. The first step will consist of simple hand calculation that is based on the research study conducted at the University of Texas-Austin. Completion of this simple approach will require completion of the recommended pooled fund study, as described within the report.

The second approach is referred to as the notional approach. The notional approach considers finite element analysis as the main method to assess performance of damaged twin steel box-girder bridges. However, performing a detailed nonlinear finite element analysis on every single twin steel box-girder bridge within inventory of a given state requires a significant amount of labor and financial resources. To address this challenge, the notional approach suggests grouping twin steel box-girder bridges in the inventory into groups and developing a notional simple span twin steel box-girder that represents all of the bridges within a given group. The detailed nonlinear finite element analysis is then carried out on the notional simple-span bridge only. By doing so, a significant amount of the effort and resources required will be reduced.

The details of the notional approach are provided in Chapter 2 of this report. The majority of the information needed to evaluate the redundancy of the twin steel box-girder bridges using the notional approach has been addressed within this report. The remaining works are left to be completed under future research.

Following are elements of the notional approach of evaluating the redundancy of twin steel box-girder bridges.

1. Access to calibrated nonlinear finite element model that accurately depicts the modes of failure under types of loading specified by AASHTO *LRFD Bridge Design Specifications*. This project has developed a test verified nonlinear FEM model.
2. Criteria to group twin steel box-girder bridges within the inventory of a given state DOT and develop notional simple-span twin steel box-girder bridge representing the group. This project provides preliminary approaches for grouping the state inventory of twin steel box-girder bridges. However, additional work is recommended, to be carried out under pooled fund study.
3. Establishment of the load level that damaged twin steel box-girder bridges must resist, as well as establishment of other serviceability limit states that must be checked to ensure public safety. The procedure for establishing a load level that damaged twin steel box-girder bridges must carry is outlined in this report. The use of arbitrary load level is questioned by many bridge owners and has remained one of the obstacles for resolving the question of redundancy of twin steel box-girder bridges.
4. Development of a Guide for application of the notional approach for assessing redundancy of damaged twin steel box-girder bridges with examples and other documentations, such as video tapes that would assist state DOTs. It is recommended that this task be completed after completing the proposed pooled fund study.

Discussions on approaches to develop the load level as well as other serviceability criteria for a damaged twin steel box-girder bridge have been presented in Chapter 2 of this report. The efforts to develop calibrated and verified detailed nonlinear finite element models are documented from Chapter 3 through Chapter 8. Chapter 9 provides a summary of the results of a parametric study on twin steel box-girder bridges and the start of the process for establishing the notional simple-span bridge model and grouping criteria.

The remaining portion of this summary and conclusion provides highlights of the results obtained in this project. Complete discussions of each of the following sections can be found in the appropriate chapters within this project.

Summaries of the important observations obtained from the different activities carried out within this project follow. The summary is provided in the context of experimental work; however, within each section, associated numerical works that have been carried out are included.

10.2 Field Tests of In-Service Bridge

Elastic field tests on a twin steel box-girder Ft. Lauderdale bridge were conducted and its performance was observed. Following are conclusions obtained from the results of the field testing and associated finite element analysis:

- In general, the test-observed deflections were in good agreement with results obtained from FEM analysis, within 5%.

- Comparison of the collected testing strains (and corresponding computed stresses) in the structure and the resulted stresses from finite element analysis of the bridge shows a partial fixity at the abutment in contrast to the ideal pin assumed in the finite element models. This observation agrees with the conclusions of previous field tests conducted by other bridge researchers.
- For the type of truck and load used, the field test result indicated a dynamic amplification factor of approximately 12%. It is important to note that this finding is based on the experimental results of two dynamic tests. One test was carried out with the truck moving at crawling speed (~3mph) while in the other test, the truck was moving at roadway speed (~30mph)
- The strain response histories showed evidence of slight thermal drift, which is typical for load tests that occur over several hours. In an attempt to reduce the impact of the thermal drift, a thermal correction based on a linear drift was applied to all of the selected processed data in order to reduce this effect.

10.3 Laboratory Tests on Small-Scale Specimen

To comprehend the behavior of twin steel box-girder bridges in nonlinear range, examine the modes of failure, and calibrate three dimensional 3-D finite element models, a small-scale test specimen was constructed and numerous tests were carried out including elastic tests, a cyclic fatigue test, and ultimate load tests. The following sections provide a brief discussion of the results obtained. For a more detailed discussion refer to various chapters within this report.

The laboratory test specimen was subjected to a number of tests before and after simulating damage in the test specimen. The first series of tests were elastic tests, in which the test specimen was subjected to a single concentrated load over the EG, or two concentrated loads with one load over each girder. The purposes of these elastic tests were to examine linear elastic responses of the laboratory bridge specimen, the effects of railing system and continuity as well as the effects of different loading configuration on the specimen before and after the damage was simulated.

The second test was a cyclic fatigue test. The purpose of this cyclic test was to see what would happen to the bridge specimen under the traffic load assuming a fracture or damage occurred in the bottom flange without being noticed.

Ultimate load tests were the last series of tests, in which the laboratory specimen was loaded to failure. All the ultimate load tests were carried out under the damage condition in which one girder was completely fractured. The purposes of the ultimate load tests were to investigate the behavior, the maximum load-carrying capacity, and failure mode of twin steel box-girder bridges when the web and bottom flange of one of the girders was completely fractured.

10.3.1 Conclusions from Elastic Tests Conducted on Laboratory Test Specimen

In general, a total of 18 elastic tests were carried out. The effects of both rail and continuity on linear-elastic behavior of the bridge specimen were investigated under either unsymmetrical loading or symmetrical loading configuration. The responses of bridge corresponded to different damage levels were interpreted and are summarized as follows:

- The rail and continuity was found to increase the stiffness of the structure; therefore enhancing the load-carrying capacity of the specimen.
- In addition to the deck, the cross-frames played an important role in transferring the applied load from the damaged girder to the intact girder. It should be noted, however, that depending on the loading configuration, the contribution of cross-frames might vary.
- In general, the elastic responses of the undamaged specimen and of the specimen with bottom flange fractured in one girder were comparable. The maximum displacement increased by an average of 6.5 % as the bottom flange was fractured.
- As a result, the strain in the intact girder was found to increase significantly, as the damage intensity increased. This indicates that as the damage takes place, the load resisted by the damaged girder is transferred to the intact girder.
- When the bottom flange and webs were completely fractured, the flexural stiffness of that damaged girder was negligible.

10.3.2 Conclusions from Cyclic Tests Conducted on Laboratory Test Specimen

In this cyclic load test, the laboratory bridge specimen was loaded unsymmetrically at mid-span on the damaged girder with the rail on but no continuity. Assumption was made that the governing fatigue category is type C. Further it was assumed that the details were designed for infinite life with a corresponding threshold stress value of 10 ksi. This in turn demanded that the specimen be subjected to a single concentrated load of about 60 kips, directly over the damaged girder. Before the start of the cyclic test, the bottom flange of one of the girders was completely cut to simulate complete fracture of bottom tension flange. The objective of this particular cyclic test was to observe the time that it would take for crack to propagate from the bottom flange to the bottom of deck and to observe the behavior of the small-scale test specimen in the process. After applying about 213,000 loading cycles, the crack propagated from the bottom tension flange, through the web and to bottom of concrete deck. With an assumed ADTT of 1286 trucks, this would translate to approximately 5.5 months for the crack to grow from bottom flange, all the way to bottom of concrete deck. When the crack reached the bottom of concrete deck, the deflection increased approximately 0.3 in. for the damaged girder and 0.13 in. for the intact girder. The changes to global deflection and deck performance during entire cyclic test were relatively small.

10.3.3 Conclusions from Ultimate Load Tests Conducted on Laboratory Test Specimen

A total of five ultimate load tests were carried out under the full-web fracture damage condition, in which one girder had its web and bottom flange completely fractured. The first ultimate test (ultimate Test A) was carried out after the elastic and cyclic tests. The steel box-girders after conclusions of Test A were in a good condition, except for the complete fracture of bottom tension flange and web in one of the girders. Therefore, a decision was made to reconstruct the specimen using the same girders. By doing so, only the new deck is needed and savings can be made. The other four ultimate load tests were carried out on the reconstructed test specimen. The following sections provide a brief summary of each ultimate load test carried out.

In ultimate Test A, the load was applied through the 9 in. x 36 in. loading pad covering the entire width of the damaged girder. The bridge showed a maximum capacity of 156 kips which was two times more than the weight of one HS-20 truck. After reaching the maximum capacity, the specimen capacity dropped to 133 kips at a displacement of 2.5 in. due to crushing of concrete deck, under the applied concentrated load. The bridge specimen was still able to hold this load level before the test was halted due to a significant drop in load-carrying capacity at 5.5-in. displacement. During this extended loading period, the collected data indicated that the stiffness of the deck played a major role in redistributing the load to intact girder. Furthermore, several cross-frame connections connecting two steel box-girders failed by shear, indicating the cross-frame forces increasing. The intact girder did not yield during the entire test.

In ultimate Test B, the same loading configuration as in Test A was used, but with loading moved over the intact girder. The test was stopped when the loading plateau occurred at 270 kips. The testing was stopped to limit the damage to the test specimen and allow conduct of additional tests. No major damage occurred, just minor cracking on the top surface of the deck. The intact girder showed significant yielding at the bottom flange with more than 8,000 $\mu\epsilon$ while the strain in the damaged girder was negligible. Strain data in both longitudinal and transverse reinforcements, located over the damaged girder and center of the deck, were small compared to those located over the intact girder. This strain distribution pattern, in addition to the observation that both girders experienced similar displacements along the length, indicated that the applied load was mainly resisted by the intact girder. The calculated plastic moment capacity of the intact girder was 248 kips. As mentioned earlier, the test was stopped before complete failure of intact girder. Therefore, the ultimate load carrying capacity of intact girder or its approximate plastic moment capacity was not obtained experimentally.

In ultimate Test C, the load was applied through a 10 in. square loading pad placed over the center of the intact girder. The specimen carried up to 180 kips before the loading pad suddenly punched through the deck. In general, the specimen showed similar behaviors to those observed in Test B, such that both girders experienced similar displacements and the applied load was

mainly resisted by the intact girder. The recorded strains indicated that the girders did not yield at the time of failure. The fact that neither of the girders yielded and the participation of the damaged girder was negligible indicates the capacity of the specimen, for the type of the loading used, is primarily dependent on the capacity of the deck and its interaction with the intact girder.

In ultimate Test D, the load was applied through a 10 in. square loading pad again, but over the center of the damaged girder. The specimen carried up to 83 kips of load before the loading pad suddenly punched through the deck. This failure mode was similar to that observed in Test C. No yielding was observed in the steel girders at the time of failure. The strain data at the bottom flange suggested the load was transferred to the intact girder uniformly within 5-ft distance measured from the mid-span. The load transferred through the cross-frames was found to be less than 2 kips. This suggested that most of the applied load was transferred to the intact girder through the deck. Although this test and Test C showed identical failure modes, the specimen failed much sooner than it in Test C. This suggests that the punching shear capacity of deck is influenced by existence of damage in the girder.

In ultimate Test E with a four-point loading configuration, the specimen carried up to 230 kips. The area of each loading point was 10 in. x 10 in., the same as it was in Tests C and D. This improvement in the load-carrying capacity of the specimen was due to the spreading of the applied load into four-point loading. The deck was cracked and damaged significantly along the center line of the bridge, especially where the wheel loads were applied. The intact girder was just right at yielding point. Data from both girders and cross-frames suggested that the load was transferred to the intact girder mainly through the deck.

Overall, the concrete deck was found to fail dominantly in shear in all the tests, except Test B in which loading was stopped before the specimen reached its load carrying capacity. Under single concentrated loading configuration, the specimen deck failed predominantly in two-way shear failure modes, commonly referred to as punching shear failure. When the specimen loaded over the entire width of the girder or with more than one loading point, one-way shear failure mode prevailed. The capacities obtained in these tests were found to be much higher than empirical shear capacities recommended by ACI 318- building code design provisions.

In general, a good match between experimental data and finite element analysis results was observed. The percentage differences between FEM analysis results and elastic test data in term of maximum displacement obtained was 5.1% on average. The finite element models were also able to capture the overall behaviors, the modes of failure, and the maximum load-carrying capacity as well as damages that were observed in the ultimate load tests. This verified the accuracy of the finite element modeling techniques that have been employed to study the behavior of steel twin box-girder systems in this project.

It should be noted that no previous research studies dealing with redundancy of twin steel box-girder bridges address shear failure of deck. This is an extremely important point when developing

methodology to assess the redundancy of twin steel box-girder bridges after experiencing fracture of tension elements.

10.4 Suggestions for Future Study

In general, this report provides an in-depth understanding of the performance of twin steel box-girder bridges and develops calibrated three dimensional nonlinear finite element models that can be used in future research. This project also provides a roadmap for development of a complete procedure for assessing redundancy of twin steel box-girder bridges and possibly removing them from fracture critical list. Discussions in Chapter 2 and in this summary chapter identify the remaining tasks that are required to completely develop the comprehensive methodology that allows DOTs to assess the performance of damaged twin steel box-girder bridges and determine whether or not these bridges are redundant. These remaining tasks and approaches to complete these tasks will be proposed for future research to be submitted to the Florida DOT. In future research, other possible loading conditions will be also considered before a full recommendation that shear failure in the deck is the governing failure mode of twin steel box-girder bridges.

References

- Altidis, P., and Adams, V. (2005). *Analyzing Hyperelastic Materials with Some Practical Considerations*. Retrieved from <http://www.ewp.rpi.edu/hartford/~ernesto/S2015/FWLM/TermProject/Misulia/Altidis2005-ANSYSUsersGroup-HyperelasticMaterials.pdf>
- American Association of State Highway Transportation Officials (2010). *AASHTO LRFD Bridge Design Specifications*. Washington, D.C.
- Barnard, T. J. (2006). *Constructing a Full-Scale Horizontally-Curved Twin Steel Trapezoidal Box Girder Bridge Segment to Determine Redundancies in Fracture Critical Bridges*. M.S. Thesis, University of Texas at Austin, Austin, TX.
- Barnard, T., Hovell, C.G., Sutton, J. P., Mouras, J.M., Neuman, B.J., Samaras, V.A., Kim, J., William, E.B, and Frank, K.H. (2010). *Modeling the Response of Fracture Critical Steel Box-Girder Bridges*. Report FHWA/TX-10/9-5498-1, Center for Transportation Research, University of Texas at Austin, Austin, TX.
- Connor, R.J., Dexter, R., and Mahmoud, H. (2005). *NCHRP Synthesis 354: Inspection and Management of Bridges with Fracture-Critical Details*. Transportation Research Board, National Academy Press, Washington, D.C.
- Dassault, S. (2007). *ABAQUS Analysis User's Manual*, Version 6.7, ABAQUS, Inc., Rising Sun Mills, R.I.
- Federal Highway Administration (2012). *Clarification of Requirements for Fracture Critical Members. Memorandum*. Retrieved from <https://www.fhwa.dot.gov/bridge/120620.cfm>
- Fisher, J.W., Pense, A.W., and Roberts, R. (1977). Evaluation of Fracture of Lafayette Street Bridge. *ASCE Journal of the Structural Division*, Vol. 103, No. ST7, pp.1339-1357.
- Frangopol, D.M., and Nakib, R. (1991). Redundancy in Highway Bridges. *Engineering Journal*, 28 (1), 45-50.
- Frangopol, D.M., and Liu, M. (2007). Maintenance and management of civil infrastructure based on condition, safety, optimization and life-cycle cost. *Structure and Infrastructure Engineering*, 3 (1), 29-41.
- Ghosn, M., and Moses, F. (1998). *NCHRP Report 406: Redundancy in Highway Bridge Superstructures*. Transportation Research Board, National Research Council, Washington, D.C.
- Ghosn, M., Moses, F., and Frangopol, D. M. (2010). Redundancy and robustness of highway bridge superstructures and substructures. *Structure and Infrastructure Engineering*. 6.1-2: 257-278.

- HNTB-Milwaukee Transportation Center (2005). *A Study of the Marquette Interchange HPS Twin Box Girder Structures*. Report WI-1060-05-1222, Milwaukee, WI.
- Hognestad, E. (1951). *A Study of Combined Bending and Axial Load in Reinforced Concrete Members*. University of Illinois Engineering Experimental Station, Bulletin Series, No. 399, pp. 128.
- Hovell, C. (2007). *Evaluation of Redundancy in Trapezoidal Box-Girder Bridges Using Finite Element Analysis*. M.S. Thesis, University of Texas at Austin, Austin, TX
- Kachlakev, D., Miller, T., and Yim, S. (2001). *Finite Element Modeling of Reinforced Concrete Structures Strengthened with FRP Laminates*. Final Report SPR 316, Oregon, USA.
- Lee, D.J. (1994). *Bridge Bearings and Expansion Joints*, 2nd Ed. London: E & FN Spon.
- Natario, F., Ruiz M.F., Muttoni, A. (2014). *Shear Strength of RC Slabs under Concentrated Loads near Clamped Linear Supports*. Engineering Structures, Vol 76, pp. 10-23.
- National Transportation Safety Board (2008). *Collapse of I-35W Highway Bridge Minneapolis, Minnesota, August 1, 2007*. Highway Accident Report NTSB/HAR-08/03. Washington, DC.
- Neuman, Bryce J. (2009). *Evaluating the Redundancy of Steel Bridges: Full-Scale Destructive Testing of a Fracture Critical Twin Box-Girder Steel Bridge*. M.S. Thesis, University of Texas at Austin, Austin, TX.
- Podolny, W. Jr., and Muller, J. M. (1982). *Construction of Design of Prestressed Concrete Segmental Bridges*. New York, NY: John Wiley and Sons.
- Schwendeman, L.P., and Hedgren, A.W. (1978). Bolted repair of fractured I-79 girder. *ASCE Journal of the Structural Division*, Vol. 104, No. 2, pp. 134-143.
- West Virginia DOT (2016). *Silver Bridge*. Retrieved from http://www.transportation.wv.gov/highways/bridge_facts/Modern-Bridges/Pages/Silver.aspx
- Willam, K.J., and Warnke, E.P. (1975). Constitutive model for the triaxial behavior of concrete. *Proceedings of International Association for Bridge and Structural Engineering*, Vol. 19, pp. 174.